

# **Precise Measurement of the Neutron Skin Thicknesses of $^{208}\text{Pb}$ and $^{48}\text{Ca}$**

A Dissertation Presented

by

**Weibin Zhang**

to

The Graduate School

in Partial Fulfillment of the Requirements

for the Degree of

**Doctor of Philosophy**

in

**Physics**

Stony Brook University

**May 2023**

**Stony Brook University**

The Graduate School

**Weibin Zhang**

We, the dissertation committee for the above candidate for the Doctor of Philosophy degree, hereby recommend acceptance of this dissertation.

**Abhay Deshpande – Dissertation Advisor**  
**Distinguished Professor, Department of Physics and Astronomy**

**James M. Lattimer – Chairperson of Defense**  
**Distinguished Professor, Department of Physics and Astronomy**

**Jiangyong Jia**  
**Adjunct Professor, Department of Physics and Astronomy**

**Ciprian Gal**  
**Assistant Research Professor**  
**Mississippi State University**

This dissertation is accepted by the Graduate School.

**Celia Marshik**  
**Dean of the Graduate School**

Abstract of the Dissertation

**Precise Measurement of the Neutron Skin  
Thicknesses of  $^{208}\text{Pb}$  and  $^{48}\text{Ca}$**

by

**Weibin Zhang**

**Doctor of Philosophy**

in

**Physics**

Stony Brook University

**2023**

Despite great leaps of development in nuclear physics over the past century, we still do not have a comprehensive understanding of nuclear structure. This is mainly due to the lack of precise knowledge of the neutron distribution inside nucleus. Electromagnetic probes are ineffective in probing neutrons, unlike their charged partners, the protons. Therefore, it is of great importance to constrain the neutron distributions experimentally. Heavy nuclei have more neutrons than protons in order to balance the repulsion between protons. In such neutron-rich nuclei, the extra neutrons are pushed out to the surface by the nuclear symmetry energy, forming the so-called “neutron skin”. The neutron skin can be probed with a well-established experimental technique – parity-violating electron scattering (PVES). Using the scattering of longitudinally polarized electrons by an unpolarized target, PREX-II and CREX measure the small parity-violating asymmetry in cross sections. Employing electrons with opposite helicities the weak form factor, the neutron distribution and the neutron skin thickness of the target nucleus are extracted. With excellent beam qualities and dedicated instrumentation at Jefferson Lab, the asymmetry measurements are statistics-limited. We report the results of these two high-precision measurements and their implications on broad topics, from the nuclear structures to the neutron stars.

# Contents

<b>List of Figures</b>	<b>vii</b>
<b>Acknowledgements</b>	<b>xi</b>
<b>1 Introduction</b>	<b>1</b>
1.1 Point-Neutron Radius and Neutron Skin . . . . .	1
1.1.1 Theoretical Models . . . . .	5
1.2 Symmetry Energy . . . . .	9
1.3 Nuclear Structure and Neutron Stars . . . . .	14
1.3.1 Ab-initio Method . . . . .	14
1.3.2 Nuclear Density Functional Theory (DFT) . . . . .	16
1.3.3 Neutron Stars . . . . .	18
1.4 Symmetry and Asymmetry . . . . .	19
1.4.1 Parity Symmetry . . . . .	20
1.4.2 Parity Violation . . . . .	22
1.5 Dynamics . . . . .	29
1.6 Why Pb208 and Ca48 . . . . .	30
<b>2 Experimental Setup</b>	<b>32</b>
2.1 Beam Parameters . . . . .	34
2.1.1 Uncertainty Budget . . . . .	35
2.1.2 Figure Of Merits (FOM) . . . . .	36
2.1.3 Helicity Flip Frequency . . . . .	39
2.2 Continuous Electron Beam Accelerator Facility (CEBAF) . . . . .	40
2.3 Polarized Electron Beam . . . . .	43
2.3.1 Polarized Electron Source . . . . .	43
2.3.2 Polarization Control . . . . .	45
2.3.3 Polarimeters . . . . .	50
2.4 Monitors . . . . .	55
2.4.1 BPMs . . . . .	55
2.4.2 BCMs . . . . .	57
2.4.3 SAMs . . . . .	58
2.4.4 Beam Modulation . . . . .	59
2.5 Target . . . . .	60

2.5.1	Target Cooling . . . . .	62
2.5.2	Raster . . . . .	62
2.5.3	Beamline Collimator and Sieve Slit Collimators . . . . .	63
2.5.4	Septum . . . . .	65
2.5.5	High Resolution Spectrometer (HRS) . . . . .	66
2.5.6	Detector Package . . . . .	67
2.5.7	Data AcQuisition (DAQ) . . . . .	71
<b>3</b>	<b>Data Analysis</b>	<b>76</b>
3.1	Raw Data . . . . .	76
3.1.1	Cut . . . . .	81
3.1.2	Beam Conditions . . . . .	82
3.1.3	Raw Asymmetry . . . . .	84
3.2	Beam False Asymmetry Correction . . . . .	84
3.2.1	Regression . . . . .	85
3.2.2	Beam Modulation (Dithering) . . . . .	92
3.2.3	Lagrange Multiplier . . . . .	95
3.3	Result . . . . .	97
<b>4</b>	<b>Transverse Asymmetry</b>	<b>99</b>
4.1	Motivation for the Transverse Asymmetry . . . . .	100
4.2	Measurement of the Transverse Asymmetry: the Method . . . . .	106
4.3	Data . . . . .	108
4.3.1	Data Analysis . . . . .	109
4.3.2	Systematic Uncertainties . . . . .	111
4.3.3	Dynamics . . . . .	115
4.3.4	Final Result . . . . .	115
<b>5</b>	<b>Systematic Uncertainties</b>	<b>118</b>
5.1	$Q^2$ and $\theta$ . . . . .	119
5.2	Carbon Contamination in PREX-II . . . . .	119
5.3	The CREX Acceptance Function . . . . .	126
5.3.1	Transportation Matrix . . . . .	127
5.3.2	Scattering Angle $\theta_{\text{lab}}$ . . . . .	129
5.3.3	Data . . . . .	130
5.3.4	Simulation . . . . .	132
5.4	Other Systematic Uncertainties . . . . .	139
<b>6</b>	<b>Results and Discussion</b>	<b>140</b>
6.1	Final Numbers . . . . .	140
6.1.1	Neutron Skin Thickness . . . . .	140
6.1.2	Density Dependence of the Symmetry Energy . . . . .	143
6.1.3	Difference Between the Charge and Weak Form Factors . . . . .	143
6.2	Physical Implication . . . . .	145
6.2.1	Nuclear Structure . . . . .	145

6.2.2	Neutron Stars . . . . .	148
6.3	Future Outlook . . . . .	150
<b>Bibliography</b>		<b>153</b>
<b>A</b>	<b>Symmetry Energy</b>	<b>163</b>
A.1	$^{208}\text{Pb}$ Foils Measurement . . . . .	163

# List of Figures

1.1	Characteristic of FFs w.r.t. different density distribution functions . . . . .	4
1.2	eA scattering . . . . .	6
1.3	Cross section of $^{48}\text{Ca}$ . . . . .	7
1.4	fermi distribution . . . . .	7
1.5	Neutron distribution from FSUGold . . . . .	8
1.6	Coulomb distortion . . . . .	9
1.7	PV asymmetry for $^{208}\text{Pb}$ and $^{48}\text{Ca}$ . . . . .	9
1.8	Correlation between the neutron skin thickness of $^{208}\text{Pb}$ and the slope of the symmetry energy ( $L$ ). The linear fit is $\Delta r_{np} = 0.101 + 0.00147L$ . [21]	13
1.9	Neutron EOS with different slope values . . . . .	13
1.10	Separation of nuclear forces. . . . .	15
1.11	Feynman diagrams for nuclear interactions . . . . .	16
1.12	An ab-initio calculation of the neutron skin thickness of $^{48}\text{Ca}$ . . . . .	17
1.13	Schematic plot of space reflection. . . . .	20
1.14	Parity transformation of the eA scattering . . . . .	21
1.15	Equivalent plot of Fig. 1.14: flip spin instead of momentum. . . . .	22
1.16	Fermi's interpretation of beta decay, current $j_{n \rightarrow p}$ convert $n$ into $p$ and current $j_{\nu_e \rightarrow e}$ creates $(e, \bar{\nu}_e)$ pair. . . . .	22
1.17	W-boson exchange picture of $\beta$ decay . . . . .	25
1.18	Feynman diagrams of elastic e-N scattering in PREX-II/CREX. . . . .	28
1.19	Nuclear Landscape. Figure from [40] . . . . .	30
2.1	Evolution of PVES experiments. . . . .	33
2.2	Scattering rate . . . . .	38
2.3	Asymmetry and sensitivity for $^{208}\text{Pb}$ . . . . .	38
2.4	Asymmetry and sensitivity for $^{48}\text{Ca}$ . . . . .	38
2.5	FOM . . . . .	39
2.6	JLab aerial view . . . . .	41
2.7	CEBAF . . . . .	42
2.8	Hall A . . . . .	42
2.9	Excitation of electrons in the semiconductor. Excited electrons with $J_z = +1/2$ (-1/2) are right (left)-handed. . . . .	44
2.10	Energy band diagram of GaAs . . . . .	44
2.11	Layout of a strained GaAs electron source and corresponding excitation plot. . . . .	45
2.12	The laser system at the CEBAF injector . . . . .	46

2.13	Schematic plot of the laser table. . . . .	47
2.14	Phase shift by going through the PC. . . . .	47
2.15	Schematic plot of the double Wien filters. The electron beam travels from left to right. [64] . . . . .	50
2.16	Mott polarimeter . . . . .	50
2.17	Sherman function . . . . .	51
2.18	Compton Chicane . . . . .	52
2.19	Compton analyzing power . . . . .	53
2.20	Schematic plot of the Moller Polarimeter. . . . .	55
2.21	Schematic plot of the Hall A beam monitor system and beam modulation system . . . . .	56
2.22	Schematic plot of a stripline BPM. . . . .	56
2.23	Hall A BCM system [68]. . . . .	57
2.24	Up: Schematic plot of the current converter; Down: $TM_{010}$ and $TM_{110}$ modes, the red arrows indicate the electric field. . . . .	58
2.25	Layout of SAMs [69]. . . . .	59
2.26	Scattering chamber . . . . .	61
2.27	Actual pictures of the production (left) and calibration (right) ladders. . . . .	61
2.28	Raster pattern . . . . .	63
2.29	Picture of $^{208}\text{Pb}$ targets after data collection. One can clearly see the shape of the raster pattern. Target 1 and 4 are melted. . . . .	63
2.30	Target temperature . . . . .	64
2.31	beamline collimator . . . . .	64
2.32	Target degradation . . . . .	65
2.33	sieve slit collimators . . . . .	66
2.34	pivot region . . . . .	66
2.35	HRS . . . . .	67
2.36	Q1 Collimator pairs . . . . .	68
2.37	Picture of the detector package. . . . .	68
2.38	VDC . . . . .	69
2.39	quartz . . . . .	70
2.40	photo-electron spectrum of quartz . . . . .	70
2.41	Electron position distribution, projected on the quartz plane. . . . .	71
2.42	Scatter plot of electrons on the left arm AT monitor plane. . . . .	72
2.43	Helicity timing diagram . . . . .	73
2.44	Integrating timing . . . . .	75
3.1	charge accumulation . . . . .	77
3.2	Runtime and charge statistics of CREX runs ( <code>ErrorFlag == 0</code> ). . . . .	77
3.3	Helicity pattern . . . . .	78
3.4	A ‘run’ plot: detector yield and asymmetry distribution in run 6600 . . . . .	79
3.5	A minirun plot . . . . .	80
3.6	A slug plot . . . . .	80
3.7	BPM4aX distribution in run 8019 . . . . .	82

3.8	Asymmetry slug-wise plot . . . . .	83
3.9	Slug-wise plot of beam position and angle . . . . .	84
3.10	Slug-wise mean values of the beam energy dispersion. Overall, an energy difference of $\sim 10$ ppb is achieved. . . . .	85
3.11	Slug-wise raw asymmetry average (left) and difference (right) for CREX. The right plot has three less slugs because there are three single-arm slugs. . . . .	85
3.12	Mulplots . . . . .	86
3.13	Correlation plot in run 7679 . . . . .	86
3.14	Minirun-wise energy slope ( $\partial(\text{asymmetry average})/\partial (\text{BPM12X})$ ) distribution in slug 202. The X-axis is the run number attached by a minirun number. . . . .	90
3.15	False asymmetry correction caused by the energy difference (BPM12X) in slug 202. . . . .	91
3.16	Regression correction asymmetry . . . . .	92
3.17	Slug-wise scatter plot (left) and experiment-wise histogram (right) of the regression-corrected null asymmetry. . . . .	92
3.18	An example of beam modulation. . . . .	93
3.19	Dithering corrected asymmetry . . . . .	95
3.20	Comparison of the asymmetry values corrected using regression (black), dithering (blue) and the Lagrange multiplier (red). . . . .	97
3.21	Part-wise and pitt-wise scattering plot of asymmetry values corrected with the Lagrange multiplier. . . . .	98
4.1	Transverse asymmetries measured in PREX-I [76]. . . . .	99
4.2	Feynman diagrams of AT . . . . .	104
4.3	Rotation by $\pi$ around the normal direction of the scattering plane. . . . .	105
4.4	Feynman diagrams of the OPE (left) and TPE (right) interactions. . . . .	106
4.5	Schematic plot of the scattering of a transversely polarized electron. . . . .	106
4.6	AT $^{48}\text{Ca}$ Mulplots . . . . .	109
4.7	AT $^{48}\text{Ca}$ asymmetry plot . . . . .	110
4.8	Sign-corrected transverse asymmetry in chronological order. Each data-point represents one slug. . . . .	112
4.9	PCREX AT result . . . . .	117
5.1	Momentum distribution of an watercell run . . . . .	119
5.2	Post target electron momentum distribution. The lower end tail comes from multi-scattering and radiation. . . . .	121
5.3	Theoretical asymmetries of the $e-^{12}\text{C}$ and $e-^{208}\text{Pb}$ scattering . . . . .	125
5.4	HRS transportation plots. . . . .	128
5.5	HCS and TCS . . . . .	129
5.6	Schematic plot of the vertex and apparent quantities. . . . .	130
5.7	Sieve pattern plots for the -10% septum current . . . . .	131
5.8	Sieve pattern plots for the nominal (scaled from PREX-II) . . . . .	132
5.9	Inner edge search (left arm) . . . . .	133

5.10	Sieve plot of the CREX tune. Centered at (-0.3, -1.5), the new beam position for the new target. . . . .	133
5.11	Sieve pattern plots from simulations with different septum currents. The red circles label extra or missing holes. . . . .	135
5.12	Position of the pinch point and the Q1 collimator. . . . .	135
5.13	Ratio plot of simulation to data . . . . .	136
5.14	Theta ratio plot . . . . .	136
5.15	$\theta_{lab}$ and $Q^2$ comparison between the best models and data (apparent values). The red line is the simulation result while the blue line comes from data. . . . .	138
5.16	Acceptance function extracted with the best models. . . . .	138
6.1	Correlation between the weak radius/neutron skin thickness and $\mathcal{A}_{PV}$ . .	142
6.2	Correlation plot between L and Rskin . . . . .	144
6.3	The difference between the charge and weak FFs for $^{48}\text{Ca}$ . . . . .	144
6.4	FF and Rskin difference . . . . .	145
6.5	2-neutron separation energy . . . . .	146
6.6	Density distributions for the EM charge (red), weak charge (blue) and baryon (black) in the $^{208}\text{Pb}$ nucleus [80]. . . . .	148
6.7	Light flux curve . . . . .	149
6.8	Tidal deformability versus Rskin . . . . .	150
6.9	Direct Urca threshold . . . . .	151
6.10	Various (proposed) measurements of the running weak mixing angle along the energy scale. . . . .	151
A.1	charge asymmetry outlier in run 4117, minirun 0 . . . . .	164

# Acknowledgements

I hardly ever imagine the moment of completing my graduate studies, but here I am. I would not have made it this far without the invaluable and generous help and support from various individuals, including my supervisor, colleagues, friends and family.

I would like to express my deepest gratitude to my advisor, Dr. Abhay Deshpande for his unwavering support throughout my Ph.D. studies, his meticulous care for me and his thoughtful guidance in my academic and research journey.

I still remember my first meet with Abhay in the small garden during a Friday social. That was my first month at Stony Brook and I was even not very fluent in English. Abhay warmly introduced his research and invited me to talk to him later, that was how I knew him and joined his group for my Ph.D. study. Obviously, he is super busy that I was first working with KK and then Ciprian, and finally Abhay himself. That does not mean he is neglecting his students. Actually, you can ask for his suggestions or helps whenever he is available, that is also what he always encourages us to do and what I would urge you to do, whenever you have a chance to talk to him.

I would like to extend my sincere thanks to Dr. Ciprian Gal, for his invaluable guidance and support in the PREX-II/CREX experiments. His expertise and advice regarding research have been instrumental in shaping my studies. Additionally, I am truly thankful for his assistance in various aspects of my work. I want to extend my thanks to Dr. Sanghwa Park for her help during the experiment and the contamination analysis afterward. It is highly beneficial to work with them.

I would like to thank Dr. Krishna Kumar, Dr. Kent Paschke, Dr. Paul King and all the other spokespersons of the PREX-II/CREX Collaboration. It is a great honor to be part of the collaboration. I am also grateful to every hard working postdoc and graduate student, especially the SBU group, including Dr. Chandan Ghost, Tao Ye, Cameron Clarke, and Ryan Richard. Thank you for making the measurements high-precision.

I also want to thank my friends and colleagues here at Stony Brook and those in Newport News. The fun time with you is an indispensable supplement to the research.

Last but not least, I would like to thank my parents, sister and relatives. Although I have not been able to meet them in person due to Covid, I can feel their presence around me, providing me with reliable support. Thank you so much!

# Chapter 1

## Introduction

The Lead Radius Experiment-II (PREX-II) and the Calcium Radius Experiment (CREX) are high-precision experiments that measure the tiny parity-violating (PV) asymmetry at the parts-per-million (ppm) level. These experiments use longitudinally polarized electrons to scatter off neutron-rich targets such as  $^{208}\text{Pb}$  and  $^{48}\text{Ca}$ , allowing for the extraction of weak form factor, weak charge, neutron distribution, and the neutron skin thickness of the target nucleus.

The PV asymmetry ( $\mathcal{A}_{\text{PV}}$ ) arises due to the interference between the electromagnetic (EM) and neutral weak one-boson exchange amplitudes, as weak interactions violate parity. As the EM interaction has been well-understood, the PV asymmetry measurement enables the extraction of the weak charge, and consequently, the distribution of the neutron (which carries almost all of the weak charge) inside a nucleus.

Parity-violating electron scattering (PVES) experiments require a longitudinally polarized electron beam of high quality, which was provided by the Continuous Electron Beam Accelerator Facility (CEBAF) at Thomas Jefferson National Accelerator Facility (TJNAF, also known as JLab) for PREX-II and CREX experiments. The excellent beam quality and dedicated instrumentation at JLab allowed for statistics-limited asymmetry measurements.

### 1.1 Point-Neutron Radius and Neutron Skin

Despite the advances in modern physics, we still lack a clear way to compute the size of a nucleus, and we may not even fully understand what we mean by “size”. In a simple model, one can estimate the nuclear radius as  $R = R_0 A^{1/3}$ , where  $A$  is the nuclear mass number and  $R_0$  is an experimentally determined constant ( $R_0 \approx 1.20 \text{ fm}$ ) [1]. However, this model only works for spherical nuclei and fails for deformed nuclei. It is better to calculate the radius of a nucleus from its nucleon density distribution, treating the nucleons as point particles. Physicists have successfully calculated and precisely measured the point-proton radii of many nuclei [2, 3]. However, the neutron, being neutral, poses a significant challenge to measuring the inner structure of nuclei. This is especially true for heavy nuclei, where more neutrons than protons are needed to bind

the nucleus. In such cases, it is the point-neutron radius (referred to hereafter as simply the neutron radius), rather than the point-proton radius (proton radius), that dominates the size of the nucleus.

When discussing the proton or neutron radius, we are referring to a concept within the framework of quantum mechanics (QM) rather than classical mechanics. In QM, a particle is described by a wave function, and the square of its normalized magnitude corresponds to the probability of finding the particle in a specific state. Therefore, the proton (neutron) root-mean-square (RMS) radius is defined as:

$$R_{p,n} \equiv \langle R_{p,n}^2 \rangle^{1/2} = \sqrt{\frac{\int d^3\mathbf{r} r^2 \rho_{p,n}(\mathbf{r})}{\int d^3\mathbf{r} \rho_{p,n}(\mathbf{r})}} \quad (1.1)$$

where  $\rho(\mathbf{r})$  is the normalized proton (neutron) density at position  $\mathbf{r}$ .

$$\int d^3\mathbf{r} \rho_{p,n}(\mathbf{r}) = 1 \quad (1.2)$$

There are numerous papers in the literature reporting high-precision measurements (with an uncertainty at the 0.01 fm level) of the proton radius ( $R_p$ , also called the charge radius) of various nuclei through atomic and nuclear experiments [2, 3]. In contrast, determining the neutron radius ( $R_n$ ) precisely is more challenging due to the neutron's lack of electric charge. This means its size can only be measured through strong or weak interactions, and both of which suffer from their limitations.

The weak interaction has a coupling constant ( $\alpha_W$ ) between  $10^{-7}$  and  $10^{-6}$  [4], which is much weaker than the electromagnetic coupling constant ( $\alpha$ ) of about  $10^{-2}$ . As a result, it is difficult to control systematic uncertainties if measured directly. To overcome this challenge, scientists have turned to the measurement of the parity-violating (PV) asymmetry. By taking the asymmetry between two electron beams with opposite helicities, many systematic uncertainties can be cancelled, leading to high precision measurements.

In terms of the strong interaction, the effective coupling has large theoretical uncertainties rooted in the non-perturbative nature of the underlying quantum chromodynamics (QCD) at low energy scale. Therefore, interpreting hadronic measurements often relies on theoretical models, leading to model-dependent results.

Despite the many challenges involved, there has been significant effort and progress from the scientific community to explore different aspects of the neutron radius (and neutron skin thickness). Hadronic probes, including pion [5], proton [6, 7], antiproton [8] and alpha particle [9], as well as atomic experiments such as electric dipole polarizabilities [10] and pygmy dipole resonances [11], provide valuable inputs to our understanding. Currently, experimental measurements of  $R_n$  have a resolution of better than 1%. On the theory side, the most precise estimate of  $R_n$  comes from nuclear models that have been constrained primarily by data other than measurements of neutron radii. Therefore, a precise measurement of  $R_n$  would provide a powerful independent check of the basic nuclear theory.

Experimentally, the nucleon radius is obtained from the corresponding form factors (FFs). In QM, under the Born approximation, the matrix element (ME) for the scattering of a plane wave (a free particle) from a Coulomb-like potential (a target nucleus) is:

$$\begin{aligned}
\mathcal{M}_{fi} &= \langle \Psi_f | V(\mathbf{r}) | \Psi_i \rangle = \int e^{-i\mathbf{p}_f \cdot \mathbf{r}} V(\mathbf{r}) e^{i\mathbf{p}_i \cdot \mathbf{r}} d^3 \mathbf{r} \\
&= \int e^{i(\mathbf{p}_i - \mathbf{p}_f) \cdot \mathbf{r}} d^3 \mathbf{r} \int \frac{Q_t \rho(\mathbf{r}')}{4\pi |\mathbf{r} - \mathbf{r}'|} d^3 \mathbf{r}' \\
&= \int \int e^{i\mathbf{q} \cdot \mathbf{r}} \frac{Q_t \rho(\mathbf{r}')}{4\pi |\mathbf{r} - \mathbf{r}'|} d^3 \mathbf{r} d^3 \mathbf{r}' \\
&= \int \int e^{i\mathbf{q} \cdot (\mathbf{r} - \mathbf{r}')} \frac{Q_t \rho(\mathbf{r}')}{4\pi |\mathbf{r} - \mathbf{r}'|} e^{i\mathbf{q} \cdot \mathbf{r}'} d^3 \mathbf{r} d^3 \mathbf{r}' \\
&= \int e^{i\mathbf{q} \cdot \mathbf{R}} \frac{Q_t}{4\pi |\mathbf{R}|} d^3 \mathbf{R} \int \rho(\mathbf{r}') e^{i\mathbf{q} \cdot \mathbf{r}'} d^3 \mathbf{r}' \\
&= (\mathcal{M}_{fi})_{\text{Mott}} F(\mathbf{q})
\end{aligned} \tag{1.3}$$

where  $\mathbf{p}_i$  and  $\mathbf{p}_f$  denote momentum of the incoming and outgoing particles respectively, and  $\mathbf{q} = \mathbf{p}_i - \mathbf{p}_f$  refers to the momentum transfer during the scattering, while  $Q_t$  represents the total charge of the target nucleus. The ME can be factorized into two parts: the amplitude of a Mott scattering, which describes the scattering of a particle from a point-like nucleus with charge  $Q_t$ , and a modification due to the inner structure of the target nucleus, known as the FF:

$$F(\mathbf{q}) = \int \rho(\mathbf{r}) e^{i\mathbf{q} \cdot \mathbf{r}} d^3 \mathbf{r} \tag{1.4}$$

The FF is the Fourier transform of the spatial density distribution. Conversely, once the FFs at different  $\mathbf{q}$  are known or measured, the charge distribution can be derived:

$$\rho(\mathbf{r}) = \int F(\mathbf{q}) e^{-i\mathbf{q} \cdot \mathbf{r}} d^3 \mathbf{q} \tag{1.5}$$

What is more,  $F(\mathbf{q})$  can be experimentally measured, as shown in Eq. 1.3:

$$F(\mathbf{q}) = \frac{\mathcal{M}_{fi}}{(\mathcal{M}_{fi})_{\text{Mott}}} = \sqrt{\frac{\sigma_{\text{measured}}}{\sigma_{\text{Mott}}}} \tag{1.6}$$

The problem is, experimentally, it is not feasible to cover the entire phase space of  $\mathbf{q}$ , and therefore, only a limited number of data points at selected  $\mathbf{q}$  can be measured. Consequently, phenomenological models are required to extract the charge density distribution.

For a spherically symmetric density distribution,  $\rho(\mathbf{r}) = \rho(|\mathbf{r}|) = \rho(r)$ , the corresponding FF is calculated as:

$$F(\mathbf{q}) = \int \rho(r) e^{iqr \cos \theta} 2\pi r^2 \sin \theta dr d\theta = 4\pi \int r \rho(r) \frac{\sin(qr)}{q} dr \tag{1.7}$$

One can observe that for a Coulomb-like potential,  $F(\mathbf{q})$  does not depend on the direction of  $\mathbf{q}$ , but solely on its magnitude:  $q$ . For the sake of Lorentz invariance,  $F$  is usually expressed in terms of  $Q^2 = -q^2$ , rather than  $q$ . Therefore, we will use  $F(q^2)$  or  $F(Q^2)$  in the following discussions.

Some typical spherically symmetric density distributions and their corresponding FFs are shown in Fig. 1.1.

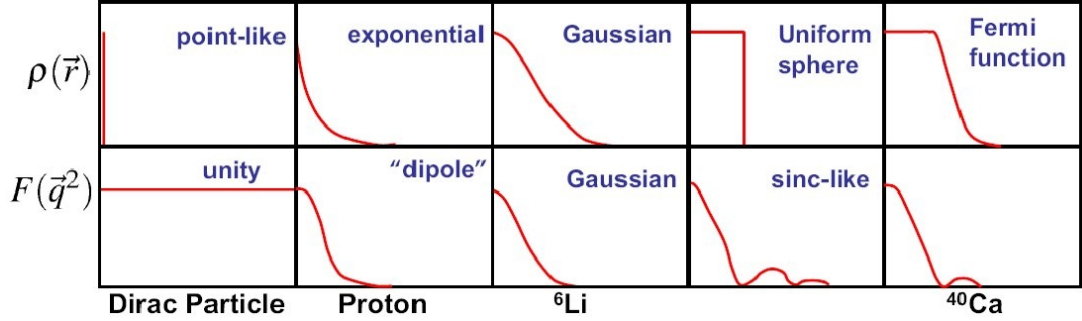


Figure 1.1: Characteristic of FFs w.r.t. different density distribution functions

In the small  $q^2$  limit ( $q^2 \ll 1$ ), one can perform a Fourier expansion on both sides of Eq. 1.7:

$$F(q^2) = F(0) + \frac{dF}{dq^2} \Big|_{q^2=0} \times q^2 + \dots \quad (1.8)$$

$$\begin{aligned} F(q^2) &= 4\pi \int r \rho(r) \frac{\sin(qr)}{q} dr \\ &= 4\pi \int \rho(r) r \left( r - \frac{1}{6} q^2 r^3 + \dots \right) dr \\ &= \int \rho(r) \left( 1 - \frac{1}{6} q^2 r^2 + \dots \right) 4\pi r^2 dr \\ &= 1 - \frac{1}{6} q^2 \langle R^2 \rangle + \dots \end{aligned} \quad (1.9)$$

Matching Eq. 1.8 to 1.9 yields

$$\langle R^2 \rangle = \int r^2 \rho(r) d^3 \mathbf{r} = -6 \frac{dF(q^2)}{dq^2} \Big|_{q^2=0} \quad (1.10)$$

This equation hints how to measure the RMS radius. One can measure the FFs at several small  $q^2$  points, extrapolate them to  $q^2 = 0$ , and then calculate the slope at  $q^2 = 0$  to obtain the RMS radius.<sup>1</sup>

---

<sup>1</sup>This is why we use the RMS radius rather than the more physically intuitive definition of:  $\langle R \rangle = \int r \rho(\mathbf{r}) d^3 \mathbf{r}$ .

For electrically charged proton, the FF will be the precisely measured EM FF:

$$\langle R_p^2 \rangle \approx \langle R_{ch}^2 \rangle = -6 \frac{dF_{EM}(q^2)}{dq^2} \Big|_{q^2=0} \quad (1.11)$$

Since neutron is electrically neutral, its RMS radius will be measured from its weak charge FF:

$$\langle R_n^2 \rangle \approx \langle R_W^2 \rangle = -6 \frac{dF_W(q^2)}{dq^2} \Big|_{q^2=0} \quad (1.12)$$

The difference between the neutron and the proton RMS radii is referred to as the neutron skin thickness:

$$R_{\text{skin}} = R_n - R_p = \sqrt{\langle R_n^2 \rangle} - \sqrt{\langle R_p^2 \rangle} \quad (1.13)$$

a concept that was first suggested by Johnson and Teller [12] and first observed in the  $K^-$  meson capture processes [13].

The neutron skin is founded in neutron-rich atomic nuclei that contain more neutrons than protons. Analogous to the atomic electron shell model, the nuclear shell model proposes that protons and neutrons also arrange themselves in shells from low to high energy levels without disturbing each other. The higher the energy level, the larger the orbital radius. For symmetric nuclei, we expect similar neutron radii to proton radii. However, in neutron-rich nuclei, the extra neutrons must occupy higher energy orbits after filling all the low energy ones, resulting in a larger radius than that of the proton, and therefore, the formation of a neutron skin.

The deep reason why these extra neutrons form a neutron skin instead of a neutron core lies in the symmetry energy and its dependence on nucleon density. The symmetry energy represents the penalty for breaking the proton-neutron symmetry, whose value increases with nucleon density [14]. As the core has a higher nucleon density than the surface, the higher the density, the larger the symmetry energy, leading to a lower binding energy <sup>2</sup>, and less stable nuclei. So it is the symmetry energy that pushes these extra neutrons to the surface. On the other hand, as the number of nucleons on the surface increases, so does the surface tension, which favors squeezing extra neutrons into the core. The balance between the symmetry energy and the surface tension determines the thickness of the neutron skin.

### 1.1.1 Theoretical Models

Though we lack knowledge of the actual neutron distribution, it is reasonable to assume that protons and neutrons share the same distribution function, with only minor variations in function parameters, even in nuclei with asymmetric numbers of protons and neutrons. Hence, the proton distribution provides a good starting point for studying the neutron distribution, considering our comprehensive understanding of proton distribution

---

<sup>2</sup>the energy needed to break down a bounded nuclear system:  $BE(N, Z) = M(N, Z)c^2 - Zm_p c^2 - Nm_n c^2$

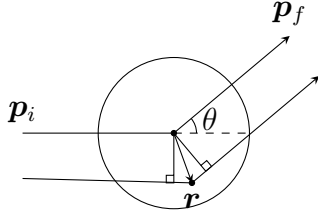


Figure 1.2: Schematic plot of eA scattering. As one can see, the wave scattered at position  $\mathbf{r}$  will travel extra distance compared to the one scattered at the object center, which leads to a phase difference of:  $\delta = e^{i[\mathbf{p}_i \cdot \mathbf{r} + (-\mathbf{p}_f) \cdot \mathbf{r}]} = e^{i\mathbf{q} \cdot \mathbf{r}}$ .

through various eA and AA scatterings. The elastic scattering cross-section is described in [15].

$$\frac{d\sigma}{d\Omega} = \left( \frac{d\sigma}{d\Omega} \right)_{\text{Mott}} |F(q^2)|^2 \quad (1.14)$$

The FF encodes information about the charge distribution of a nucleus. It is an interference effect: the finite size of the scattering center introduces a phase difference between different plane waves scattered from different points in space.

Consider a simple hard ball model:

$$\rho(r) = \begin{cases} \frac{3}{4\pi R^3} & r \leq R \\ 0 & r > R \end{cases} \quad (1.15)$$

Then the FF will be:

$$F(q^2) = \frac{3}{(qR)^3} (\sin(qR) - qR \cos(qR)) \quad (1.16)$$

where  $q = 2p \sin(\theta/2)$ .

Given the Mott cross section [15]:

$$\left( \frac{d\sigma}{d\Omega} \right)_{\text{Mott}} = \frac{Z^2 \alpha^2}{4E^2 \sin^4(\theta/2)} \cos^2(\theta/2) \quad (1.17)$$

the resulting cross section, as a function of the scattering angle, is shown in Fig. 1.3.

While the hard ball model does not reproduce the experimental distribution, it does characterize the real distribution and demonstrate how the FF modifies the cross section: the oscillating dips. A more realistic model for the density distribution is the Woods-Saxon distribution (also known as the Fermi two-parameter model or the Fermi distribution):

$$\rho(r) = \frac{\rho(0)}{1 + \exp((r - R)/t)} \quad (1.18)$$

where  $R = (1.2A^{1/3} - 0.48)$  fm denotes the nuclear force radius at which  $\rho(r) = \frac{\rho(0)}{2}$ . The parameter  $t$ , which is typically in the range of  $0.4 - 0.5$  fm for  $A > 40$ , indicates the

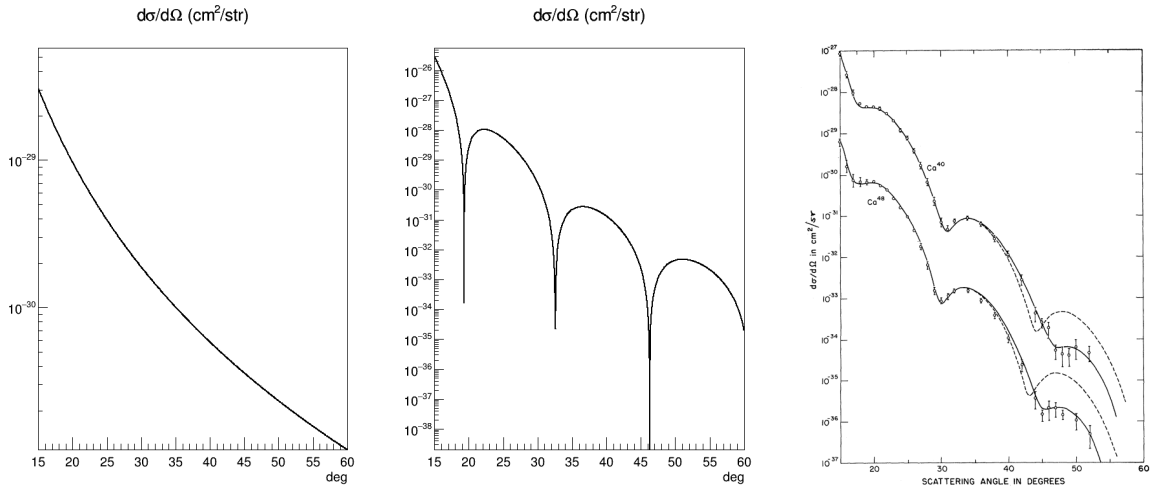


Figure 1.3: Left: Mott cross section for electron elastically scattered off a  $^{48}\text{Ca}$  target with parameters:  $p = E = 757.5$  MeV. Middle: cross section for electron elastically scattered off  $\text{Ca48}$  with the hard ball model (1.15) with parameters:  $E = 757.5$  MeV,  $R = A^{1/3}$  fm. Right: experimental values (dots) and theoretical prediction (solid line) assuming the charge distribution as a three-parameter Fermi function (1.19). for  $^{48}\text{Ca}$  ( $^{40}\text{Ca}$ ) targets, which are multiplied by  $10^{-1}$  ( $10$ ) to differentiate them [16]. A similar cross section plot for  $^{208}\text{Pb}$  can be found in [17].

surface thickness, over which  $\rho(r)$  falls from 90% to 10%.

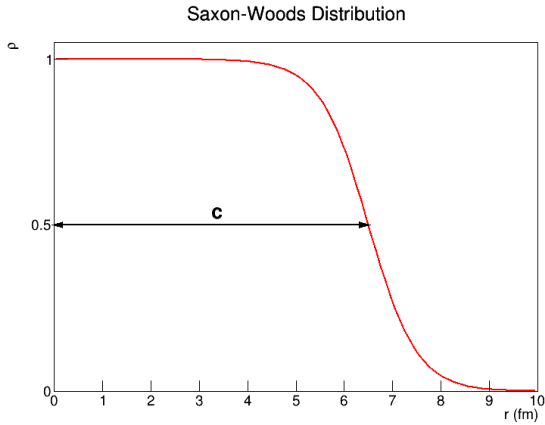


Figure 1.4: In the nuclear shell model, it is assumed that nucleons occupy different eigenstates of the same spherically symmetric average potential. However, unlike in the atomic shell model, this potential must be guessed. It turns out that the Woods-Saxon model is a good candidate for this potential:  $V(r) = -\frac{V(0)}{1+\exp((r-c)/a)}$  ( $c$  is the half-height radius and  $a$  represents diffuseness of the distribution). This potential is formed by all other nucleons and is approximately proportional to the nucleon density, therefore the same distribution for nucleon density.

Fig. 1.3 (right) uses a fine tuned three-parameter Fermi function:

$$\rho(r) = \frac{\rho_0(1 + \omega r^2/R^2)}{1 + \exp((r - R)/t)} \quad (1.19)$$

the central depression parameter  $\omega$  allows the central density to be depressed or raised, depending on the sign of  $\omega$ . More detailed discussion about the Fermi distribution can be found in [18].

One example model based on the Fermi distribution is the FSUGold [19], the neutron distribution of  $^{208}\text{Pb}$  predicted by FSUGold is shown in Fig. 1.5.

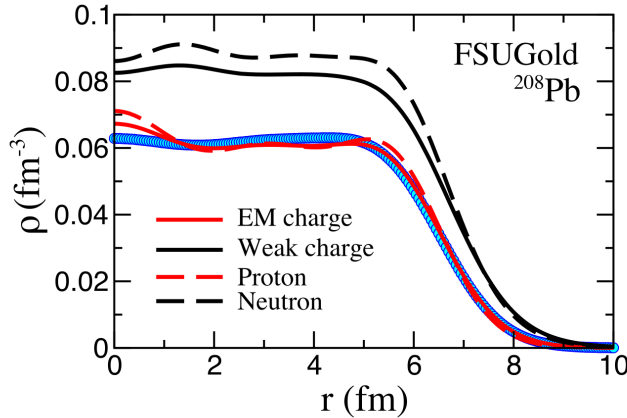


Figure 1.5: Neutron and weak charge distribution in  $^{208}\text{Pb}$  predicted by the FSUGold model. The blue dots are experimental measurements of the charge distribution.

For medium and heavy nuclei, the Born approximation, which assumes that the incoming and outgoing waves are plane waves, is no longer valid. Because the waves are distorted by the strong nuclear EM field. Therefore, the Coulomb distortion effect needs to be taken into account, which significantly modifies the PV asymmetry.

Coulomb distortion can be understood as multiple EM interactions with the same nucleus, so the distortion correction is proportional to  $Z\alpha$ . This correction is particularly important for heavy nuclei like  $^{208}\text{Pb}$  due to their large  $Z$  values. Coulomb-distortion can reduce the PV asymmetry by as much as 30%, as shown in Fig. 1.6.

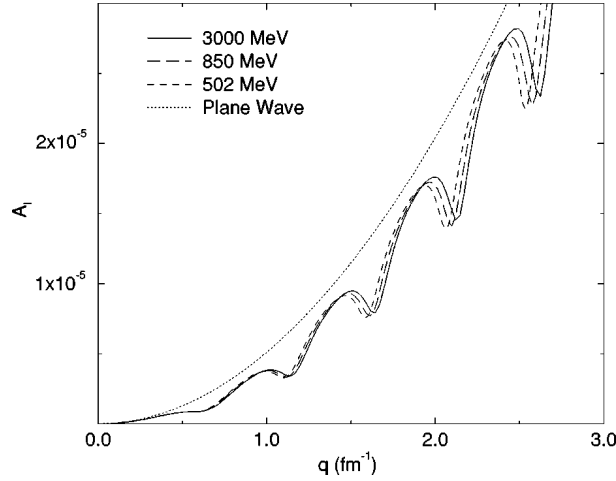


Figure 1.6: Comparison of PV asymmetries with and without the effect of Coulomb distortion for  $^{208}\text{Pb}$ . The calculation assumes the same weak and charge densities, which are taken to be the three-parameter Fermi function [20].

With these information, one can solve the Dirac equation directly to obtain the PV asymmetry, as illustrated in Fig. 1.7.

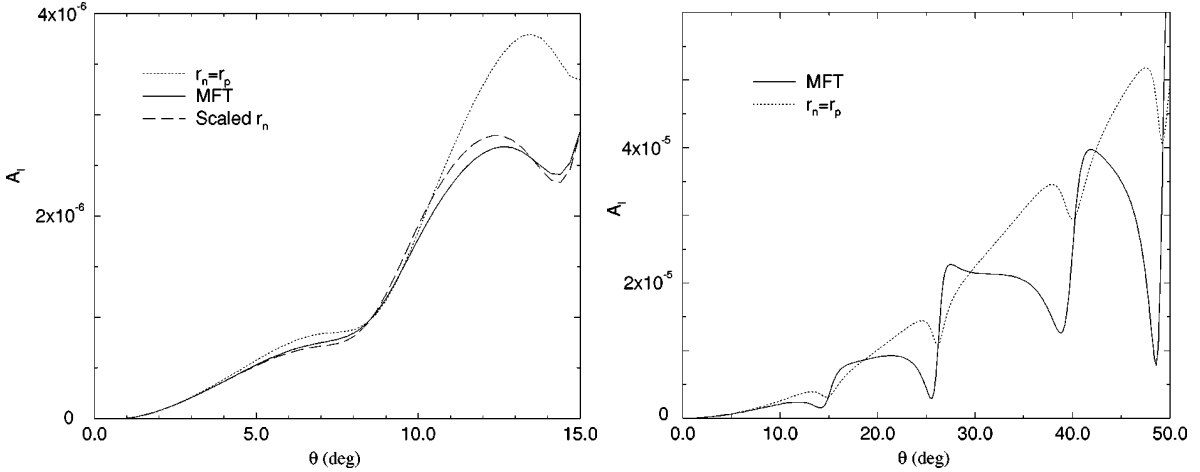


Figure 1.7: PV asymmetry for  $^{208}\text{Pb}$  (left) and  $^{48}\text{Ca}$  (right) versus scattering angle at 850 MeV, including the Coulomb distortion effect. The dotted curve assumes the same weak and charge distributions (three-parameter Fermi function), while the solid curve is based on relativistic mean field densities. The dashed curve uses a stretched density distribution based on the three-parameter Fermi function [20].

## 1.2 Symmetry Energy

The binding energy of a nuclear system depends on both the total number of nucleons ( $A$ ), and the difference between the numbers of protons and neutrons. To describe it, we

can use the liquid drop model (LDM), which gives rise to the Bethe-Weizsäcker Semi-empirical Mass Formula:

$$E \text{ (MeV)} = a_V A - a_S A^{2/3} - a_C \frac{Z(Z-1)}{A^{1/3}} - a_A \frac{(N-Z)^2}{A} + \delta a_p A^{-3/4}$$

$$\delta a_p A^{-3/4} = \begin{cases} +a_p A^{-3/4} & Z, N \text{ even} \\ 0 & A \text{ odd} \\ -a_p A^{-3/4} & Z, N \text{ odd (A even)} \end{cases} \quad (1.20)$$

- Volume term ( $a_V$ ): strong force between nearby nucleons ( $a_V \sim 16$  MeV)
- Surface term ( $a_S$ ): correction to the volume term ( $a_S \sim 18$  MeV)
- Coulomb term ( $a_C$ ): repulsion due to EM charge ( $a_C \sim 0.7$  MeV)
- Asymmetry term ( $a_A$ ): correction from the Pauli exclusion principle ( $a_A \sim 24$  MeV)
- Pairing term ( $\delta$ ): correction caused by the spin coupling effect ( $a_p \sim 34$  MeV)

The first three terms have a natural explanation: the volume term reflects the short-range nature of the strong interaction; the surface term arises due to the incomplete surrounding of nucleons on the surface by other nucleons; and the Coulomb term represents the EM interactions among protons.

The asymmetry term may not be immediately obvious. It is based solely on the Pauli exclusion principle. In heavy nuclei, more neutrons than protons are needed to balance the repulsion between protons. Due to the Pauli exclusion principle, the energy of these extra neutrons will be higher than that of the rest, introducing a correction term.

The pairing term is a small correction due to nuclei's preference for 'paired spin'. Nuclei with even numbers of protons ( $Z$ ) and neutrons ( $N$ ) are more stable than those with an odd number of  $Z$  and  $N$ .

Regarding the nuclear system as a free Fermi gas <sup>3</sup> of protons and neutrons, the kinetic energy ( $E_k$ ) of this system will be:

$$E_k = E_N + E_Z = \frac{3}{5} Z E_F^p + \frac{3}{5} N E_F^n \quad (1.21)$$

Since the Fermi energy is proportional to  $n^{2/3}$ ,  $E_k$  can be written as:

$$E_k = C(Z^{5/3} + N^{5/3}) \quad (1.22)$$

where  $C$  is a constant coefficient. Expanding it in terms of the neutron-proton asymmetry

---

<sup>3</sup>an ensemble of non-interacting fermions

$(N - Z)$ , we get: (see appendix A)

$$\begin{aligned} E_k &= 2^{-2/3}C \left( A^{5/3} + \frac{5}{9} \frac{(N - Z)^2}{A^{1/3}} \right) + O((N - Z)^4) \\ &= \frac{3}{5}E_F A + \frac{1}{3}E_F \frac{(N - Z)^2}{A} + O((N - Z)^4) \end{aligned} \quad (1.23)$$

The first term in Eq. 1.23 contributes to the volume term of the binding energy and the second term is minus the asymmetry term because  $E_k$  contributes to the binding energy negatively.

To facilitate a general discussion, we can neglect the Coulomb term in Eq. 1.20 to focus on the homogeneous nuclear interaction between nucleons. Additionally, the pairing term is comparatively small and can be ignored. By doing so, we can broaden the scope of our discussion to include any nuclear system that consists of  $Z$  charge-less protons and  $N$  neutrons. As a result, the equation of state (EOS) for nuclear matter becomes simplified.

$$\begin{aligned} E &= a_V A - a_S A^{2/3} - a_A \frac{(N - Z)^2}{A} \\ e &= \frac{E}{A} = a_V - a_S A^{-1/3} - a_A \frac{(N - Z)^2}{A^2} \end{aligned} \quad (1.24)$$

We can further simplify the equation by omitting the surface term in Eq. 1.24. It is worth noting that since we cannot assume a specific shape for the nuclear system, the surface term becomes insignificant. Moreover, in the case of an infinite nuclear system, the surface term is unnecessary as there is no surface to consider. By disregarding the surface term, we write:

$$\begin{aligned} E &= a_V A - a_A \frac{(N - Z)^2}{A} \\ e &= \frac{E}{A} = a_V - a_A \frac{(N - Z)^2}{A^2} = e_0(A) - a_A \beta^2 \end{aligned} \quad (1.25)$$

Here we define  $\beta = \frac{N - Z}{N + Z}$  as the isospin asymmetry, which represents the difference between the number of neutrons and protons in the nucleus.

In the case of an infinite system, the nucleon density, denoted by  $\rho$ , is a more appropriate parameter than  $A$  for characterising the EOS. Consequently, we can substitute the parameters  $N$ ,  $Z$  and  $A$  with their corresponding densities:  $\rho_n$ ,  $\rho_p$  and  $\rho$  ( $\beta = \frac{\rho_n - \rho_p}{\rho}$ ). Likewise,  $E$  is replaced by its density counterpart  $e$ .

Thus, we are considering an infinite uniform nuclear system at zero temperature that interacts solely through the nuclear force. For any given density  $\rho$ , Eq. 1.25 will be:

$$e(\rho, \beta) = e(\rho, 0) + S(\rho) \beta^2 + O(\beta^4) \quad (1.26)$$

where  $S(\rho)$  is a density dependent coefficient.

This is an expansion of the binding energy per nucleon around  $\beta = 0$ . Since the proton

and neutron exhibit isospin symmetry, any isoscalar quantity  $F$  remains unchanged when interchanging neutrons and protons ( $n \leftrightarrow p$ ), while isovector quantity  $G$  changes sign. As  $\beta$  is an isovector, the expansion of a smooth function  $F(\beta)$  around  $\beta = 0$  includes only even terms:

$$F(\beta) = F_0 + F_2\beta^2 + F_4\beta^4 + \dots$$

On the other hand, for a smooth function  $G(\beta)$ , its expansion around  $\beta = 0$  contains only odd terms:

$$G(\beta) = G_1\beta + G_3\beta^3 + \dots$$

As evident from Eq. 1.25,  $e$  is an isoscalar quantity and remains unchanged under the  $n \leftrightarrow p$  interchange. The coefficient  $S(\rho) = \frac{\partial^2 e(\rho, \beta)}{\partial \beta^2}$  is what we call the symmetry energy, a crucial parameter in describing a wide range of nuclear properties and phenomena. It quantifies the energy release by changing all protons to neutrons in a symmetric nuclear system.

The dependence of  $S$  on  $\rho$  is just as important as the symmetry energy itself. By convention,  $S(\rho)$  is expanded around the nuclear saturation density  $\rho_0$ , based on the free Fermi gas assumption:

$$S(\rho) = S(\rho_0) + \frac{dS}{d\rho} \bigg|_{\rho_0} (\rho - \rho_0) + \frac{1}{2} \frac{d^2 S}{d\rho^2} \bigg|_{\rho_0} (\rho - \rho_0)^2 + \frac{1}{6} \frac{d^3 S}{d\rho^3} \bigg|_{\rho_0} (\rho - \rho_0)^3 + \dots \quad (1.27)$$

From this expansion, we have some auxiliary parameters defined:

$$\begin{aligned} S_0 &= S(\rho_0) \\ L &= 3\rho_0 \frac{dS}{d\rho} \bigg|_{\rho_0} \\ K_{\text{sym}} &= 9\rho_0^2 \frac{d^2 S}{d\rho^2} \bigg|_{\rho_0} \\ Q_{\text{sym}} &= 27\rho_0^3 \frac{d^3 S}{d\rho^3} \bigg|_{\rho_0} \end{aligned} \quad (1.28)$$

Among them,  $L$  represents the dependence of  $S$  on  $\rho$ .

Being such an important parameter, great efforts have been devoted to extracting  $S$  and  $L$ . By comparing Eq. 1.25 and 1.26, we can directly obtain:

$$S(\rho) \approx -a_A \quad (1.29)$$

The problem is that this only tells the symmetry energy at the nuclear density ( $\sim 1 \times 10^{44} \text{ m}^{-3}$ ). It does not provide any information about the symmetry energy at other density values, particularly at the nuclear saturation density of approximately  $1.5 \times 10^{44} \text{ m}^{-3}$ , let alone the density dependence of the symmetry energy.

A more practical strategy to calculate  $S(\rho)$  is the energy density functionals (EDF), which fits the binding energy throughout the nuclear mass table to find out the best

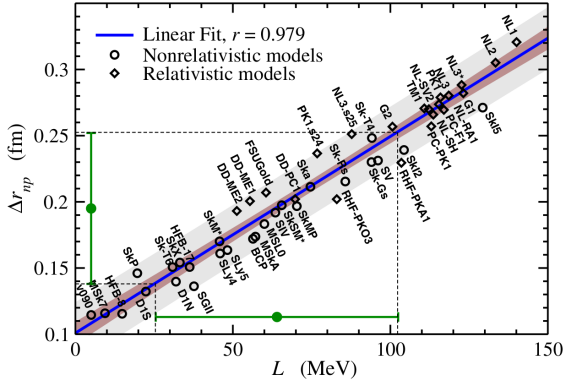


Figure 1.8: Correlation between the neutron skin thickness of  $^{208}\text{Pb}$  and the slope of the symmetry energy ( $L$ ). The linear fit is  $\Delta r_{np} = 0.101 + 0.00147L$ . [21]

EDF, then use it to calculate  $S(\rho)$ . Fitting parameterizations are constrained by nuclear densities, proton RMS radii and nuclear binding energies. The issue is many EDFs can fit equally well with these constraints, but have quite different  $L$  values, as shown in Fig. 1.9. An experiment that could identify  $S(L)$  value without model dependence, would be helpful in understanding the symmetry energy and the EOS.

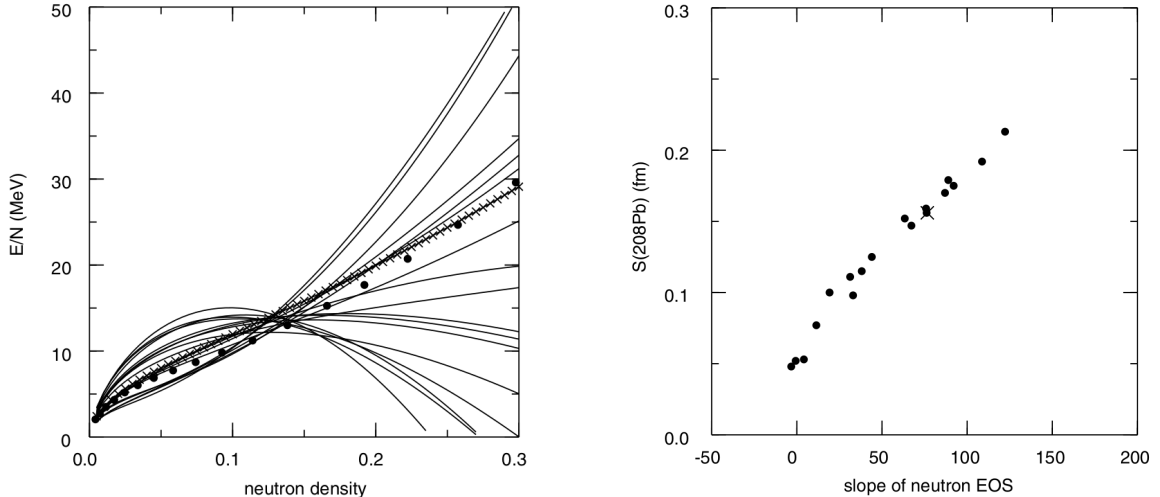


Figure 1.9: Left: Neutron EOS for 18 Skyrme [22] parameter sets. The filled circles represent the Friedman-Panharipande (FG) variational calculations and the crosses are SkX predictions [23]. It is apparent that different models exhibit significant variations in their symmetry energies. Right: Density dependence of the symmetry energy (in units of MeV fm $^3$ /neutron) at  $\rho_n = 0.1$  neutron/fm $^3$  vs the neutron skin thickness in  $^{208}\text{Pb}$  for the 18 Skyrme parameter sets. The cross corresponds to SkX. Determination of the neutron skin thickness in  $^{208}\text{Pb}$  will greatly narrow down the list of possible candidates. [24].

## 1.3 Nuclear Structure and Neutron Stars

Unlike particle physics, which has a standard model to describe the fundamental particles and their interactions, there is no such standard model in nuclear physics that can accurately capture the static properties and dynamics of atomic nuclei, such as the ground state binding energy, nuclear size, and excitation spectrum.

The fundamental building blocks of nuclei are quarks and gluons. Theoretically, all properties of a nucleus can be derived directly from the interactions of these elementary particles using QCD. Many groups work in this direction, attempting to derive nuclear structure from underlying QCD. Unfortunately, at the low energy scale where nuclei exist, the non-perturbative nature of QCD makes the problem so complicated that even the state-of-the-art lattice QCD technique can only resolve a small nuclear system with a few nucleons. This suggests that quarks and gluons are not the most suitable degrees of freedom to describe nuclei using current techniques.

Instead of quarks and gluons, nucleons and their intermediary particles, pions, are a more natural choice of degrees of freedom for the description of nuclei since they are the direct components of nuclei. This was the approach physicists used to study nuclear systems in the beginning (1930s [25]). Many nuclear models were developed based on the meson-exchange phenomenology, called phenomenological interactions, up until the mid-1990s. With the uncovering of QCD, this approach was re-discovered from the aspect of QCD: quarks and gluons are confined in colorless nucleons and pions, the nuclear force is just the residual interaction between quarks and gluons. Since it is rooted in underlying QCD, it is appropriate to describe nuclear systems in terms of nucleons and pions.

### 1.3.1 Ab-initio Method

Although it is still unknown how the nuclear force emerges from the underlying QCD interaction, it is expected that both the force and the interaction should share the same properties, particularly the same symmetries and symmetry-breaking patterns. Among these properties, the spontaneously broken chiral symmetry is considered the most significant. With this in mind, S. Weinberg proposed a new framework in the 1990s called chiral effective field theory ( $\chi$ EFT), which is an effective realization of the underlying QCD Lagrangian based on chiral symmetry [26].

Ab-initio methods try to calculate the wave function of nuclei by solving the many-body Schrödinger equation:

$$H |\psi\rangle = E |\psi\rangle \quad (1.30)$$

where the Hamiltonian is

$$H = T + V = \frac{1}{A} \sum_{i < j}^A \frac{(\mathbf{p}_i - \mathbf{p}_j)^2}{2m} + \sum_{i < j}^A V_{ij}^{NN} + \sum_{i < j < k}^A V_{ijk}^{NNN} + \dots \quad (1.31)$$

In  $\chi$ EFT, the potential must adhere to the same symmetries as QCD, such as space-time translation, rotation, parity transformation, and others. Most importantly, the

potential should preserve the spontaneously broken chiral symmetry. Constrained by these symmetries, the operator for the potential takes the form of:

$$\mathcal{O}_V = \{\mathbb{1}, \boldsymbol{\sigma}_i \cdot \boldsymbol{\sigma}_j, \mathbf{L} \cdot \mathbf{S}, S_{ij}\} \times \{\mathbb{1}, \boldsymbol{\tau}_i \cdot \boldsymbol{\tau}_j\} \quad (1.32)$$

where  $\boldsymbol{\sigma}_i \cdot \boldsymbol{\sigma}_j$  ( $\boldsymbol{\tau}_i \cdot \boldsymbol{\tau}_j$ ) denotes the spin (isospin) interaction,  $\mathbf{L} \cdot \mathbf{S}$  indicates the spin-orbit interaction and the tensor interaction is represented by

$$S_{ij}(\mathbf{x}) = 3(\boldsymbol{\sigma}_i \cdot \hat{\mathbf{x}})(\boldsymbol{\sigma}_j \cdot \hat{\mathbf{x}}) - \boldsymbol{\sigma}_i \cdot \boldsymbol{\sigma}_j \quad (1.33)$$

where  $\hat{\mathbf{x}}$  is the unit vector along vector  $\mathbf{x}$ .

The typical momentum (soft scale) in nuclei is of the order of  $p \sim m_\pi \sim \mathcal{O}(100 \text{ MeV})$ , while the short-range structure involving heavier meson (hard scale) is about  $\Lambda_\chi \sim m_\rho \sim \mathcal{O}(700 \text{ MeV})$ . The clear gap between the soft and hard scales allows for the separation of the long-range force from the short-range one, as shown in Fig. 1.10. The term ‘effective’ in the name of  $\chi$ EFT refers to the fact that only the long-range pion exchange in the low-energy scale will be considered, while heavier mesons will be integrated out as low-energy constants (LECs), which are phenomenologically fitted.

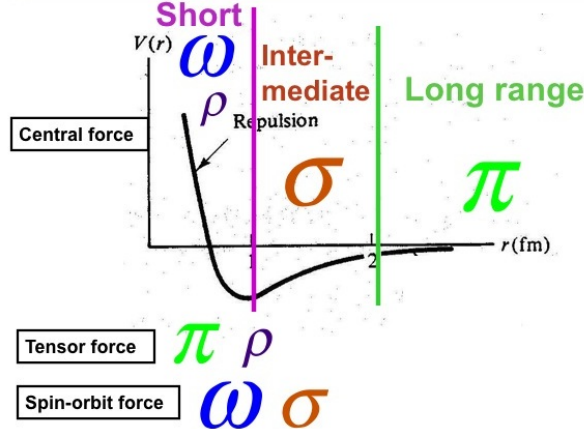


Figure 1.10: Separation of nuclear forces.

By employing the effective theory, one can expand the potential in terms of  $\left(\frac{Q}{\Lambda_\chi}\right)^\nu$ , where  $Q$  is the momentum transfer between two nucleons and  $\Lambda_\chi$  is the cut-off scale where short-range interactions become important, and  $\nu$  is the power that defines the order of the interaction. The order of the expansion determines the accuracy of the calculation, with higher orders resulting in more accurate results, as illustrated in Fig. 1.11.

$$V = \sum_i V^{(i)} = V_{LO}^{(0)} + V_{NLO}^{(2)} + V_{NNLO}^{(3)} + V_{NNNLO}^{(4)} \dots \quad (1.34)$$

In this way, one can calculate nuclear force to any precision, by including more higher order terms, if not limited by computing power.

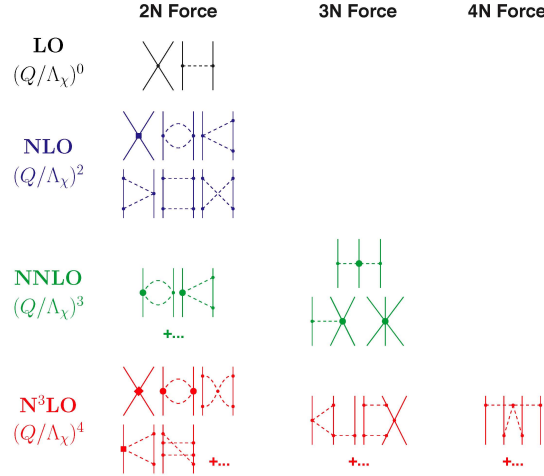


Figure 1.11: Feynman diagrams for nuclear interactions. Solid lines refer to nucleons while dashed lines represent exchanged pions. The first column shows nucleon-nucleon force, and the following two columns correspond to the three-nucleon and four-nucleon forces. Rows show diagrams of leading order (LO), next-to-leading order (NLO) and so forth.

For example, the  $1\pi$ -exchange potential between two nucleons is:

$$V_{2N}^{1\pi} = -\frac{g_A^2}{4F_\pi^2} \frac{(\boldsymbol{\sigma}_1 \cdot \mathbf{q})(\boldsymbol{\sigma}_2 \cdot \mathbf{q})}{\mathbf{q}^2 + M_\pi^2} \boldsymbol{\tau}_1 \cdot \boldsymbol{\tau}_2 \quad (1.35)$$

where  $g_A$  and  $F_\pi$  are the axial-vector coupling constant and the pion decay constant.

After choosing the nuclear force potential, one can solve the Schrödinger equation to obtain the eigenstate wave functions, which can then be used to extract various properties. Ab-initio methods can be extended to nuclei with multiple nucleons using many-body techniques such as self-consistent Green's function, coupled cluster, and renormalization group.

### 1.3.2 Nuclear Density Functional Theory (DFT)

While ab-initio methods have been successful in calculating properties of light and some medium nuclei, they currently lack the computational resources needed to handle heavy nuclei, due to the exponential growth in the number of nucleons. As an alternative approach, nuclear DFT begins with nuclear phenomenology and attempts to derive the underlying QCD theory from there.

The DFT method originates from solid-state physics, where it was first used to tackle the many-electron problem. It is based on the Hohenberg and Kohn (HK) theorem [20], which states that the total energy of a system can be expressed in terms of its fermion (electron) density (density functional). Minimizing this density functional leads to the

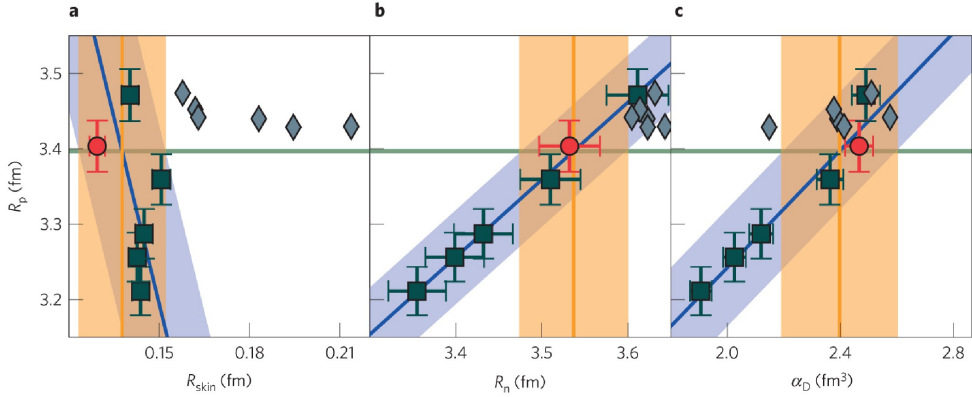


Figure 1.12: An ab-initio calculation of the neutron skin thickness of  $^{48}\text{Ca}$ . From left to right, the neutron skin thickness (a), neutron radius (b) and electric dipole polarizability (c) of  $^{48}\text{Ca}$  are plotted against its proton radius. The ab-initio predictions are shown as red circles and dark squares, while DFT results are represented by gray diamonds. The blue line represents a linear fit to ab-initio predictions and the blue band represents the corresponding uncertainty of the blue line. The experimental value of  $R_p$  is marked by the horizontal green line, and its intersection with the blue line and blue band yields the vertical orange line and orange band, respectively. [27].

ground-state density distribution, thereby reducing the number of degrees of freedom from  $3N$  to 3. The only problem is that the HK theorem does not provide a prescription for constructing the density functional.

Unlike the Coulomb interaction, nuclear interactions are more complex because the three-nucleon interaction cannot be ignored. Fortunately, nuclear interactions are short-range, and experimental observations suggest that nucleons in nuclei do not interact frequently because their mean free path is about or larger than the nuclear radius. This validates the use of the mean-field method, where nucleons move in a one-body potential that averages over interactions with all other nucleons. The Woods-Saxon potential is the most commonly used potential for this purpose.

Given the Hamiltonian of a nuclear system:

$$H = \sum_i^N -\frac{\hbar^2}{2m} \nabla_i^2 + \frac{1}{2} \sum_{i \neq j=1}^N V(i, j) \quad (1.36)$$

The Hartree-Fock (HF) energy of the system is:

$$E_{HF}(\rho) = \langle \Phi | H | \Phi \rangle \quad (1.37)$$

where  $|\Phi\rangle$  is the Slater determinant made up with the single-particle wave function  $|\phi\rangle$ .

The HK theorem states that:

$$\frac{\delta}{\delta \rho(\mathbf{r})} \left( E_{HF} - \epsilon \int d^3 r' \phi_j^*(\mathbf{r}') \phi_j(\mathbf{r}') \right) = 0 \quad (1.38)$$

With

$$\rho(\mathbf{r}) = \sum_i^N \phi_i^*(\mathbf{r})\phi_i(\mathbf{r}) \quad (1.39)$$

It leads to the well-known HF equations:

$$\begin{aligned} -\frac{\hbar^2}{2m}\nabla^2\phi_j(\mathbf{r}) + \sum_{l=1}^N \int d^3\mathbf{r}'\phi_l^*(\mathbf{r}')V(\mathbf{r}, \mathbf{r}')(\phi_l(\mathbf{r}')\phi_j(\mathbf{r}) - \phi_l(\mathbf{r}')\phi_l(\mathbf{r}')) &= \epsilon_j\phi_j(\mathbf{r}) \\ \langle j | \frac{-\hbar^2}{2m}\nabla^2 | j \rangle + \sum_{l=1}^N \langle jl | V(1 - P_{12}) | jl \rangle &= \epsilon_j \end{aligned} \quad (1.40)$$

where  $P_{12}$  exchanges particles 1 and 2. So the total energy is:

$$E_{HF} = T + \frac{1}{2} \sum_{jl} \int d^3rd^3r' \phi_j^*(\mathbf{r}')\phi_l^*(\mathbf{r}')V(\mathbf{r}, \mathbf{r}')(\phi_j(\mathbf{r}')\phi_l(\mathbf{r}') - \phi_l(\mathbf{r}')\phi_j(\mathbf{r}')) \quad (1.41)$$

where T is the kinetic energy.

Given the interaction (the potential term  $V(\mathbf{r}, \mathbf{r}')$ ), one can calculate the density distribution, and consequently, the total energy of the system as well as other relevant properties. One widely used model in this paradigm is the Skyrme force.

$$\begin{aligned} V_{\text{Skyrme}}(\mathbf{r}_1, \mathbf{r}_2) &= t_0(1 + x_0P_\sigma)\delta(\mathbf{r}_1 - \mathbf{r}_2) + \frac{1}{2}t_1(1 + x_1P_\sigma)(\mathbf{k}^{\dagger 2}\delta(\mathbf{r}_1 - \mathbf{r}_2) + \delta(\mathbf{r}_1 - \mathbf{r}_2)\mathbf{k}^2) \\ &+ t_2(1 + x_2P_\sigma)\mathbf{k}^\dagger \cdot \delta(\mathbf{r}_1 - \mathbf{r}_2)\mathbf{k} + \frac{1}{6}t_3(1 + x_3P_\sigma)\delta(\mathbf{r}_1 - \mathbf{r}_2)\rho^\alpha\left(\frac{\mathbf{r}_1 + \mathbf{r}_2}{2}\right) \\ &+ iW_0(\boldsymbol{\sigma}_1 + \boldsymbol{\sigma}_2) \cdot \mathbf{k}^\dagger \times \delta(\mathbf{r}_1 - \mathbf{r}_2)\mathbf{k} \end{aligned} \quad (1.42)$$

which has up to 10 parameters that are constrained by experimental data, such as nuclear mass, radius and binding energy.

By measuring the neutron skin thicknesses of  $^{208}\text{Pb}$  and  $^{48}\text{Ca}$ , we can verify the credibility of these ab-initio and DFT methods, and greatly constraint the parameter space of each model. This can help in developing a more general nuclear theory.

### 1.3.3 Neutron Stars

A neutron star is the densest celestial body known, the pressure due to gravity is so strong that even atoms inside the star collapse, crushing together electrons and protons into neutrons, giving the star its name. Neutron stars are primarily observed as pulsars or in binary systems. Exploring the basic properties of neutron stars can shed light on fundamental questions shared between nuclear physics and astrophysics. For example:

- What is the high density phase of QCD?

- What is the structure of many compact and energetic celestial bodies? and what determines their EM, neutrino and gravitational radiations?

Despite a 18 orders of magnitude difference in size (fm vs km), the neutron star and the nuclear neutron skin share the same EOS. It is the pressure of neutron-rich matter that supports the neutron skin against its surface tension and a neutron star against its own gravity. Thus, the neutron skin thickness and the size of a neutron star are connected through the pressure of neutron-rich matter, specifically the density dependence of the symmetry energy  $L$ . The larger the neutron skin thickness, the larger the symmetry energy slope  $L$ , the larger the pressure, and therefore the larger the radius of a neutron star, at the same mass.

Quantitatively, a neutron star is predominantly composed of neutrons, with only a few protons, resulting in a high isospin asymmetry parameter,  $\beta \approx 1$ . Thus, Eq. 1.26 can be simplified to:

$$e(\rho) = e(\rho, 0) + S(\rho) \quad (1.43)$$

Pressure is derived to be:

$$P = \rho^2 \frac{de}{d\rho} \simeq \rho^2 \frac{dS}{d\rho} \approx \frac{L\rho^2}{3\rho_0} \quad (1.44)$$

It is seen that the pressure of neutron-rich matter depends on  $L$ .

For a cold neutron star, the correlation between its radius and pressure is [28]:

$$R \simeq C(\rho, M) P^{0.23-0.26} \quad (1.45)$$

where  $C$  is a coefficient that depends on the density  $\rho$  and the stellar mass  $M$ , and  $P$  is evaluated at the density  $\rho$ . This formula works for  $\rho$  in the range of 1 to 1.5 times the nuclear saturation density.

Once the value of  $L$  is fixed by an experimental measurement of the neutron skin thickness in  $^{208}\text{Pb}$ , one is able to calculate the radius of a cold neutron star, providing guidance for experimental observations.

## 1.4 Symmetry and Asymmetry

Symmetry is a powerful framework in modern physics. For any physical system, by applying proper symmetry requirements, one can derive or predict the Lagrangian of the system, which in turn yields its properties and Equation of Motion (EOM).

Common space-time symmetries can be categorized into continuous and discrete symmetries. Continuous symmetries include translation, rotation and boost, while discrete symmetries involve space reflection (P) and time reversal (T). Another important discrete symmetry is charge conjugation (C).

Giving their crucial role, the violation of symmetries holds significant importance. Presently, it is widely accepted that continuous symmetries are conserved by all interactions, while weak interaction violates certain discrete symmetries, specifically C, P, and

their combination CP. There are some speculations that the strong interaction can violate the CP symmetry, but no experimental observation reported thus far [29].

### 1.4.1 Parity Symmetry

Parity symmetry is a discrete symmetry that asserts the equivalence of physical laws between the mirror (reflection) world and the real world, as shown in Fig. ??.

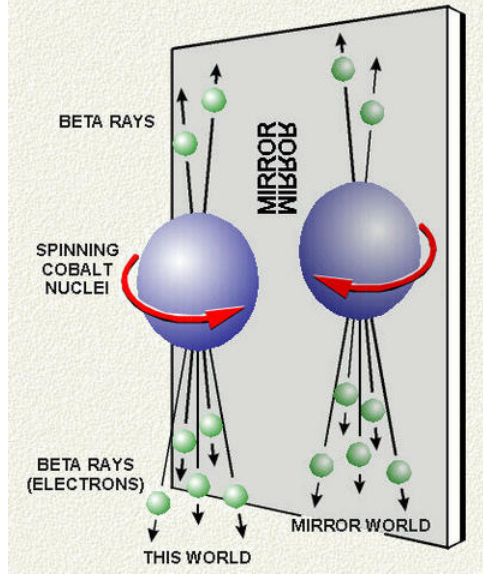


Figure 1.13: Schematic plot of space reflection.

The parity operation will flip the sign of any spatial coordinate:

$$P : \mathbf{r} \rightarrow -\mathbf{r} \quad (1.46)$$

The same for any spatial vector, like momentum ( $\mathbf{p}$ ), angular momentum ( $\mathbf{L}$ ) and the EM vector potential ( $\mathbf{A}$ ).

In the language of QM, the parity operator ( $\hat{\pi}'$ ) will transform a wave function, as shown in Eq. 1.47.

$$\hat{\pi}'\psi(x, y, z) = \eta\psi(-x, -y, -z) \quad (1.47)$$

where  $\eta$  is a coefficient picked up by the transformation. It is expected that the state goes back to itself after 2 times of parity transformations:

$$|\hat{\pi}'^2\psi(x, y, z)|^2 = |\psi(x, y, z)|^2 \quad \hat{\pi}'\psi(x, y, z) = e^{i\phi/2}\psi(-x, -y, -z) \quad (1.48)$$

which means  $\hat{\pi}'$  is a unitary operator. The pick up phase can be absorbed into the operator to get the new parity operator (what we use hereafter):

$$\hat{\pi} = \hat{\pi}'e^{-i\phi/2} \quad (1.49)$$

Then we have

$$\hat{\pi}^2 = 1 \quad (1.50)$$

So  $\hat{\pi}$  has eigenvalues of  $p = \pm 1$ . States with eigenvalue of +1 are called parity-even states and the others with eigenvalue of -1 the parity-odd states.

For a scalar potential,  $V(\mathbf{r}) = V(r)$  ( $[\hat{\pi}, V] = 0$ ), the parity operator  $\hat{\pi}$  commutes with the Hamiltonian ( $[\hat{\pi}, \mathcal{H}] = 0$ ). Therefore, the energy eigenstates are also eigenstates of  $\hat{\pi}$ . Among these states, the orbital angular momentum eigenstates are particularly interesting. Given an orbital angular momentum  $\mathbf{L}$  with z-axis projection  $L_z$ , one will have:

$$\hat{\pi} |\mathbf{L}, L_z\rangle = (-1)^L |\mathbf{L}, L_z\rangle \quad (1.51)$$

Another quantity similar to orbital angular momentum in many aspects but distinct in terms of parity is spin. Spin, like orbital angular momentum, is an angular momentum, but it is an intrinsic property rather than a result of space-time motion. Unlike  $\hat{\pi}$ , which is an operation of space, spin is not affected by  $\hat{\pi}$ . Consequently, the parity of a spin state is arbitrary assigned as long as particles and their antiparticles have opposite parities. For instance, electrons, protons and neutrons are assigned even parity while their antiparticles have odd parity.

Now, let us delve into the concept of helicity, which represents the projection of the spin onto the direction of momentum:

$$H \equiv \frac{\mathbf{s} \cdot \mathbf{p}}{|\mathbf{s} \cdot \mathbf{p}|} \quad (1.52)$$

If a particle's spin is aligned (opposite) to its momentum, we refer to it as a right-handed (left-handed) particle. When we apply the parity operator to a helicity eigenstate, the helicity gets reversed due to the flip in momentum's sign, while the spin remains unchanged. This can be observed in Fig. 1.14.

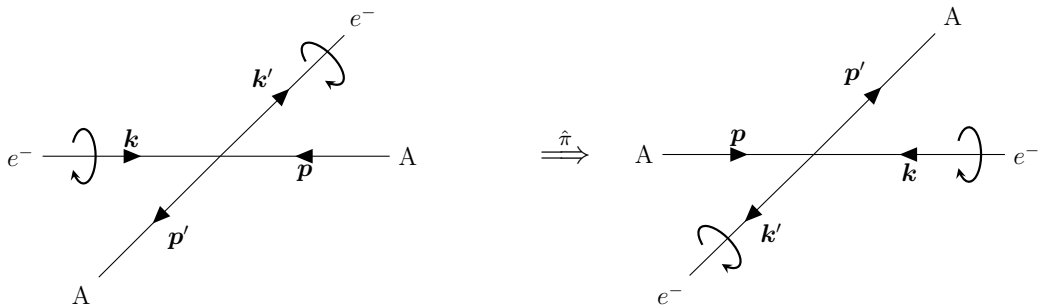


Figure 1.14: Parity transformation of the  $eA$  scattering

If parity is not conserved, a discrepancy will arise between the two scattering processes depicted in Fig. 1.14, which aligns with the measurement conducted in PREX-II/CREX. In experimental practice, it is more convenient to reverse the spin direction rather than the momentum direction, as exemplified in Fig. 1.15, which serves as an equivalent representation of Fig. 1.14.

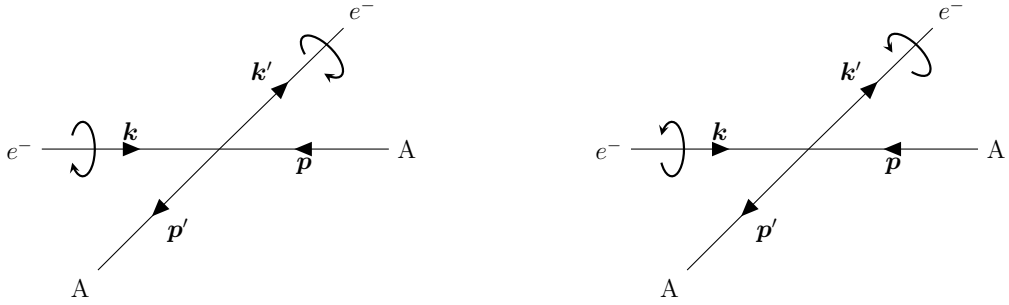


Figure 1.15: Equivalent plot of Fig. 1.14: flip spin instead of momentum.

### 1.4.2 Parity Violation

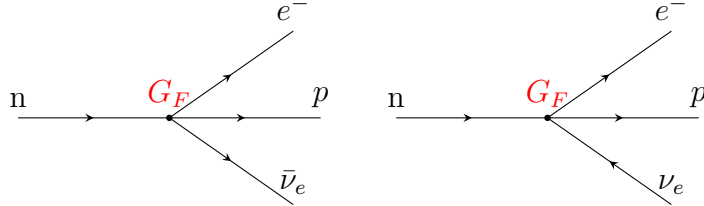


Figure 1.16: Fermi's interpretation of beta decay, current  $j_{n \rightarrow p}$  convert  $n$  into  $p$  and current  $j_{\nu_e \rightarrow e}$  creates  $(e, \bar{\nu}_e)$  pair.

The history of parity violation can be traced back to the early days of particle physics. In 1933, Fermi proposed the concept of four-fermion interaction, also known as Fermi's interaction, to explain beta decay [30]. This interaction serves as a low-energy approximation of the weak interaction. In Fermi's theory, by drawing an analogy to the EM interaction where an electron emits a photon:  $\mathcal{M} = e j_\mu^{em} A^\mu$ ,  $\beta$  decay was interpreted as the emission of an electron and an electron antineutrino  $(e, \bar{\nu}_e)$  pair. During the process, a neutron transforms into a proton, and thus, it involves the coupling of two currents:

$$\mathcal{M} = G_F (\bar{p} \mathcal{O}^\mu n) (\bar{e} \mathcal{O}_\mu \nu_e) = G_F j_{(n \rightarrow p)}^\mu j_{\nu_e \rightarrow e}^{(\nu_e \rightarrow e)} \quad (1.53)$$

Where  $G_F = 1.166 \times 10^{-5} \text{ GeV}^{-2}$  is the coupling constant that can be experimentally determined, and  $\mathcal{O}$  represents the possible operators. Among the five possible Lorentz invariant bilinear forms (Scalar (S:  $\mathcal{O} = \mathbb{1}$ ), pseudo-scalar (P:  $\mathcal{O} = \gamma^5$ ), Vector (V:  $\mathcal{O} = \gamma^\mu$ ), Axial vector (A:  $\mathcal{O} = \gamma^\mu \gamma^5$ ) and Tensor (T:  $\mathcal{O} = \sigma^{\mu\nu} = \frac{i}{2}(\gamma^\mu \gamma^\nu - \gamma^\nu \gamma^\mu)$ ), Fermi selected the vector current to maintain consistency with the EM interaction:  $j^\mu = \bar{u} \gamma^\mu u$ .

### V-A Theory

In 1956, T. D. Lee and C. N. Yang, both of whom were students of Fermi, put forward the groundbreaking concept of parity violation to address the  $\tau - \theta$  puzzle [31], and they achieved success. Just one year later, their hypothesis was experimentally tested by Wu

et al. in the decay of polarized  $^{60}\text{Co}$  nuclei [32], providing evidence that parity is not conserved in weak interactions and consequently, the weak current is not pure vector-like. The experimental observation of maximal violation of parity, where left-handed electrons interact weakly while right-handed electrons do not [33], prompted Sudarshan and Marshak [34], as well as Feynman and Gell-Mann [35], to revise Fermi's theory. They introduced a new current in place of the vector current to account for parity violation:

$$\mathcal{M} = \frac{G_F}{\sqrt{2}} (\bar{p}\gamma^\mu(\mathbb{1} - \gamma^5)n)(\bar{e}\gamma_\mu(\mathbb{1} - \gamma^5)\nu_e) \quad (1.54)$$

The factor of  $\frac{1}{\sqrt{2}}$  was introduced to keep  $G_F$  unchanged (Fermi's original theory did not account for the left-handed nature of neutrinos, leading to a decay phase space twice the actual value in nature. To address this issue, one can either modify the value of  $G_F$  or introduce a correction factor  $\frac{1}{\sqrt{2}}$ ). In the V-A theory, the 'V' and 'A' parts refer to the vector and axial vector currents, respectively, which are responsible for Fermi transitions and Gamow-Teller transitions.

$$j_V^\mu = \bar{u}\gamma^\mu u \quad j_A^\mu = \bar{u}\gamma^\mu\gamma^5 u \quad (1.55)$$

The form of V-A as  $\mathbb{1} - \gamma^5$  happens to be the projection operator:

$$P_R = \frac{\mathbb{1} + \gamma^5}{2} \quad P_L = \frac{\mathbb{1} - \gamma^5}{2} \quad (1.56)$$

By definition of  $\gamma$  matrix, one can easily verify that:

$$\begin{aligned} \left(\frac{\mathbb{1} - \gamma^5}{2}\right)^2 &= \frac{\mathbb{1} - \gamma^5}{2} & \gamma^\mu \frac{\mathbb{1} - \gamma^5}{2} &= \frac{\mathbb{1} + \gamma^5}{2} \gamma^\mu \\ \gamma^\mu \frac{\mathbb{1} - \gamma^5}{2} &= \frac{\mathbb{1} + \gamma^5}{2} \gamma^\mu \frac{\mathbb{1} - \gamma^5}{2} \end{aligned} \quad (1.57)$$

Then one can see the handedness of the new current:

$$\mathcal{M} = \frac{4G_F}{\sqrt{2}} (\bar{p}\gamma^\mu \frac{\mathbb{1} - \gamma^5}{2} n)(\bar{e}\gamma_\mu \frac{\mathbb{1} - \gamma^5}{2} \nu_e) = \frac{4G_F}{\sqrt{2}} (\bar{p}_L \gamma^\mu n_L)(\bar{e}_L \gamma_\mu \nu_{e,L}) \quad (1.58)$$

Only left-handed particles (and right-handed antiparticles) can participate in weak interactions. Analogous to EM interactions, the strength of the weak interaction is proportional to a weak charge, known as weak isospin ( $T_3$ ). Right-handed fermions (and left-handed antifermions) have a weak isospin of 0, while left-handed fermions possess non-zero weak charges.

Due to the conservation of lepton number in weak interactions and the charge current's ability to change the electric charge of particles, it is natural to organize them in a lepton doublet:

$$f_L = \begin{pmatrix} \nu_l \\ l \end{pmatrix}_L \quad (1.59)$$

This implies that for left-handed fermions:  $T = \frac{1}{2}, T_3 = \pm \frac{1}{2}$

By extending the application of the V-A theory to include additional decay and scattering processes, such as  $\mu^+ \rightarrow e^+ + \nu_e + \bar{\nu}_\mu$  and  $\pi^- \rightarrow l + \bar{\nu}_l$ , we will need two charge currents:

$$j_\mu^- = \bar{\nu}_{e,L} \gamma_\mu e_L \quad j_\mu^+ = \bar{e}_L \gamma_\mu \nu_{e,L} \quad (1.60)$$

which can be expressed more concisely using the lepton doublet notation:

$$j_\mu^\pm = \bar{f}_L \gamma_\mu t^\pm f_L \quad (1.61)$$

where,

$$t^+ = \begin{pmatrix} 0 & 1 \\ 0 & 0 \end{pmatrix} = \frac{1}{2}(\sigma^1 + i\sigma^2) \quad t^- = \begin{pmatrix} 0 & 0 \\ 1 & 0 \end{pmatrix} = \frac{1}{2}(\sigma^1 - i\sigma^2) \quad (1.62)$$

The SU(2) symmetry becomes evident when examining the expressions for  $t^\pm$ , which are combinations of the first two Pauli matrices, serving as raising ( $t^+$ ) and lowering ( $t^-$ ) operators. Now, let us consider the third component:

$$j_\mu^3 = \bar{f}_L \gamma_\mu \frac{1}{2} t^3 f_L = \frac{1}{2}(\bar{\nu}_{e,L} \gamma_\mu \nu_{e,L} - \bar{e}_L \gamma_\mu e_L) \quad (1.63)$$

This current, known as the neutral current, posed a question regarding its interpretation. At that time, the only known neutral current was the EM current. However, it could not be attributed to the EM current since neutrinos are electrically neutral. The nature of the neutral current remained a mystery until Glashow [36], Weinberg [37] and Salam [38] proposed the GWS model. In this model, the neutral current is considered to be a part of a more comprehensive neutral current – the so-called  $SU(2)_L \times U(1)$ .

## W Bosons

One problem with Fermi's theory is that the cross section ( $\sigma \sim G_F^2 E^2$ ) diverges at high energy. The solution to this problem came with the introduction of mediating bosons:  $W^\pm$ . Unlike the electrically neutral photon responsible for EM interactions, the W boson is charged and has a heavy mass, as implied by the short-range behavior of the weak interaction. The introduction of W fields makes the weak interaction more similar to the EM interaction:

$$\mathcal{L} = g_W (J^+ W^+ + J^- W^-) \quad (1.64)$$

Recognizing the similarities between the weak and EM interactions, it becomes natural to unify them within a multiplet of gauge fields. Building upon Yang and Mills' non-abelian gauge theory, Salam and Weinberg successfully developed a unified framework for both interactions, known as the  $SU(2)_L \times U(1)$  structure, which was initially proposed by Glashow. In this framework, The  $SU(2)$  part is generated by the 'weak isospin', with the subscript L denoting that only left-handed fermions couple to  $SU(2)$  gauge bosons. The

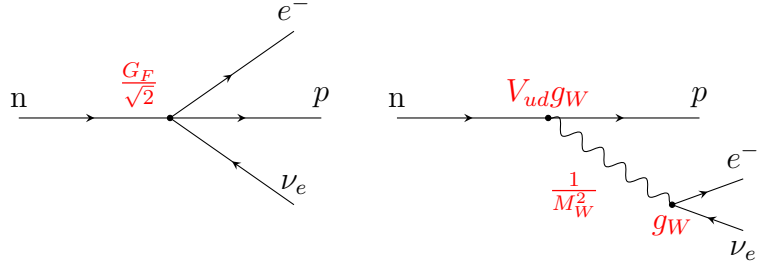


Figure 1.17: W-boson exchange picture of  $\beta$  decay

$U(1)$  part arises from the ‘weak hypercharge’. Together, There are 4 vector bosons:

$$W^1, W^2, W^3, B$$

These bosons interact with both left-handed and right-handed fermions. To simplify the discussion, let us consider only the first generation leptons here:

$$\psi_1 = \begin{pmatrix} \nu_e \\ e^- \end{pmatrix} \quad \psi_2 = \nu_{e,R} \quad \psi_3 = e_R^- \quad (1.65)$$

The left-handed doublet  $\psi_1$  interacts with all bosons, so the covariant derivative is:

$$D_\mu = \partial_\mu - ig \frac{\sigma^a}{2} W_\mu^a - ig' y_1 B_\mu \quad (1.66)$$

where  $y_1$  is the hypercharge of  $\psi_1$ . The corresponding coupling Lagrangian is:

$$\mathcal{L}_{int,L} = -i\bar{\psi}_1 \gamma^\mu (g \frac{\sigma^a}{2} W_\mu^a + g' y_1 B_\mu) \psi_1 = -i(g \mathbf{j}^\mu \mathbf{W}_\mu + g' y_1 \bar{\psi}_1 \gamma^\mu \psi_1 B_\mu) \quad (1.67)$$

Right-handed singlets do not couple to weak vector bosons, therefore the covariant derivative for right-handed fermions is:

$$D_\mu = \partial_\mu - ig' y_{2(3)} B_\mu \quad (1.68)$$

$y_{2(3)}$  is the hypercharge of  $\psi_{2(3)}$  and the Lagrangian:

$$\mathcal{L}_{int,R} = -ig' (y_2 \bar{\psi}_2 \gamma^\mu \psi_2 + y_3 \bar{\psi}_3 \gamma^\mu \psi_3) B_\mu \quad (1.69)$$

So the complete interacting Lagrangian is:

$$\mathcal{L}_{int} = \mathcal{L}_{int,L} + \mathcal{L}_{int,R} = -i(g \mathbf{j}^\mu \mathbf{W}_\mu + g' j_Y^\mu B_\mu) \quad (1.70)$$

where  $\mathbf{j}^\mu$  is the weak isospin current. It couples to a weak isotriplet of vector bosons:  $\mathbf{W} = (W^1, W^2, W^3)$  with a coupling strength denoted as  $g$ . Additionally, the weak hypercharge current  $j_Y^\mu = \sum_{i=1}^3 y_i \bar{\psi}_i \gamma^\mu \psi_i$  couples to an isosinglet vector boson  $B^\mu$  with a

coupling strength of  $g'$ .

## Weak Neutral Current

Due to the preservation of the SU(2) structure in the GWS model, it is straightforward to reproduce the charged current:

$$W^\pm = \frac{1}{\sqrt{2}}(W^1 \mp iW^2) \quad j^\pm = j^1 \pm ij^2 \quad (1.71)$$

$$j^1W^1 + j^2W^2 = \frac{1}{\sqrt{2}}(j^+W^+ + j^-W^-) \quad (1.72)$$

However, when it comes to the other two bosons, it is not possible to satisfy the conditions  $y_1 = y_2 = y_3$  and  $g'y_i = eQ_i$  simultaneously. This means that the  $B$  boson cannot be a pure  $A$  (photon). Since both fields are neutral, it is necessary to mix them in order to obtain a combination that matches experimental results:

$$\begin{pmatrix} A \\ Z \end{pmatrix} = \begin{pmatrix} \cos \theta_W & \sin \theta_W \\ -\sin \theta_W & \cos \theta_W \end{pmatrix} \begin{pmatrix} B \\ W^3 \end{pmatrix} \Leftrightarrow \begin{pmatrix} B \\ W^3 \end{pmatrix} = \begin{pmatrix} \cos \theta_W & -\sin \theta_W \\ \sin \theta_W & \cos \theta_W \end{pmatrix} \begin{pmatrix} A \\ Z \end{pmatrix} \quad (1.73)$$

The mixing angle is known as the Weinberg angle.

Rewrite Eq. 1.70 in terms of  $W^\pm$ ,  $Z$  and  $A$ :

$$\begin{aligned} i\mathcal{L} = & \frac{g}{\sqrt{2}}(j^+W^+ + j^-W^-) \\ & + \sum_{i=1}^3 \bar{\psi}_i \gamma^\mu \left\{ \left[ g \frac{\sigma^3}{2} \sin \theta_W + g'y_i \cos \theta_W \right] A_\mu + \left[ g \frac{\sigma^3}{2} \cos \theta_W - g'y_i \sin \theta_W \right] Z_\mu \right\} \psi_i \end{aligned} \quad (1.74)$$

where  $g_W = g/\sqrt{2}$  is the coupling constant of weak charged current.

The neutral part can be expressed in terms of the corresponding charge:

$$\begin{aligned} i\mathcal{L}_{NC} = & \sum_{i=1}^3 \bar{\psi}_i \gamma^\mu \psi_i [(g \sin \theta_W I_3 + g' \cos \theta_W Y) A_\mu + (g \cos \theta_W I_3 - g' \sin \theta_W Y) Z_\mu] \\ = & ej_{EM}^\mu Q A_\mu + g_Z j_Z^\mu Q_Z Z_\mu \end{aligned} \quad (1.75)$$

where  $I_3$  is the weak isospin and  $Y$  denotes the weak hypercharge. Similarly,  $Q$  represents the EM charge in units of the electron charge, and  $Q_Z$  is the weak neutral charge. The coupling constants for EM and neutral weak interactions are represented by  $e$  and  $g_Z$ , respectively. Given that  $I_3$  and  $Y$  can take different values for various fermions, we can establish the following relationship:

$$e = g \sin \theta_W = g' \cos \theta_W = \frac{gg'}{g^2 + g'^2} \quad (1.76)$$

So the Weinberg angle is identified as:

$$\tan \theta_W = \frac{g'}{g} \quad (1.77)$$

and:

$$Q = I_3 + Y \implies Y = Q - I_3 \quad (1.78)$$

The value of weak hypercharge depends on the definition, if one keeps the  $\frac{1}{2}$  factor in the B current, then one get:

$$\frac{Y}{2} = Q - I_3 \implies Y = 2(Q - I_3) \quad (1.79)$$

This is the traditional formula. In this thesis we will use the definition of Eq. 1.78.

As for the neutral weak current, the specific values of  $g_Z$ ,  $Q_Z$  and  $J_Z$  depend on our choice, as long as the following condition is satisfied:

$$g_Z Q_Z J_Z = (g \cos \theta_W I_3 - g' \sin \theta_W Y) \bar{\psi} \gamma^\mu \psi \quad (1.80)$$

The traditional choice is:

$$\begin{aligned} g_Z &= \frac{g}{\cos \theta_W} = \frac{e}{\sin \theta_W \cos \theta_W} \\ Q_Z &= I_e \cos^2 \theta_W - Y \sin^2 \theta_W = I_3 - Q \sin^2 \theta_W \end{aligned} \quad (1.81)$$

One can also absorb  $Q_Z$  into  $J_Z$  to get:

$$J_Z = \sum \bar{\psi}_i \gamma^\mu (I_3 - Q \sin^2 \theta_W) \psi_i = \sum_f \bar{f} \gamma^\mu \frac{c_v - c_a \gamma^5}{2} f \quad (1.82)$$

with

$$c_v = I_3 - 2Q \sin^2 \theta_W \quad c_a = I_3 \quad (1.83)$$

So we come to a remarkable prediction of the GSW model: the existence of the neutral weak interaction. This prediction was experimentally confirmed in 1973 through the Gargamelle neutrino experiment [39].

## PREX-II and CREX Observations

What we measured in PREX-II and CREX originates from the interference between this neutral weak current and the EM current.

$$\mathcal{A}_{PV} = \frac{\left(\frac{d\sigma}{d\Omega}\right)^R - \left(\frac{d\sigma}{d\Omega}\right)^L}{\left(\frac{d\sigma}{d\Omega}\right)^R + \left(\frac{d\sigma}{d\Omega}\right)^L} = \frac{|\mathcal{M}^R|^2 - |\mathcal{M}^L|^2}{|\mathcal{M}^R|^2 + |\mathcal{M}^L|^2} \quad (1.84)$$

where:  $\mathcal{M}^{R,L} = \mathcal{M}_\gamma + \mathcal{M}_Z^{R,L}$ . Because EM amplitude is much larger than the weak amplitude:  $\mathcal{M}_\gamma \gg \mathcal{M}_Z^{R,L}$

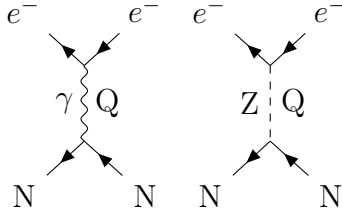


Figure 1.18: Feynman diagrams of elastic e-N scattering in PREX-II/CREX.

$$\begin{aligned}
\mathcal{A}_{PV} &\approx \frac{2\mathcal{M}_\gamma(\mathcal{M}_Z^R - \mathcal{M}_Z^L)}{2\mathcal{M}_\gamma^2} \\
&= \frac{\mathcal{M}_Z^R - \mathcal{M}_Z^L}{\mathcal{M}_\gamma} \propto \left(\frac{\frac{d\sigma}{d\Omega}}{\frac{d\sigma}{d\Omega}}\right)_{EM} \\
&= \left(\frac{\mathcal{M}_Z^R - \mathcal{M}_Z^L}{\mathcal{M}_\gamma}\right)_{point} \times \frac{Q_W}{Z} \frac{F_W(Q^2)}{F_{EM}(Q^2)} \\
&\approx \frac{g_Z^2/M_Z^2}{e^2/Q^2} \frac{(j_Z^{e,R} - j_Z^{e,L})j_Z^n}{j_\gamma^e j_\gamma^p} \times \frac{Q_W}{Z} \frac{F_W(Q^2)}{F_{EM}(Q^2)} \quad (Q^2 \ll M_Z^2) \\
&= -\frac{8G_F/\sqrt{2}}{4\pi\alpha/Q^2} \frac{(\bar{e}_L \gamma^\mu I_3 e_L) \frac{1}{2} (\bar{n}_L \gamma_\mu I_3 n_L)}{(\bar{e}_L \gamma^\mu e_L)(\bar{p} \gamma_\mu p)} \times \frac{Q_W}{Z} \frac{F_W(Q^2)}{F_{EM}(Q^2)} \\
&= -\frac{G_F Q^2}{4\pi\alpha\sqrt{2}} \frac{Q_W}{Z} \frac{F_W(Q^2)}{F_{EM}(Q^2)}
\end{aligned} \tag{1.85}$$

The weak isospins for electrons and neutrons are:  $I_3(e^-) = I_3(n) = -\frac{1}{2}$ . The factor of  $\frac{1}{2}$  in line 5 of Eq. 1.85 arises from the fact that the target is unpolarized. In the low  $Q^2$  region of  $Q^2 \sim 0.01 - 1 \text{ GeV}^2$ , one can estimate the PV asymmetry as

$$-\mathcal{A}_{PV} \sim \frac{G_F Q^2}{4\pi\alpha\sqrt{2}} \lesssim 10^{-7} - 10^{-4} \tag{1.86}$$

The FFs can be further decomposed into point-nucleon FFs:

$$\begin{aligned}
F_{EM}(q) &= Q_p^\gamma F_p(q) + Q_n^\gamma F_n(q) = F_p(q) \\
F_W(q) &= Q_p^Z F_p(q) + Q_n^Z F_n(q)
\end{aligned} \tag{1.87}$$

Where  $Q^\gamma$  and  $Q^Z$  are the EM charge and weak charge respectively.  $F_p(q)$  and  $F_n(q)$  are the FFs of point-proton and neutron density distributions.

$$F_{p,n}(q) = \int d^3r j_0(qr) \rho_{p,n}(r) \tag{1.88}$$

For weak charges including radiative corrections

$$\begin{aligned} Q_p^\gamma &= 1 & Q_n^\gamma &= 0 \\ Q_p^Z &= 0.0719 & Q_n^Z &= -0.9877 \end{aligned} \quad (1.89)$$

Ignoring the proton's weak charge, one will get:

$$\mathcal{A}_{PV} = -\frac{G_F Q^2}{4\pi\alpha\sqrt{2}} \frac{Q_{wk}}{Z} \frac{F_n(q)}{F_p(q)} \quad (1.90)$$

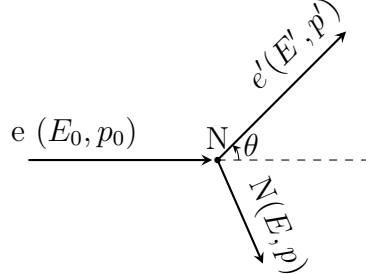
A more precise result by including the proton's weak charge is:

$$\mathcal{A}_{PV} = -\frac{G_F Q^2}{4\pi\alpha\sqrt{2}} \frac{Q_{wk}}{Z} \left[ \frac{F_n(q)}{F_p(q)} - \frac{Z}{N} (1 - 4 \sin^2 \theta_W) \right] \quad (1.91)$$

When neglecting the nuclear inner structure (at tree level), Eq. 1.91 reduces to:

$$\mathcal{A}_{PV} = -\frac{G_F Q^2}{\pi\alpha\sqrt{2}} \left( \sin^2 \theta_W + \frac{1}{4} \left[ \frac{N}{Z} - 1 \right] \right) \quad (1.92)$$

## 1.5 Dynamics



Energy and momentum are conserved in elastic scattering:

$$E_0 + M = E' + E \quad \mathbf{p}_0 = \mathbf{p}' + \mathbf{p}$$

where  $M$  is the mass of the target nucleus.

Ignore the electron's mass, we have  $E_0 \approx p_0$  and  $E' \approx p'$ :

$$\begin{aligned} E^2 &= M^2 + \mathbf{p}^2 = M^2 + (\mathbf{p}_0 - \mathbf{p}')^2 \\ &= M^2 + (E_0 - E' \cos \theta)^2 + (E' \sin \theta)^2 \\ &= M^2 + E_0^2 + E'^2 - 2E_0 E' \cos \theta \\ &= (E_0 + M - E')^2 \end{aligned} \quad (1.93)$$

So we get:

$$M(E_0 - E') = E_0 E' (1 - \cos \theta) \implies E' = \frac{M E_0}{M + E_0 (1 - \cos \theta)} \quad (1.94)$$

$Q^2$  dependence on the scattering angle  $\theta$  is calculated as:

$$Q^2 = -q^2 = -[(E_0 - E')^2 - (\mathbf{p}_0 - \mathbf{p}')^2] = 2E_0 E' (1 - \cos \theta) \quad (1.95)$$

## 1.6 Why Pb208 and Ca48

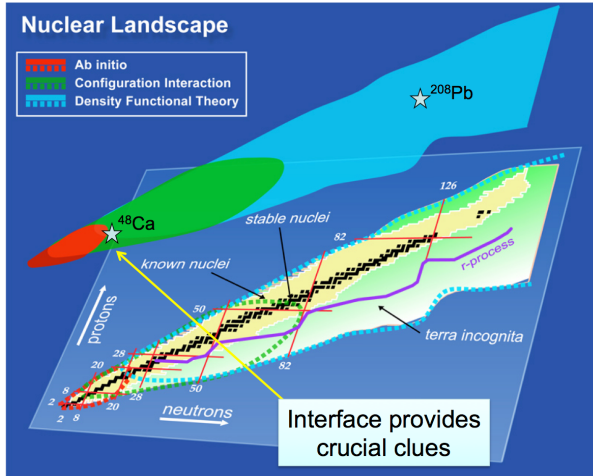


Figure 1.19: Nuclear Landscape. Figure from [40]

As tiny as the neutron skin thickness, to obtain a relatively accurate measurement, it is preferable to have a thicker neutron skin. Therefore, it is desirable to use a target element with a large neutron excess. Unfortunately, most medium and heavy nuclei with extra neutrons are unstable due to the presence of those additional neutrons. Nonetheless, there are specific nuclei with certain numbers of protons and neutrons that are stable. These numbers are known as the magic numbers, which arise from the nucleon shell structure. In a magic nucleus, the outmost shell is fully filled and the next higher energy shell is empty. This configuration creates a barrier that makes it difficult to remove a nucleon from the closed shell.

Nuclei that possess magic numbers of both protons and neutrons are referred to as doubly magic nuclei. These nuclei are exceptionally stable compared to single magic nuclei. Among the known neutron-rich doubly magic nuclei: <sup>10</sup>He, <sup>28</sup>O, <sup>48</sup>Ca, <sup>78</sup>Ni, <sup>132</sup>Sn and <sup>208</sup>Pb, <sup>48</sup>Ca and <sup>208</sup>Pb are the only two stable isotopes. Therefore, they are chosen as the target nuclei for the PREX-II and CREX.

Double magic nuclei exhibit a significant energy gap between their ground state and the first excited state. In the case of <sup>48</sup>Ca and <sup>208</sup>Pb, the energies required to excite

them are 3.84 and 2.6 MeV respectively. This energy separation enables us to effectively distinguish between inelastic scatterings and elastic ones, thanks to the high momentum resolution of our spectrometers.

Other advantages of  $^{48}\text{Ca}$  and  $^{208}\text{Pb}$  include

- Both nuclei are spin-0, so that we do not need to worry about the target polarization.
- $^{208}\text{Pb}$  is heavy and  $^{48}\text{Ca}$  is moderately heavy. As discussed in the previous section, elastic scattering is not exact but rather quasi-elastic. The small energy change observed in the scattering is primarily due to the recoil of the target nucleus. Since heavier target nuclei experience smaller recoil effects, using a heavier nucleus like  $^{208}\text{Pb}$  improves the accuracy of our measurements for determining  $Q^2$  and the scattering angle.

Finally, one more reason for the choice of  $^{48}\text{Ca}$ :  $^{48}\text{Ca}$  lies in the medium region of the nuclear landscape, as depicted in Fig. 1.19. In comparison to  $^{208}\text{Pb}$ , it is a smaller system that can be effectively studied using ab-initio methods [27]. This allows for direct comparison to calculations based on chiral effective field theory (EFT), which is highly sensitive to three-nucleon forces. In other words,  $^{48}\text{Ca}$  serves as a valuable probe for investigating three-nucleon forces. Additionally,  $^{48}\text{Ca}$  is large enough to apply DFT methods. By measuring the neutron skin thickness of  $^{48}\text{Ca}$ , we aim to provide insights that can bridge these two approaches and contribute to a deeper understanding of nuclear physics.

# Chapter 2

## Experimental Setup

Over the past 30 years, PVES has become a well-established and powerful experimental technique in atomic, nuclear, and particle physics. Its success can be traced back to Lee and Yang’s prediction of parity violation in beta decay in 1956, followed by Wu’s experimental proof in 1957. Shortly thereafter, Zel’dovich predicted the existence of parity-violating weak neutral current in 1959 [41], proposing to measure it in electron-proton scattering. However, it took about 20 years for the PV asymmetry to be experimentally observed in electron scattering experiments.

In 1978, C.Y. Prescott et al. conducted the E122 experiment at SLAC, measuring the PV asymmetry in the inelastic scattering of longitudinally polarized electrons from an unpolarized deuterium target [42]. With this successful demonstration, more efforts were made to improve this experimental technique, which matured and flourished at the turn of the last century. Numerous experiments were conducted to investigate the contribution of strange sea quarks to nucleons’ electromagnetic form factors (SAMPLE, G0, HAPPEX, and A4) and to test the electroweak sector of the Standard Model (SB) at low-energy scales (E158, PVDIS, Qweak).

It was the PREX-I experiment that first proposed the application of PVES to probe the structure of nuclei, followed by PREX-II and CREX. Future programs such as Moller, SoLID, and MESA experiments will continue to develop PVES and enhance its precision.

The idea behind PVES experiments is straightforward: scatter longitudinally polarized electrons off an unpolarized target (such as H, D, He, C, Ca, Pb, etc.) and measure the number of scattered electrons ( $N$ ). Then, reverse the beam helicity and repeat the measurement. The PV asymmetry between different helicities can be calculated as follows:

$$\mathcal{A}_{PV} = \frac{N^+/I^+ - N^-/I^-}{N^+/I^+ + N^-/I^-} \quad (2.1)$$

where  $I$  is the beam current, and the superscript denotes the beam helicity. The procedure described above should be repeated millions of times to obtain a statistically precise result, as the asymmetry being measured is typically extremely small.

Attention to detail is crucial in PVES experiments. Typically, two essential conditions are required: a high-energy polarized electron beam and rapid flipping of the beam

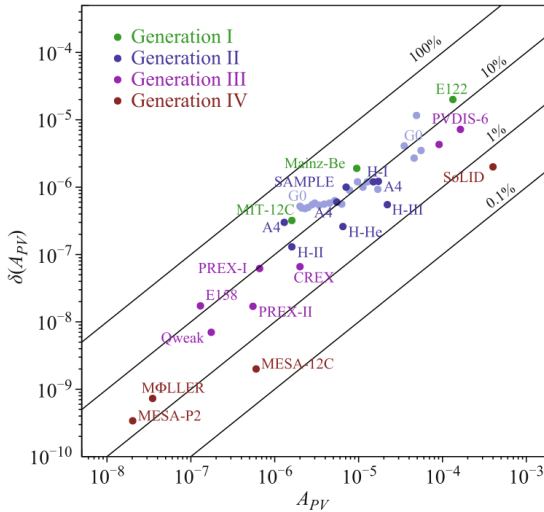


Figure 2.1: The evolution of PVES experiments is depicted by solid lines, which represent the relative precision achieved. Generation I experiments, including E122 (1978) [42], MIT-12C (1989) [43], and Mainz-Be (1990) [44], laid the foundation for PVES research. Generation II experiments focused on exploring strange form factors (FFs) in nucleons and involved collaborations such as SAMPLE [45] at the MIT-Bates accelerator, G0 [46] and HAPPEX [47] at JLab, and A4 [48] at the Maizer Mikrotron (MAMI) accelerator. Generation III experiments, including E158 at SLAC [49], Qweak [50], and PVDIS [51], focused on testing the SM at low energy and measuring the neutron skin thickness of nuclei. Additionally, the PREX-I/II and CREX experiments were conducted to probe the structure of nuclei. The planned Generation IV experiments, namely the SoLID program [52] and the MOLLER experiment [53] at JLab, and the P2 experiment at the future Mainz Energy-recovery Superconducting Accelerator (MESA) [54], aim to further test the SM and explore the nucleon structure with even higher precision. It's worth noting that MESA-12C refers to the same experiment as MESA-P2 but with a different target, namely  $^{12}\text{C}$ .

polarization. Interestingly, both requirements share a common dependency: the need for an intense source of polarized electrons with a swift response. It took several decades to develop such an electron source. At present, the electron source at JLab has achieved a polarization of approximately 90%. Ongoing efforts are being made to further improve the polarization.

The fast flipping requirement in PVES experiments arises from the need to minimize various sources of noise. When measuring such a minute quantity, it is crucial to maintain consistent experimental conditions across different helicity states. One effective and practical method to meet this requirement is through fast helicity flipping, typically in the range of  $10^2 - 10^3$  Hz. By increasing the speed of helicity reversal, random noise in beam conditions, target density, and other experimental apparatus is reduced, thereby minimizing the introduction of false asymmetry.

While the fast reversal of electron helicity helps in PVES experiments, significant

efforts are still required to minimize beam fluctuations. This involves achieving a “parity-quality beam” (PQB) by carefully controlling and reducing beam fluctuations to the greatest extent possible. Systematic uncertainties arising from the source (injector) and accelerator are managed through the slow reversal of the beam helicity.

In terms of the target’s response to electron bombardment, a high-speed raster scanning technique, typically in the range of kHz, is employed to minimize uncertainties associated with target deformities. This rapid scanning helps ensure a more uniform electron beam distribution on the target surface.

Regarding the detection of scattered electrons, instead of counting individual electrons, the electron flux is typically measured due to the high scattering rates in such experiments, which can reach values on the order of MHz per microampere (MHz/ $\mu$ A). This approach allows for efficient and accurate detection given the high rate of electron scattering.

The two sister experiments were conducted in Hall A at JLab. The CEBAF accelerator [? ] at JLab is one of the few facilities worldwide that can carry out PVES experiments (other facilities capable of conducting PVES experiments include MIMA and its successor MESA, the Facility for Antiproton and Ion Research (FAIR) and the Facility for Rare Isotope Beams (FRIB)). It delivered excellent polarized electron beams with helicity correlated difference at a sub-nanometer level to Hall A. Together with dedicated apparatus in Hall A, such as polarimeters, a target chamber, high resolution spectrometer (HRS) and other equipment [55], we were able to measure the extremely small PV asymmetry with remarkable precision.

## 2.1 Beam Parameters

PREX-II and CREX are follow-up experiments to PREX-I, which also ran at JLab in 2010. With quite good control over systematic uncertainties, but unfortunately, many technical challenges were encountered during the experiment, PREX-I’s result was statistics-limited, resulting in an achieved precision of 10% [56]:

$$\mathcal{A}_{\text{Pb}} = 656 \pm 60 \text{ (stat)} \pm 14 \text{ (syst) parts-per-billion (ppb)}$$

Based on the experience and lessons learned from PREX-I, PREX-II and CREX have been designed with more robustness and well-established methodologies to achieve high-precision measurements.

A notable feature of these experiments is the redundancy design implemented for critical components. This includes two independent slow helicity reversal systems to control systematic uncertainties, two polarimeters for accurate polarization measurement, multiple beam position monitors (BPMs) and beam current monitors (BCMs) for precise

---

<sup>1</sup><sup>208</sup>Pb target composes of 3 foils: upstream Diamond + <sup>208</sup>Pb + downstream Diamond

<sup>2</sup>Only 1 was prepared for the experiment. After the target accident, a new one was prepared.

<sup>3</sup>This rate does not include the contribution from the diamond foils

	PREX-II	CREX
Target	$^{208}\text{Pb}$	$^{48}\text{Ca}$
Target Thickness (mm)	$0.2554 + 0.5520 + 0.2566^1$	6
Target Density (g/cm <sup>3</sup> )	11.38	1.855
Number of Target	10	$1 + 1^2$
Number of Used Target	6	2
Beam Energy (GeV)	0.953	2.18
Beam Current ( $\mu\text{A}$ )	50-85	100-150
Average Beam Polarization (%)	89.7	87.1
Helicity Flip Rate (Hz)	120/240	120
Power on the Target	$\sim 100 \text{ W}@70 \mu\text{A}$	$\sim 350 \text{ W}@150 \mu\text{A}$
Scattering Angle (deg)	4.7	4.51
$Q^2$ (GeV <sup>2</sup> )	0.00616	0.0297
Scattering Rate (MHz/ $\mu\text{A}$ /arm)	$\sim 30^3$	$\sim 0.2$
Cross section (mbarn)	3930.6	5.3
Acceptance (msr)	0.0037	0.0037
Collected Charge (C)	114	412
Predicted $\mathcal{A}_{\text{PV}}$ (ppm)	0.6	2
Proposed Precision	3%	2.4%
Error on $R_n$ (fm)	0.05	0.02

Table 2.1: Summary of experimental design and setup for PREX-II and CREX.

monitoring of beam parameters, multiple  $^{208}\text{Pb}$  targets, and finally, two high-resolution spectrometers to detect the scattered electrons. These redundant designs enhance the reliability and quality of the experiments.

### 2.1.1 Uncertainty Budget

The goal of PREX-II is to achieve a precision of 1% in the measurement of the neutron radius of  $^{208}\text{Pb}$ , as proposed by PREX-I. This requires improving the precision of the PV asymmetry measurement to better than 3% [21].

Similarly, CREX aims to reach a precision of 0.02 fm ( $\sim 0.6\%$ ) in the determination of the neutron radius of  $^{48}\text{Ca}$ . This precise measurement will serve as a crucial benchmark for testing various microscopic models [57]. Achieving this level of precision corresponds to a total uncertainty of 2.4% in the PV asymmetry measurement.

As mentioned above, PREX-I has demonstrated a remarkable level of control over systematic uncertainties at 2.1%, so will the PREX-II and CREX. The main concern for both experiments is to collect as much scattered electrons as possible to reduce statistical uncertainty, which is inversely proportional to  $\sqrt{N}$ , with  $N$  being the total number of scattered electrons.

$$\frac{\delta \mathcal{A}}{\mathcal{A}} = \sqrt{\sigma_{\text{stat}}^2 + \sigma_{\text{sys}}^2} \quad \sigma_{\text{stat}} = \frac{\sigma_{\text{det}}}{\mathcal{P}\sqrt{N}} \quad (2.2)$$

where  $\sigma_{\text{det}}$  is the detector uncertainty and  $\mathcal{P}$  refers to the beam polarization.

Experiment	PREX-I (%)	PREX-II (%)	CREX (%)
Charge Normalization	0.2	0.1	0.1
Beam Asymmetry	1.1	1.1	0.3
Detector Non-Linearity	1.2	1.0	0.3
Transverse Asymmetry	0.2	0.2	0.1
Polarization	1.3	1.1	0.8
Target Contamination	0.4	0.4	0.2
Inelastic Scattering	< 0.1%	< 0.1	0.2
Effective $Q^2$	0.5	0.4	0.8
Total Systematic	2.1	2	1.2
Statistical	9.1	2.2	2.1
Total	9.2	3	2.4

Table 2.2: Proposed budget for systematic and statistical uncertainties in both experiments [57, 58]

### 2.1.2 Figure Of Merits (FOM)

The choice of beam energy and scattering angle involves a trade-off between various factors. The PV asymmetry prefers higher beam energies and a larger scattering angles. However, the scattering rate decreases significantly with increasing beam energy and scattering angle. On the other hand,  $Q^2$  favors lower beam energies and smaller scattering angles. Additionally, calculations demonstrate that the sensitivity of PV asymmetry to the neutron radius oscillates as a function of beam energy. All these considerations are incorporated into the FOM, which is defined as:

$$\text{FOM} = R \times \mathcal{A}^2 \times \epsilon^2 \quad (2.3)$$

where  $R$  is the scattering rate,  $\mathcal{A}$  the PV asymmetry and  $\epsilon$  the sensitivity of  $\mathcal{A}$  with respect to  $R_n$ . It is worth noting that the FOMs used in most PVES experiments typically consider only  $R$  and  $\mathcal{A}^2$ . The inclusion of  $\epsilon$  in our FOM helps to enhance the precision of the  $R_n$  measurement.

#### Rate

For a data set of  $N$  independent events sampled from a normal distribution  $X \sim N(x_0, \sigma_0)$ , the statistical uncertainty on the measured mean value is:

$$\text{var}(\bar{x} = \frac{1}{n} \sum x_i) = \frac{1}{n^2} \text{var}(x_i) = \frac{\sigma_0^2}{n} \implies \sigma(\bar{x}) = \frac{\sigma_0}{\sqrt{n}}$$

Assuming one wants to measure a 1 ppm asymmetry with a statistical uncertainty of

1%,

$$\frac{\sigma_{\mathcal{A}}}{\mathcal{A}} = \frac{1}{\mathcal{A}} \frac{\sigma_{det}}{\sqrt{2N}} \approx \frac{1}{\mathcal{A}\sqrt{2N}} = 1\% \implies N = 5 \times 10^{15} \quad (2.4)$$

a factor of 2 is included because there are two HRS arms. One needs to count  $\sim 10^{15}$  scattered electrons. Given a counting rate of 1 MHz, it will take  $\frac{5 \times 10^{15}}{1 \text{ MHz}} = 5 \times 10^9 \text{ s} \approx 160 \text{ years}$ , a completely unacceptable time scale. As a solution, the integrated flux technique is adopted for a higher scattering rate, which is:

$$\frac{dR(\theta)}{d\Omega} = \frac{d\sigma}{d\Omega} I t \frac{\rho}{A} \times N_A \quad (2.5)$$

- $\frac{d\sigma}{d\Omega}$  is the fractional cross section in the unit of  $\text{cm}^2/\text{str}$ .
- $I$  is the beam current in the unit of electrons/s.
- $t$  is the target thickness in the unit of cm.
- $\rho$  is the target density in the unit of  $\text{g}/\text{cm}^3$ .
- $A$  is the atomic number.
- $N_A = 6.022 \times 10^{23}$  is the Avogadro constant.

The differential cross sections are calculated to be 3930.6 mbarn and 5.3 mbarn for  $^{208}\text{Pb}$  and  $^{48}\text{Ca}$ , respectively, at their corresponding kinematics. Other parameters can be checked out in Table 2.1.

The total rate will be the integration over the acceptance:

$$R = \int \frac{dR(\theta)}{d\Omega} d\Omega = \frac{dR}{d\Omega} d\Omega \quad (2.6)$$

PREX-II and CREX have an acceptance defined by the septum magnet and the Q1 collimator (see discussions below), which is  $d\Omega = 0.0037 \text{ str}$ .

As shown in Fig. 2.2, the scattering rate decreases rapidly with increasing beam energy and scattering angle for both  $^{208}\text{Pb}$  and  $^{48}\text{Ca}$ . Therefore, in order to achieve a high scattering rate, it is preferable to use a low beam energy and a small scattering angle (or equivalently, a small momentum transfer  $\mathbf{q}$ ).

## Asymmetry and Sensitivity

As shown in Eq. 2.4, the size of the asymmetry plays a crucial role, a 2 times larger asymmetry allows for a reduction of the run time to one quarter, a significant savings in beam time. Therefore, it is important to choose a kinematic region where the asymmetry is large. Furthermore, the sensitivity of the asymmetry to the neutron radius ( $\epsilon$ ) is also important. Since our ultimate goal is to extract the neutron radius from the PV asymmetry, a higher sensitivity leads to a more precise determination of the neutron

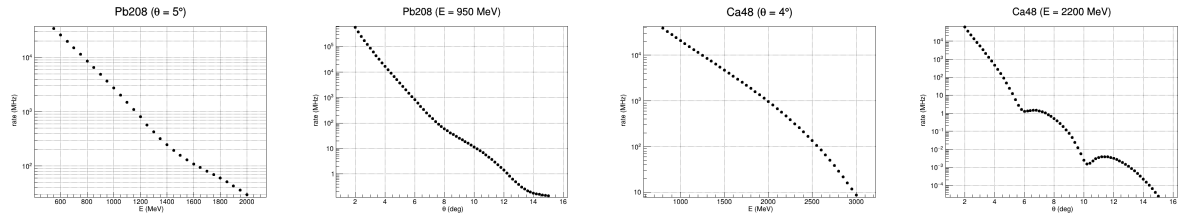


Figure 2.2: Scattering rate versus the beam energy and the scattering angle for  $^{208}\text{Pb}$  and  $^{48}\text{Ca}$ , the other parameters (energy in the scattering angle plot and vice versa) are fixed to their design values.

radius. The sensitivity is calculated as the relative change of  $\mathcal{A}$  with 1% change in the neutron radius.

$$\epsilon = \frac{\delta \mathcal{A}/\mathcal{A}}{\delta R/R} = \frac{|\mathcal{A}_{\text{stretched}} - \mathcal{A}|/\mathcal{A}}{1\%} \quad (2.7)$$

Though asymmetry is what will be measured, it is possible to estimate its value based on some theoretical models, as is calculated in [20].

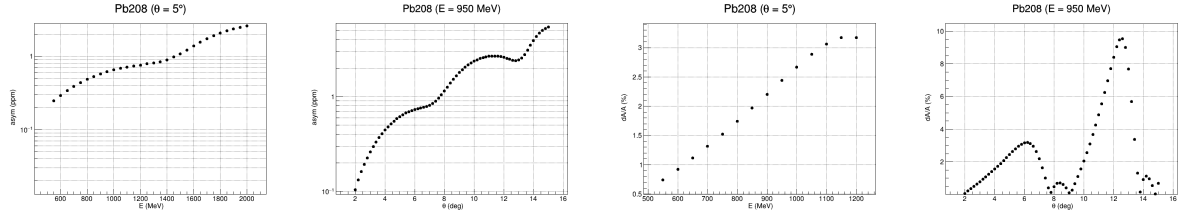


Figure 2.3: Asymmetry and sensitivity plots for  $^{208}\text{Pb}$ . The asymmetry increases along the beam energy and oscillates upward along the scattering angle. Similar trends can be observed in the sensitivity plot. The sensitivity plot is calculated with 1% change in the neutron radius and the y-axis represent the absolute value. At a beam energy of 950 MeV, a local maximum is observed around  $\theta \sim 6^\circ$ .

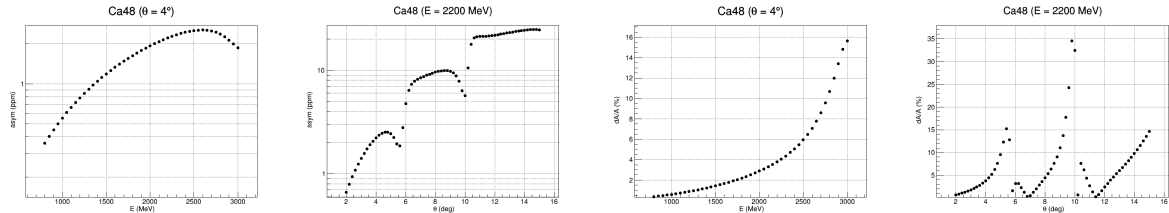


Figure 2.4: Asymmetry and sensitivity plots for  $^{48}\text{Ca}$ , the asymmetry maximizes around 2500 MeV with  $\theta = 4^\circ$  and there is a local maximum about  $4.5^\circ$  at a beam energy of 2200 MeV. As for the sensitivity, it increases monotonously along the beam energy and comes to a regional maximum around  $5^\circ$  with  $E = 2200$  MeV.

Based on the theoretical result, we can optimize the kinematics for both nuclei (con-

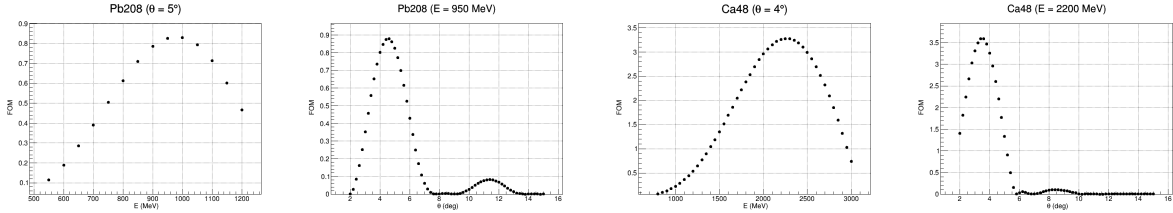


Figure 2.5: For both nuclei, FOM supports a small scattering angle. As for the beam energy, FOM maximizes around 950 (2200) MeV for  $^{208}\text{Pb}$  ( $^{48}\text{Ca}$ ).

sider only the statistical uncertainty here):

$$\frac{\delta R}{R} = \frac{\delta \mathcal{A}}{\mathcal{A}} \frac{1}{\epsilon} = \frac{\sigma_{det}}{\mathcal{P}} \frac{1}{\sqrt{N} \mathcal{A} \epsilon} \quad (2.8)$$

To minimize  $\delta R/R$ , it is equivalent to maximize

$$\text{FOM} = N \times \mathcal{A}^2 \times \epsilon^2 \quad (2.9)$$

Given practical constraints on how low an angle ( $4^\circ$ ) we can reach with septum magnets, the beam energy and the scattering angle were chosen to be 950 (2200) MeV and  $5$  ( $4$ ) degree for  $^{208}\text{Pb}$  ( $^{48}\text{Ca}$ ). The beam energy for CREX is exactly a natural 1-pass (1-turn) beam energy in CEBAF in the 12 GeV era.

### 2.1.3 Helicity Flip Frequency

The main consideration for the choice of the 120 Hz (240 Hz) flip frequency was to effectively cancel out the 60 Hz power line noise.

Depending on the desired precision, there are a few methods to mitigate or eliminate this low frequency noise:

1. Set the flip frequency to a very high value, say 1 kHz, then the change of fluctuations caused by this low frequency noise becomes negligible between two nearby helicity windows and canceled in the asymmetry calculation. This method can eliminate many low frequency noises and was adopted in the Qweak experiment.
2. Integrate over this 60 Hz noise within a helicity window. This integration is performed at a frequency of  $f = \frac{60}{n}$  Hz, where  $n$  is an integer ( $1, 2, \dots$ ) representing the helicity window number. This way no 60 Hz line noise will be recorded in the final data at all.
3. Select a flip frequency of  $f = n \times 60$  Hz where  $n$  is an integer. A helicity pattern is then used to cancel the 60 Hz noise. For example, if  $f = 120$  Hz, then every  $f/30 = 4$  continuous helicity windows form a helicity pattern, asymmetry will be calculated based on these helicity patterns. This was used in PREX-II/CREX.

In terms of canceling the 60 Hz line noise, the second method works best as it completely removes the line noise. The other two methods also cancel the noise in their asymmetry calculation, but result in a broadening of the asymmetry width. However, when considering other low frequency noises, the frequency used in the second method may not be high enough to cancel them effectively.

The first method is the best for removing low frequency noises, but it has the drawback of a fixed settle time ( $T_{\text{settle}}$ ) required to stabilize a helicity state. With higher frequencies, the stable time window ( $T_{\text{stable}}$ ) during which scattered electrons are integrated becomes shorter, leading to longer run times.

As a compromise, the third method was chosen for PREX-II/CREX. It provides a reasonable balance between canceling low frequency noises and maintaining an acceptable settle time and run time.

## 2.2 Continuous Electron Beam Accelerator Facility (CEBAF)

CEBAF is capable of delivering multi-GeV continuous wave (cw) electron beams with varying energies and intensities to four experimental halls simultaneously. With the 12 GeV upgrade, the injector energy has been increased from 67.5 MeV to 123 MeV. The north and south 1497 MHz linear accelerators (LINACs) each consist of 25 superconducting radial frequency (SRF) cryomodules, allowing for electron acceleration at a peak rate of  $1.1 \times 2 = 2.2$  GeV/turn. The LINACs are connected by 11 arcs of magnets, allowing Hall A, B and C to receive cw beams with energies of up to  $2.2 \times 5 = 11$  GeV. Hall D, with an additional half circle, can receive beams with energies up to 12 GeV. This design enables different nuclear experiments to be conducted in separate halls without interfering each other, in theory.

As shown in Fig. 2.7, laser pulse ( $\lambda = 780$  nm) from four lasers (Hall D laser is not shown in the plot) shoot in the electron gun (two electron guns in total) that operates at  $-130$  kV to excite electrons. These excited electrons interweave with each other, forming a chain of electron bunches. Adjacent bunches have a phase difference of  $120^\circ$  (Hall D does not have its own slit in the beam chopper. Therefore, the electron bunch from hall D follows either Hall A or Hall C). The electron chain is initially sent into the north LINAC by the injector and accelerated by both LINACs. Once they reach the desired energy, they are expelled at the exit of the south LINAC and subsequently directed towards the experimental halls (A, B and C) for various experiments.

At CEBAF, the maximum beam current available is  $200 \mu\text{A}$ . This current limitation was primarily determined by two factors: the available radiofrequency (rf) power and the power deposited on the beam dump. The rf power was limited to 1 MW, which corresponded to the product of the old highest beam energy (5 GeV) and the maximum beam current ( $200 \mu\text{A}$ ).

While Hall B and Hall D require only a small amount of cw beams at the nA level, it is actually Hall A and Hall C that consume the majority of the electron beams. Both

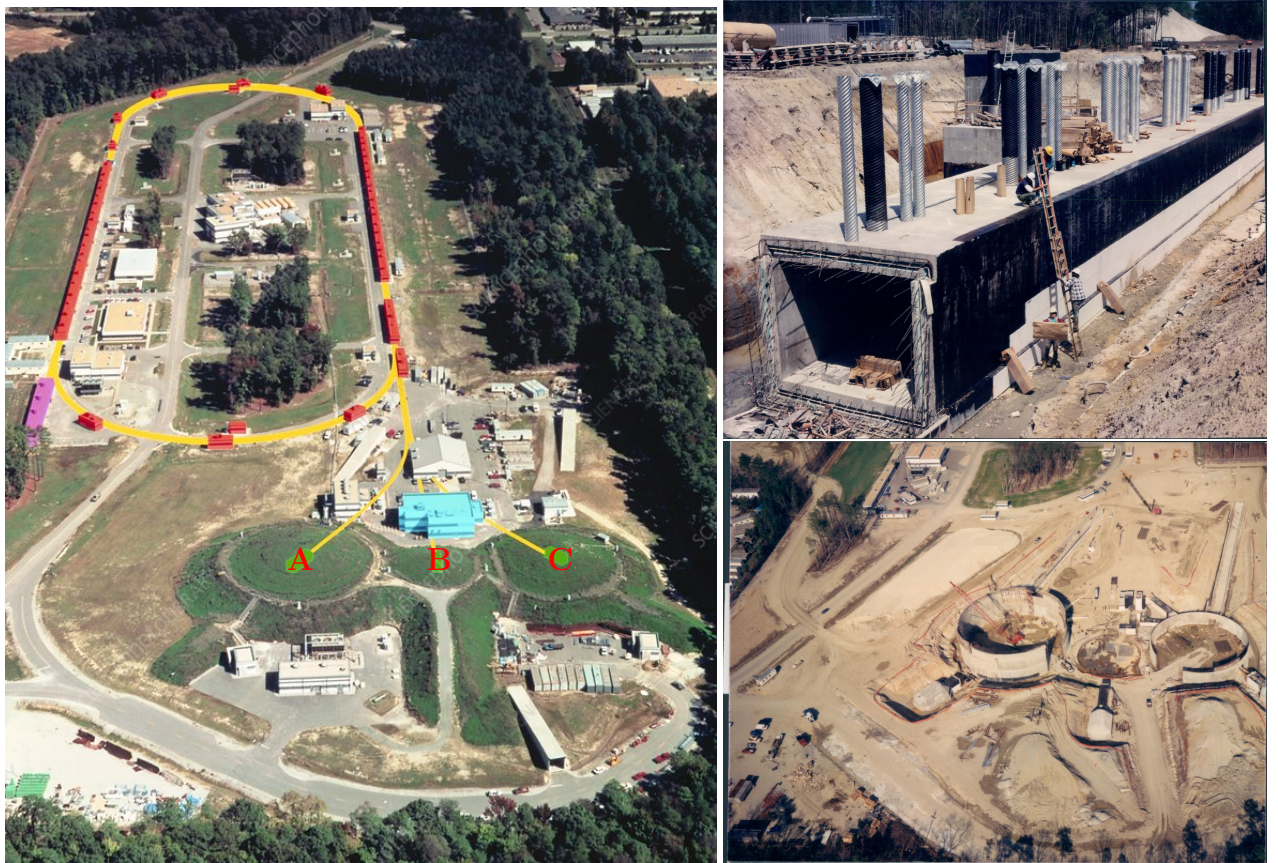


Figure 2.6: Aerial view of JLab accelerator site. The yellow line indicates the position of the CEBAF accelerator, while the three experimental halls are labeled as A/B/C (Hall D is situated at the top left corner, after the exit of the north LINAC). The accelerator tunnel is located 30 feet ( $\sim 9$  m) underground and has a height of 10 feet ( $\sim 3$  m). It has a circumference of about  $7/8$  mile (1.4 km). There are two superconducting LINACs depicted as red lines, each of  $1/4$  mile (400 m). The pink section on the mid-left represents the location of the injector. The two plots on the right show the ongoing construction of the tunnel and experimental halls.

halls can receive cw beams ranging from a few tenths to over one hundred  $\mu$ A.

While all four halls at JLab are dedicated to the study of nuclear structure, they focus on different aspects. Hall A concentrates on form factors of various nuclei, Hall B focuses on generalized parton distributions, Hall C is dedicated to precise determination of valence quark properties in nuclei, and finally, the newly established Hall D explores the origin of confinement through exotic mesons.

Since all four halls share the same electron source and accelerator, coordination is required to ensure their simultaneous operations. In order to maintain the quality of the polarized electron beam, PVES experiments are typically given priority over other experiments when it comes to the electron source. Regarding the LINACs, adjustments are made to accommodate different energy requirements. For instance, if one hall requests

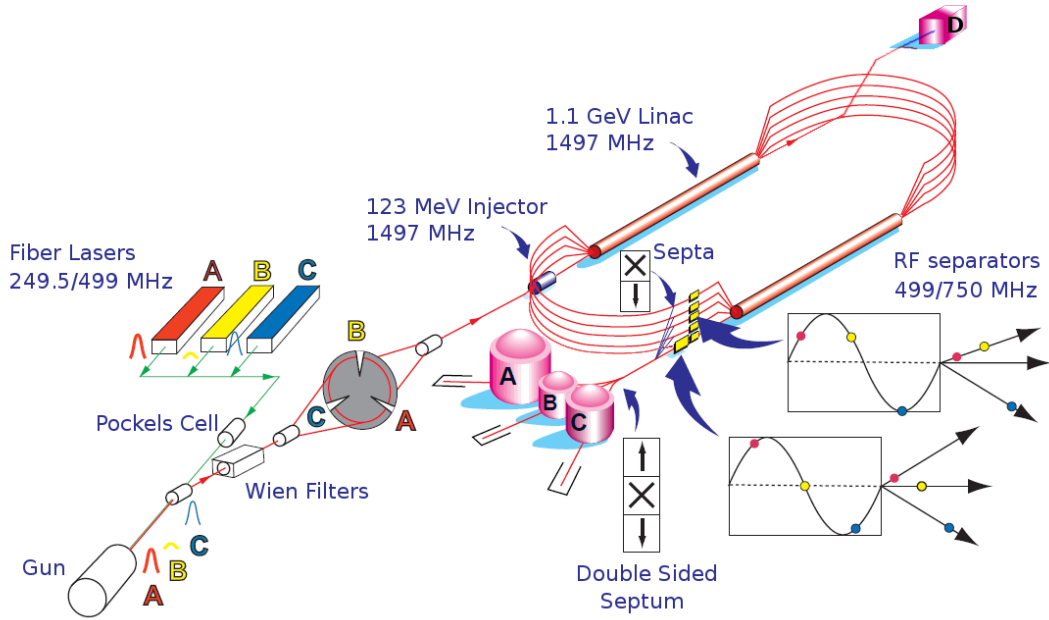


Figure 2.7: Schematic plot of CEBAF. The circular plate with three slits is the beam chopper, which does not have a slit for Hall D. As a result, Hall D beams must follow the electron beams of other halls. During acceleration, low-energy beams are kicked into higher arcs, while high-energy beams pass through lower arcs. The magnetic field increases from the higher arcs to the lower arcs to ensure that electron trajectories have the same radii.

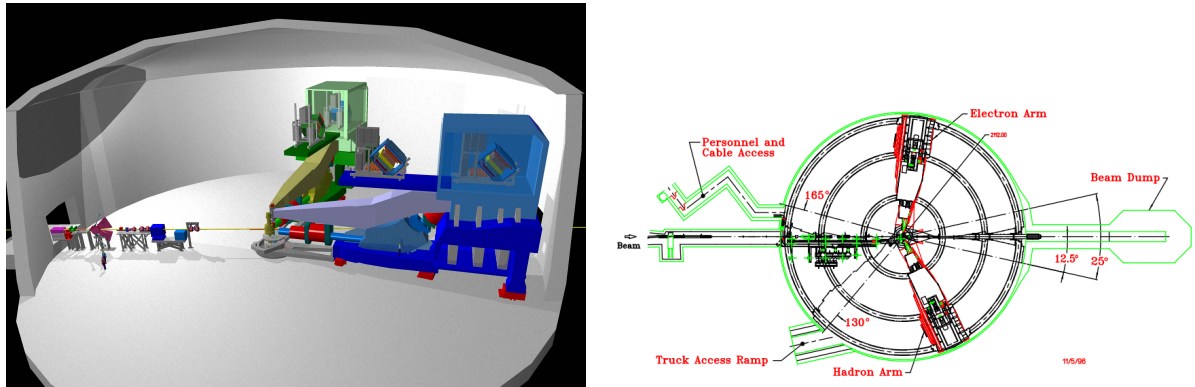


Figure 2.8: 3D and bird view of Hall A [59]. Originally, the 2 spectrometers were called High Resolution Hadron Spectrometer (HRHS) and High Resolution Electron Spectrometer (HRES), but they are essentially identical to each other and can be used interchangeably. So now they are called left arm (LHRS) and right arm HRS (RHRS).

a lower energy, such as 1 GeV, the LINAC power will be adjusted accordingly to deliver 1 GeV per turn. However, this adjustment affects the available energy for other halls since the reduced LINAC power is applied to all electron beams. Consequently, careful scheduling is necessary to allocate the appropriate energy levels to each hall based on

their specific experimental needs.

## 2.3 Polarized Electron Beam

### 2.3.1 Polarized Electron Source

PVES experiments are a driving force behind the development of polarized electron sources. These sources are essential for generating consistently high-polarization electron beams across a wide range of intensities, from nA to A, depending on the specific experiment. Additionally, the source should be capable of rapid helicity reversal, at a frequency of  $\sim 100 - 1000$  Hz, while having minimal impact on other properties of the electron beam.

Currently, the GaAs-based semiconductor photoemission source is the sole option available on the market as a polarized electron source. Historically, this kind of electron source was the only one capable of meeting the high peak current requirements of older accelerators with low duty factors and the rapid helicity reversal demands of PVES experiments. That is why it is the only player on the market now. Over the past few decades, pulsed beam has been replaced by continuous beam while the GaAs-based electron source is inherited and further developed. The polarized electron source utilized by CEBAF, for instance, can produce electron beams with a polarization exceeding 85%, much larger than the 37% polarization achieved during its inauguration at SLAC. [42]

The design was first proposed independently by Garwin, Pierce and Siegmann [60] and by Lampel and Weisbuch [61]. The idea is straightforward: by illuminating the semiconductor with circularly polarized laser light of carefully chosen energy  $E_{\text{gap}} < h\nu < E_{\text{gap}} + \Delta$ , only electrons in the valance band  $P_{3/2}$  are excited into the conduction band  $S_{1/2}$ . The selection rule ensures that only transitions satisfying  $\Delta m_j = +1$  ( $-1$ ) can occur for right (left) circularly polarized photons, as shown in Fig. 2.9. The transition rates can be calculated easily using Clebsch-Gordan coefficients, and the ratio of these rates is indicated within the circle in the plot. As a result, the excited electrons become polarized, with different states having different pumping rate. In this way, a polarized electron beam is produced, with a polarization given by  $\mathcal{P} = (3-1)/(3+1) = 50\%$ , for both helicities.

The next challenge is to liberate the polarized electrons from the material without significantly degenerating the polarization. As illustrated in Fig. 2.10, bare GaAs possesses an electron affinity (EA) of 4.07 eV, which hinders the escape of any electrons from the surface. To overcome this hurdle, a condition known as negative electron affinity (NEA) is employed. This involves reducing the energy of the electron in the vacuum just outside the surface to a level lower than the conduction band energy. This is achieved by applying a layer of cesium oxide on the surface of a pure GaAs semiconductor.

While the NEA technique enables the generation of polarized electron beams, it falls short of achieving the ideal 50% polarization. Instead, the achieved polarization typically ranges from 25% to 43%. This loss in polarization occurs due to spin dilution as electrons

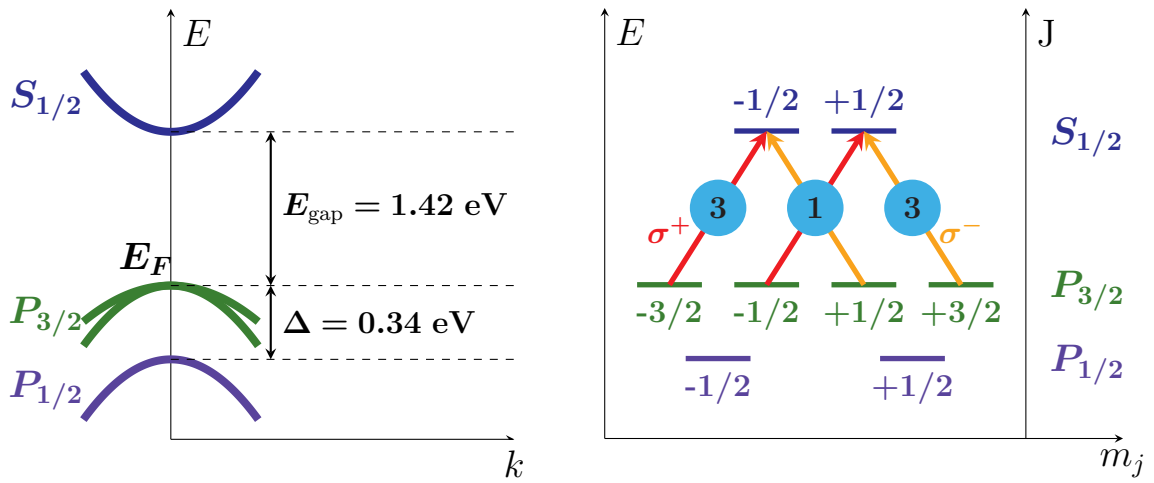


Figure 2.9: Excitation of electrons in the semiconductor. Excited electrons with  $J_z = +1/2$  ( $-1/2$ ) are right (left)-handed.

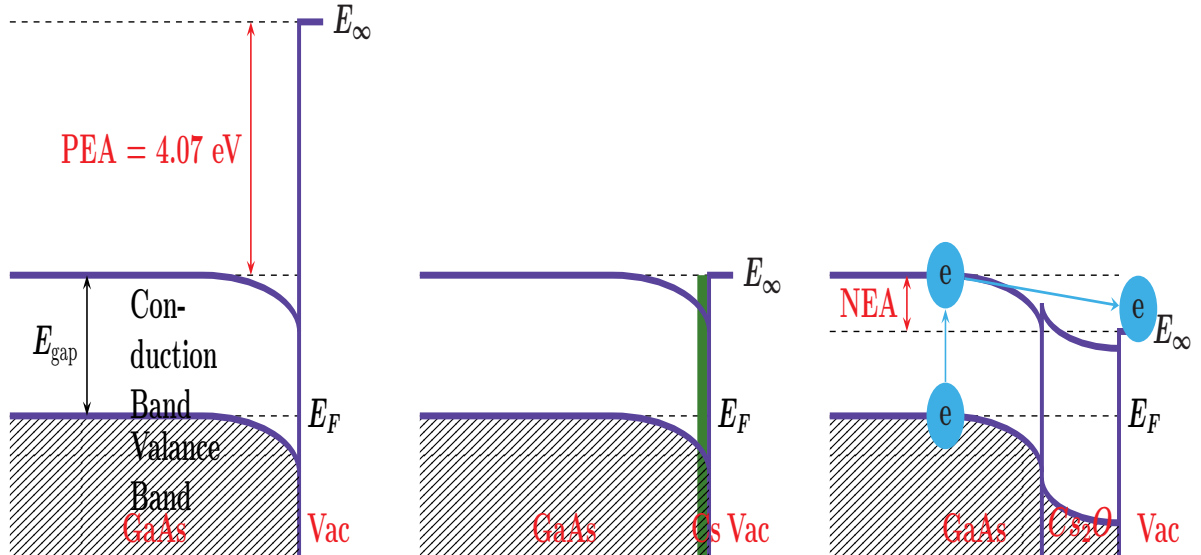


Figure 2.10: The energy band diagram of GaAs near its surface. Left: bare p-type GaAs, the large positive electron affinity (PEA) prevents electrons from escaping the surface; Middle: p-type GaAs with a cesiated surface, the electron affinity (EA) is 0, but electrons still cannot escape the surface easily; Right: GaAs with a layer of cesium oxide; the electron vacuum energy  $E_\infty$  is lowered to make a negative EA so that electrons can break free from the surface easily. [62]

diffuse towards the semiconductor surface. To increase polarization, one approach is to reduce the thickness of the GaAs crystal. However, even with the thinnest possible GaAs crystal, a polarization greater than 50% cannot be achieved. This calls for new strategies and the answer is the strained GaAs [62].

By introducing a strained layer, the degeneracy of the  $P_{3/2}$  state in GaAs is split. Only states with  $m_j = \pm 3/2$  will be selectively pumped, leading to a theoretical maximum polarization of 100%. In practice, the achieved polarization is lower due to various factors. In the case of the CEBAF electron source, the real polarization achieved is approximately 88%.

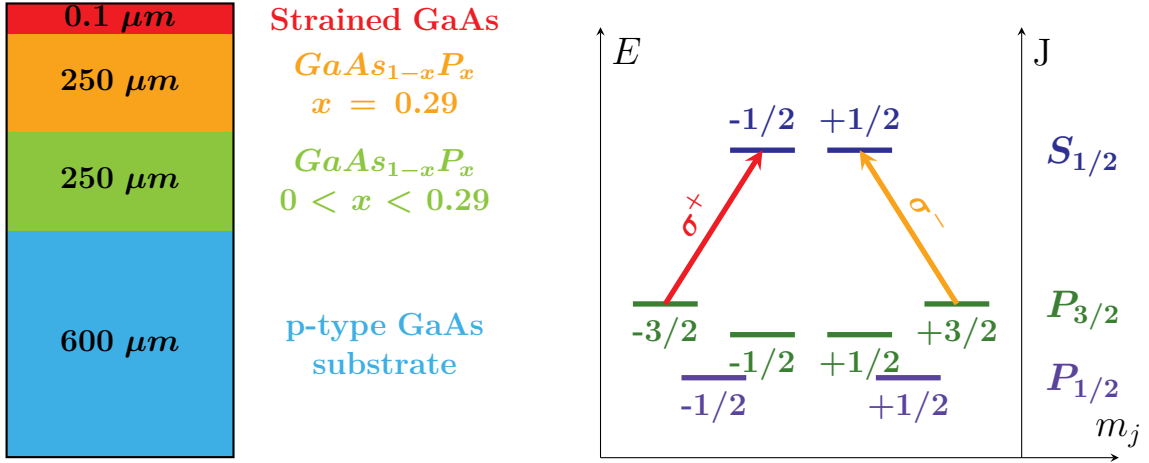


Figure 2.11: Layout of a strained GaAs electron source and corresponding excitation plot.

### 2.3.2 Polarization Control

#### Pockels Cell

To achieve better control over the beam polarization in the production of polarized electron beams, it is necessary to have the ability to quickly flip the polarization while maintaining its stability. Direct manipulation of electrons can be challenging and time-consuming, whereas manipulating photons is comparatively easier. By reversing the circular polarization of the incident laser pulse, the polarization of the electron beam can be flipped. One convenient method to accomplish this is by using a half-wave plate. By inserting or retracting the half-wave plate into/from the optical path, the phase of the laser pulse will be altered by  $\pi$ , resulting in the reversal of the laser's circular polarization. This simple adjustment provides an effective means of flipping the electron beam polarization.

The drawback of the half-wave plate is that its relatively slow mechanical movement is insufficient for the rapid flipping of beam polarization required in PVES experiments. To address this issue, a component called Pockels cell (PC) is employed. The PC is a Rubidium Titanyle Phosphate (RTP) crystal that operates based on the Pockels effect. The Pockels effect refers to the induction of birefringence in the crystal when subjected to an electric field. The magnitude of the induced birefringence is directly proportional to the strength of the applied electric field. By applying an appropriate high voltage of  $\sim 1.5$  kV, the PC acts as a quarter-wave plate. This means that when a linearly polarized laser beam passes through the PC, the electric field components along the fast and slow

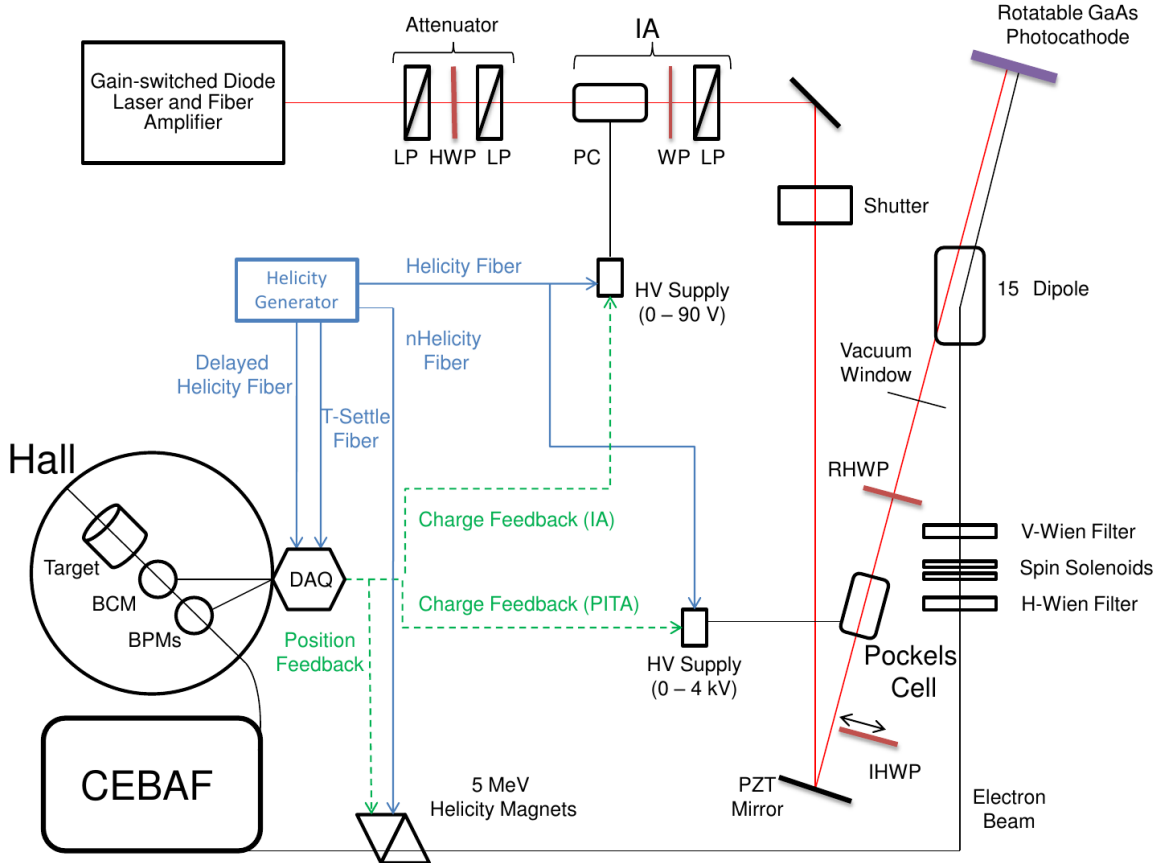


Figure 2.12: The laser system at the CEBAF injector

axes of the crystal, denoted as  $E_x$  and  $E_y$  respectively, acquire a phase difference of  $\pm\frac{\pi}{2}$  depending on the polarity of the applied electric field. Consequently, the PC converts the linearly polarized laser beam into a circularly polarized one. Reversing the electric field polarity in the PC allows for the reversal of the laser beam's polarization. This transition in the PC can be accomplished swiftly, reaching frequency of up to 1 kHz, with a dead time of about 60  $\mu$ s.

### Polarization Induced Transport Asymmetry (PITA, or Phase Induced Transmission Asymmetry) [63]

The above discussion presented an ideal scenario where the PC functions as a precise quarter-wave plate, and all other optical components operate flawlessly. However, in reality, there are always deviations from perfect circular polarization, leading to systematic effects on beam position, spot size, and intensity. These deviations, when correlated with polarization, can introduce a false asymmetry in our PV asymmetry measurement. This phenomenon is known as the PITA effect. The PITA effect constitutes the dominant component of the helicity-correlated beam asymmetry (HCBA) and represents the largest

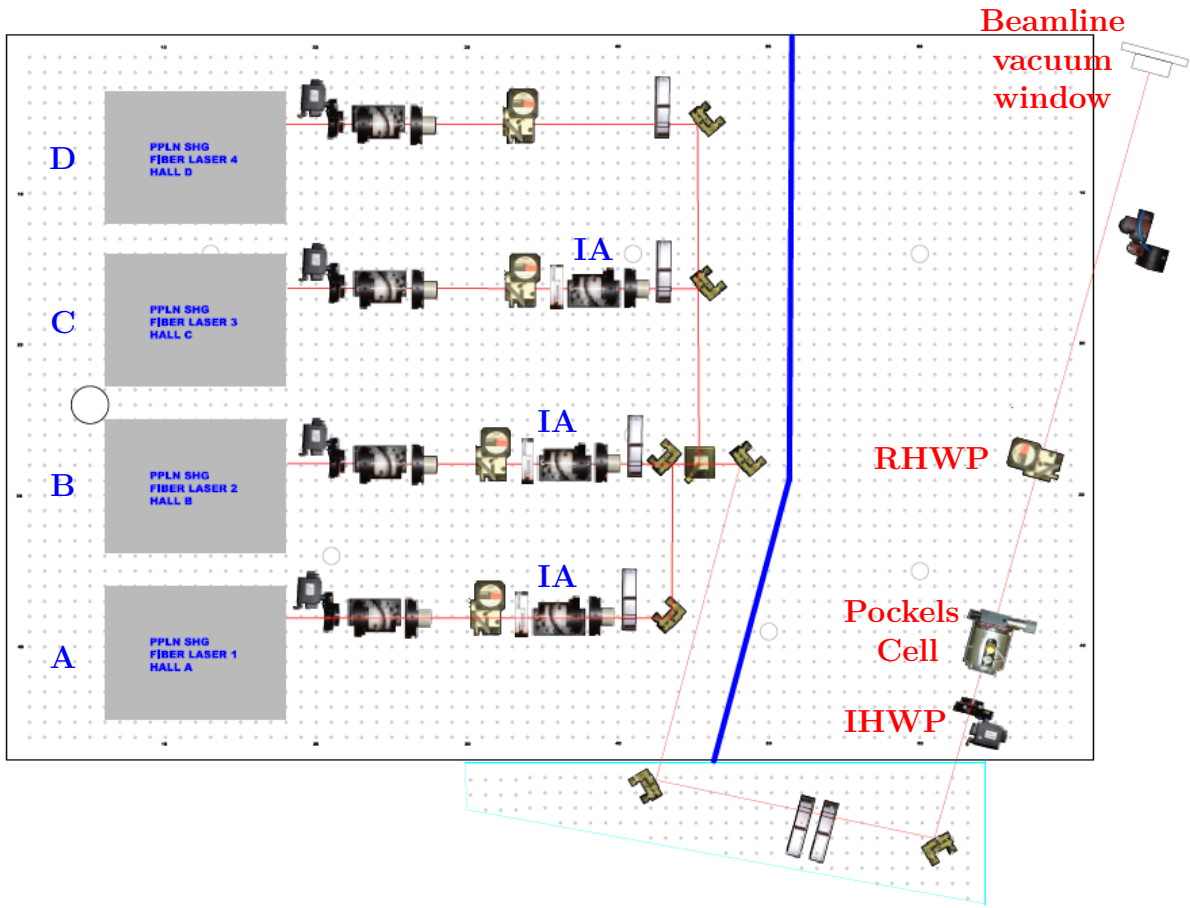


Figure 2.13: Schematic plot of the laser table.

false asymmetry in our measurement.

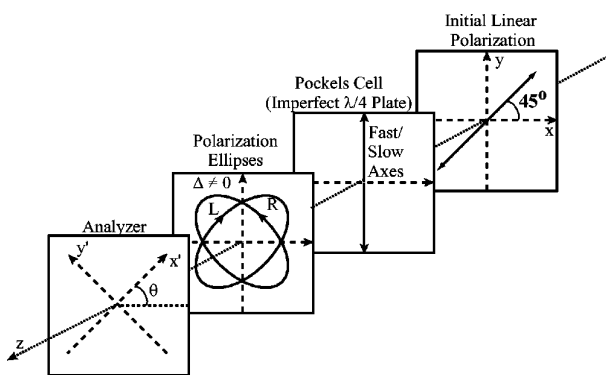


Figure 2.14: Phase shift by going through the PC.

The PITA effect is characterized by the PC induced phase shift  $\delta$ :

$$\delta^{R(L)} = \mp \left( \frac{\pi}{2} + \alpha \right) - \Delta \quad (2.10)$$

where  $\alpha$  and  $\Delta$  represent the symmetric and asymmetric offset phase shift, respectively. The slightly elliptical beam resulting from the deviations in circular polarization possesses a residual linear component. This residual linear component gives rise to an intensity asymmetry (to first order):

$$\mathcal{A}_I = \frac{I^R - I^L}{I^R + I^L} = -\frac{\epsilon}{T}[\Delta \cos(2\theta)] \quad (2.11)$$

where  $\epsilon/T$  ( $\ll 1$ ) defines the “analyzing power” with  $\epsilon = T_{x'} - T_{y'}$  and  $T = (T_{x'} + T_{y'})/2$ .  $T_{x'(y')}$  is the transmission coefficient along the axis  $x'$  ( $y'$ ) of the downstream analyzer.  $\theta$  is the angle between the PC’s fast axis and the  $x'$  axis of the analyzer.

Considering other optical components along the laser path, like the rotatable half-wave plate (RWP) and the vacuum window, the unknown tiny birefringence in these components will also contribute to  $\Delta$ , resulting in a modified intensity asymmetry:

$$\mathcal{A}_I = \frac{I^R - I^L}{I^R + I^L} = -\frac{\epsilon}{T}[\cos(2\theta) \cdot (\Delta - \Delta^0)] \quad (2.12)$$

where  $\Delta^0$  represents the asymmetric offset phase shift due to all other components.

To minimize the intensity asymmetry, it is desirable to keep  $\Delta - \Delta^0$  as small as possible. Fortunately, *Delta* is adjustable by varying the applied electric field. In order to achieve this, a charge feedback system, as shown in Fig. 2.12, is employed. This system continuously monitors the charge intensity asymmetry and automatically adjust the HV supplied to the PC to maintain a small  $\mathcal{A}_I$ . Throughout the PREX-II and CREX, the average charge intensity asymmetry has been successfully maintained at about 100 ppb.

As illustrated in Fig. 2.12, the charge feedback system also regulates the HV supply of the Intensity Attenuator (IA). The IA, in conjunction with the slit in the beam chopper, controls the intensity of the outgoing electron beams ( $\Delta$  does a fine tune to the beam intensity). This feature is essential for equalizing the beam intensities across different helicity states, contributing to the goal of minimizing the charge intensity asymmetry.

Another important element in the setup is the RWP, which lies downstream of the PC. It works by equalizing any residual linear polarization that may remain after passing through the PC, to establish a quantum efficiency independent of the helicity of the incoming beam.

## Slow Helicity Reversal

The fast reversal of the PC can effectively reduce random noise caused by fluctuations in beam and target density. However, certain helicity-correlated (HC) false asymmetries still persist, like residual birefringence effect. The responsibility of the slow helicity reversal is to eliminate these systematic false asymmetries.

Two methods are commonly used for implementing slow helicity reversal: the insertable half-wave plate (IHWP) and the double Wien filters. Before 2009, the IHWP was the sole approach employed at CEBAF for achieving slow helicity reversal. Dur-

ing the PREX-I and Qweak experiments, a new mechanism called the Wien filters was introduced to enhance the systematic precision.

The IHWP is positioned upstream of the PC, allowing for convenient manipulation of the beam helicity by inserting or retracting the IHWP. Slow helicity reversal enables us to identify possible systematic uncertainties. The idea is straightforward: assuming the true asymmetry to be  $\mathcal{A}_0$  and the presence of a systematic false asymmetry  $\Delta\mathcal{A}$ , the measured asymmetry by inserting or retracting the IHWP will be:

$$\mathcal{A}^{(+/-)} = \pm\mathcal{A}_0 + \Delta\mathcal{A} \quad (2.13)$$

Because the IHWP has no impact on systematic uncertainties, the true asymmetry will be:

$$\mathcal{A}_0 = \frac{\mathcal{A}^+ - \mathcal{A}^-}{2} \quad (2.14)$$

While the IHWP is effective in addressing certain HC beam variations, such as residual birefringence from the laser optical system, it is not capable of mitigating other HC effects. One notable example is the HC beam size variations caused by PC focusing [64]. The Wien filter, on the other hand, is specifically designed to tackle such HC effects.

The double Wien filters manipulate the electron spin directly using EM fields without affecting the electron's trajectory. This mechanism allows for achieving any desired spin orientation. The setup involves two Wien filters with two solenoids positioned between them, as illustrated in Fig. 2.15. A Wien filter is a cavity that incorporates electric and magnetic fields ( $qE = qvB$ ) arranged perpendicular to each other and to the direction of electron motion. This configuration ensures that only the electron spin is rotated while leaving the trajectory unaffected.

The electrons emitted from the photocathode initially possess longitudinal polarization. The vertical Wien filter will orient the electron spin vertically. Subsequently, the spin solenoid following the Wien filter will rotate the spin either to the left or right, depending on the polarity of the solenoid. The process of changing the polarity of the spin solenoid is referred to as a Wien flip. Finally, the horizontal Wien filter is utilized to finely adjust the spin direction, aiming to optimize the longitudinal polarization in the experimental hall.

Note that electrons exiting the double Wien filters are not longitudinally polarized. This is because the electron spin undergoes precession as it travels through the accelerator, resulting in a rotation in the horizontal plane. Consequently, a carefully chosen initial spin direction is required to ensure that the spin is (anti)parallel to the electron momentum at the target. This aspect highlights an additional role of the double Wien filters: to establish a non-longitudinal initial spin orientation that compensates for the shift caused by spin precession during acceleration, ensuring that the electron beam becomes precisely longitudinally polarized at the target.

By utilizing both the IHWP and the double Wien filters, it becomes possible to mitigate a significant portion of systematic false asymmetries, resulting in exceptionally small systematic errors.

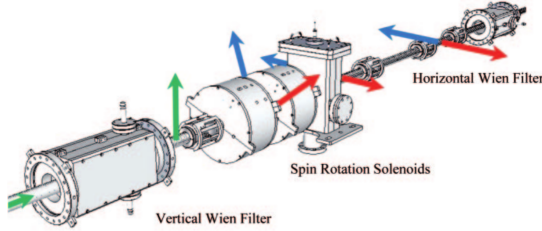


Figure 2.15: Schematic plot of the double Wien filters. The electron beam travels from left to right. [64]

### 2.3.3 Polarimeters

With polarized electron beams, we need to measure their polarizations. There are three polarimeters to measure the beam polarization: the Mott polarimeter located at the injector, and the Compton and Moller polarimeters situated in Hall A. As their names imply, they utilize the cross section asymmetry of the Mott, Compton and Moller scatterings to determine the beam polarization. Since these scatterings are pure quantum electrodynamics (QED) processes, their cross sections are well-understood and the analyzing powers can be accurately calculated to high orders.

Because the Mott and Moller measurements are invasive, they cannot be conducted frequently (Moller measurement happens about every 10 days). The non-invasive Compton polarimeter is the only choice for beam polarization monitoring. The Mott polarimeter measures the beam polarization prior to its entry into the accelerator, so it is not used for the determination of the beam polarization in PREX-II/CREX.

#### Mott Polarimeter

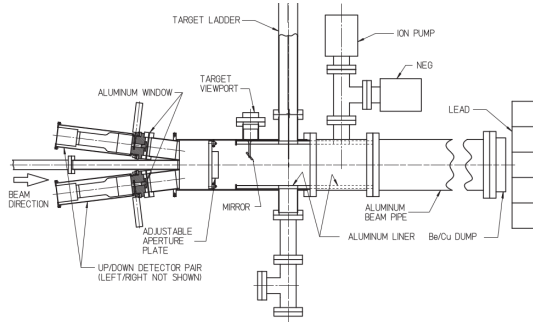


Figure 2.16: Schematic plot of the Mott polarimeter. It has 4 symmetric detector ports (up and down, left and right – left/right detectors are not shown in the plot). The back scattering angle is  $172.6^\circ$ , where the highest analyzing power is achieved from theoretical calculations of the Sherman function. [65]

The 5-MeV Mott polarimeter is positioned at the CEBAF injector, situated between the double Wien filters and the Injection Chicane. It measures the single spin cross

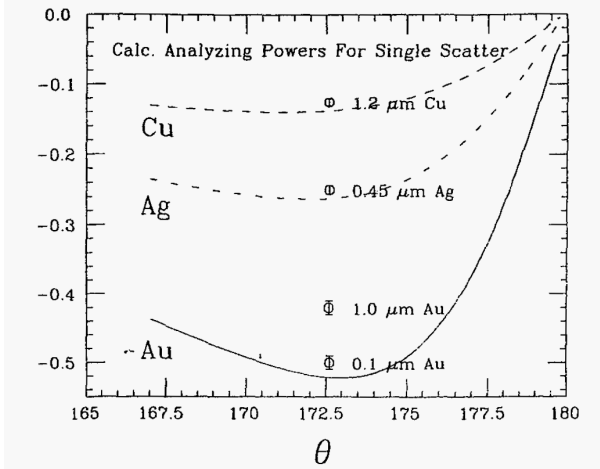


Figure 2.17: The Sherman function for different high-Z targets at 5 MeV, dots represent experimental measurements.

section asymmetry of 5 MeV electron beams scattered off a high-Z target. By comparing the measurement result with the Sherman function  $S$  [66], which represents the analyzing power for the scattering process, the transverse polarization of the beam can be derived:

$$\mathcal{A}_{LR} = \frac{N_L - N_R}{N_L + N_R} = S(\theta) \mathcal{P} \cdot \hat{\mathbf{n}} \quad (2.15)$$

where  $\theta$  is the scattering angle and  $\hat{\mathbf{n}}$  is the unit normal vector of the scattering plane. The same formula is applicable to the up-down asymmetry. Because the asymmetry arises from the coupling between the electron spin and the induced magnetic field generated by the nucleus in the rest frame of the electron (the spin-orbit coupling), the scattering potential is:

$$V(r, \mathbf{L}, \mathbf{S}) = V_{\text{Coulomb}} + V_{\text{so}}(r, \mathbf{L}, \mathbf{S}) = \frac{Ze}{r} + \frac{Ze^2}{2m^2r^3} \mathbf{L} \cdot \mathbf{S} \quad (2.16)$$

Therefore, only the transverse polarization, rather than the longitudinal one, can be measured with the Mott polarimeter. Nevertheless, it provides an independent check of the initial beam polarization at the injector. Its high precision measurements, with a total uncertainty that can be as low as 0.61% [65], helps to normalize the polarization measurement in the experimental halls.

### Compton Polarimeter

The Compton polarimeter, located at the entrance to Hall A (about 20 m upstream from the target chamber), employs elastic scattering between polarized photons and electrons to measure the polarization of the electron beam. As shown in Fig. 2.18, when the Compton polarimeter is on, the electron beam is directed into the Compton Chicane, where it interacts nearly head-on with the polarized photons. The interaction occurs

with a small crossing angle of 23.5 mrad. The Fabry-Perot Cavity is precisely locked to and filled with circularly polarized ( $> 99\%$ ) green laser beam operating at  $\lambda = 532$  nm ( $E = 2.334$  eV).

The back-scattered photons resulting from the interaction are detected by a Gadolinium Orthosilicate (GSO) crystal calorimeter located to the right of the interaction region. Meanwhile, the unscattered electron beam is redirected back to the beam pipe to proceed with bombarding the target. As a consequence of the photon-electron interaction, the scattered electrons are less energetic than the incoming ones. Under the influence of the same dipole field, the scattered electrons experience a greater deflection compared to the unscattered ones, as indicated by the red dashed line in Fig. 2.18. This spatial separation facilitates the counting of the scattered electrons. Combined with the measurement of the scattered photons, the scattering asymmetry can be determined, enabling the accurate determination of the electron beam polarization.

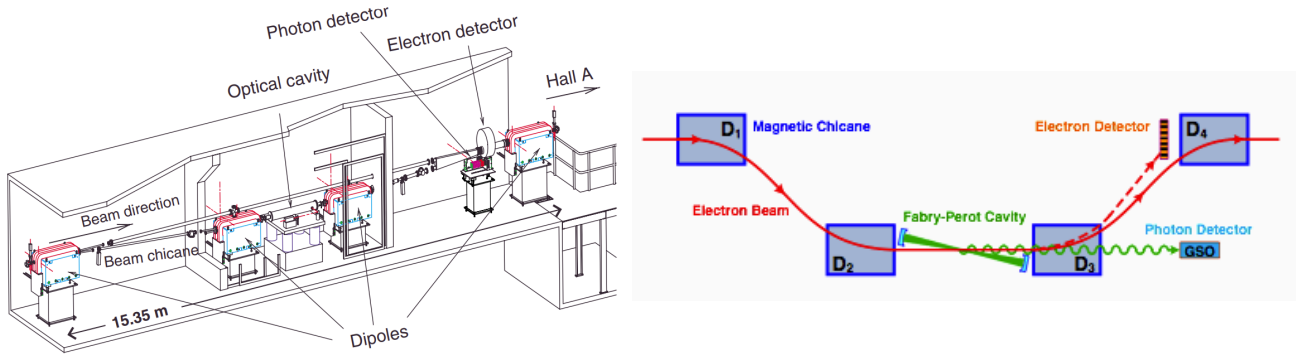


Figure 2.18: Left: schematic plot of the Compton Chicane [67]; Right: schematic plot of the electron-photon scattering.

The energy of a scattered photon is:

$$E_\gamma \approx E_{\text{laser}} \frac{4a\gamma^2}{1 + a\theta_\gamma^2\gamma^2} \quad (2.17)$$

where  $\gamma = E_{\text{beam}}/m_e$  is the Lorentz factor of the incoming electron,  $a = \frac{1}{1+4\gamma E_{\text{laser}}/m_e}$  and  $\theta_\gamma$  is the scattering angle relative to the momentum of electron. The maximum energy of the scattered photons appears at  $\theta_\gamma = 0$ , which corresponds to backscattering. For the PREX-II (CREX) beam energy of 0.95 (2.2) GeV,  $E_\gamma^{\text{max}} \sim 32.55$  (167.02) MeV.

Define  $\rho = \frac{E_\gamma}{E_\gamma^{\text{max}}}$ , the cross section for the unpolarized Compton scattering can be expressed as:

$$\frac{d\sigma}{d\rho} = 2\pi r_0^2 a \left[ \frac{\rho^2(1-a)^2}{1-\rho(1-a)} + 1 + \left( \frac{1-\rho(1+a)}{1-\rho(1-a)} \right)^2 \right] \quad (2.18)$$

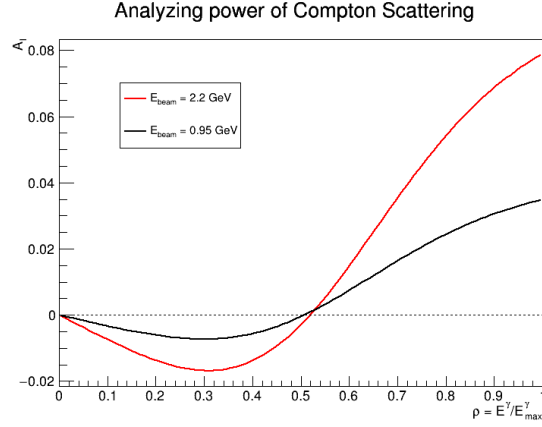


Figure 2.19: The Compton analyzing power increases with the incoming electron energy. Note that the analyzing power will change sign at  $\rho \sim 0.5$  for both PREX-II and CREX beam energies.

$r_0 = \frac{\alpha \hbar c}{mc^2}$  is the classical electron radius; then the analyzing power is:

$$\mathcal{A}_l = \frac{\sigma_{\Rightarrow}^{\rightarrow} - \sigma_{\Rightarrow}^{\leftarrow}}{\sigma_{\Rightarrow}^{\rightarrow} + \sigma_{\Rightarrow}^{\leftarrow}} = \frac{2\pi r_0^2 a}{d\sigma/d\rho} (1 - \rho(1 + a)) \left[ 1 - \frac{1}{(1 - \rho(1 - a))^2} \right] \quad (2.19)$$

The measured asymmetry will be:

$$\mathcal{A}_{\text{exp}} = \mathcal{P}_e \mathcal{P}_\gamma \mathcal{A}_l = \frac{N_\gamma^R - N_\gamma^L}{N_\gamma^R + N_\gamma^L} \Rightarrow \mathcal{P}_e = \frac{\mathcal{A}_{\text{exp}}}{\mathcal{P}_\gamma \mathcal{A}_l} \quad (2.20)$$

The advantage of the Compton polarimeter is that it can tolerate high current, reaching  $\sim 200 \mu\text{A}$  at JLab. Furthermore, its non-invasive operation makes it suitable for use as a beam polarization monitor. However, compared to the Mott or Moller polarimeter, its analyzing power is relatively low at GeV energy levels, while increasing the beam energy will lead to a high background noise in the photon detection due to synchrotron radiation. Overall, the Compton polarimeter is able to achieve a 1% absolute systematic uncertainty.

## Moller Polarimeter

The Moller polarimeter is positioned downstream of the Compton polarimeter and upstream of the target chamber. It uses elastic electron-electron scattering to measure

the cross section asymmetry between beams with different polarizations.

$$\begin{aligned}\frac{d\sigma}{d\Omega} &= \frac{d\sigma_0}{d\Omega} \left(1 + \sum_{i,j=x,y,z} \mathcal{P}_b^i \cdot \mathcal{P}_t^j \cdot \mathcal{A}_{ij}(\theta_{CM})\right) \\ \frac{d\sigma_0}{d\Omega} &= \frac{\alpha^2}{s} \left( \frac{4 - \sin^2 \theta_{CM}}{\sin^2 \theta_{CM}} \right)^2\end{aligned}\quad (2.21)$$

With  $\frac{d\sigma_0}{d\Omega}$  being the unpolarized Moller scattering cross section,  $s$  the Mandelstam variable:  $s = 2m_e(E + m_e) \approx 2m_e^2\gamma$ ,  $\mathcal{P}_b$  ( $\mathcal{P}_t$ ) the polarization of the beam (target),  $\theta_{CM}$  and  $\mathcal{A}_{ij}$  the scattering angle and analyzing power in the COM frame.

Assuming incoming electrons move in the  $z$  direction and the scattering takes place in the  $xz$ -plane, then under the ultra-relativistic limit:

$$\begin{aligned}\mathcal{A}_{zz} &= \frac{\sin^2 \theta_{CM} (7 + \cos^2 \theta_{CM})}{(3 + \cos^2 \theta_{CM})^2}, \quad \mathcal{A}_{xx} = -\mathcal{A}_{yy} = \frac{\sin^4 \theta_{CM}}{(3 + \cos^2 \theta_{CM})^2} \\ \mathcal{A}_{xz} = \mathcal{A}_{zx} &= \frac{2 \sin^4 \theta_{CM} \cos \theta_{CM}}{\gamma (3 + \cos^2 \theta_{CM})^2}, \quad \mathcal{A}_{xy} = \mathcal{A}_{yz} = \mathcal{A}_{yz} = \mathcal{A}_{zy} = 0\end{aligned}\quad (2.22)$$

$\mathcal{A}_{zz}$  is maximized to be  $\frac{7}{9}$  at  $\theta_{CM} = 90^\circ$ . This  $\theta_{CM}$  value was used in the Moller measurement.

The polarized target electrons come from a magnetized Fe-alloy foil, which is saturated by a very strong (4 T) longitudinal magnetic field created by superconducting Helmholtz coils, as illustrated in Fig. 2.20. Consequently, Eq. 2.21 is simplified to:

$$\frac{d\sigma}{d\Omega} = \frac{d\sigma_0}{d\Omega} (1 + \mathcal{P}_b^z \cdot \mathcal{P}_t^z \cdot \mathcal{A}_{zz}(\theta_{CM})) \quad (2.23)$$

The Moller pair, consisting of the scattered incident electron and recoil target electron, is centered around  $\theta_{CM} = 90^\circ$  ( $\theta_{lab} < 3^\circ$ ). After being separated from the undeflected beam by set of magnets, the Moller pair passes through collimators (located at the dipole's exit, not shown in Fig. 2.20), which define the acceptance of the system, and finally is detected by electron detectors in coincidence. The asymmetry between cross sections for spin-parallel and spin-anti-parallel configurations is measured as:

$$\mathcal{A}_{exp} = \frac{N^+ - N^-}{N^+ + N^-} = \mathcal{P}_b \mathcal{P}_t \langle \mathcal{A}_{zz} \rangle \Rightarrow \mathcal{P}_b = \frac{\mathcal{A}_{exp}}{\mathcal{P}_t \langle \mathcal{A}_{zz} \rangle} \quad (2.24)$$

with  $\langle \mathcal{A}_{zz} \rangle$  being the average analyzing power over the acceptance, which is about 0.75 for PREX-II and CREX.

To prevent damage to the target polarization, the target foil is cooled through conduction. When the beam current increases, the temperature of the target will rise rapidly, posing a risk to the target polarization. Therefore, the Moller polarimeter is limited to very low current operation ( $\lesssim 1\mu A$ ). Extrapolating from polarization measurements at low currents to the high currents used in PREX-II and CREX introduces a significant

source of systematic uncertainty. During PREX-II and CREX, the target polarization was measured to be  $\mathcal{P}_t \sim 8\%$ , leading to an effective analyzing power of  $\mathcal{A}_{\text{eff}} = \mathcal{P}_t \langle \mathcal{A}_{zz} \rangle \approx 6\%$ . This relatively large analyzing power makes the Moller measurement quite precise. Overall, the Moller polarimeter in Hall A can achieve a systematic uncertainty less than 1%.

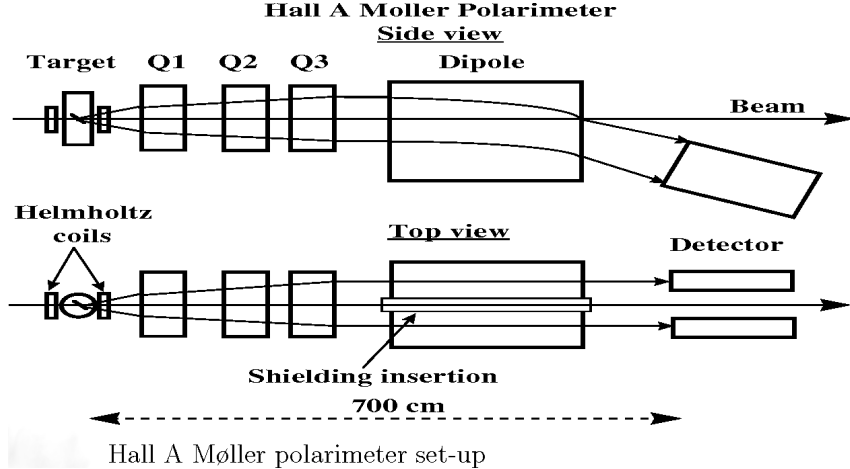


Figure 2.20: Schematic plot of the Moller Polarimeter.

## 2.4 Monitors

In addition to beam polarization, another substantial source of systematic uncertainty is the beam false asymmetry. This refers to the difference in beam position, angle, energy and current between different helicity states. Even with fast helicity flipping, it is challenging to ensure precisely identical beam parameters across different helicity states. We monitor these quantities with redundant specialized devices – beam position monitors and beam current monitors. For PREX-II and CREX, an additional independent monitoring system called small angle monitors (SAMs). is utilized. These monitors are capable of measuring the beam difference with a high degree of precision:

$$\Delta x \sim 10 \text{ nm} \quad \Delta x' \sim 1 \text{ nrad} \quad \Delta p/p \sim 0.0001 \quad \Delta I/I \sim 100 \text{ ppb}$$

### 2.4.1 BPMs

In Hall A, a series of BPMs are installed along the beam pipe leading to the target chamber to monitor the beam conditions. Among them, of particular importance for PREX-II and CREX are the six switched electrode electronics (SEE) stripline BPMs, as shown in Fig. 2.21. They provide readouts for the determination of beam parameters. BPM4a and BPM4e are located 5.725 m and 1.642 m upstream of the target chamber, respectively. They are used to determine the beam position and angle at the target

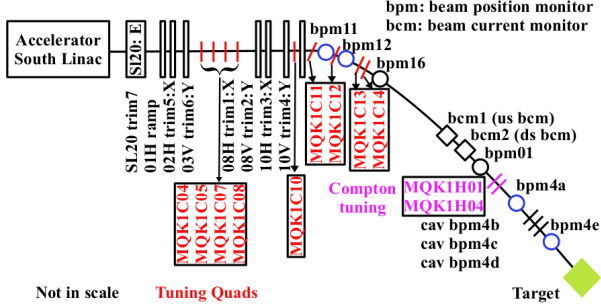


Figure 2.21: Schematic plot of the Hall A beam monitor system and beam modulation system

location. On the arc area, BPM11 and BPM12 can measure the beam energy using the bending radius of the electron trajectory. BPM1 and BPM16 serve as backup monitors.

A stripline BPM consists of a 4-wire antenna array of open ended thin wire striplines. The voltage induced in each electrode by the passing electron bunch is highly sensitive to the beam position. As a result, one can extract the ( $x'$ ,  $y'$ ) positions from the pickup signals.

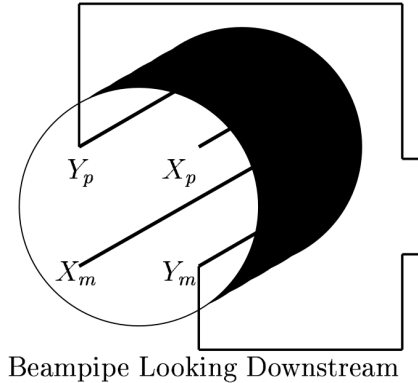


Figure 2.22: Schematic plot of a stripline BPM.

$$x' = \frac{1}{S_x} \frac{X_p - X_m}{X_p + X_m} \quad y' = \frac{1}{S_y} \frac{Y_p - Y_m}{Y_p + Y_m} \quad (2.25)$$

where the proportional constant  $S_x$  ( $S_y$ ) is the position sensitivity. The pickup voltage responds linearly to the beam displacement when it is small. In the case of Hall A BPMs, the four striplines are rotated  $45^\circ$  with respect to the hall coordinate system, so a  $-45^\circ$  rotation is needed to recover the hall ( $x$ ,  $y$ ) positions from the extracted BPM ( $x'$ ,  $y'$ ) positions.

In addition to the stripline BPMs, PREX-II and CREX made use of three cavity BPMs (see discussion below), labeled as bpm4b/c/d between BPM4a and BPM4e in Fig. 2.21. These cavity BPMs were used to measure beam conditions during low current calibration runs. This is necessary because stripline BPMs do not work when the beam

current falls below  $0.5 \mu\text{A}$ . However, during regular production runs, these cavity BPMs were not used.

### 2.4.2 BCMs

One commonly used technique to measure the beam current is the current transformation. Various BCMs based on this idea may have distinct designs, features and performances; they share a common key component: the current transformer (CT). As a beam bunch travels through the beam pipe, it induces a magnetic field in the beam pipe (the core), which in turn generates a current in the secondary winding (toroid) of the CT. The output of the CT is directly proportional to the beam current. To ensure precise measurement, it is crucial to shield the BCM from any external magnetic fields and isolate the segment of beam pipe containing the BCM from the rest.

The BCM system in Hall A consists of two radio frequency (rf) cavities with an unser monitor located between them, as shown in Fig. 2.23. The unser monitor functions as a parametric current transformer. It generates a direct current voltage output that corresponds to  $4 \text{ mV}$  per  $\mu\text{A}$  of beam current [68].

During PREX-II and CREX, the unser monitor was not used for the beam current measurement, because its voltage output drifted quickly after only a few minutes of operation. Instead, it was used to calibrate the rf-cavity monitors on either side of it, allowing for accurate and reliable beam current measurements during the experiments.

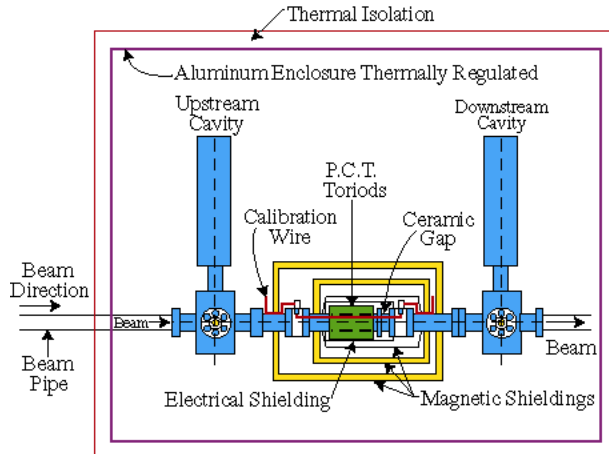


Figure 2.23: Hall A BCM system [68].

A rf cavity is a metallic chamber that sustains an EM field, which consists of an infinite number of resonant EM modes. By carefully shaping the cavity, a specific EM mode can efficiently transfer energy to or from a charged particle. In the case of an accelerating cavity, it is designed to provide an electric field along the direction of the beam velocity. On the other hand, a decelerating cavity is designed to absorb energy from the incoming charged particles. It can be used as a beam diagnostic monitor since the induced voltage

in the cavity is proportional to the charge  $q$  of the traversing particles.

$$V = 2k_{loss}q \quad (2.26)$$

where  $k_{loss}$  is the loss factor, which depends solely on the electric field distribution. Therefore, it is sensitive to the beam position and the particle velocity. To accurately measure beam intensity, it is preferable to utilize an EM mode in which the electric field does not depend on the radial position ( $r$ ). These modes are  $TM_{010}$  like modes. On the other hand, when measuring the beam position, it is desirable to use an mode in which the electric field has an azimuthal angle the radial dependence. These are  $TM_{110}$  like modes.

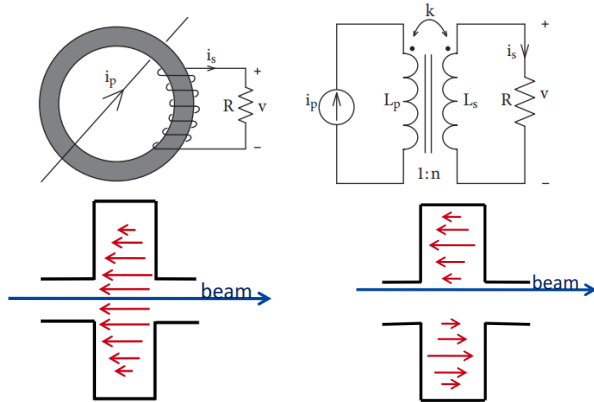


Figure 2.24: Up: Schematic plot of the current converter; Down:  $TM_{010}$  and  $TM_{110}$  modes, the red arrows indicate the electric field.

The two rf-cavity current monitors are of the Pill box type. These monitors operate in the the  $TM_{010}$  mode, where the the electric field is concentrated near the axis, while the magnetic field is concentrated at the outer cylindrical wall. The voltage readout from these monitors is down-converted to lower frequencies signals, and subsequently filtered, amplified and further processed before being written into the data stream. Due to the non-linearity of the readout converter at low beam currents ( $\lesssim 5 \mu\text{A}$ ), actually 3 signals (the same signal with different gains: x1, x3 and x10) are recorded to extend the linear region to lower beam currents, at the expense of saturation at high beam currents [59].

### 2.4.3 SAMs

To gain further insights into beam dynamics, electronic noise and the possible target boiling effect, a luminosity monitoring system, called the small angle monitors, was installed in the dump pipe, about 7 m downstream of the target pivot. As shown in Fig. 2.25, the SAMs system consists of eight detector modules, symmetrically positioned around the dump pipe. Each detector module comprises a quartz tile, serving as the active detector, which is connected to a lightguide. the Cherenkov light radiated by

electrons will be read out by a Photomultiplier Tube (PMT) located at the end of the lightguide.

As its name implies, the SAMs system is specifically designed to monitor the flux of small-angle ( $\sim 1^\circ$ ) scattered and secondary particles emanating from the target, making it suitable for inspecting the target conditions. E.g., a bubble in the target that forms and disappears within one helicity window is unknown to both BPMs and BCMs, but SAMs will see it.

The readout of each SAMs detector is sensitive to various beam parameters. For instance, the sum of the readout from a symmetric pair of monitors is sensitive to changes in beam current and energy, while their difference provides information about fluctuations in beam position and angle. The symmetric design helps to disentangle these beam parameters, allowing for an independent cross-check of measurements obtained from BPMs and BCMs. Additionally, the SAMs system can help to mitigate potential sources of beam or electronic noise.

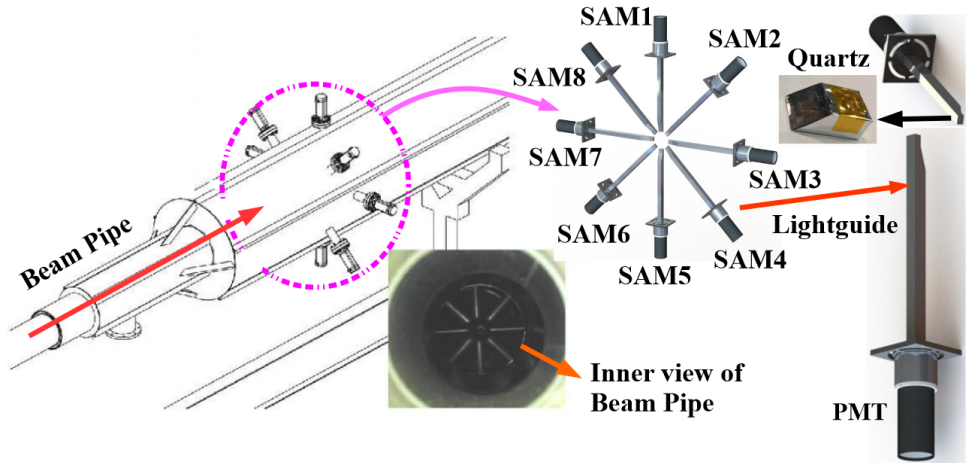


Figure 2.25: Layout of SAMs [69].

#### 2.4.4 Beam Modulation

Another system shown in Fig. 2.21 is the beam modulation system, which is located in the beamline arc immediately after the Beam Switch Yard, where electron chains are separated into Hall A/B/C beams. This system comprises six air-core coils and an energy vernier situated in the fianl cavity of the south LINAC. With a total of seven coils, redundancy is ensured with respect to the number of free degrees in the beam phase space, thus covering the entire beam phase space at the target. Coils (trim) 1, 3, 5 are responsible for modulating the beam's x position, while coils 2, 4, 6 modulate the beam's y position. These coils (vernier) are driven by a VME-DAC (Digital-Analog Converter), which in turn, is controlled by the parity data acquisition (DAQ). It takes 4.267 s for each coil (vernier) to modulate the beam. A complete modulation cycle, involving all coils, lasts 85.68 s. During runtime, the beam modulation occurs about every 10 mins.

The beam modulation system is used for beam false asymmetry correction. During the beam modulation process, BPMs and detectors record the corresponding changes in their readout. These values are used to calculate the sensitivity of the detector to jitters in beam parameters. The obtained sensitivity values are then employed to correct the measured asymmetry. Therefore, the magnitude of the modulation should be significantly larger than the inherent jitters present in the beam. A typical position modulation is a sinusoid with an amplitude of about  $200\text{ }\mu\text{m}$  and the energy vernier will result in a beam displacement of 0.75 mm at BPM11/12.

## 2.5 Target

For the sake of high statistics, the designed current is quite large, as shown in Table 2.1. However, such high currents pose a challenge as the electron beam deposits a significant amount of heat on the target. It will be a disaster if the heat is not dissipated quickly to maintain a stable target temperature. For PREX-II, since  $^{208}\text{Pb}$  itself is not a good thermal conductor ( $\kappa = 35\text{ W}/(\text{m}\cdot\text{K})$ ), auxiliary diamond foils ( $\kappa > 1000\text{ W}/(\text{m}\cdot\text{K})$ ) are used to form a D-Pb-D sandwich target, aiming in heat dissipation. The thickness of the diamond foil matters. A lesson learned from PREX-I is that a thin (0.15 mm) diamond foil experiences a significant drop in its thermal conductivity (from  $1000\text{ W}/(\text{m}\cdot\text{K})$  to  $100\text{ W}/(\text{m}\cdot\text{K})$ ) after about one week of cw beam operation at  $70\text{ }\mu\text{A}$ , resulting in some  $^{208}\text{Pb}$  targets being melted. On the other hand, a thicker diamond foil (0.25 mm) effectively prevents  $^{208}\text{Pb}$  foils from melting under the same conditions. In PREX-II, a factor of 2 safety margin was adopted. Assuming a conservative one week running period for each  $^{208}\text{Pb}$  target, 35 days of beam time requires 5 targets. To ensure the success of PREX-II, 10 isotopically pure Pb sandwich targets with thick diamond layers were deployed, with each new target capable of sustaining up to  $85\text{ }\mu\text{A}$  cw beams.

While Ca itself is an excellent thermal conductor ( $\kappa = 200\text{ W}/(\text{m}\cdot\text{K})$ ), there is no need for auxiliary materials to allow for high currents. The isotopically pure  $^{48}\text{Ca}$  is much more expensive than pure  $^{208}\text{Pb}$  foils, so only one  $^{48}\text{Ca}$  target (with a purity of 95.99%) was prepared for CREX. Unfortunately, this  $^{48}\text{Ca}$  target was accidentally damaged when the electron beams were locked to a wrong position and hit the copper frame. Following the target accident, the new  $^{48}\text{Ca}$  target was a stack of three separated foils with a total thickness similar to that of the previous one.

The targets are firmly mounted in bays on target ladders. These ladders have their axes positioned perpendicular to the beam line. Each ladder is movable along its axis, driven by an alternating current (AC) servo motor. This motor can be remote controlled through the internet. The motion along the ladder axis can be precise to 0.1 mm.

There are two target ladders in total, one for production targets and the other one for calibration targets. The production ladder has 16 target slots, which are allocated as follows: 10 slots for  $^{208}\text{Pb}$  targets, two slots for Calcium isotope targets ( $^{40}\text{Ca}$  and  $^{48}\text{Ca}$ ), and four slots for calibration and diagnostic targets. On the other hand, the calibration ladder has only 5 targets, including a carbon hole, a watercell, a thin C foil, a thin natural

Pb and a thin  $^{40}\text{Ca}$  target. The production ladder is positioned horizontally, while the calibration ladder is rotated  $45^\circ$  counterclockwise with respect to the production ladder, as shown in Fig. 2.26 and 2.27.

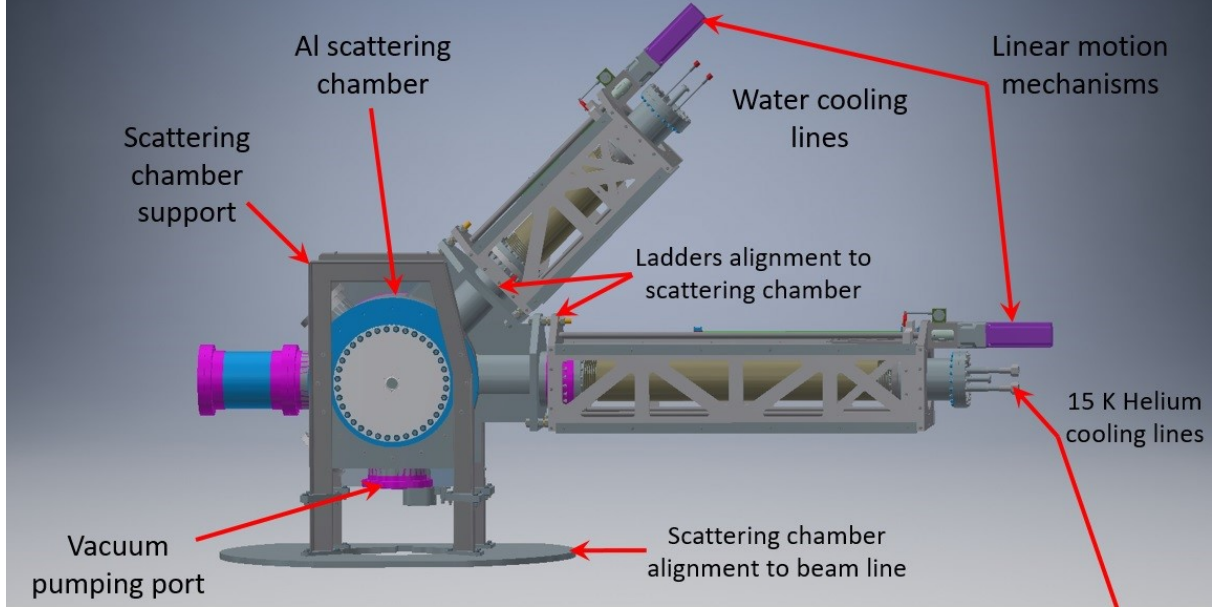


Figure 2.26: Design plot of the scattering chamber and the two target ladders. The horizontal one is the production ladder and the other one being the calibration ladder.

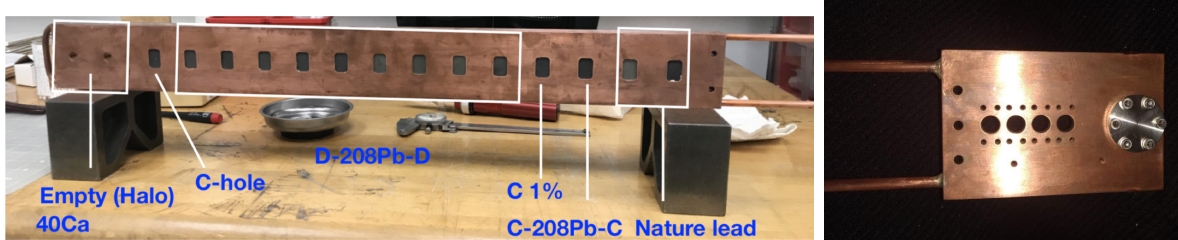


Figure 2.27: Actual pictures of the production (left) and calibration (right) ladders.

The  $^{40}\text{Ca}$  and  $^{48}\text{Ca}$  targets are installed on the cold heat sink in dedicated cylindrical sockets at the end of the production ladder. The fact that the  $^{48}\text{Ca}$  and the  $^{208}\text{Pb}$  targets share the same ladder means they actually have the same z location, and therefore, the same scattering angle, despite different proposed scattering angles ( $5^\circ/4^\circ$  for PREX-II/CREX). This choice simplifies the design, construction and installation of the target chamber.

Special care is needed for the  $^{48}\text{Ca}$  target, the pressure of the target chamber should be less than  $10^{-6}$  torr to avoid Ca oxidation. To maintain the required vacuum, a turbo-molecular pumping system is employed for the target chamber, which creates a vacuum level of  $10^{-7}$  ( $10^{-8}$ ) torr for the calibration (production) ladder within the target chamber. When the beam is not in use, gate valves are closed to isolate the target chamber from

upstream and downstream beam pipes. As an additonal precaution, a nitrogen purge system is installed to purge air in case of long-term vacuum loss or if the chamber needs to be brought up to atmospheric pressure. Every time we warmed up the  $^{48}\text{Ca}$  target, gas boiling was necessary before restarting the data collection process.

### 2.5.1 Target Cooling

The production ladder is cryogenically cooled due to high power generated by electron beams, while the calibration ladder is water-cooled. The calibration runs require only a beam current of  $\lesssim 1 \mu\text{A}$ .

Both ladders are made of copper. The copper frame of the production ladder is cooled by 15 K, 12 atm gaseous helium, which runs through the cooling tube surrounding the frame. Contact between the target and the frame, as well as within each layer of the  $^{208}\text{Pb}$  sandwich target is also important. Belleville washers are used to clamp the lead and diamond foils to ensure proper contact. Additionally, a thin layer of Apiezon L vacuum grease is applied to their interface to improve thermal conductivity. One hypothesis for the sudden failure of the Pb target after one week of running is that the vacuum grease does not last long. In the diamond/copper interface, a silver-based paste compound is used for the same purpose.

For a D-Pb-D sandwich target with a thick diamond foil, the heat loading will be  $\sim 100 \text{ W} @ 70 \mu\text{A}$  with a  $4 \text{ mm} \times 6 \text{ mm}$  raster. Assuming good contact and smooth heat conduction, the cooling system would keep the  $^{208}\text{Pb}$  target at  $\sim 60 \text{ K}$  (melting point at 600 K) For the  $^{48}\text{Ca}$  target, the  $150 \mu\text{A}$  beam current will produce about 370 Watts heat on the target, raising the target temperature to  $\sim 300 \text{ K}$  (melting point at 1115 K).

### 2.5.2 Raster

Despite the helium cooling, the target foil still experiences deformation, and in some cases, even melting, due to electron bombardment. Small variations in the thickness of the target foil lead to non-uniformity, which in turn affect the scattering rate. Over the duration of the experiment, these non-uniformities gradually accumulate, resulting in significant noise that overwhelms the weak-scattering signal. In fact, this phenomenon serves as an indicator of the target's condition and prompts us to replace it if the measured asymmetry width exhibits a significant increase.

The solution to this problem is the raster system, which is a set of dipole magnets positioned between the Compton and the Moller polarimeters, that deflects the beam at a frequency of 25 kHz to spread the beam on the target. One thing we learned from PREX-I is that we could significantly reduce the sensitivity to variations in target thickness by synchronizing the helicity flip frequency with the raster frequency. By doing so, we ensure that the beam samples exactly the same areas on the target. As a result, any noise arising from variations in target thickness can be eliminated by taking the difference between helicity pairs or quadruplets.

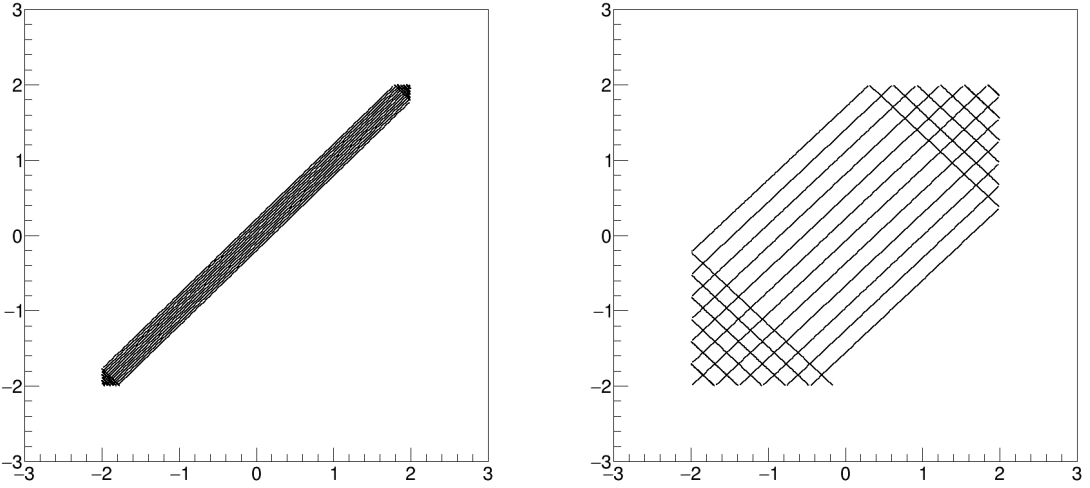


Figure 2.28: Raster pattern with different frequency difference between X and Y. Left:  $|f_y - f_x| = 120$  Hz; Right:  $|f_y - f_x| = 8 * 120$  Hz. The raster shape is a  $4\text{ mm} \times 4\text{ mm}$  square.



Figure 2.29: Picture of  $^{208}\text{Pb}$  targets after data collection. One can clearly see the shape of the raster pattern. Target 1 and 4 are melted.

As shown in Fig. 2.28, the Lissajous pattern depends on the frequency difference between X and Y axes, the larger the frequency difference, the larger the scanning area. The ratio of  $f_y/f_x$  should be an irrational number to prevent a closed Lissajous pattern. The actual frequencies used are  $f_x = 25.44$  and  $f_y = 24.48$  kHz. for PREX-II, the raster size is  $4\text{ mm} \times 6\text{ mm}$ , and CREX has a raster size of  $2\text{ mm} \times 2\text{ mm}$ .

Another reason for having the raster is heat dissipation. A larger raster size facilitates quicker heat dissipation, resulting in a lower target temperature, as illustrated in Fig. 2.30.

### 2.5.3 Beamline Collimator and Sieve Slit Collimators

One problem that failed PREX-I was the excessive radiation, which damaged electronics in the hall and the o-ring on the target exit flange, leading to leaks and ultimately

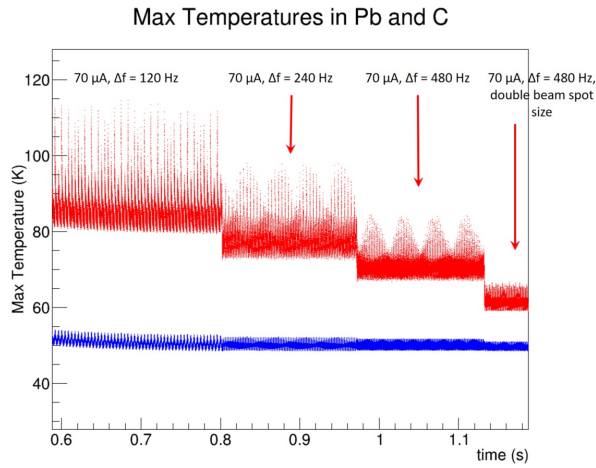


Figure 2.30: Simulation of the target temperature evolution with different raster frequency differences. The larger the raster frequency difference ( $\Delta f$ ), the larger the size of the raster area, the lower the highest target temperature.

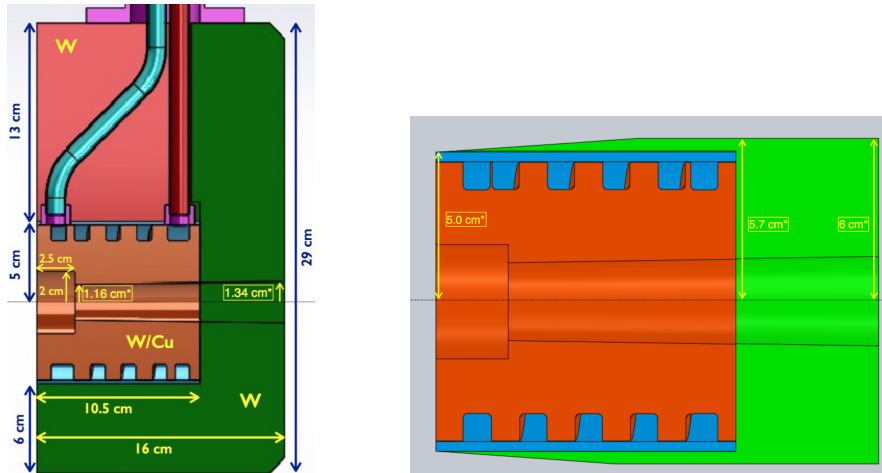


Figure 2.31: Side and top view of the beamline collimator. Beam travels from left to right.

halting the experiment. Taking this experience into account, the new design of the pivot area, which is the central region between the two HRS where the target chamber is located, has paid more attention to mitigating radiation near the target region. The idea is to redirect as much radiation as possible towards the beam dump, while absorbing the remaining radiation using a crucial component called the beamline collimator.

The beamline collimator, positioned 83 cm downstream from the production target, is composed of two main components: an inner collimator and a housing jacket. Both components are constructed using sintered tungsten material. The inner collimator itself consists of a structure comprised of a 70% tungsten/30% copper (W/Cu) alloy collimator and a copper jacket. As shown in Fig. 2.31. There is a cylinder notch in the front of the inner collimator, to ensure effective absorption of electrons and radiation.

The beamline collimator is water cooled, with a maximum heat loading of about 3.65 kW from the  $^{208}\text{Pb}$  target. The power on the beamline collimator is another signal for the degradation of the target. When the temperature of the outgoing water increases dramatically, it signals to replace the running  $^{208}\text{Pb}$  target, as shown in Fig. 2.32.

In addition to the beamline collimator, several other devices are installed to further eliminate the radiation levels in the hall. These devices include the high-density polyethylene neutron shield around the beamline collimator region and a skyshine shield consisting of a 6 cm thick tungsten block and massive concrete blocks. These extra shields are used to block high energy neutrons from the collimator.

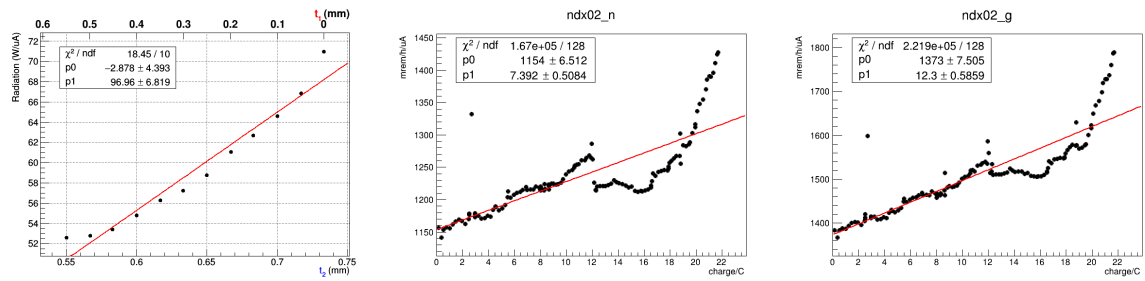


Figure 2.32: Left: a simple model of target degradation – assuming the raster area ( $t_1$ ) is becoming thinner and the rest is becoming thicker ( $t_2$ ), both areas are uniform and the total mass keeps intact. The plot shows how the power deposition on the beamline collimator changes in this model. Middle and Right: actual neutron and photon radiation levels monitored along charge accumulation.

Located on both sides of the beamline collimator, approximately 1.1 m away from the target, are the 5 mm thick stainless steel sieve slit collimators, which are used for optics studies, helping electron trajectory reconstruction.

During production data collection, the sieve slit collimators are moved out of the spectrometer acceptance. However, when conducting optics data measurements to determine the scattering angle and  $Q^2$ , these collimators are inserted to cover the entire spectrometer acceptance, without interfering with the inner bore of the beamline collimator. With known (x, y) position of each hole on the sieve plane, and the track information obtained from the vertical drift chamber (VDC), we can reconstruct the beam transport matrices.

## 2.5.4 Septum

The septum magnet is required to bridge the scattered electrons at small angle into the HRS. As said before, the designed scattering angle is about  $5^\circ$  while the minimum angle that HRS can reach is  $12.5^\circ$ . Therefore, a septum magnet is needed to bend the scattered electrons into the HRS.

The septum magnets are normal conducting magnets composed of three coils. By applying a large current, they will produce a strong magnetic field (up to  $\sim 1$  T in the central region). A non-magnetic stainless vacuum box connects the upstream collimator

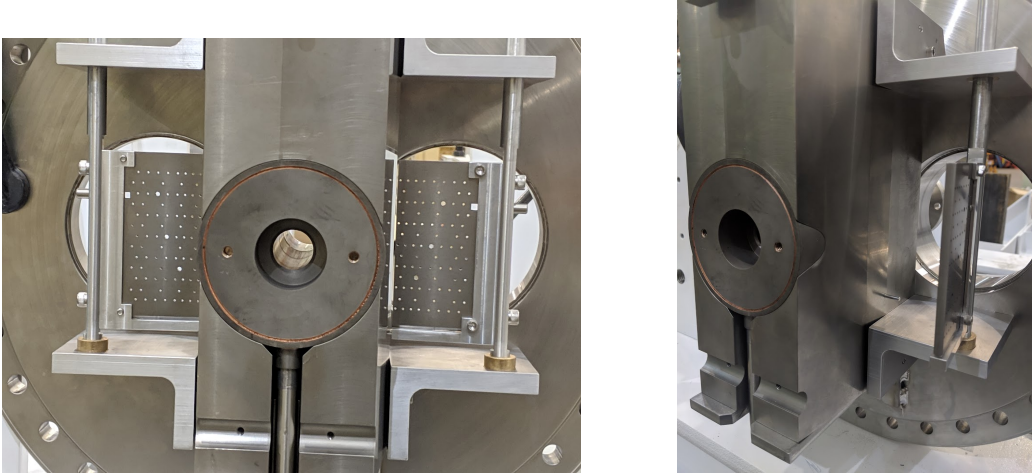


Figure 2.33: Front pictures of the beamline collimator and sieve slit collimators, looking downstream. In the left picture, one can clearly see that a cylinder is removed from the central collimator. The sieve planes are located after the beamline collimator and are movable like windows, they can be opened or closed from outside.

box and the downstream HRS vacuum pipe, serving as the connecting points for the septum. The septum beam pipe, which leads to the beam dump, is constructed from magnetic stainless steel to shield the magnetic field generated by the septum. Magnetic steel boxes are installed on both ends of the septum beam pipe to further shield the fringe magnetic field produced by the septum.

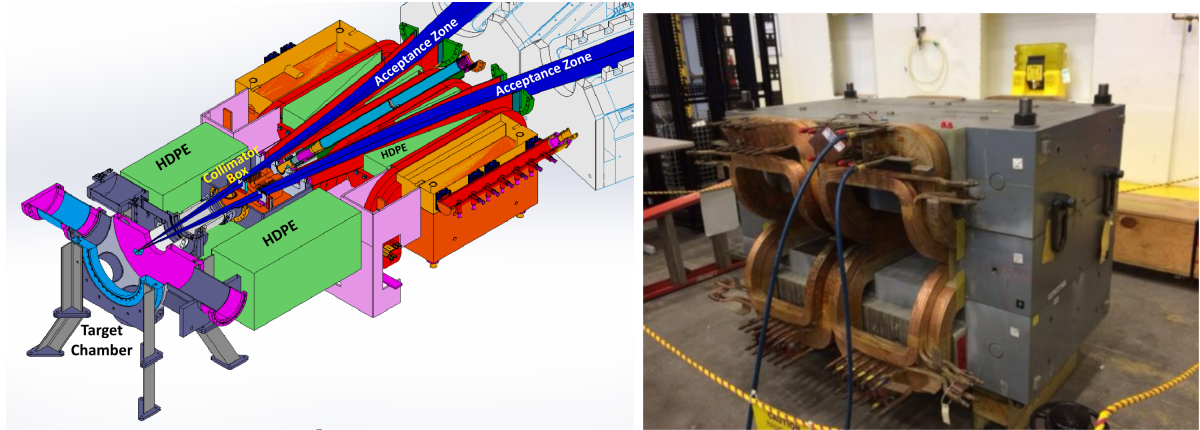


Figure 2.34: Left: the design plot of the pivot region; septums are represented by red coils. Right: a actual picture of septums.

## 2.5.5 High Resolution Spectrometer (HRS)

Spectrometer is a key component for every Hall A experiment. PREX-II and CREX use the HRS pair. Each HRS consists of three superconducting quadrupoles and one

dipole. The maximum magnetic field of the three quadrupoles are 1.2, 1.0 and 1.0 T respectively, while the dipole can provide a field up to 1.7 T [59]. The incoming electrons are bent upward by  $45^\circ$  in the vertical plane and then received by electron detectors.

The HRS has a small angular acceptance, with a range of  $\pm 28$  mrad horizontally, and  $\pm 60$  mrad vertically, resulting in a solid angle being  $7.8 \text{ msr}$ . However, it can be positioned over a wide range of angle within the hall, from  $12.5^\circ - 165^\circ$ . As its name implies, it achieves a very high momentum resolution at the level of  $dp/p \sim 10^{-4}$  over a wide range of momentum (0.8 - 4 GeV). This capacity is crucial in rejecting most inelastically scattered electrons. Even a small difference in momentum (2-3 MeV) leads to a large separation in the detector plane, resulting in relatively clean data with minimal background from inelastic scattering, as illustrated in Fig. 2.35.

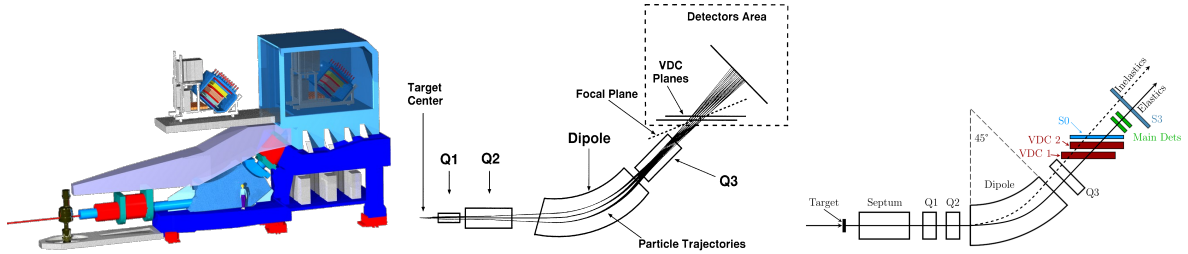


Figure 2.35: Schematic plot of the HRS and particle rays inside. [70] The ‘focal plane’ in the middle plot, by design, should be positioned at an angle of  $45^\circ$  with respect to the central ray. However, due to the absence of sextupole winding in Q3, it is actually rotated to  $70^\circ$ . When we talk about the HRS focal plane, we typically refer to the VDC lower plane.

Prior to the entrance of the Q1 quadrupoles, there is a Q1 collimator that defines the acceptance of the spectrometer. It is strictly required that the symmetry between left/right, and up/down of the Q1 collimators should be preserved to reduce any possible systematic uncertainties.

### 2.5.6 Detector Package

The standard HRS detector package in each arm consists of trigger scintillators for triggering, a pair of VDCs for particle tracking, Cherenkov-type detectors and shower counters (calorimeters) for particle identification (PID). In PREX-II and CREX, only parts of these detectors are needed, namely VDCs and S0/S3 triggers, others are removed for safety. We built our own Cherenkov counters that can suffer high electron flux to integrate scattered electrons. The complete configuration of the detector package is shown in Fig. 2.37.

#### Vertical Drift Chamber (VDC)

Each VDC detector package consists of two drift chambers: a lower chamber and an upper chamber. These chambers are vertically separated by a distance of 0.23 m, with

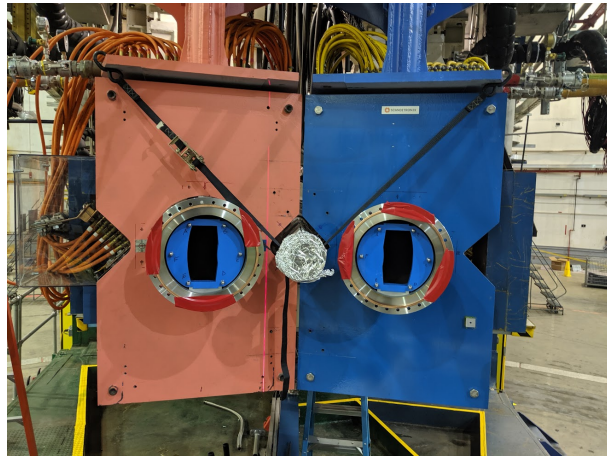


Figure 2.36: Picture of the Q1 collimator pairs, looking downstream. Q1 collimator is the blue piece surrounded by a circular steel. The pipe between the two Q1 collimators, covered by tin foils, is the beam pipe leading to the beam dump.

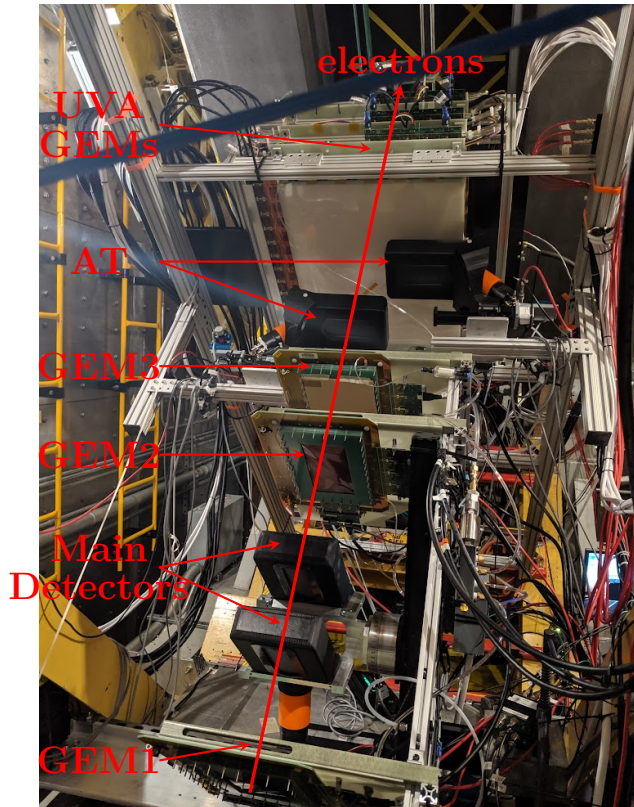


Figure 2.37: Picture of the detector package.

a spacing of 0.335 m between the corresponding U or V planes of the lower and upper chambers. This design enables precise measurement of position and angle.

The drift chamber is actually a multiwire proportional chamber (MWPC) with two layers of sense wires: the U plane and the V plane. These wire planes are positioned

horizontally and are orthogonal to each other, with a vertical separation of 26 mm. Each wire plane contains 368 tungsten wires. The width of adjacent wires is 4.24 mm, which corresponds to 6 mm in the cross section of the spectrometer due to the 45° cross angle between the axis of the spectrometer and the VDC plane.

The VDC utilizes the drift time of ionized particles in the chamber to reconstruct the trajectory of electrons. A single wire plane can achieve a position resolution of approximately 235 mm full width at half maximum (FWHM). The angular resolution is 6 mrad FWHM for  $\theta$  (out-of-plane angle) and 2.3 mrad FWHM for  $\phi$  (in-plane angle) [71].

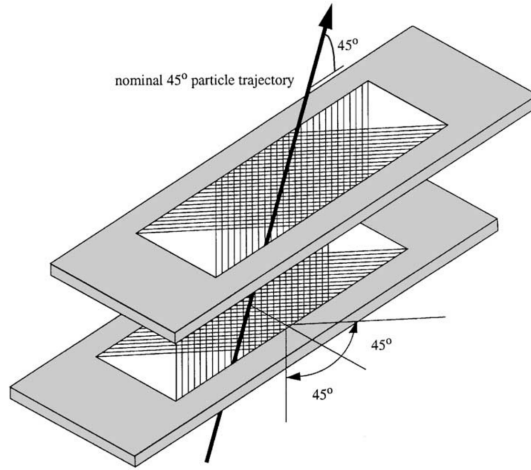


Figure 2.38: Schematic plot of a VDC detector with two drift chambers. U and V wires are shown in each chamber. The black arrow indicates the incoming electron [71].

VDCs are active only for optics runs during PREX-II and CREX, when electrons are collected one by one to measure their scattering angle and energy. Otherwise they are turned off during normal production runs.

## Trigger

Similar to the VDCs, triggers are exclusively used in counting mode for optics study. The standard detector package consists of multiple trigger planes, only two of them are used: the S0 and S3 plastic scintillators. The S0 scintillator is located between the VDCs and the main detectors while S3 is situated behind the main detectors. Both scintillators possess a sensitive area of 170 cm in length by 25 cm in width. Their signals are logically combined to provide different trigger rates. The trigger rate is controlled to be less than 50 kHz most of the time (the upper limit of a VDC is about 250 kHz).

## Main Detector

The main detector of PREX-II and CREX is the 5 mm thick fused silica (quartz) tiles, with dimensions of 16 cm long by 3.5 cm wide (3 cm  $\times$  3 cm active area). Two

identical quartz detectors are installed with the upstream one used as the main detector and the downstream one acting as the backup (also used for cross-checking in PREX-II). They are tilted to be perpendicular to the electron rays.

The high refractive index of quartz ( $n \approx 1.45$ ) means the opening angle ( $\theta \approx \arccos \frac{1}{n}$ ) in Fig. 2.39 is about  $46^\circ$ , larger than the critical angle ( $\theta_c = \arcsin \frac{1}{n} = 43.6^\circ$ ). Therefore, the Cherenkov light produced by high energy electrons will be totally reflected inside the quartz and ultimately collected by the PMT. The high photon yield enables better resolution of the electron peak, which is beneficial given the fact that non-linearity of the PMTs is one of the major contributors to systematic uncertainties.

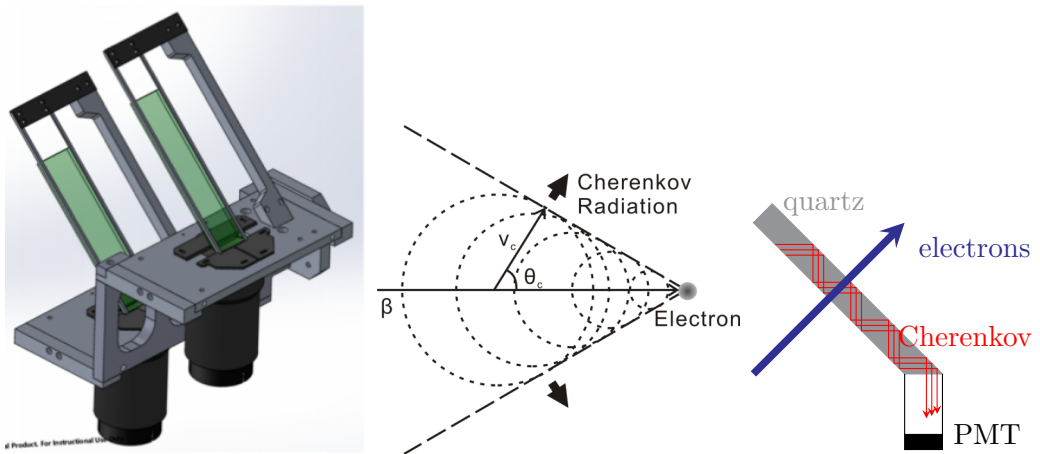


Figure 2.39: Left: CAD drawing of the quartz detector; Middle: schematic plot of the Cherenkov radiation, the angle between the electron and the Cherenkov radiation is  $\cos \theta = \frac{v_c}{v_e} = \frac{c}{nv_e} = \frac{1}{n\beta} \approx \frac{1}{n}$ ; Right: electron flux goes through a quartz detector.

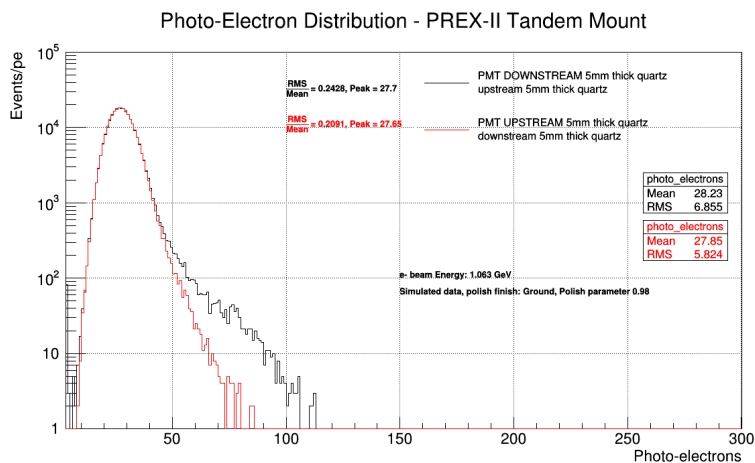


Figure 2.40: Simulation result of the photo-electron (PE) spectrum for single electron passing through the main detectors. The wider tail in the downstream detector is due to particle showering in the upstream quartz [69].

The width of the photon-electron distribution will increase the statistical uncertainty:

$$\sigma_{\mathcal{A}} = \sigma_{\text{stat}} \times \sqrt{1 + \left( \frac{\sigma_{\text{PE}}}{\langle \text{PE} \rangle} \right)^2} \quad (2.27)$$

where  $\sigma_{\text{PE}}$  is the RMS of the distribution. The RMS can be parameterized into two parts: the Gaussian principle part which is inversely proportional to the quartz thickness and a Landau tail which comes from the showering process and is proportional the thickness. A thicker thickness enhance the photon-electron yield while a thinner one can reduce the showering effect. The final decision of a 5 mm thickness is a compromise between these two factors to minimize the detector resolution  $\sigma_{\text{PE}}/\langle \text{PE} \rangle$ .

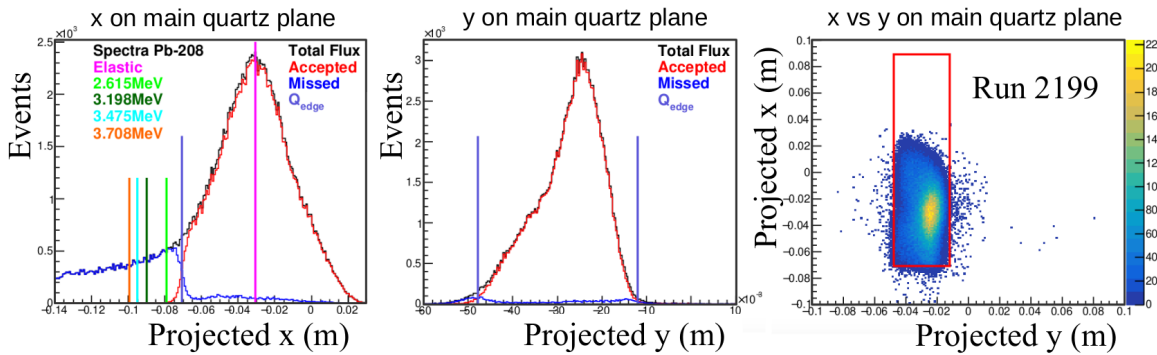


Figure 2.41: Electron position distribution, projected on the quartz plane. The positions of the first four excited states are shown in the left plot. The red rectangle on the right plot shows the relative position of the quartz. Plots from Devi Adhikari [69].

There is a custom motion control system in each arm to move the main detectors. The control system can be operated remotely, providing the convenience of easily adjusting the position of the main detectors whenever there are changes in the beam conditions or any other aspects of the experimental setup.

## AT Monitors

About 1 m downstream the main detector is a pair of AT monitors, as shown in Fig. 2.37, which use exactly the same quartz piece as the main detectors. They are used to monitor transverse polarization in the beam.

### 2.5.7 Data AcQuisition (DAQ)

JLab has its own framework of hardwares and softwares for data acquisition, known as CODA (CEBAF Online Data Acquisition) [72]. CODA is a distributed system that can be scaled from a few detector channels to tens of thousands of channels needed in an experiment. CODA version 2.6.2 is used for PREX-II and CREX.

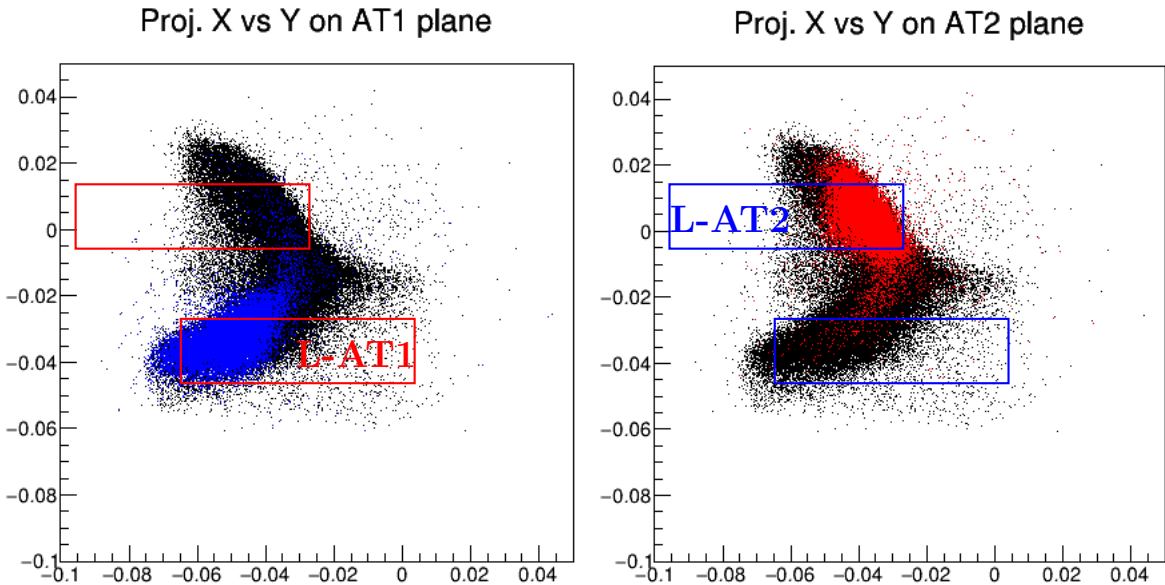


Figure 2.42: Scatter plot of electrons on the left arm AT monitor plane. Red and blue dots represent electrons scattered either above or below the horizontal scattering plane, respectively. The red and blue rectangles show the relative positions of the two AT detectors.

Data acquisition operates in 2 modes: the integrating mode and the counting mode, both have their own DAQs, because they have different triggers and read from different detectors.

### Integrating DAQ

The integrating DAQ consists of four primary DAQ systems distributed acrosss the injector, Counting House (CH) and the hall (LHRS/RHRS). They are controlled by the CODA Run Control system in the CH, and triggered by the helicity signal.

The helicity signal is generated by a helicity control board [73], which is an advanced programmable logic generator, located in the Injector Service Building. It offers four timing modes: three fixed-frequencies of 30, 120 and 240 Hz as well as a fourth free-running mode. In the fixed-frequency mode, as used for PREX-II/CREX, the phase is locked to the ‘beam sync’, which refers to the 60 Hz AC line signal of the accelerator acting as a global timing reference. Consequently, the duration of the last helicity window in a helicity pattern may vary from the others due to the intermittent wandering of the 60 Hz line signal, as depicted as beam sync jitter in the second timing diagram in Fig. 2.43.

To ensure that all helicity windows have the same integrating time, an artificial dead-time is introduce, which is  $T_{\text{dead}} = 51.33 \mu\text{s}$ , as shown in Fig. 2.44. This slightly reduces the integration time:  $T_{\text{int}} = T_{\text{stable}} - T_{\text{dead}}$ .

The helicity signal sent to injector components (PCs, IAs and double Wien filters) can be regarded as real-time due to their close proximity. The Tsettle signal, transmitted to

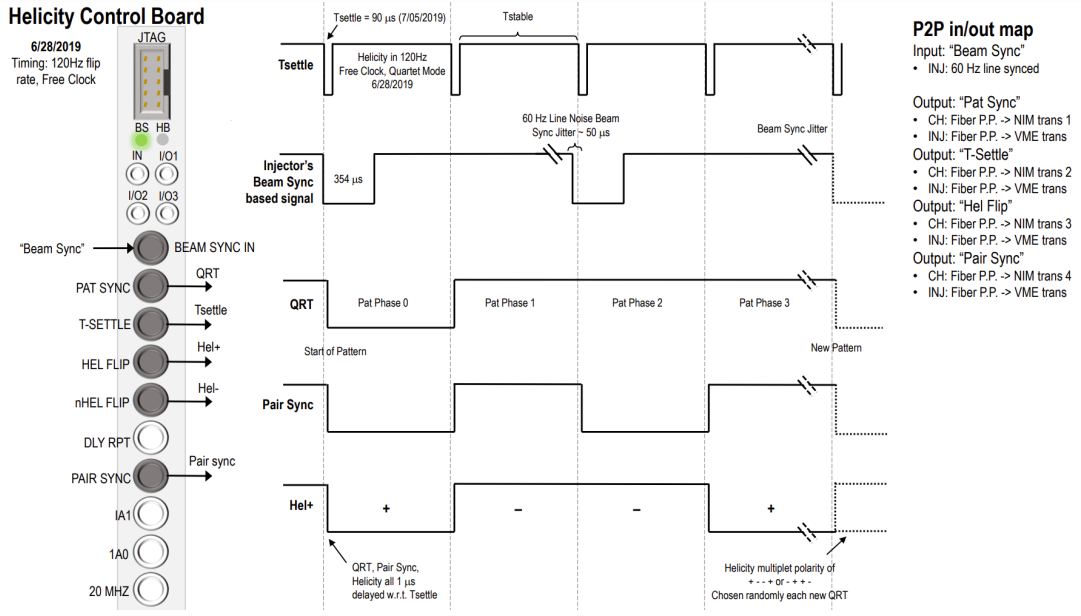


Figure 2.43: Helicity timing diagram. The Tsettle signal (falling edge) marks the beginning of a new helicity window and serve as the reference point ( $t=0$ ) for all timing diagrams. It is transmitted to the CH/hall. The QRT (Pattern Sync) signal indicates the start of each helicity pattern, it goes to the CH. The Pair Sync signal toggles between 0 and 1, signifying the start and end of a helicity pair. It is sent to the CH. This signal is not important, all it tells can be inferred from the QRT signal. The Hel+ signal decides the helicity of the current window, it goes to the laser table in the injector. The Hel- signal acts as the complementary signal to Hel+, so that the board always keeps the same current regardless of the helicity state, preventing helicity correlated electrical pickup from the board. This signal is not shown in the plot, it goes to the helicity magnets (the double wien filters). The delayed helicity (DLY RPT) signal is delayed by  $n$  (specified by the user) windows with respect to the Hel+ signal. It tells what the helicity state was  $n$  windows before. It goes to the CH. This signal is not shown in the plot.

Hall A, serves several purposes. When the falling edge of  $T_{\text{settle}}$  is received, it indicates the end of data acquisition in the previous helicity window. It then remains in a hold state for  $T_{\text{settle}}$  time to allow for the settling of high voltages in the PCs and the readout of data from the previous helicity window.

The rising edge of  $T_{\text{settle}}$  signifies the start time of data acquisition in the current helicity window. Due to the signal transportation delay in fiber optic cables to Hall A, which is approximately 100 ns, an additional 1  $\mu\text{s}$  is reserved between  $T_{\text{settle}}$  and the helicity signals to notify Hall A of the helicity change, as depicted in Figure 2.43.

Actually, this 1  $\mu\text{s}$  delay is not necessary, because  $T_{\text{settle}} = 90 \mu\text{s}$  is already long enough to account for the signal transportation delay in fiber optics cables, as well as the delay caused by beam transportation in the accelerator, which is  $1.4 \text{ km}/c = 4.7 \mu\text{s}$ .

The actual helicity signal (DLY RPT) sent to Hall A is intentionally delayed by 8 helicity windows in PREX-II/CREX. This delay ensures that no monitors along the beamline or detectors in the hall know the helicity of the current window, making sure that these monitors and detectors are not sensitive to helicity.

On the DAQ side, we need to verify that observed the helicity pattern aligns with expected pattern based on the helicity pattern signal and the measured helicity, thus ensuring the accuracy of the helicity information.

During data analysis, the collected data needs to be shifted by number of delayed helicity windows to match the actual helicity pattern. The helicity pattern is pseudo-randomly chosen by the helicity board using a 30-bit shift register.

The analog signals from the main detectors and various beam monitors are first converted to voltage by a customized I-to-V preamplifier developed for the Qweak experiment. The voltage output is then fed to a 18-bit ADC (Analog-Digital-Converter) for sampling and integration. This 18-bit ADC was also a product of previous parity experiments. The detector signal is sampled every 2  $\mu\text{s}$  and integrated into four sub-blocks within each helicity window. Each sub-block consists of 1024 samples, resulting in a total of 4096 samples per helicity window at a helicity frequency of 120 Hz.

To ensure proper operation, the ADC is triggered 80  $\mu\text{s}$  after the start of  $T_{\text{settle}}$ , as shown in Fig. 2.44. This 80  $\mu\text{s}$  delay allows for a 10  $\mu\text{s}$  waiting time for the ADC to void any possible effects from external triggering Nuclear Instrument Module (NIM) pulse on the internal signal processing.

To synchronize the data collection (integration), a HAPPEX Timing Board (HAPTB) is used, which receives the  $T_{\text{settle}}$  signal and produces the integration gate signals, distributing them to each ADC/scalar to trigger the signal integration/collection.

Each DAQ is housed in its own VME crate, which contains all the necessary hardware modules. A read out controller (ROC) controls the VME crate. All these crates (ROCs) are managed by a trigger supervisor (TS), which has its own VME crate. The TS is triggered by the  $T_{\text{settle}}$  signal, and in turn, it triggers the ROCs. When triggered, each ROC reads the data stored in their memory buffer and send it to the CODA system, which will build, transport and store events. An analyzer called JAPAN (Just Another Parity Analyzer) will monitor the quality of data in real-time. Additionally, JAPAN can

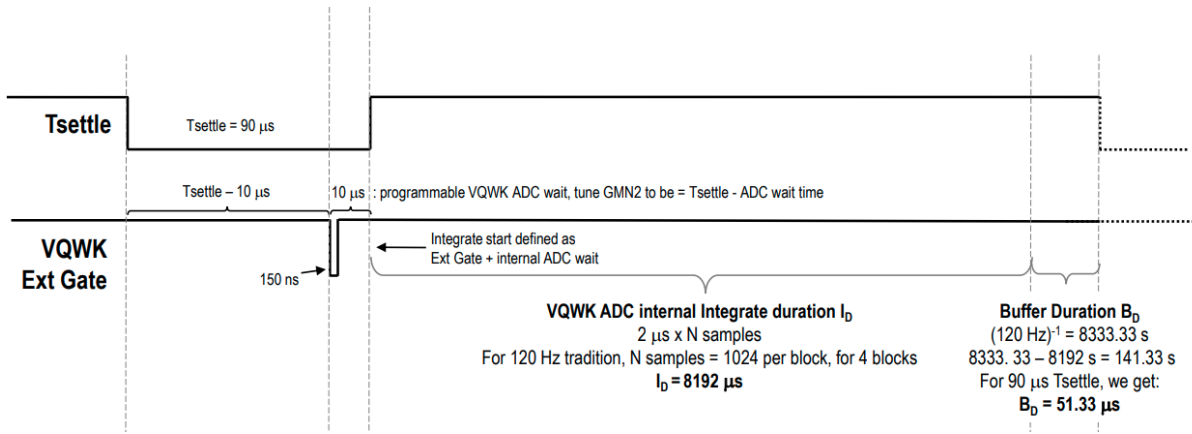


Figure 2.44: Integrating timing

also be used for offline data analysis.

## Counting DAQ

The two counting DAQs, one for each HRS, differ from the integrating DAQs, in terms of hardwares and softwares. In contrast to integrating electrons, the counting DAQ are specifically designed for recording and reconstructing tracks of scattered electrons on an individual basis.

The counting DAQ reads data from the scintillators, VDCs and GEMs, and the main detectors. It is triggered by the scintillators, different logical combinations of the scintillator signals could trigger varying counting rates. Most of the time, we used the S0 trigger signal, as discussed in the scintillator sector.

The analyser used for decoding counting mode data is the general Hall A analyser. This analyzer reads the hit information from each detector and utilizes this information to reconstruct the trajectory of the scattered electron. By reversing the optics matrix, it can calculate the electron information such as position, angle and energy at the target. These information enables the measurements of the scattering angle and  $Q^2$ , aiding in the fine-tune of the optics matrix, detector alignment and background verification.

## EPICS

In addition to the two DAQ systems, there is a site-wise slow (relative to the helicity frequency) control system, called Experimental Physics and Industrial Control System (EPICS) [74]. EPICS monitors and controls various important components and parameters throughout the experimental setup. This includes magnets, beam current/position/energy, vacuum level, temperature, gas flow, high voltage supply etc. EPICS polls a series of input/output controllers (IOCs) and record their average values about every second. It allows for real-time monitoring of the entire system: both the accelerator and detectors. It provides continuous monitoring and enables the operators to trace the status of the system, facilitating troubleshooting and problem resolution whenever issues arise.

# Chapter 3

## Data Analysis

As mentioned earlier, despite the fast helicity flipping and extensive effort to maintain the electron beam under identical conditions during opposite helicity states, achieving this goal completely is practically impossible. Various noises are inevitably generated in different parts of the accelerator. While these noises are generally small, they can still have a significant impact on our measurements if not properly addressed.

We used the same methods for processing both the PREX-II and CREX data sets. Therefore, we will discuss only CREX data here, anything that is different in PREX-II will be highlighted.

### 3.1 Raw Data

CREX started commissioning around December 2019, the first good run was taken on December 12th. Six slugs (slug 100 - 105. See discussion below for the definition of slug) were collected before the Christmas break. Data taking resumed after the break and continued until January 18th, 2020 when the first  $^{48}\text{Ca}$  target was damaged. It took five days to prepare a new target. Following the target replacement, the experiment proceeded smoothly. From February 10th to February 12th, we conducted a two-day

Number of Good Slugs	121
Number of Good Runs	1384
Number of Good Miniruns	8525
Number of Good Quadruplets	86832046
Charge Asymmetry	$\sim 100$ ppb
Position Difference	$\sim 10$ nm
Angle Difference	$\sim 1$ nrad
Energy Difference	$\sim 10$ ppb
Raw Asymmetry	2087 ppm
Regressed Asymmetry	2090 ppm

Table 3.1: CREX data statistics.

measurement of the transverse asymmetry (AT). We have collected slightly more than half of the desired charge when Covid-19 hit, which led to the shutdown of the lab at the end of March 2020. Fortunately, the lab reopened four months later, providing us with an opportunity to resume electron bombardment for another month. The data taking phase of the experiment concluded on September 18th, 2020. In total, a charge of 480 C was collected, with 390 C considered to be of good quality.

The data set is clearly separated into three distinct periods: before the AT, after the AT but before the Covid, and after the Covid, in chronological order. A more reasonable split is to separate them based on the Wien-flip states, whose result aligns closely with the chronological divisions.

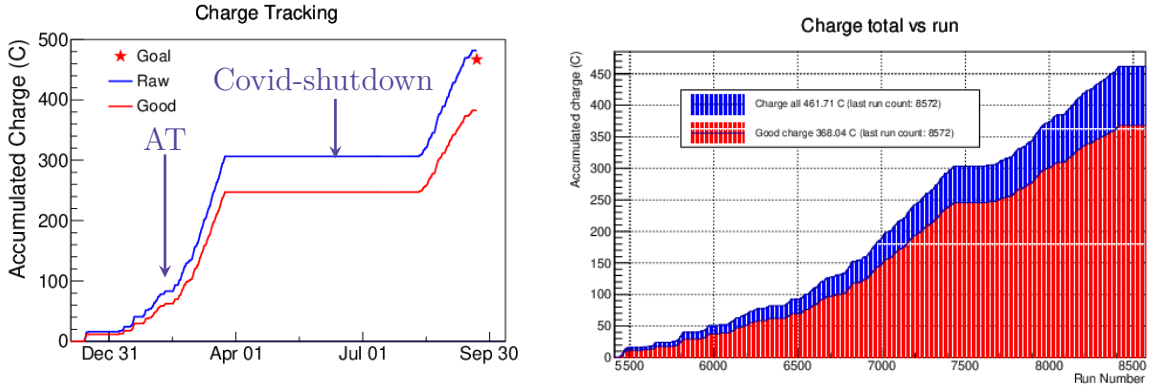


Figure 3.1: Charge accumulation versus time (left) and the run number (right). The extended plateau in the left plot corresponds to period of the the Covid-19 shutdown, which is shown around run 7500 in the right plot. One sees that data taking is most efficient after the AT and before the Covid. The last month (after the Covid) shows reasonably efficient data taking, while the first two months of data collection are less efficient due to various hardware problems encountered.

In total, CREX collected 1451 production runs. Out of these, 1386 were identified as ‘Good’ and were used for final analysis. The good runs consists of 1362 both arms runs, 6 left arm runs and 18 right arm runs. Each good production run lasts about 1 hour and collects about 0.3 C with a charge efficiency of 80%.

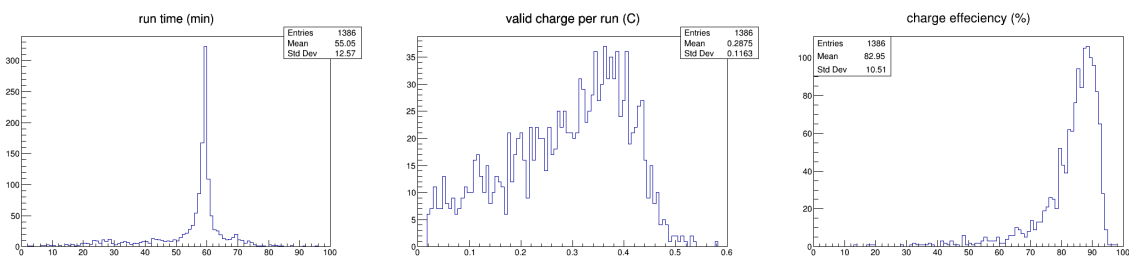


Figure 3.2: Runtime and charge statistics of CREX runs (`ErrorFlag == 0`).

Although electrons arrive in bunches, with a bunch frequency of 499 MHz, this fre-

quency is much higher than the helicity flip frequency of 120 Hz. Consequently, the electron beams can be regarded as continuous. In each helicity window, all scattered electrons are integrated into a single readout (event). Every four continuous helicity events are grouped into one quadruplet (in case of the 240 Hz flipping frequency in PREX-II, every eight helicity events form one octuplet). To mitigate the impact of 60 Hz line power noise, the PV asymmetry is calculated based on helicity quadruplets (or octuplets in the case of a 240 Hz flipping frequency). Every four continuous helicity events form a quadruplet (or every eight events form an octuplet in PREX-II). The frequency of the helicity quadruplets is 30 Hz, as shown in Fig. 3.3. This choice of frequency allows for effective cancellation of the 60 Hz line power noise. Throughout the CREX experiment, approximately 87 million good helicity quadruplets were collected.

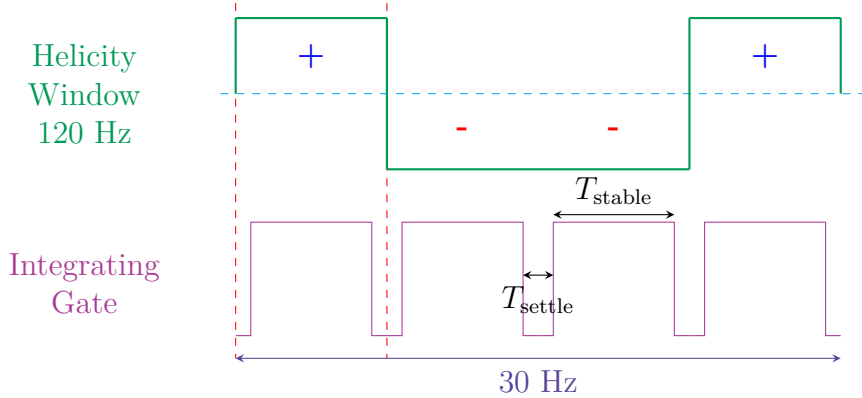


Figure 3.3: Schematic plot of the helicity pattern. In CREX,  $T_{\text{settle}} = 90 \mu\text{s}$ , which allows the PC to stabilize after a voltage polarity flipping, avoiding any cross-effect from the previous helicity state. The corresponding deputy factor is 98.92%.

To account for the rapidly changing beam conditions, each run is divided into multiple miniruns. Calculating the detector slope, which is the detector's response to beam fluctuations, over a 60 mins time scale is inappropriate. It is more appropriate to do the calculation over the duration of a minirun since the beam conditions, and consequently the slope value, tend to be more stable within a shorter time period.

Every minirun contains 9000 good helicity quadruplets, corresponding to about 5 mins of data collection. The last minirun in each run contains the remaining quadruplets that cannot be divided into two separate miniruns.

Miniruns with a number of samples less than half of the standard (4500) are discarded. In total, CREX has 8543 miniruns from 1386 good runs. Among these, 2 miniruns are discarded due to their small sample size, while 16 miniruns are discarded due to noisy beam conditions or large beam shifts that were not caught in the previous two analysis campaigns (respin). To avoid another respin, these miniruns are simply removed. The discarded miniruns are listed out in Table 3.2 and 3.3.

Runs are grouped into slugs. A slug is defined as the collection of runs between two changes of the IHWP. Under stable beam conditions, we could collect three slugs per

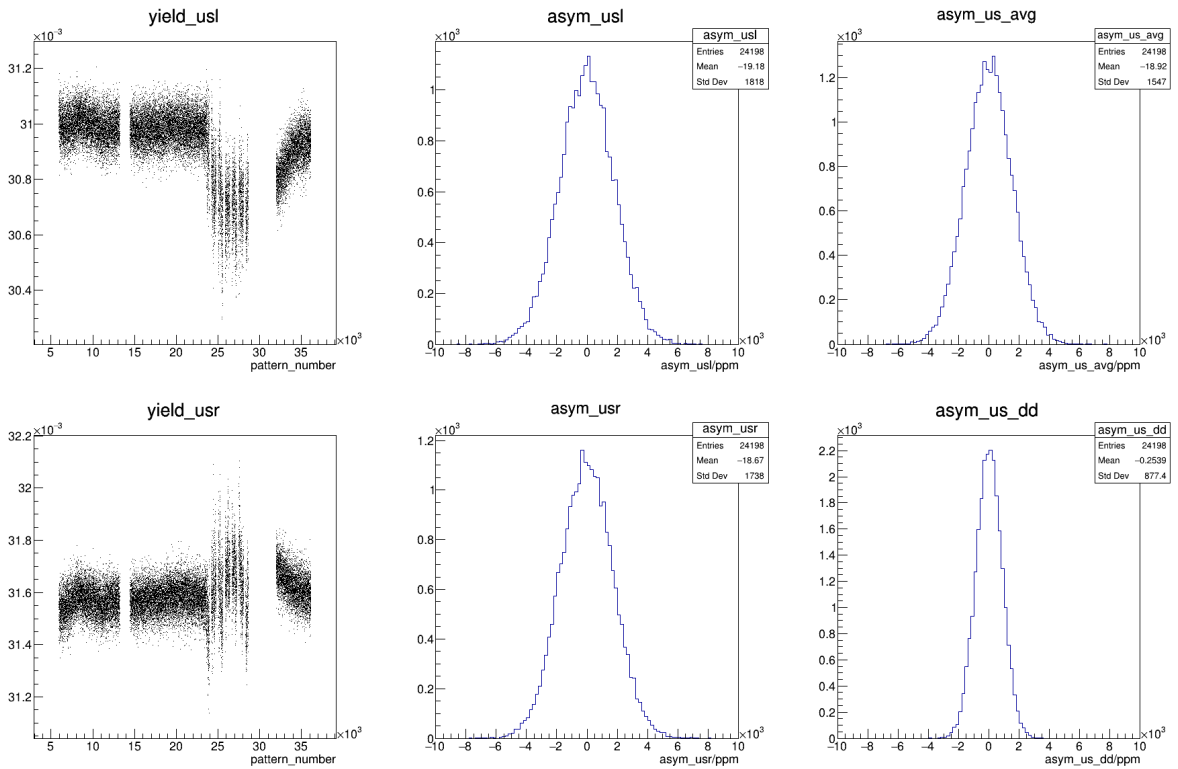


Figure 3.4: A ‘run’ plot: detector yield and asymmetry distribution in run 6600, selected with `ErrorFlag == 0`. The observed shift in the second half of the yield plot can be attributed to fluctuations in the beam position and angle. The right two plots display the average and difference of the asymmetry between the LHR and RHR. Ideally, the difference should be zero and the average is what we want to measure.

run	minirun	number of samples
7720	0	4352
8082	0	4391

Table 3.2: Two miniruns that have too small good samples (with cut `ErrorFlag == 0`).

run	minirun	run	minirun
6564	4	7211	4
6567	2, 4	7889	0
6571	3, 4	7942	5
6593	2	8036	2
6983	8	8240	1
7149	6	8549	0, 1, 4

Table 3.3: List of Miniruns that had larger asymmetry outliers and therefore are removed.

day. Therefore, each slug corresponds to about 8 hours of data collection, although this

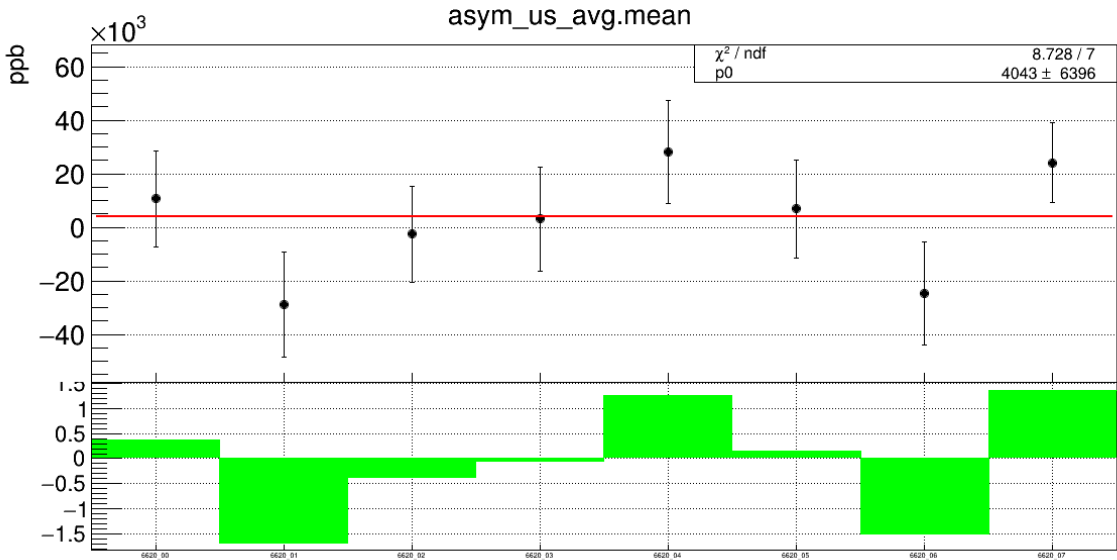


Figure 3.5: A ‘minirun’ plot: mean values of `asym_us_avg` of each minirun in run 6620 (`ErrorFlag == 0`). The red line is a zero-order polynomial fit and the bottom histogram is the ratio of the deviation to the mean fit value with respect to each point’s uncertainty.

duration may be extended in case of any issues. In total, CREX collects 124 slugs. After the data cleaning and combining slugs to remove those with only one run, 121 slugs are retained.

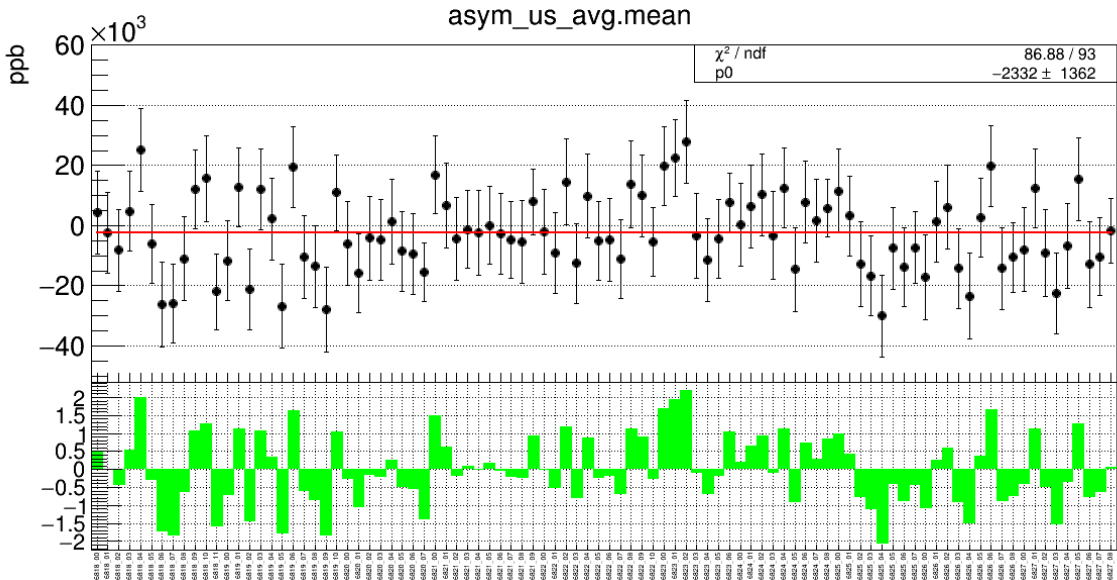


Figure 3.6: A slug plot: minirun-wise distribution of `asym_us_avg` in slug 150 (`ErrorFlag == 0`).

Finally, slugs are further divided into periods based on their Wien flip states. As mentioned earlier, there are three distinct periods.

Wien-flip	slugs
Right	100-137
Left	138-185
Right	186-223

Table 3.4: Wien-flip separation in terms of slugs.

### 3.1.1 Cut

A loose cut is applied at the event level to maximize the selection of good events. During the data taking process, the JAPAN monitors various aspects, such as hardware failures, beam stability, helicity information and others. These parameters are checked against a total of 23 criteria. Based on the results of these checks, an error code (ErrorFlag) is assigned to each event. The error code is obtained by performing a bitwise OR operation on the results of all the checks. Events that pass all 23 checks will have a null error code (ErrorFlag == 0).

The various hardware failure checks are designed to detect issues related to the ADC readout in the detectors and monitors. These checks ensure that the recorded data does not contain saturated or null values. These checks help to identify the problematic hardware channels in case of any hardware failures.

The beam stability level checks monitor the beam conditions by analyzing the mean and RMS values of detector and monitor readouts. These checks compare the readout values to user-defined upper and lower limits to identify outliers. Additionally, for some ADC channels, there are cuts based on the RMS values calculated over a moving time window of 200 (configurable) consecutive events, if the RMS value exceeds a certain threshold, all events within that time window fail the RMS check. Furthermore, the burplevel check compares the current event readout with the average value of the previous 10 (configurable) events. If the difference between the current event and the average value exceeds a specific threshold (burplevel cut), the event fails the burplevel check.

One example of such stability cuts is the beam current cut. In the event of a beam trip caused by accidents or other factors, the beam intensity drops and then recovers quickly. During this falling and rising process, the beam stability is typically compromised. To ensure the quality of the data, a requirement is imposed that the event beam current should be larger than the stable beam current minus 30  $\mu\text{A}$  (15  $\mu\text{A}$  in PREX-II).

By implementing these beam stability level checks, we can make sure that the collected data meets quality standards.

In addition to these checks, we have an analysis shift worker to check monitor/detector yields and their differences/asymmetries for each run. If the shift worker observes large beam excursions, drifts, or any other irregularities in the monitor/detector yields or their differences/asymmetries, additional cuts can be applied. These cuts are specific to each run and are added one by one as needed.

During both the online and the offline analyser, we used cut `ErrorFlag == 0` to select good quadruplets. This cut excludes all beam modulation events. However, some beam

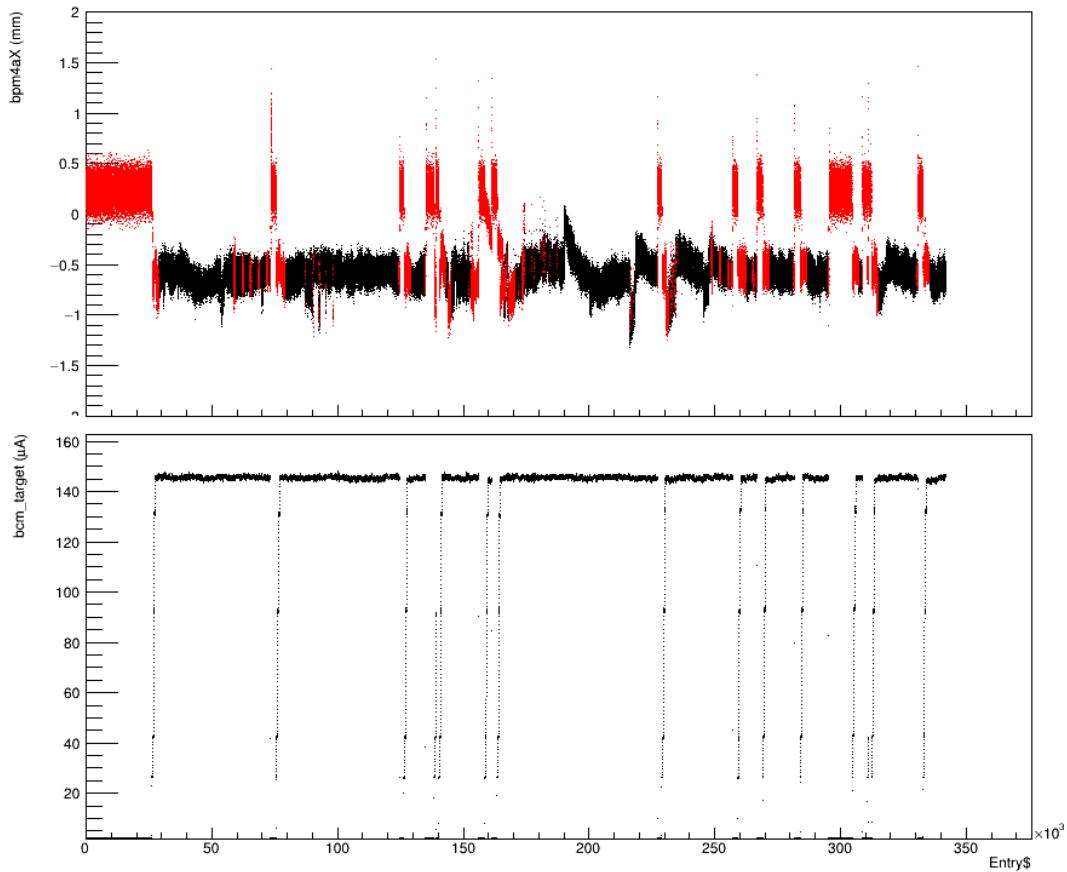


Figure 3.7: BPM4aX distribution (top) in run 8019, the bottom plot is the corresponding beam current distribution. Black points are good events (`ErrorFlag == 0`) and red points are bad ones (`ErrorFlag != 0`). One can clearly see that all beam trips and most beam jitters are recognized by our stability checks.

modulation events are actually usable for our asymmetry analysis and were included in the final published result. These modulation events counts for about 5% of the CREX data set. To be consistent with the published result, all following plots are produced with the cut `ErrorFlag&0xda7e6bff == 0` if not mentioned otherwise.

### 3.1.2 Beam Conditions

As explained before, maintaining consistent experimental conditions is crucial for accurately measuring small asymmetry values. Among these conditions, the most challenging one to control is the beam condition. Fluctuations in any component along the lengthy accelerator line can lead to changes in the beam condition, potentially introducing noise asymmetry into our measurements.

Despite these challenges, the dedicated CEBAF staff has made significant efforts to

provide us with excellent beams that exhibit minimal differences between different helicity windows.

## Beam Current

The raw asymmetry is normalized to the beam current in order to account for variations in beam current between runs and within a single run, where the beam currents may differ slightly between helicity windows. The normalized raw asymmetry is:

$$\mathcal{A}_{\text{raw}} = \frac{(D/I)^+ - (D/I)^-}{(D/I)^+ + (D/I)^-} \approx \frac{D^+ - D^-}{D^+ + D^-} - \frac{I^+ - I^-}{I^+ + I^-} = \mathcal{A}_D - \mathcal{A}_I \quad (3.1)$$

where  $D$  represents the detector readout.

This equation demonstrates that the charge asymmetry contributes to the raw asymmetry directly. Therefore, it is desirable to minimize the charge asymmetry, which is achieved through the charge feedback system. The charge asymmetry is typically on the order of hundreds of ppb, as shown in Fig. 3.8. From this figure, one can also observe that period 2 has relatively more stable beam conditions compared to the other two periods.

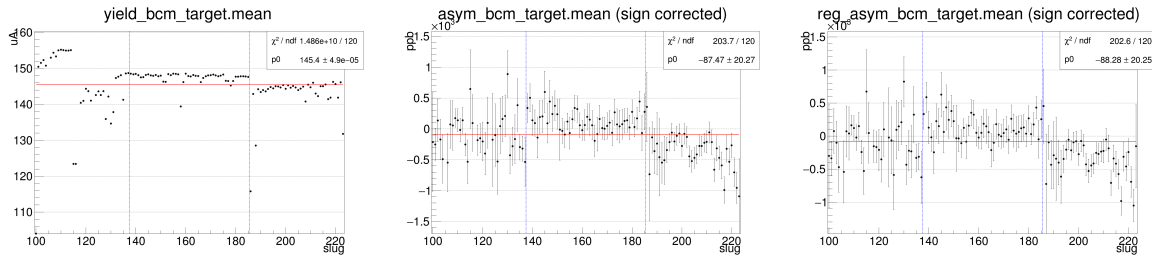


Figure 3.8: Slug-wise mean values of the beam current, asymmetry and regressed asymmetry in CREX. The blue dashed lines separate the data set into three periods with different Wien-flip states. Most of the time, CREX run at  $\sim 150 \mu\text{A}$ , an overall  $\sim 100$  ppb charge asymmetry is achieved.

## Beam Position, Angle and Energy

We do not have a direct measurement of the beam position and angle at the target, these information can be inferred from various BPMs. Given the distance between the target and BPM4a as  $D1 = 5.725$  m and the distance between BPM4a and BPM4e as  $D2 = 4.083$  m, the beam position and angle at the target will be:

$$T_{X,Y} = \text{BPM4a}_{X,Y} + \frac{\text{BPM4e}_{X,Y} - \text{BPM4a}_{X,Y}}{D2} D1 \quad (3.2)$$

$$\theta_{X,Y} = \frac{\text{BPM4e}_{X,Y} - \text{BPM4a}_{X,Y}}{D2}$$

Using Eq. 3.2, the overall difference of the beam position/angle at the target is calculated to be:

$$\text{diff}_{X,Y} \sim 10 \text{ nm} \quad \text{diff}_{\theta_{X,Y}} \sim \text{nrad}$$

Again, the second period has a more stable beam than the other two periods.

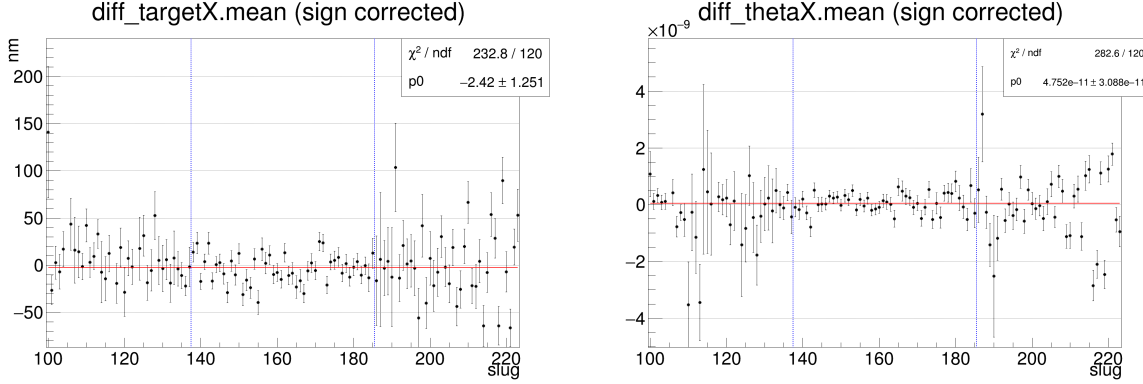


Figure 3.9: Slug-wise mean values of the beam position (left) and angle (right) difference at the target. Very precise control of the beam conditions is achieved. The Y dimension plots are similar and are not shown here.

The beam momentum/energy is measured by BPM12X, whose dispersion tells the deviation ( $dp$ ) from the standard momentum value ( $p0$ ). The design value of the dispersion for CREX is  $D = 4.0$  m, and an actual measurement gives  $\sim 3.8$  m. I use 4.0 m here. As can be seen in Fig. 3.10, CEBAF provides a beam with energy dispersion as small as  $\sim 10$  ppb.

$$\frac{dp}{p} = \frac{\text{diff\_BPM12X}}{D} \quad (3.3)$$

### 3.1.3 Raw Asymmetry

The raw asymmetry is calculated as:

$$\mathcal{A}_{\text{raw}} \equiv \begin{cases} \frac{d^+ - d^- - d^- + d^+}{d^+ + d^- + d^- + d^+} & (+ - - + \text{ pattern}) \\ \frac{-d^- + d^+ + d^+ - d^-}{d^+ + d^- + d^- + d^+} & (- + + - \text{ pattern}) \end{cases} \quad (3.4)$$

where  $d = \frac{D}{I}$  is the normalized detector integrating yield in one helicity window, the upper-script indicates the helicity of the beam. The detector yield is calibrated with their corresponding pedestals.

## 3.2 Beam False Asymmetry Correction

As shown in the previous few plots illustrating beam conditions, it is evident that there are false asymmetries resulting from the beam. The primary contributor is the

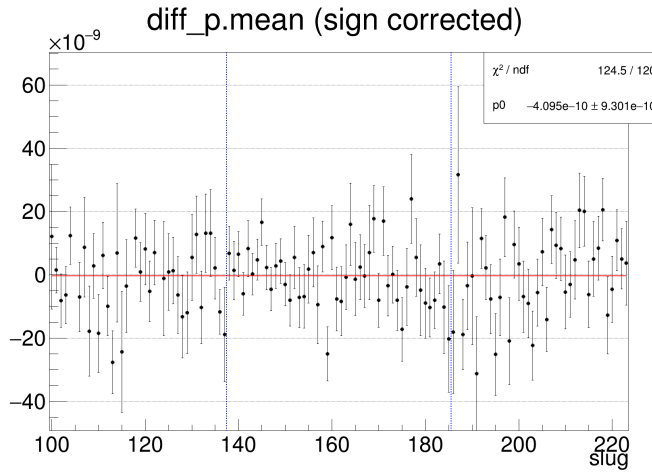


Figure 3.10: Slug-wise mean values of the beam energy dispersion. Overall, an energy difference of  $\sim 10$  ppb is achieved.

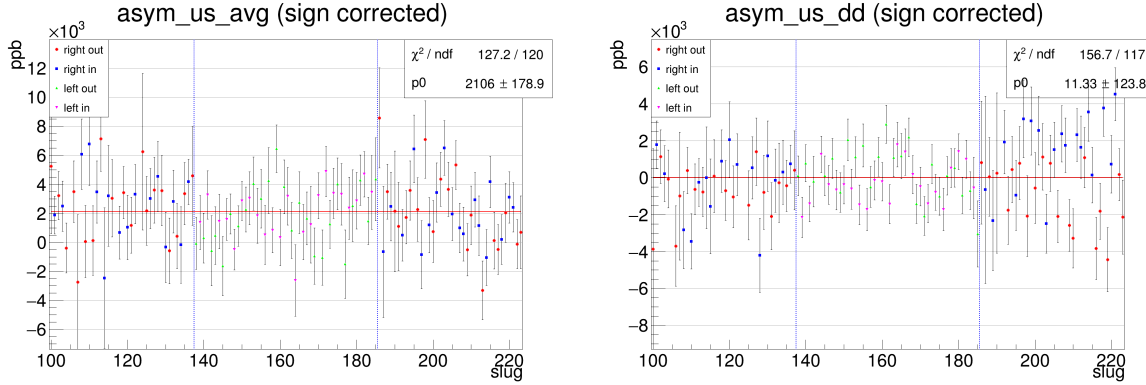


Figure 3.11: Slug-wise raw asymmetry average (left) and difference (right) for CREX. The right plot has three less slugs because there are three single-arm slugs.

helicity correlated beam asymmetry (HCBA).

As observed in Fig. 3.13, any beam jitter introduces fluctuations in the detector yield, exhibiting approximately a linear correlation. Therefore, to eliminate the false asymmetries caused by beam jitters, we just need to know the correlation between the detector yield and each beam parameter, specifically the detector slope.

There are 2 methods to calculate the slope values, regression and beam modulation, we will delve into the details of these two methods in the following sections.

### 3.2.1 Regression

The first method to calculate the slope is regression. Our data analysis provides a perfect scheme for the application of this statistical tool.

Bear in mind that regression alone does not establish relationships or rules. Instead, it works based on the assumption that the relationship between variables is predictable

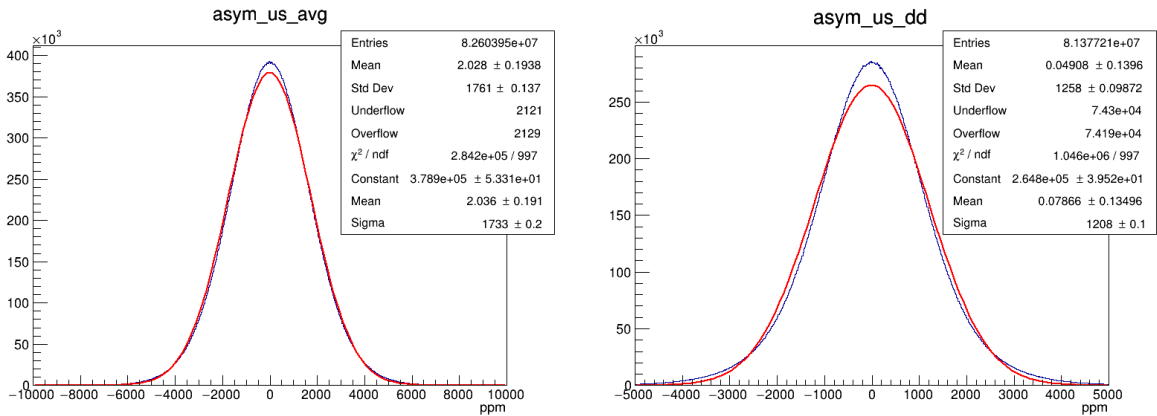


Figure 3.12: Mulplots of the CREX raw asymmetry average (left) and difference (right). The blue line is the data and the red line is a Gaussian fit to the data. The difference plot has less entries because single arm runs have no difference values.

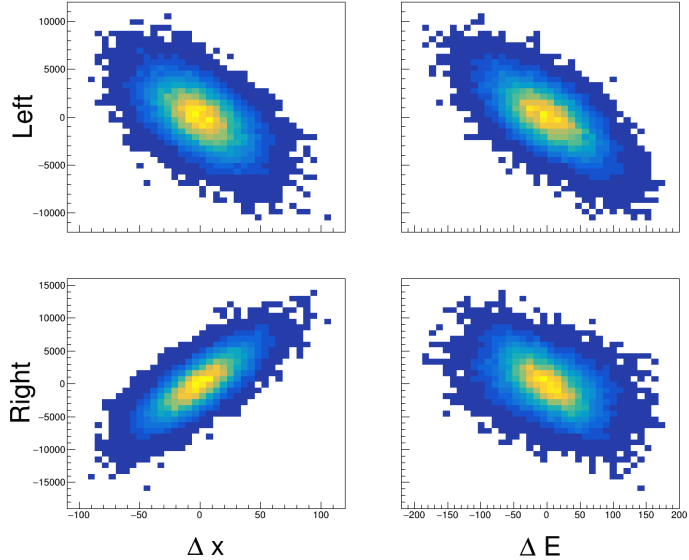


Figure 3.13: Correlation between the detector yield and the beam position/energy in run 7679. The left/right detector yields undergo opposite changes, when the beam position shifts, and they move in the same direction with respect to fluctuations in the beam energy.

(given by the user). Additionally, it assumes that the dependent variables follow a known distribution function  $P(\epsilon)$ , which is also provided by the user:

$$Y = f(X) + \epsilon$$

With these prior knowledge, regression is capable of extracting the most likely coefficients in the predicted model.

## The Model

Considering the scenario of only one monitor and one detector. Assuming that the reading noise of the detector follows a Gaussian distribution and the monitor is precise (one can absorb the monitor noise into the beam fluctuation):

$$\begin{aligned} M &= m \\ D &= d + \epsilon(0, \sigma_0^D) \end{aligned} \tag{3.5}$$

here, the capital letters (D and M) represent the measured values while the small letters (m and d) denote the true values.  $\sigma_0^D$  is the variance of the noise in the detector.

Then the difference between beams of opposite polarization will follow also the Gaussian distribution with a larger variance:

$$\begin{aligned} \Delta M &= M^+ - M^- = m^+ - m^- = \Delta m \\ \Delta D &= D^+ - D^- = (d^+ + \epsilon(0, \sigma_0^D)) - (d^- + \epsilon(0, \sigma_0^D)) = \Delta d_0 + \epsilon(0, \sqrt{2}\sigma_0^D) = \Delta d + \epsilon(0, \sigma_1^D) \end{aligned} \tag{3.6}$$

Again,  $\Delta m$  and  $\Delta d$  are the real differences, whereas  $\Delta M$  and  $\Delta D$  are the measured values.

The probability for measuring  $\Delta D$  will be:

$$P(\Delta D) = \frac{1}{\sigma_1^D \sqrt{2\pi}} e^{-\frac{1}{2} \left( \frac{\Delta D - \Delta d}{\sigma_1^D} \right)^2} \tag{3.7}$$

We will have a collection of independent data points:  $(\Delta M, \Delta D)_i$ . Our objective is to determine the relationship between  $\Delta d$  and  $\Delta m$ :  $\beta \equiv \frac{\partial d}{\partial m}$ . Since  $\Delta m$  is significantly smaller compared to its normal yield, a first-order correlation is considered precise enough for our analysis.

This is exactly a linear regression problem.

$$\begin{aligned} \Delta d &= 0 + \beta \Delta m \\ \mathcal{A}_{\text{cor}} &= \mathcal{A}_{\text{raw}} - \beta \Delta M \end{aligned} \tag{3.8}$$

where  $\mathcal{A}_{\text{cor}}$  is the corrected asymmetry.

For any real data point  $(\Delta m, \Delta d)_i$ , the possibility to measure  $(\Delta M, \Delta D)_i$  is:

$$P_i(\Delta D | \Delta M) = \frac{1}{\sigma_1^D \sqrt{2\pi}} e^{-\frac{1}{2} \left( \frac{\Delta D - \beta \Delta M}{\sigma_1^D} \right)^2} \tag{3.9}$$

For the accumulated data of one minirun, the total probability will be:

$$P = \prod_i^n P_i(\Delta D | \Delta M) = \prod_i^n \frac{1}{\sigma_1^D \sqrt{2\pi}} e^{-\frac{1}{2} \left( \frac{\Delta D_i - \beta \Delta M_i}{\sigma_1^D} \right)^2} \tag{3.10}$$

To maximize  $P$ , it is equivalently to minimize:

$$\chi^2 = \sum_i (\Delta D_i - \beta \Delta M_i)^2 \quad (3.11)$$

where  $i$  sums over all samples in one minirun.

Maximization of  $P$  with respect to  $\beta$  means a zero derivative:

$$\frac{\partial P}{\partial \beta} = P \times \sum_i \frac{\Delta M_i}{\sigma_1^D} \left( \frac{\Delta D_i - \beta \Delta M_i}{\sigma_1^D} \right) = 0 \quad (3.12)$$

which gives  $\beta$  as:

$$\sum_i \Delta M_i (\Delta D_i - \beta \Delta M_i) = 0 \quad (3.13)$$

$$\beta = \frac{\sum_i \Delta D_i \Delta M_i}{\sum_i \Delta M_i^2} \quad (3.14)$$

Extending the independent variable to be multi-dimensional, we have:

$$\Delta D = (\beta_1 \quad \beta_2 \quad \dots \quad \beta_m) \begin{pmatrix} \Delta M^1 \\ \Delta M^2 \\ \vdots \\ \Delta M^m \end{pmatrix} + \epsilon(0, \sigma^D) \quad (3.15)$$

where  $m$  is the number of BPMs used for the asymmetry analysis.

$$\frac{\partial P}{\partial \beta_\nu} \propto \sum_i \Delta M_i^\nu (\Delta D_i - \sum_\mu \beta_\mu M_i^\mu) = 0 \quad (3.16)$$

Arrange Eq. 3.16 in a matrix:

$$\begin{pmatrix} \sum_i \Delta D_i \Delta M_i^1 \\ \sum_i \Delta D_i \Delta M_i^2 \\ \vdots \\ \sum_i \Delta D_i \Delta M_i^m \end{pmatrix} = \begin{pmatrix} \sum_i \Delta M_i^1 \Delta M_i^1 & \sum_i \Delta M_i^1 \Delta M_i^2 & \dots & \sum_i \Delta M_i^1 \Delta M_i^m \\ \sum_i \Delta M_i^2 \Delta M_i^1 & \sum_i \Delta M_i^2 \Delta M_i^2 & \dots & \sum_i \Delta M_i^2 \Delta M_i^m \\ \vdots & \vdots & \ddots & \vdots \\ \sum_i \Delta M_i^m \Delta M_i^1 & \sum_i \Delta M_i^m \Delta M_i^2 & \dots & \sum_i \Delta M_i^m \Delta M_i^m \end{pmatrix} \begin{pmatrix} \beta_1 \\ \beta_2 \\ \vdots \\ \beta_m \end{pmatrix} \quad (3.17)$$

Define the covariance of any two variables as:

$$\text{cov}(x, y) = \sum_i x_i y_i \quad (3.18)$$

and

$$M_{m \times m} = \begin{pmatrix} \text{cov}(\Delta M^1, \Delta M^1) & \text{cov}(\Delta M^1, \Delta M^2) & \cdots & \text{cov}(\Delta M^1, \Delta M^m) \\ \text{cov}(\Delta M^2, \Delta M^1) & \text{cov}(\Delta M^2, \Delta M^2) & \cdots & \text{cov}(\Delta M^2, \Delta M^m) \\ \vdots & \vdots & \ddots & \vdots \\ \text{cov}(\Delta M^m, \Delta M^1) & \text{cov}(\Delta M^m, \Delta M^2) & \cdots & \text{cov}(\Delta M^m, \Delta M^m) \end{pmatrix} \quad (3.19)$$

The coefficient vector will be extracted as:

$$\begin{pmatrix} \beta_1 \\ \beta_2 \\ \vdots \\ \beta_m \end{pmatrix} = M^{-1} \begin{pmatrix} \text{cov}(\Delta D, \Delta M^1) \\ \text{cov}(\Delta D, \Delta M^2) \\ \vdots \\ \text{cov}(\Delta D, \Delta M^m) \end{pmatrix} \quad (3.20)$$

Both theoretically and practically, it is possible to cover the entire phase space beam motion using only 5 BPMs. The 5 BPMs we chose in CREX analysis were BPM1X, BPM4aY, BPM4eX, BPM4eY and BPM12X.

## Slope Values

Using Eq. 3.20, the slope values with respect to the selected BPMs can be calculated. Fig. 3.14 shows the asymmetry's response to changes in the beam energy, providing justification for utilizing miniruns. As observed in the plot, miniruns within the same run may have different slope values, varying by a few percent. This variation is expected because the detector slope is not a constant, it depends on the detector yield. Remember Eq. 3.8 is based on the assumption that the beam fluctuations are tiny. In cases where there are relatively large shifts in the beam, new slopes are needed. Therefore, a minirun-wise slope value is more stable than a run-wise one, enabling a more precise correction of false asymmetry. Furthermore, this implies that the regression correction is most effective for handling small fluctuations around the mean value. It is imprecise to apply the same correction for outliers. That's why we need to remove miniruns with beam condition outliers.

Table 3.5 summarizes the approximate slope values with respect to the five BPMs we chose. Overall, our detector exhibits sensitivity to fluctuations in the X direction, which is the dispersed direction, and the beam energy. On the other hand, the detector is relatively insensitive to jitters in the Y direction.

## Corrections

With the slope values, we can calculate the corresponding false asymmetry correction:

$$\mathcal{A}_{\text{false}} = \beta \times (\text{diff in BPM}) \quad (3.21)$$

The primary correction comes from differences in the X direction and the beam energy. A typical correction amounts to a few ppm, as shown in Fig. 3.14. Since the detector

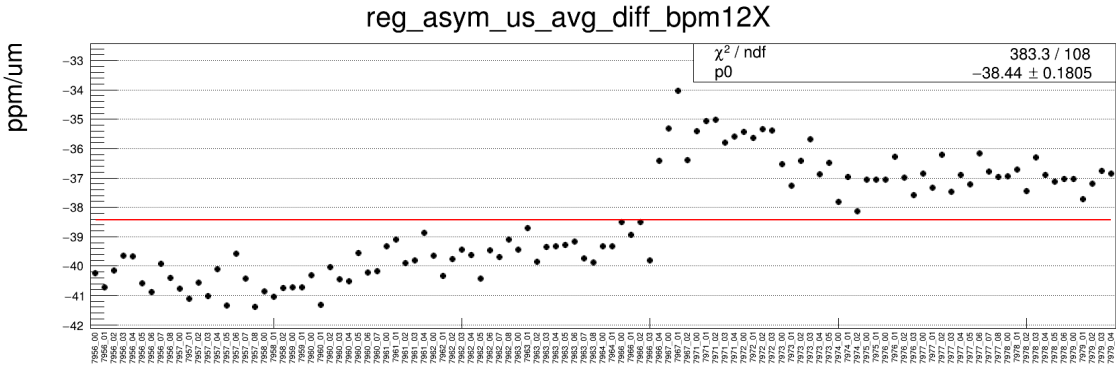


Figure 3.14: Minirun-wise energy slope ( $\partial(\text{asymmetry average})/\partial (\text{BPM12X})$ ) distribution in slug 202. The X-axis is the run number attached by a minirun number.

BPM	slope (ppm/μm)
1X	$\sim -40$
4aY	$\sim 15$
4eX	$\sim 40$
4eY	$\sim 0$
12X	$\sim -40$

Table 3.5: Slope values of the asymmetry average with respect to different BPMs.

exhibits low sensitivity to fluctuations in the Y direction, the corresponding correction is relatively small, typically at the level of a few hundred ppb. Note that corrections from each beam parameter do not accumulate; instead, they cancel each other out, leading to a relatively small total correction, typically a few ppm.

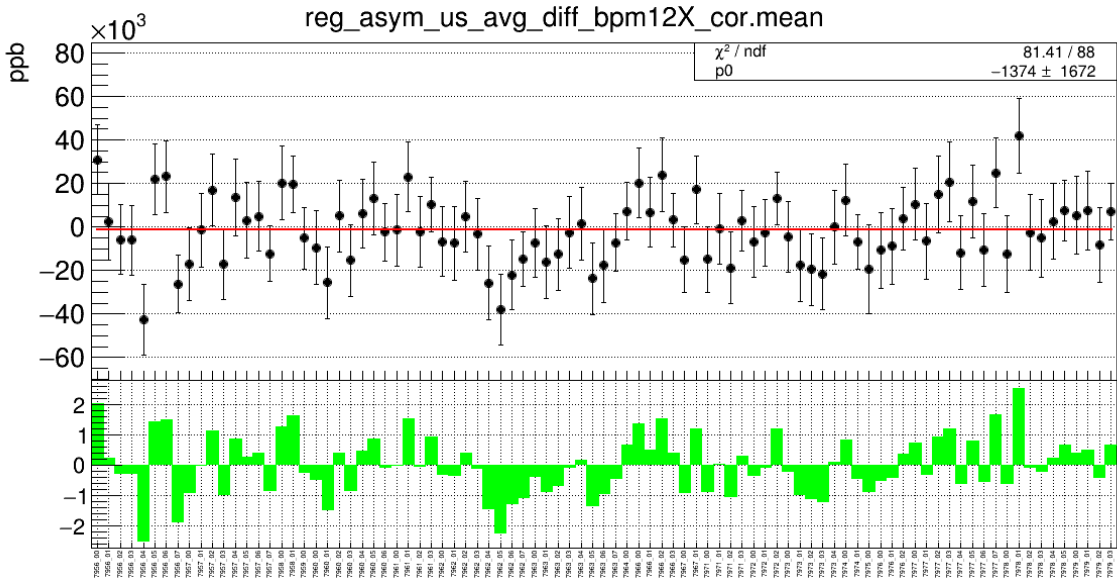


Figure 3.15: False asymmetry correction caused by the energy difference (BPM12X) in slug 202.

BPM	correction
1X	a few tenths ppm
4aY	a few hundreds ppb
4eX	a few tenths ppm
4eY	a few hundreds ppb
12X	a few tenths ppm

Table 3.6: Typical false asymmetry corrections from each BPM.

## Regression Result

The asymmetry after the regression correction reads  $2080 \pm 84.01$  ppb, as shown in the left plot of Fig. 3.16. In Comparison, the raw asymmetry without correction is measured as  $2106 \pm 178.9$  ppb.

As expected, the mean value of the asymmetry does not change significantly after regression correction. This outcome aligns with our assumption that the false asymmetry follows the Gaussian distribution. Therefore the regression correction primarily removes noise without altering the mean value. Moreover, the width of the asymmetry distribution considerably reduces by a factor of 2 after the regression correction, as shown in the right plot of Fig. 3.16. This reduction in width indicates that the regression correction effectively diminishes the noise.

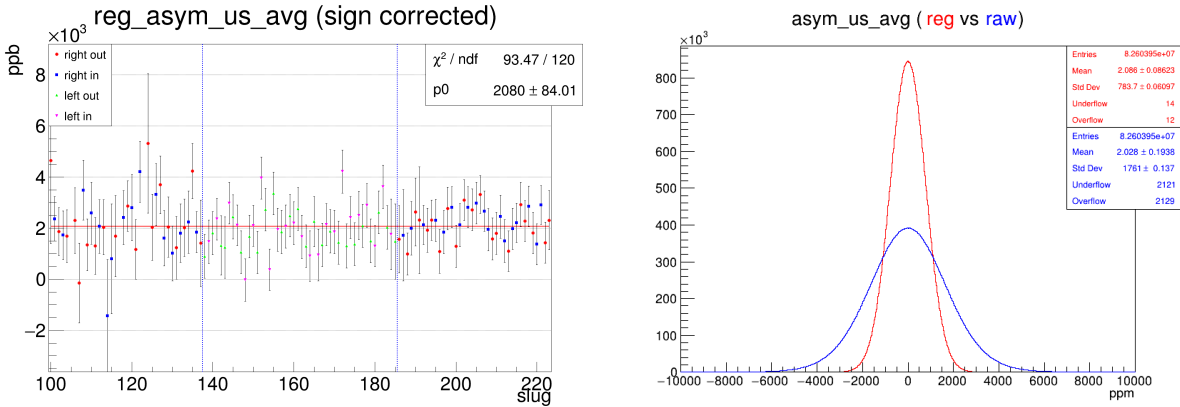


Figure 3.16: Left: slug-wise scatter plot of the asymmetry values after the regression correction. Right: Comparison of the experiment-wise distributions of the asymmetry values before and after the regression correction.

## Null Result

A reliable method for verifying the correctness of our result is by examining the null asymmetry, which is calculated as the difference between the LHRs and RHRs asymmetries divided by 2. In an ideal case, the null asymmetry should be zero. Our measurement shows exactly this expectation, the regression-corrected null asymmetry is about 85 ppb, which is very close to zero.

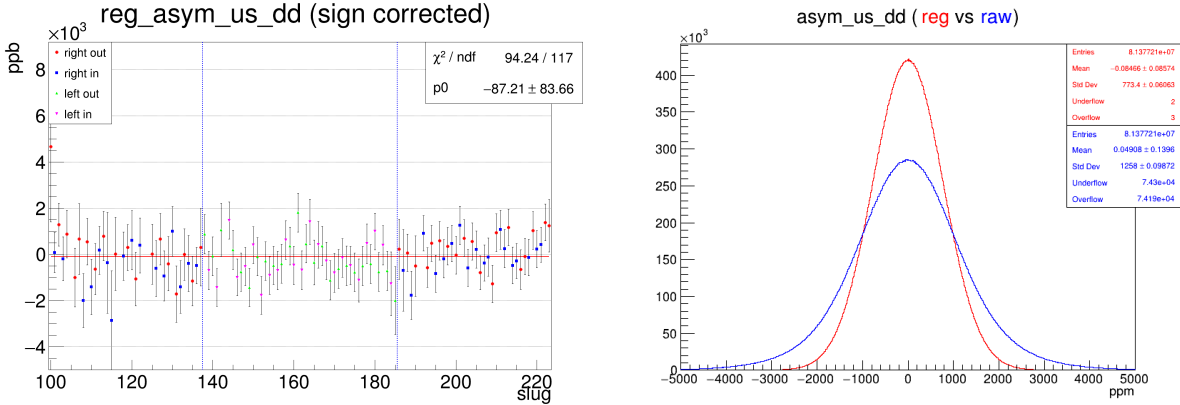


Figure 3.17: Slug-wise scatter plot (left) and experiment-wise histogram (right) of the regression-corrected null asymmetry.

### 3.2.2 Beam Modulation (Dithering)

Another approach to correcting the beam false asymmetry is through beam modulation. This method involves intentionally modulating the beam position, angle, or energy to directly measure the detector's response to the beam fluctuations. By observing the changes in the monitors and detectors during the modulation, we can determine the slope

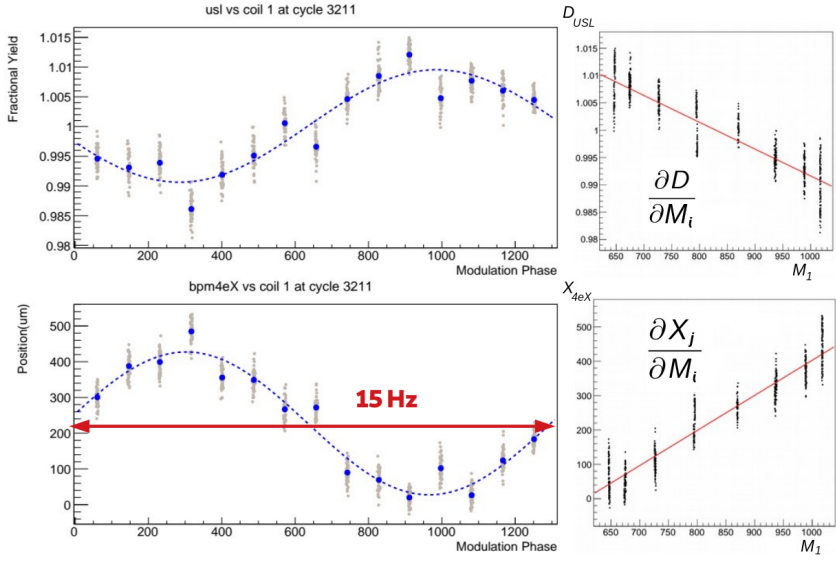


Figure 3.18: An example of beam modulation.

values. The key point is to make sure that the amplitude of the modulation is larger than that of natural beam fluctuations. This is necessary to distinguish the true response of the detector from the inherent variability of the beam.

To express the idea mathematically, let  $D(M)$  be the Detector (Monitor) yield and  $C$  be the modulation coil input, we have:

$$\frac{\partial D}{\partial C_\alpha} = \sum_\mu \frac{\partial D}{\partial M_\mu} \frac{\partial M_\mu}{\partial C_\alpha} \quad (3.22)$$

where  $\alpha$  indexes the number of the coils and  $\mu$  sums over BPMs. In an alternative form:

$$\frac{\partial D}{\partial M_\mu} = \sum_\alpha \frac{\partial D}{\partial C_\alpha} \frac{\partial C_\alpha}{\partial M_\mu} = \sum_\alpha \frac{\partial D}{\partial C_\alpha} \left( \frac{\partial M_\mu}{\partial C_\alpha} \right)^{-1} \quad (3.23)$$

the slope value  $\frac{\partial D}{\partial M}$  is what we want to know.

Define a matrix  $B$  as:

$$B_{n \times m} = \begin{pmatrix} \frac{\partial M_1}{\partial C_1} & \frac{\partial M_2}{\partial C_1} & \dots & \frac{\partial M_m}{\partial C_1} \\ \frac{\partial M_1}{\partial C_2} & \frac{\partial M_2}{\partial C_2} & \dots & \frac{\partial M_m}{\partial C_2} \\ \vdots & \vdots & \ddots & \vdots \\ \frac{\partial M_1}{\partial C_n} & \frac{\partial M_2}{\partial C_n} & \dots & \frac{\partial M_m}{\partial C_n} \end{pmatrix} \quad (3.24)$$

where  $n$  and  $m$  are the number of coils and monitors (BPMs), respectively.

The slope vector can be expressed as:

$$\begin{pmatrix} \frac{\partial D}{\partial M_1} \\ \frac{\partial D}{\partial M_2} \\ \vdots \\ \frac{\partial D}{\partial M_n} \end{pmatrix} = B^{-1} \begin{pmatrix} \frac{\partial D}{\partial C_1} \\ \frac{\partial D}{\partial C_2} \\ \vdots \\ \frac{\partial D}{\partial C_n} \end{pmatrix} \quad (3.25)$$

To make the matrix B invertible, we must have

$$n = m \quad (3.26)$$

which is the same number of monitors and coils.

The calculation of the sensitivity is the same as that of the regression slope:

$$\frac{\partial D}{\partial C} = \frac{\text{cov}(D, C)}{\bar{D} \cdot \text{cov}(C, C)} \quad \frac{\partial M}{\partial C} = \frac{\text{cov}(M, C)}{\bar{M} \cdot \text{cov}(C, C)} \quad (3.27)$$

where  $\bar{D}$  ( $\bar{M}$ ) is the average yield of the detector (monitor) and cov is the covariance. The mean yield in the denominator is for the normalization.

These sensitivities and their combinations were used for monitoring the beam quality during charge collection. In the presence of significant beam fluctuations, we may observe rapid variations or even encounter abnormal values in these monitored quantities.

## Run Segments

As mentioned before, the modulation system consists of seven coils, a complete modulation cycle takes about 2 mins. However, maintaining a stable beam throughout the entire modulation cycle is challenging. Chances are beam trips off during modulation, resulting in incomplete cycles. While only five out of the seven coils are needed to cover the entire beam parameter phase space, it still hurts if we discard those cycles that do not have the chosen five coils, considering that beam modulations occur relatively infrequently (about 1 modulation per 10 mins). To address this, a strategy is implemented where the modulation sensitivities and slopes are calculated on a run-wise basis, using all cycles in one run. By employing this approach, we can maximize the use of modulation data and mitigate the impact of incomplete cycles that do not include the desired five coils.

Although the run-wise strategy to save incomplete cycles, some runs still lack of the dithering data. To enable dithering correction for these runs, we adopt a segmentation approach based on beam conditions. By dividing runs into segments, we calculate an average dithering slope using run-wise values within each segment. This average value is then used as the dithering slope for every run within that segment. Segments are determined by changes in the beam setup or when shift in the slope values are observed. A detailed list of segments can be found in Cameron's thesis [75].

## Dithering Result

The dithering-corrected asymmetry is reported as  $2085 \pm 84.22$  ppb, which deviates from the regression-corrected result of  $2080 \pm 84.01$  ppb by 0.24%. The consistency between these two values proves the correctness of both methods. The difference between the asymmetries corrected using these two methods is shown in the right plot of Fig. 3.19. In most slugs, the difference is about zero, taking into account the uncertainty.

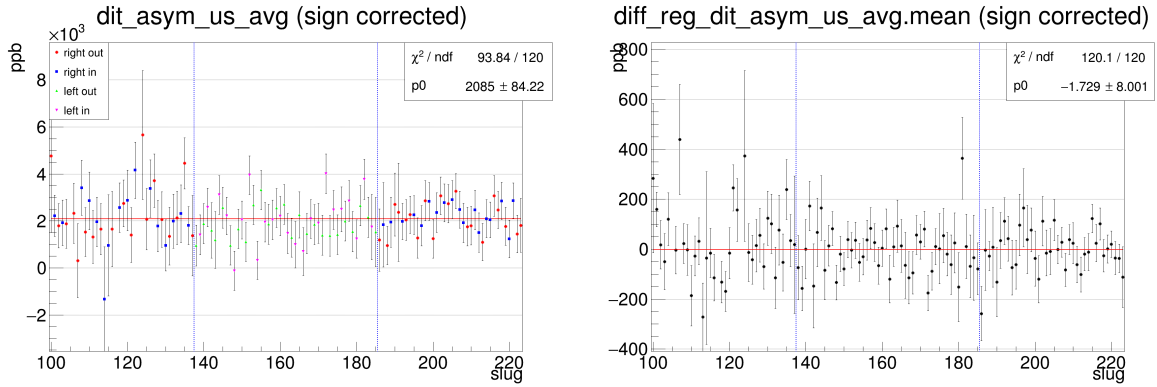


Figure 3.19: Left: slug-wise scatter plot of the asymmetry corrected with beam modulation. Right: difference between the asymmetry values corrected by regression and beam modulation.

### 3.2.3 Lagrange Multiplier

As mentioned earlier, we should use miniruns for a more precise false asymmetry correction. However, in the dithering correction, segment-wise slopes are used due to the limited availability of modulation data. While the regression method is more precise than the dithering correction, it is less accurate due to the inherent noise present in detectors and monitors. The modulation amplitude is designed to be larger than the noise level (while still being small compared to the yield, typically less than 1%). This design allows for increased accuracy by effectively suppressing the impact of those noises.

Considering the strengths and weaknesses of both methods, it is natural to explore a combination that leverages their respective advantages. This integration leads to the Lagrangian analysis, which is actually regression with constraints from beam modulation.

From Eq. 3.11, the  $\chi^2$  for the asymmetry regression is derived as:

$$\chi^2 = \sum_i \left( \mathcal{A}_{\text{raw}} - \sum_{\mu} \beta_{\mu} \Delta M_{\mu} \right)_i^2 \quad (3.28)$$

where  $i$  sums over samples and  $\mu$  iterates over selected BPMs.

The Lagrangian multiplier for this constraint problem will be:

$$\mathcal{L} = \sum_i \left( \mathcal{A}_{\text{raw}} - \sum_{\mu} \beta_{\mu} \Delta M_{\mu} \right)_i^2 + \sum_{\alpha} \lambda_{\alpha} \left( \sum_{\mu} \beta_{\mu} \frac{\partial M_{\mu}}{\partial C_{\alpha}} - \frac{\partial D}{\partial C_{\alpha}} \right) \quad (3.29)$$

$\alpha$  indexes the selected coils.

Set the gradient of  $\mathcal{L}$  to zero:

$$\begin{aligned} \frac{\partial \mathcal{L}}{\partial \beta_{\mu}} &= -2 \Delta M_{\mu} \sum_i \left( \mathcal{A}_{\text{raw}} - \sum_{\nu} \beta_{\nu} \Delta M_{\nu} \right)_i + \sum_{\alpha} \lambda_{\alpha} \frac{\partial M_{\mu}}{\partial C_{\alpha}} \\ &= 2 \left( \sum_{\nu} \beta_{\nu} \cdot \text{cov}(\Delta M_{\mu}, \Delta M_{\nu}) - \text{cov}(\mathcal{A}_{\text{raw}}, \Delta M_{\mu}) \right) + \sum_{\alpha} \lambda_{\alpha} \frac{\partial M_{\mu}}{\partial C_{\alpha}} = 0 \quad (3.30) \\ \frac{\partial \mathcal{L}}{\partial \lambda_{\alpha}} &= \left( \sum_{\mu} \beta_{\mu} \frac{\partial M_{\mu}}{\partial C_{\alpha}} - \frac{\partial D}{\partial C_{\alpha}} \right) = 0 \end{aligned}$$

The distinction between the second formula of Eq. 3.30 and the conventional beam modulation method may be confusing, because they are actually the same if we consider only five BPMs. The beam modulation constraint is so strong that it directly determines the slope values. However, as we introduce more BPMs into the analysis, surpassing the number of coils, the solution to the constraint becomes non-unique. Consequently, the Lagrange multiplier method becomes applicable.

Write Eq. 3.30 in a matrix form:

$$\begin{pmatrix} M_{m \times m} & (B^T)_{m \times n} \\ B_{n \times m} & \mathbf{0}_{n \times n} \end{pmatrix} \begin{pmatrix} \beta_1 \\ \vdots \\ \beta_m \\ \frac{\lambda_1}{2} \\ \vdots \\ \frac{\lambda_n}{2} \end{pmatrix} = \begin{pmatrix} \text{cov}(\mathcal{A}_{\text{raw}}, \Delta M_1) \\ \vdots \\ \text{cov}(\mathcal{A}_{\text{raw}}, \Delta M_m) \\ \frac{\partial D}{\partial C_1} \\ \vdots \\ \frac{\partial D}{\partial C_n} \end{pmatrix} \quad (3.31)$$

where the  $M$  and  $B$  matrices are defined in Eq. 3.19 and 3.24, and  $m$  ( $n$ ) refers to the number of BPMs (coils) with  $m > n$ . In our analysis, we used all 12 BPMs, so  $m = 12$  and  $n = 5$ .

Eq. 3.31 can be solved to be

$$\begin{pmatrix} \boldsymbol{\beta} \\ \boldsymbol{\lambda} \end{pmatrix} = \begin{pmatrix} M & B^T \\ B & \mathbf{0} \end{pmatrix}^{-1} \times \begin{pmatrix} \mathbf{Y}_1 \\ \mathbf{Y}_2 \end{pmatrix} \quad (3.32)$$

where  $\boldsymbol{\beta}$  and  $\boldsymbol{\lambda}$  are the slope vector and the Lagrange multiplier vector,  $\mathbf{Y}_1$  is the covariance between raw asymmetry and monitor difference, and  $\mathbf{Y}_2$  is the detector sensitivity. As what we did in the beam modulation, the sensitivity values are segment-wise average

values.

### Lagrange Multiplier Result

The asymmetry corrected with the Lagrange multiplier is shown in Fig. 3.20. Compared with the asymmetry values corrected using the other two methods, only a tiny difference is observed.

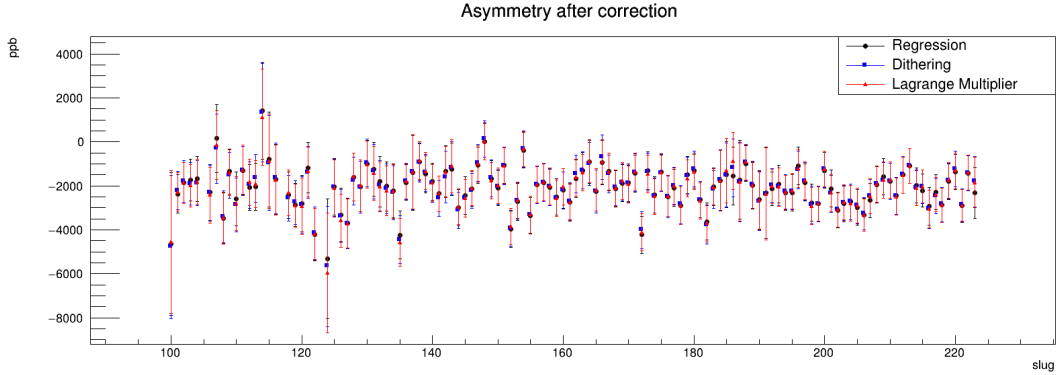


Figure 3.20: Comparison of the asymmetry values corrected using regression (black), dithering (blue) and the Lagrange multiplier (red).

## 3.3 Result

As discussed before, the slow helicity reversal involving the IHWP and the double Wien filters, allow us to investigate potential systematic biases. In this context, define a ‘part’ as a set of sharing the same IHWP and Wien-flip states. By examining the part asymmetry presented in Fig. 3.21, it is evident that the measured asymmetries with opposite IHWP states or opposite Wien-flip states overlap within a  $1\sigma$  uncertainty range. This observation verifies the unbiasedness of our measurement.

The pitt plot in Fig. 3.21 shows the asymmetry distribution for each pitt. The concept of pitt was introduced by Mark Pitt and involves grouping nearby slugs with alternating IHWP states in order to achieve a comparable number of events for opposite IHWP states within each pitt. Typically, each pitt consists of about 4 slugs, the detailed range definition of each pitt can be found in Cameron’s thesis.

### The Final Number

From the pitt plot in Fig. 3.21, the final corrected asymmetry (blinded) is read as:

$$\mathcal{A}_{\text{cor}} = 2081 \pm 83.77 \text{ ppb} \quad (3.33)$$

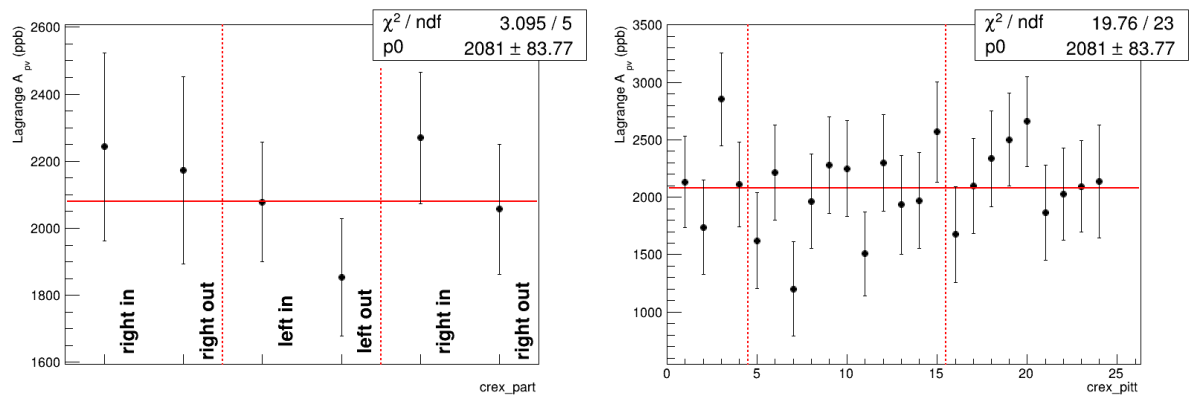


Figure 3.21: Part-wise and pitt-wise scattering plot of asymmetry values corrected with the Lagrange multiplier.

The number used in the published paper is

$$\mathcal{A}_{\text{cor}} = 2080 \pm 83.77 \text{ ppb} \quad (3.34)$$

The difference lies in the 2 miniruns I discard in Table 3.2 because of their small sample sizes.

# Chapter 4

## Transverse Asymmetry

The beam normal single spin asymmetry (BNSSA), also known as the transverse single spin asymmetry or transverse asymmetry, is distinct from the PV asymmetry. It is purely EM and, therefore, preserves parity. The BNSSA arises from the interference between the one-photon and two-photon exchanges (OPE and TPE), making it sensitive to the TPE amplitude. By measuring the BNSSA, we can probe the strength of the TPE, which plays a crucial role in electron elastic scattering that may explain the discrepancy in the proton radius measurements obtained through different methods.

The transverse asymmetry is also a significant systematic uncertainty in PV asymmetry measurements due to residual transverse polarizations in the electron beam. With  $\mathcal{A}_n \sim \alpha_{EM} m_e / E_e$ , its magnitude of  $10^{-5}$  (10 ppm) for a GeV-level electron beam is much larger than  $\mathcal{A}_{PV}$ . Therefore, a thorough understanding and precise measurement of the transverse asymmetry is necessary to ensure the accuracy of  $\mathcal{A}_{PV}$ .

Being a routine and bonus of a PV experiment, PREX-I also measured the transverse asymmetry of several nuclei, namely  $^1H$ ,  $^4He$ ,  $^{12}C$  and  $^{208}Pb$ . Surprisingly, PREX-I saw a zero transverse asymmetry in  $^{208}Pb$ , while the transverse asymmetries of other light nuclei agreed with theoretical predictions, as shown in Fig. 4.1. This discrepancy in  $^{208}Pb$  remains a puzzle and is one of the motivations for conducting PREX-II.

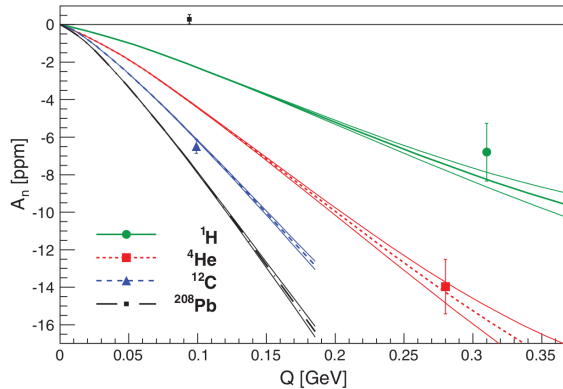


Figure 4.1: Transverse asymmetries measured in PREX-I [76].

As its name implies, the BNSSA depends on the polarization of either the target or the electron beam, but not both simultaneously. In this regard, a polarized electron beam is preferred over a polarized target, because it is hard to polarize nuclei, especially heavy nuclei.

## 4.1 Motivation for the Transverse Asymmetry

### The Scattering Theory

Consider the scattering of a free particle ( $t_0 \rightarrow -\infty$ ) initially in a state  $|i\rangle$  from a time-independent potential  $V(\mathbf{r})$ , which decays quickly as  $r \rightarrow \infty$ . In the Schrödinger picture ( $\hbar = 1$ ), the time evolution of the system is represented by the state  $|\psi(t)\rangle_S$

$$|\psi(t)\rangle_S = U(t) |\psi(t_0)\rangle = \lim_{t_0 \rightarrow -\infty} U(t, t_0) |i\rangle \quad (4.1)$$

where  $U(t, t_0)$  is the evolution operator:

$$U(t, t_0) = \exp\left(\frac{1}{i}(H_0 + V)(t - t_0)\right) = \exp(-i(H_0 + V)(t - t_0)) \quad (4.2)$$

$H_0$  is the free Hamiltonian and  $H = H_0 + V$  is the complete Hamiltonian with the interaction term.

The projection of  $\psi(t)$  to a free final state  $|f\rangle$  defines the so-called S-matrix (the order of the subscripts matters):

$$S_{if} \equiv \lim_{t \rightarrow +\infty} \langle f | \psi(t) \rangle = \lim_{t \rightarrow \infty} \lim_{t_0 \rightarrow -\infty} \langle f | U(t, t_0) | i \rangle \quad (4.3)$$

which defines the S operator:

$$S_{if} = \langle f | S | i \rangle \implies S = U(+\infty, -\infty) \quad (4.4)$$

The S-matrix describes the scattering amplitude from a free initial state  $|i\rangle$  to a free final state  $|f\rangle$ . Conservation of the probability indicates unitarity of the S matrix:

$$S^\dagger S = \sum_f |\langle f | U(+\infty, -\infty) | i \rangle|^2 = 1 \quad (4.5)$$

It is easier to evaluate  $U(t)$  in the interaction picture. Define

$$|\psi(t)\rangle_I \equiv \exp\left(-\frac{1}{i}H_0t\right) |\psi(t)\rangle_S = \exp(iH_0t) \exp(-i(H_0 + V)t) |i\rangle \quad (4.6)$$

The subscript I and S denote the interaction and Schrödinger picture respectively. The

evolution of  $|\psi(t)\rangle_I$  is:

$$\begin{aligned}
\frac{d}{dt} |\psi(t)\rangle_I &= [\exp(iH_0t)(iH_0) \exp(-i(H_0 + V)t) + \exp(iH_0t)(-i)(H_0 + V) \exp(-i(H_0 + V)t)] |i\rangle \\
&= -i \exp(iH_0t) V \exp(-i(H_0 + V)t) |i\rangle \\
&= -i \exp(iH_0t) V \exp(-iH_0t) \cdot \exp(iH_0t) \exp(-i(H_0 + V)t) |i\rangle \\
&= -iV_I(t) |\psi(t)\rangle_I
\end{aligned} \tag{4.7}$$

where  $V_I(t) = \exp(iH_0t)V \exp(-iH_0t)$  is the time dependent interaction term. Eq. 4.7 leads to the Dyson series:

$$U(t, t_0) = 1 - i \int_{t_0}^t dt_1 V_I(t_1) U(t_1, t_0) = \sum_{n=0}^{\infty} \frac{(-i)^n}{n!} \int_{t_0}^t dt_1 \cdots \int_{t_0}^t dt_n T[V_I(t_1) \cdots V_I(t_n)] \tag{4.8}$$

T means the time-ordering:

$$T(V_I(t_1)V_I(t_2)) \equiv \begin{cases} V_I(t_1)V_I(t_2) & t_1 \leq t_2 \\ V_I(t_2)V_I(t_1) & t_2 \leq t_1 \end{cases} \tag{4.9}$$

With Eq. 4.8, we have an iterative expression:

$$\begin{aligned}
\langle f | U(t, t_0) | i \rangle &= \langle f | i \rangle - i \langle f | \int_{t_0}^t dt_1 V_I(t_1) U(t_1, t_0) | i \rangle \\
&= \delta_{if} - i \sum_m \int_{t_0}^t dt_1 \langle f | \exp(iH_0t_1) V \exp(-iH_0t_1) | t_1 \rangle | m \rangle \langle m | U(t_1, t_0) | i \rangle \\
&= \delta_{if} - i \sum_m \langle f | V | m \rangle \int_{t_0}^t dt_1 \exp(i(E_f - E_m)t_1) \langle m | U(t_1, t_0) | i \rangle
\end{aligned} \tag{4.10}$$

Truncate Eq. 4.10 into the first order ( $\langle m | U(t_1, t_0) | i \rangle = \delta_{im}$ ) and define  $T_{if} = \langle f | V | i \rangle$ , we write:

$$\langle f | U(t, t_0) | i \rangle = \delta_{if} - iT_{if} \int_{t_0}^t dt_1 \exp(i(E_f - E_i)t_1) \tag{4.11}$$

and

$$\begin{aligned}
S_{if} &= \lim_{t \rightarrow +\infty} \lim_{t_0 \rightarrow -\infty} \langle f | U(t, t_0) | i \rangle \\
&= \delta_{if} - iT_{if} \int_{-\infty}^{\infty} dt_1 \exp(i(E_f - E_i)t_1) \\
&= \delta_{if} + i2\pi\delta(E_f - E_i)T_{if}
\end{aligned} \tag{4.12}$$

In the matrix form:

$$S = 1 + i2\pi T \tag{4.13}$$

$S$  being unitary implies

$$S^\dagger S = (1 - i2\pi T^\dagger)(1 + i2\pi T) = 1 + i2\pi(T - T^\dagger) + (2\pi)^2 T^\dagger T = 1 \quad (4.14)$$

which reads

$$T - T^\dagger = i(2\pi)T^\dagger T = i(2\pi)TT^\dagger \quad (4.15)$$

In terms of the matrix element:

$$\begin{aligned} \delta(E_f - E_i)(T_{if} - T_{if}^\dagger) &= \sum_m i2\pi\delta(E_f - E_m)\delta(E_m - E_i)T_{fm}T_{mi}^\dagger \\ T_{if} - T_{if}^\dagger &= \sum_m i2\pi\delta(E_m - E_i)T_{fm}T_{mi}^\dagger = ia_{if} \end{aligned} \quad (4.16)$$

where

$$a_{if} = \sum_m (2\pi)\delta(E_m - E_i)T_{fm}T_{mi}^\dagger \quad (4.17)$$

is the absorptive part of the transition amplitude  $T_{if}$ .  $|m\rangle$  extends to all on-shell intermediate states.

The two components of the S-matrix are straightforward to understand. The constant piece denotes the evolution of a free particle transforming into another free particle without any interactions. Naturally, it can only evolve into itself. The T matrix characterizes the interaction (transition amplitude) between the initial free particle state  $|i\rangle$  and the final free particle state  $|f\rangle$ . It quantifies the likelihood of the interaction.

A free particle state can be fully determined by its momentum vector  $\mathbf{p}$  (disregarding spin for now). For an incoming electron  $|\mathbf{p}_i\rangle$ , the probability of it transitioning into the final state of  $|\mathbf{p}_f\rangle$  is given by:

$$dP = (\text{phase space}) \times (\text{transition probability}) = \frac{d\mathbf{p}_f}{(2\pi)^3} \times |S_{\mathbf{p}_i\mathbf{p}_f}|^2 \quad (4.18)$$

For a non trivial case of  $|f\rangle \neq |i\rangle$ , we have:

$$S_{if} = i2\pi\delta(E_f - E_i)T_{if} \quad (4.19)$$

The differential cross section will be:

$$d\sigma = \frac{dP}{\mathcal{L}\Delta t} \quad (4.20)$$

where  $\Delta t$  is the interaction time and  $\mathcal{L}$  is the luminosity, indicating number of particles hitting the target per unit area per unit time. In our case of an incoming plane wave,  $\mathcal{L} = \rho v = v$ .

$$d\sigma = \frac{1}{v\Delta t} \frac{d\mathbf{p}_f}{(2\pi)^3} 2\pi\delta(E_f - E_i) 2\pi\delta(E_f - E_i)|_{E_f=E_i} |T_{if}|^2 \quad (4.21)$$

Transform one  $\delta$  expression back to the integrating form:

$$2\pi\delta(E_f - E_i)|_{E_f=E_i} = \int_{-\infty}^{+\infty} dt \exp(-i(E_f - E_i)t)|_{E_f=E_i} = \int_{-\infty}^{+\infty} dt \quad (4.22)$$

Physically, we do not go back or into infinity in time, because the real particle is a finite wave packet rather than a plane wave. The integration above should be finite and close to the interaction time

$$\int_{-\infty}^{+\infty} dt \rightarrow \Delta t \quad (4.23)$$

Thus we have a defined cross section

$$d\sigma = \frac{1}{v} \frac{d\mathbf{p}_f}{(2\pi)^3} 2\pi\delta(E_f - E_i)|T_{if}|^2 \quad (4.24)$$

The cross section is proportional to  $|T_{if}|^2$ , as already known to us.

## T-Symmetry

Time symmetry is a fundamental discrete symmetry in physics, which states that physical laws remains unchanged under the operation of time reversal. Time reversal refers to the reversal of the time arrow, leading to the progression of time in the opposite direction. As a consequence of time reversal, various vectors associated with first-order time derivatives undergo a sign reversal. This includes quantities like momentum, angular momentum and magnetic field.

Express the time reversal operation in QM:

$$|\tilde{\psi}\rangle = \hat{\mathcal{T}}|\psi\rangle \quad (4.25)$$

where  $\hat{\mathcal{T}} : t \rightarrow -t$  is the time reversal operator.

In terms of the scattering discussed above, a particle will flip its momentum and spin (angular momentum) under time reversal, and pick up a phase.

$$|\tilde{\psi}\rangle = \hat{\mathcal{T}}|\psi_{\uparrow}(\mathbf{k})\rangle = \eta|\psi_{\downarrow}(-\mathbf{k})\rangle \quad (4.26)$$

$\eta$  is the phase difference. It is expected that two times of time reversal operation will transform a state back to itself, which means  $|\eta|^2 = 1$ . The T matrix in terms of the time-reversed states is:

$$T_{\tilde{i}\tilde{f}} = \langle \tilde{f} | V | \tilde{i} \rangle \quad (4.27)$$

It is well known that the EM interaction is invariant under time reversal.

$$|T_{if}|^2 = |T_{\tilde{f}\tilde{i}}|^2 \quad (4.28)$$

With these concepts, one can also define T-odd quantities, which are proportional

to the difference between the magnitude of a regular T element and its time-reversed counterpart:

$$\begin{aligned}
\text{T-odd} &\propto |T_{if}|^2 - |T_{\tilde{i}\tilde{f}}|^2 \\
&= |T_{if}|^2 - |T_{fi}|^2 \\
&= |T_{if}|^2 - |T_{if}^\dagger|^2 \\
&= |T_{if}|^2 - |T_{if} - ia_{if}|^2 \\
&= -i(T_{if}a_{if}^* - T_{if}^*a_{if}) - |a_{if}|^2 \\
&= 2\text{Im}(T_{if}a_{if}^*) - |a_{if}|^2
\end{aligned} \tag{4.29}$$

### Transverse Asymmetry

Denote the incoming and outgoing transversely polarized electron as  $|\mathbf{k}\rangle$  and  $|\mathbf{k}'\rangle$ , the scattering is shown in Fig. 4.2.

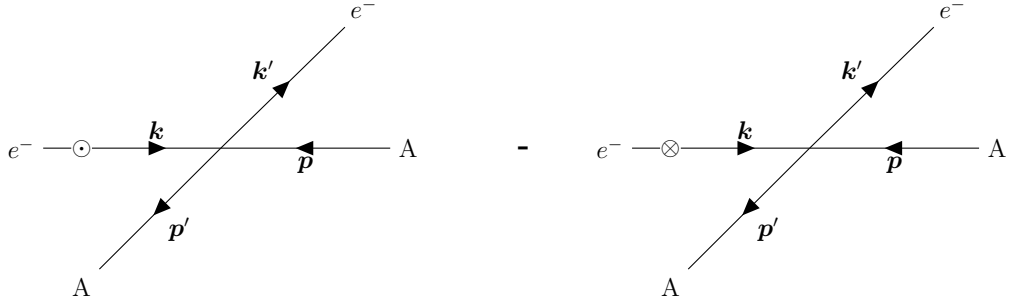


Figure 4.2: Feynman diagrams of a transversely polarized electron scatters off an unpolarized nuclear target in the COM frame. The vector in or out of the plane indicates the electron's spin direction.

The transverse asymmetry will be:

$$\mathcal{A}_n \equiv \frac{N_\uparrow - N_\downarrow}{N_\uparrow + N_\downarrow} = \frac{|T_\uparrow(\mathbf{k}, \mathbf{k}')|^2 - |T_\downarrow(\mathbf{k}, \mathbf{k}')|^2}{|T_\uparrow(\mathbf{k}, \mathbf{k}')|^2 + |T_\downarrow(\mathbf{k}, \mathbf{k}')|^2} \tag{4.30}$$

where  $T(\mathbf{k}, \mathbf{k}') = \langle \mathbf{k}' | V | \mathbf{k} \rangle$  is the scattering amplitude and the arrow subscript indicates electron's spin direction.  $T_\downarrow(\mathbf{k}, \mathbf{k}')$  is related to  $T_\downarrow(-\mathbf{k}, -\mathbf{k}')$  by a rotation around the normal direction of the scattering plane, as shown in Fig. 4.3

$$T_\downarrow(\mathbf{k}, \mathbf{k}') = e^{i\pi} T_\downarrow(-\mathbf{k}, -\mathbf{k}') \tag{4.31}$$

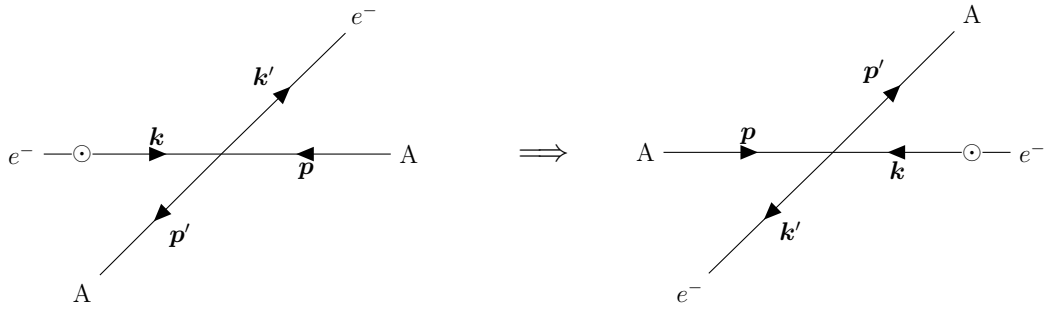


Figure 4.3: Rotation by  $\pi$  around the normal direction of the scattering plane.

Let  $T_{if} = T_{\uparrow}(\mathbf{k}, \mathbf{k}')$ , then  $T_{\tilde{i}\tilde{f}} = T_{\downarrow}(-\mathbf{k}, -\mathbf{k}')$  and

$$\begin{aligned}
 \mathcal{A}_n &\approx \frac{|T_{\uparrow}(\mathbf{k}, \mathbf{k}')|^2 - |T_{\downarrow}(-\mathbf{k}, -\mathbf{k}')|^2}{2|T_{\uparrow}(\mathbf{k}, \mathbf{k}')|^2} \\
 &= \frac{|T_{if}|^2 - |T_{\tilde{i}\tilde{f}}|^2}{2|T_{if}|^2} \\
 &= \frac{2\text{Im}(T_{if}a_{if}^*) - |a_{if}|^2}{2|T_{if}|^2}
 \end{aligned} \tag{4.32}$$

We find that the transverse asymmetry is a T-odd quantity. For the EM interaction

$$T_{if} \propto \alpha \quad a_{if} \propto \alpha^2 \tag{4.33}$$

Because  $\alpha \simeq \frac{1}{137}$  is small, we can expand Eq. 4.32 in order of  $\alpha$ . To the lowest order

$$\mathcal{A}_n = 0 \tag{4.34}$$

and to the first order

$$\mathcal{A}_n = \frac{\text{Im}(T_{if}a_{if}^*)}{|T_{if}|^2} \tag{4.35}$$

$T_{ij}$  corresponds the OPE interaction, while  $a_{ij}$  represents the TPE interaction. Therefore, the physical interpretation of Eq. 4.34 and 4.35 is as follows: the time symmetry requires the transverse asymmetry to be zero under the Born approximation (OPE only) and the (lowest order) non-zero transverse asymmetry comes from the interference between OPE and TPE.

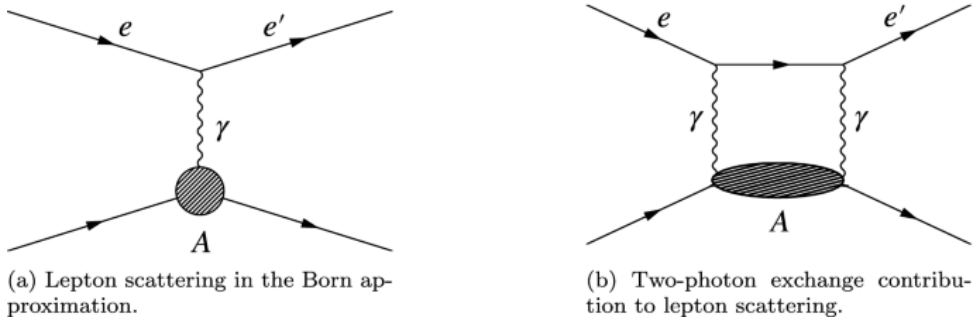


Figure 4.4: Feynman diagrams of the OPE (left) and TPE (right) interactions.

## 4.2 Measurement of the Transverse Asymmetry: the Method

The experimentally measured transverse asymmetry is given by:

$$\mathcal{A}_{\text{mea}} = \mathcal{A}_n \mathcal{P}_e \cdot \hat{n} = \mathcal{A}_n \mathcal{P}_n \sin(\phi_s - \phi_e) = \mathcal{A}_n \mathcal{P}_n \sin \phi \quad (4.36)$$

where  $\mathcal{P}_e$  is the electron spin vector, whose magnitude is the polarization;  $\mathcal{P}_n$  denotes the transverse component of the electron spin;  $\phi_s$  being the angle between the electron spin vector and the lab horizontal plane;  $\hat{n} = \frac{\mathbf{k} \times \mathbf{k}'}{|\mathbf{k} \times \mathbf{k}'|}$  is the unit normal vector of the scattering plane;  $\phi_e$  represents the angle between the scattering plane and the horizontal plane; and  $\phi = \phi_s - \phi_e$  refers to the angle between the electron spin vector and the scattering plane. These quantities are depicted in Fig. 4.5.

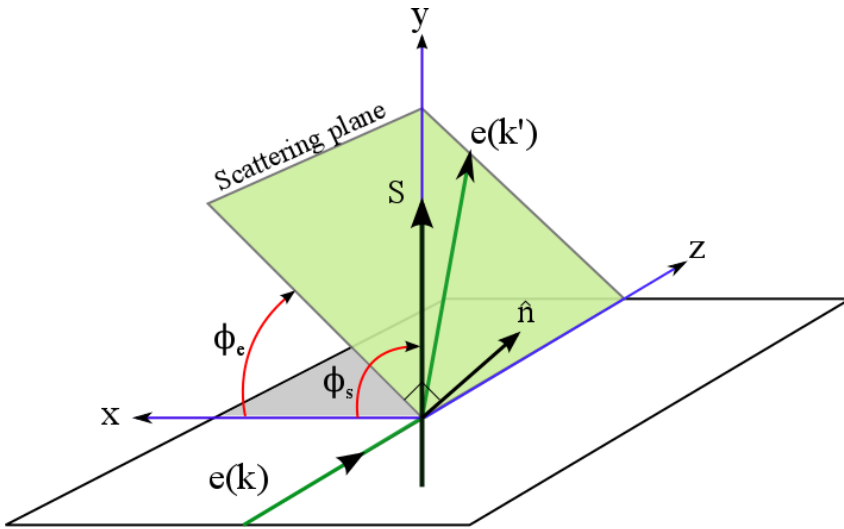


Figure 4.5: Schematic plot of the scattering of a transversely polarized electron.

Eq. 4.36 shows the angle dependence of the transverse asymmetry. Experimentally, it is convenient to choose the angle  $\phi$  to be  $90^\circ$ . By selecting the lab horizontal plane as the scattering plane, the electron spin will be vertical, being perpendicular to the scattering

Exp (Energy)	Target	$\langle \theta \rangle (\circ)$	$\langle Q^2 \rangle (\text{GeV}^2)$	$\langle \sin \phi \rangle$
PREX-II (0.95 GeV)	$^{12}\text{C}$	4.87	0.0067	0.967
	$^{40}\text{Ca}$	4.81	0.0067	0.964
	$^{208}\text{Pb}$	4.69	0.0064	0.966
CREX (2.18 GeV)	$^{12}\text{C}$	4.77	0.033	0.969
	$^{40}\text{Ca}$	4.55	0.031	0.970
	$^{48}\text{Ca}$	4.53	0.031	0.970
	$^{208}\text{Pb}$	4.60	0.032	0.969

Table 4.1: Dynamics of the AT measurement in PREX-II/CREX.

plane, as adopted in PREX-II and CREX. Detailed dynamics for the AT measurement are listed out in Table 4.1.

To achieve transverse polarization, a modified configuration of the double Wien filters is needed. In this setup, the focus is on rotating the spin to the vertical direction using the vertical Wien filter. The subsequent rotations typically performed for longitudinal polarization, as depicted in Fig. 2.15, are omitted in this case. Specifically, the rotating angle of the spin solenoid is set to approximately 0 degrees. Since the spin is parallel or antiparallel to the magnetic field within the accelerator arc region, there is no spin precession as observed in the case of longitudinal polarization. This configuration allows for the desired transverse polarization of the electron beam.

In terms of the measurement of transverse polarization, neither Moller, nor Compton polarimeter was used, because their analyzing powers go to zero in the limit of transverse polarization. Without a direct measurement of the polarization in the hall, we turned to the Mott polarimeter in the injector. As said above, the beam transportation from the injector to Hall A is symmetric and flat, which means the vertical component of the polarization is preserved (can be safely assumed  $> 99.9\%$ ), so the measurement in the injector can be used as a reliable proxy for the polarization measurement in the hall.

Apart from the configuration variance in the double Wien filters, everything else remains the same as in the case of longitudinal polarization with the Compton Chicane turned off.

## Polarization Measurement

The 5 MeV Mott polarimeter was used to verify the transverse polarization, which gave about 87% transverse polarization for both PREX-II and CREX runs. The Mott data is summarized in Table 4.2.

The actual value we used for the transverse asymmetry calculation was the average longitudinal polarization measured shortly before and after the AT runs, with confidence in our Wien filter settings and that the accelerator would not change the beam transverse polarization. The polarization results are shown in Table 4.3

exp	run	IHWP	UD (%)	LR (%)	Vertical Pol (%)
PREX-II	8966	OUT	$0.0704732 \pm 0.435101$	$-34.193 \pm 0.418556$	-87.2048
	8967	IN	$0.421465 \pm 0.432328$	$33.9616 \pm 0.419132$	86.6146
CREX	9081	IN	$-1.16128 \pm 0.334165$	$-34.1276 \pm 0.325363$	-87.0380
	9082	OUT	$-0.105704 \pm 0.328932$	$34.0755 \pm 0.324116$	86.9051
CREX	9083	IN	$-0.613295 \pm 0.333657$	$-34.3502 \pm 0.32453$	-87.6057
	9084	OUT	$-0.0248337 \pm 0.326988$	$34.4674 \pm 0.318313$	87.9046
CREX	9085	IN	$-1.15795 \pm 0.33341$	$-34.0401 \pm 0.32742$	-86.8148

Table 4.2: Mott measurements during PREX-II and CREX AT runnings. The Up-Down asymmetry measures the horizontal transverse polarization while the Left-Right asymmetry measures the vertical transverse polarization; The Mott analyzing power is  $\mathcal{A}_{\text{Mott}} = 0.3921 \pm 0.0016$ , so the vertical polarization is  $\frac{\mathcal{A}_{\text{LR}}}{\mathcal{A}_{\text{Mott}}}$ .

Exp	Compton (%)	Moller (%)	$P_n$ (%)
PREX-II	$88.5533 \pm 0.447$	$89.67 \pm 0.8$	$89.7 \pm 0.8$
CREX	$86.67 \pm 0.63$	$86.897 \pm 0.778$	$86.8 \pm 0.6$

Table 4.3: The Compton and Moller polarization measurements near the AT runs. The PREX-II AT uses only the Moller result while the CREX one uses the average value of the Compton and the Moller measurements.

### 4.3 Data

We spent one (two) day in PREX-II (CREX) for the transverse asymmetry measurement, and collected 25 (56) good AT runs in PREX-II (CREX).

exp	target	IHWP	# runs	run number
PREX-II	$^{12}\text{C}$	IN	3	4106-4107, 4133
		OUT	4	4108-4109, 4131-4132
	$^{208}\text{Pb}$	IN	7	4115-4119, 4129-4130
		OUT	6	4110-4114, 4128
CREX	$^{40}\text{Ca}$	IN	3	4123-4125
		OUT	2	4126-4127
	$^{48}\text{Ca}$	IN	9	6344-6345,6354-6355,6380-6382,6407-6408
		OUT	10	6346-6348,6356-6357,6383-6385,6405-6406
	$^{40}\text{Ca}$	IN	7	6351-6352,6394-6396,6401-6402
		OUT	7	6349-6350,6398-6400,6403-6404
	$^{12}\text{C}$	IN	6	6361-6363,6389-6391
		OUT	5	6359-6360,6386-6388
	$^{208}\text{Pb}$	IN	7	6367-6371,6377-6378
		OUT	5	6372-6376

Table 4.4: AT runs in PREX-II/CREX

### 4.3.1 Data Analysis

Using the data set after 2 respins and following the standard analysis procedure, the transverse asymmetry is extracted. As shown in Eq. 4.36,  $\hat{n}$  of the scattering plane in the LHRS and RHRS are opposite to each other. Consequently, the measured transverse asymmetries exhibit opposite signs in the LHRS and RHRS. To combine the measurements from both arms, the asymmetry difference is utilized instead of the asymmetry average used in the main analysis. The asymmetry difference is defined as (up to a ‘-’ sign):

$$\mathcal{A}_{dd} = \frac{\mathcal{A}_L - \mathcal{A}_R}{2} \quad (4.37)$$

A simple cut of `ErrorFlag == 0` is applied to select good quadruplets. In PREX-II, run 4112 is a long run with its data split into two root files, the second one contains only a small size of samples and is therefore ignored in our AT analysis. Additionally, the first minirun of run 4117 is excluded due to the large charge asymmetry observed in that minirun.

The selected good quadruplets are initially grouped into miniruns, and the average value of the asymmetry difference over these miniruns for each target is calculated, which is the desired quantity. Alternatively, the transverse asymmetry can be extracted the histogram filled with all quadruplets, known as the mulplot. The mean value of the mulplot serve as the final result.

Statistically, there is no difference between these two methods. They use the same data set and weight each sample equivalently, so they can be used to cross-check each other. As an example, The mulplots and minirun average plots for CREX  $^{48}\text{Ca}$  are shown below in Fig. 4.6 and Fig. 4.7.

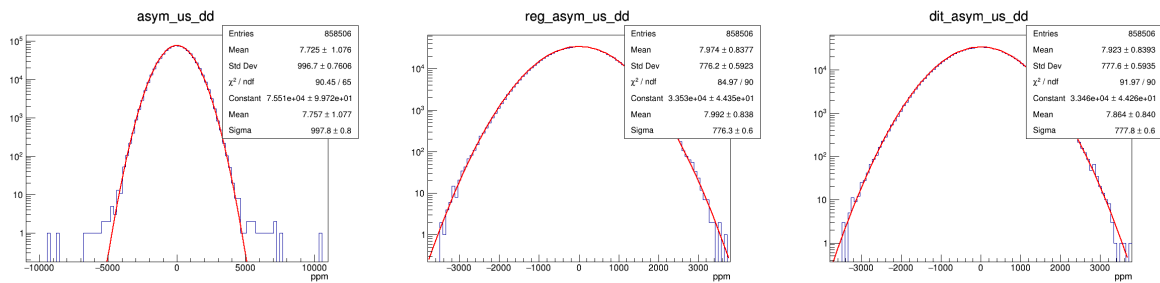


Figure 4.6: Mulplots for CREX  $^{48}\text{Ca}$ . The red line is a Gaussian fit. One can clearly see how the false asymmetry correction reduces the width of the distribution (note that the first plot has a larger X-range than the other two).

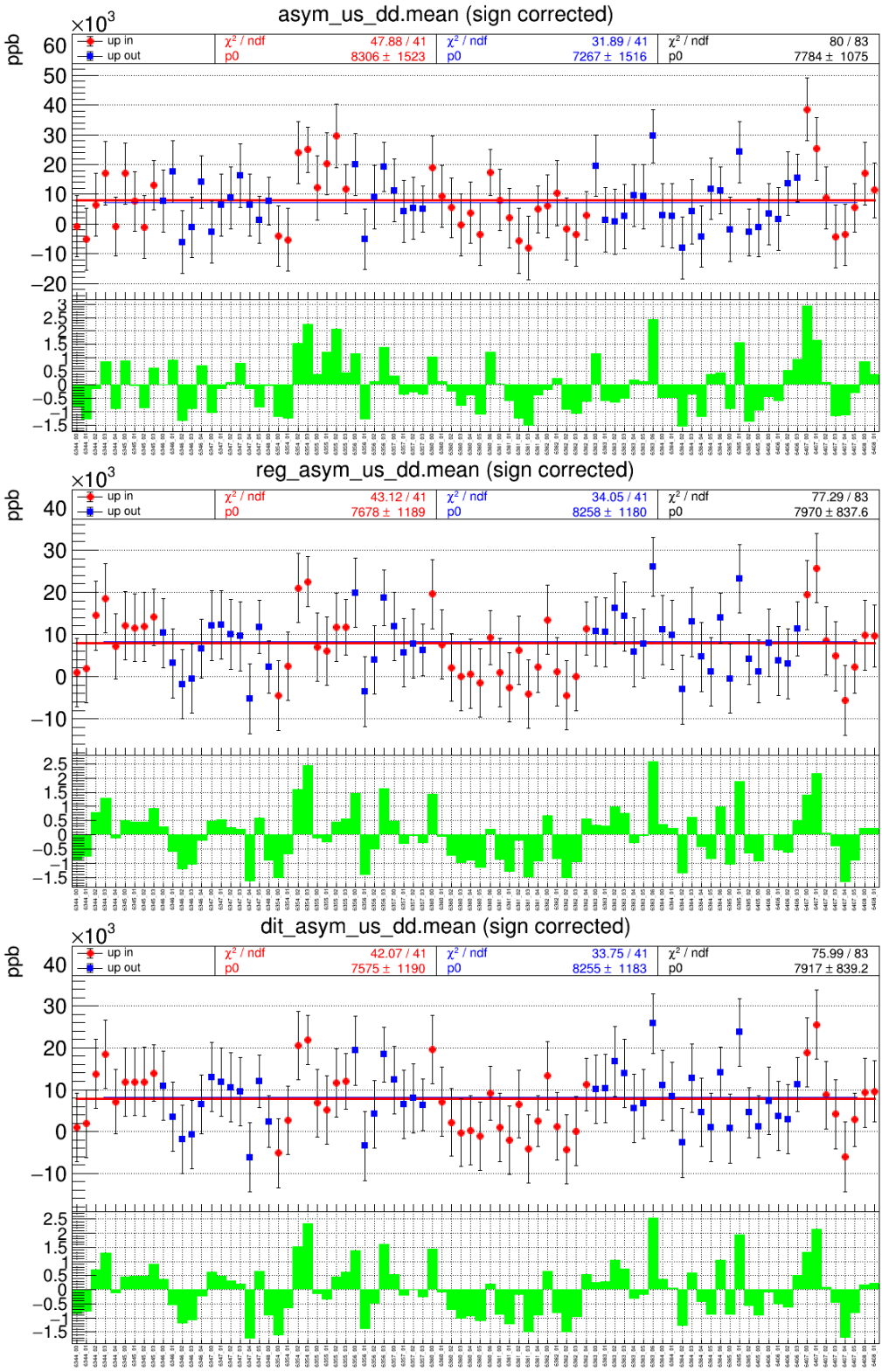


Figure 4.7: Sign-corrected minirun-wise scatter plot of the raw, regression-corrected and dithering-corrected transverse asymmetry of  $^{48}\text{Ca}$  in CREX. Different colors represent different IHWP states (in/out). In each plot, the top pad shows the mean and error of the title variable for each minirun, the three fit lines indicate the zero order polynomial fit to IHWP=in, IHWP=out and all data points respectively; the bottom pad is the pull histogram, which is the ratio of the deviation of each data point from the mean value of all data points divided by the corresponding data point's error.

The minirun mean values and mulplot mean values for each target are summarized in the following tables.

Target	Minirun Average (ppb)			Mulplot (ppb)		
	raw	reg	dit	raw	reg	dit
IHWP IN						
$^{12}\text{C}$	$4205.3 \pm 1113.7$	$5173.9 \pm 501.5$	$5169.4 \pm 502.2$	$4129.8 \pm 1117.7$	$5105.0 \pm 504.9$	$5103.5 \pm 505.6$
$^{40}\text{Ca}$	$3055.8 \pm 1762.8$	$5507.5 \pm 419.3$	$5517.4 \pm 420.7$	$2979.8 \pm 1763.3$	$5501.8 \pm 420.0$	$5511.7 \pm 421.4$
$^{208}\text{Pb}$	$-266.2 \pm 974.3$	$54.9 \pm 183.5$	$27.6 \pm 185.7$	$-381.0 \pm 975.2$	$56.0 \pm 183.5$	$22.4 \pm 185.8$
IHWP OUT						
$^{12}\text{C}$	$6111.0 \pm 992.8$	$5685.5 \pm 437.4$	$5740.6 \pm 437.9$	$6055.9 \pm 995.8$	$5619.1 \pm 440.1$	$5669.4 \pm 440.6$
$^{40}\text{Ca}$	$5707.3 \pm 1687.7$	$5069.0 \pm 397.0$	$5093.7 \pm 399.7$	$5775.6 \pm 1687.8$	$5033.6 \pm 396.7$	$5033.6 \pm 399.2$
$^{208}\text{Pb}$	$-132.7 \pm 927.4$	$-52.3 \pm 176.1$	$-26.1 \pm 178.7$	data cannot be reproduced due to lost of run 4112		
COMBINED						
$^{12}\text{C}$	$5267.8 \pm 740.8$	$5464.5 \pm 329.6$	$5493.9 \pm 330.0$	$5209.7 \pm 743.5$	$5393.2 \pm 331.8$	$5427.0 \pm 332.2$
$^{40}\text{Ca}$	$4439.2 \pm 1219.1$	$5276.3 \pm 288.3$	$5294.7 \pm 289.8$	$4444.9 \pm 1219.7$	$5275.3 \pm 288.5$	$5293.9 \pm 290.0$
$^{208}\text{Pb}$	$-196.2 \pm 671.8$	$-0.9 \pm 127.0$	$-0.3 \pm 128.8$	data cannot be reproduced due to lost of run 4112		

Table 4.5: PREX-II raw and corrected transverse asymmetry

Target	Minirun Average (ppb)			Mulplot (ppb)		
	raw	reg	dit	raw	reg	dit
IHWP IN						
$^{12}\text{C}$	$6815.5 \pm 1397.2$	$7767.7 \pm 1182.2$	$7660.5 \pm 1183.4$	$6885.1 \pm 1397.9$	$7725.7 \pm 1182.1$	$7618.8 \pm 1183.3$
$^{40}\text{Ca}$	$8661.9 \pm 1643.5$	$8777.5 \pm 1265.2$	$8764.4 \pm 1267.5$	$8581.7 \pm 1645.3$	$8743.9 \pm 1265.3$	$8733.3 \pm 1267.6$
$^{48}\text{Ca}$	$8306.5 \pm 1523.3$	$7677.5 \pm 1188.9$	$7575.2 \pm 1190.3$	$8275.7 \pm 1524.9$	$7658.9 \pm 1189.0$	$7553.5 \pm 1190.3$
$^{208}\text{Pb}$	$2742.6 \pm 2469.1$	$3052.4 \pm 2285.9$	$3079.7 \pm 2288.1$	$2771.1 \pm 2469.6$	$3101.8 \pm 2286.2$	$3129.9 \pm 2288.3$
IHWP OUT						
$^{12}\text{C}$	$8607.9 \pm 1558.2$	$8789.1 \pm 1313.5$	$8791.5 \pm 1314.6$	$8512.9 \pm 1558.8$	$8778.2 \pm 1313.6$	$8780.0 \pm 1314.7$
$^{40}\text{Ca}$	$8023.6 \pm 1751.5$	$7967.4 \pm 1353.3$	$7994.2 \pm 1355.0$	$8168.4 \pm 1755.1$	$7960.2 \pm 1353.4$	$7987.0 \pm 1355.2$
$^{48}\text{Ca}$	$7267.1 \pm 1516.3$	$8257.8 \pm 1180.2$	$8254.7 \pm 1183.3$	$7184.5 \pm 1517.6$	$8267.8 \pm 1180.3$	$8270.3 \pm 1183.5$
$^{208}\text{Pb}$	$2089.1 \pm 2456.4$	$2420.2 \pm 2263.4$	$2456.9 \pm 2266.2$	$2075.1 \pm 2456.8$	$2401.2 \pm 2263.8$	$2440.7 \pm 2266.6$
COMBINED						
$^{12}\text{C}$	$7614.4 \pm 1040.3$	$8224.8 \pm 878.7$	$8166.8 \pm 879.5$	$7600.8 \pm 1040.8$	$8235.1 \pm 878.8$	$8177.3 \pm 879.6$
$^{48}\text{Ca}$	$8363.1 \pm 1198.5$	$8399.7 \pm 924.2$	$8405.0 \pm 925.6$	$8377.3 \pm 1200.4$	$8383.5 \pm 924.3$	$8390.4 \pm 925.7$
$^{48}\text{Ca}$	$7784.4 \pm 1074.7$	$7969.8 \pm 837.6$	$7916.9 \pm 839.2$	$7725.4 \pm 1075.7$	$7974.4 \pm 837.7$	$7923.5 \pm 839.3$
$^{208}\text{Pb}$	$2414.2 \pm 1741.4$	$2733.1 \pm 1608.4$	$2765.3 \pm 1610.1$	$2422.6 \pm 1741.7$	$2751.0 \pm 1608.6$	$2784.8 \pm 1610.4$

Table 4.6: CREX raw and corrected transverse asymmetry

As shown in the above tables, the final results from the two false asymmetry correction methods – regression and dithering, agree with each other. We chose the dithering corrected values to extract the transverse asymmetry. The slug-wise plots of the transverse asymmetry are shown in Fig. 4.8

### 4.3.2 Systematic Uncertainties

Various corrections applied to the raw asymmetry introduce associated uncertainties. Such as the beam false asymmetry correction, purity and detector/monitor non-linearity correction. These uncertainties have an impact on the precision of our measurement, and it is crucial to have accurate knowledge of these uncertainties.

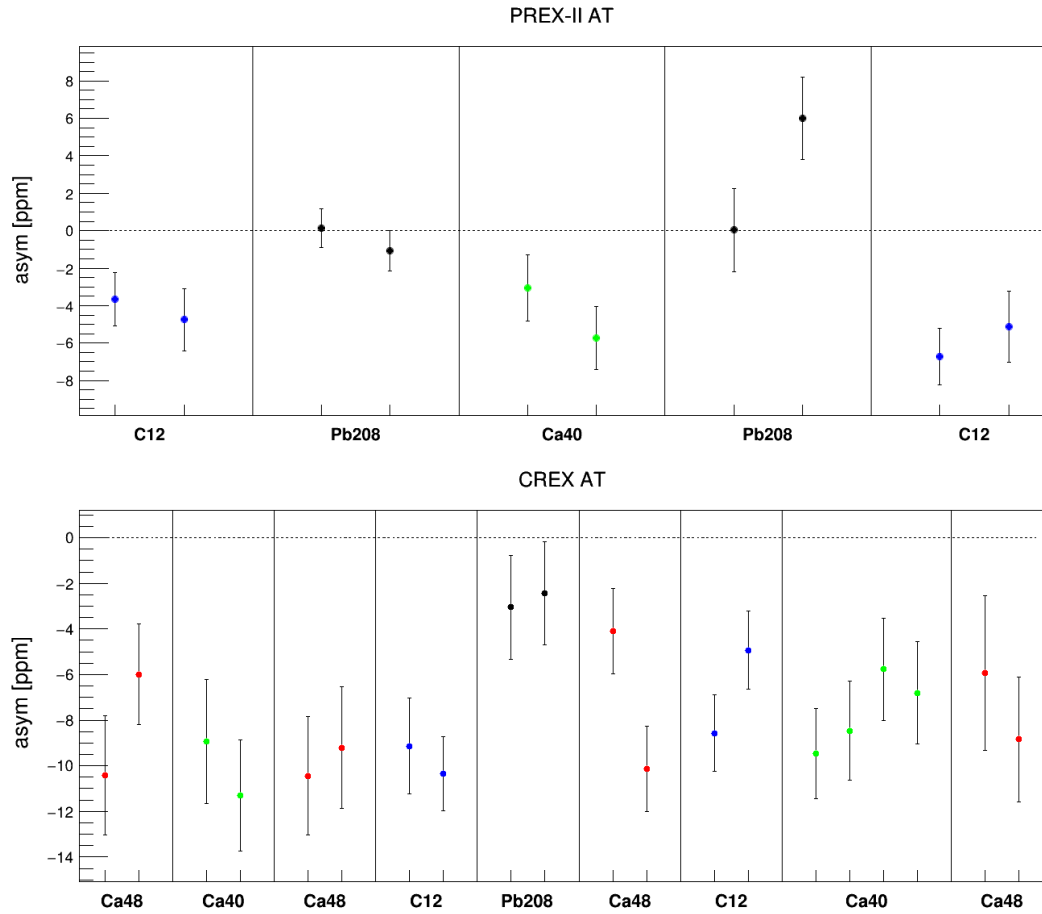


Figure 4.8: Sign-corrected transverse asymmetry in chronological order. Each datapoint represents one slug.

### Beam Correction

To quantify the uncertainty arising from the beam correction, we compare the corrections obtained using the regression and dithering methods. Specifically, we observe that for the majority of runs, the difference between the corrections derived from the most significant BPMis using these two methods is below 5%. Consequently, we conservatively estimate the systematic uncertainty of the beam false asymmetry correction as 5% of the correction obtained with the dithering method.

The correction from each BPM (or their combinations) is calculated as the product of the target-wise dithering slope and the average difference for each BPM (or their combinations). The uncertainty is obtained by taking the RMS of 5% of these individual corrections. The results are presented in Table 4.7.

Exp	Target	$\mathcal{A}_{\text{raw}} \pm d\mathcal{A}_{\text{raw}}$ (ppb)		$\mathcal{A}_{\text{dit}} \pm d\mathcal{A}_{\text{dit}}$ (ppb)		$\Delta\mathcal{A} \pm d(\Delta\mathcal{A})$ (ppb)		$d\Delta\mathcal{A}/d\mathcal{A}_{\text{dit}}$
PREX-II	$^{12}\text{C}$	-5268	741	-5494	330	226.1	29.4	9%
	$^{40}\text{Ca}$	-4439	1219	-5295	290	195.9	42.4	15%
	$^{208}\text{Pb}$	196.2	672	0.257	129	855.5	71.0	55%
CREX	$^{12}\text{C}$	-7614	1040	-8167	880	552.4	37.8	4%
	$^{40}\text{Ca}$	-8363	1198	-8405	926	351.1	48.9	5.3%
	$^{48}\text{Ca}$	-7784	1075	-7917	839	41.9	86.7	10%
	$^{208}\text{Pb}$	-2414	1741	-2765	1610	132.5	27.8	2%

Table 4.7: Beam correction to transverse asymmetry.

### Purity Correction

For the target purity correction, we need to consider only the  $^{208}\text{Pb}$  and  $^{48}\text{Ca}$  targets. As will be discussed in the following chapter, the contamination in the  $^{208}\text{Pb}$  target arises from the diamond foils sandwiching the  $^{208}\text{Pb}$  foil to cool the target. On the other hand, the main impurity in  $^{48}\text{Ca}$  target is the  $^{40}\text{Ca}$  isotope. The  $^{40}\text{Ca}$  target has an abundance larger than 99.6%, so it was regarded as a pure target.

$$\begin{aligned} \mathcal{A}_{\text{mea}} &= \frac{R_t \mathcal{A}_t + \sum_i R_i \mathcal{A}_i}{R_t + \sum_i R_i} = \frac{\mathcal{A}_t + \sum_i f_i \mathcal{A}_i}{1 + \sum_i f_i} \\ \mathcal{A}_t &= (1 + \sum_i f_i) \mathcal{A}_{\text{mea}} - \sum_i f_i \mathcal{A}_i \end{aligned} \quad (4.38)$$

where  $R$  and  $\mathcal{A}$  are the scattering rate and the transverse asymmetry for each target nucleus. The subscript  $t$  and  $i$  refer to the target and various impurity elements present in the target, respectively.  $f_i = \frac{R_i}{R_t}$  is the rate fraction. We used simulations to calculate the scattering rate for each different target and the asymmetry values came from measurements directly. The diamond (C) rate fraction in the  $^{208}\text{Pb}$  target is:

$$f_C = \frac{R_C}{R_{Pb}} = \begin{cases} 0.0671 \pm 0.0057 & E = 0.95 \text{ GeV} \\ 0.6089 \pm 0.0609 & E = 2.2 \text{ GeV} \end{cases} \quad (4.39)$$

The  $^{48}\text{Ca}$  case is a little complicated, because the  $^{48}\text{Ca}$  target is a stack of 3 different pieces with varying purities. The upstream two pieces are the remnants of the old target with a  $^{48}\text{Ca}$  abundance of 95.99%, while the downstream piece is a new foil with a  $^{48}\text{Ca}$  abundance of 90.04%.

Considering that the contamination primarily arises from different isotopes of  $^{48}\text{Ca}$ , namely  $^{40}\text{Ca}$  ( $\sim 10\%$ ),  $^{42}\text{Ca}$  ( $\sim 0.1\%$ ) and  $^{44}\text{Ca}$  ( $\sim 0.2\%$ ), whose scattering rates and asymmetries are similar to that of  $^{48}\text{Ca}$ , so we simply count the non- $^{48}\text{Ca}$  fraction in the  $^{48}\text{Ca}$  target, which leads to:

$$f\left(\frac{\text{non-}^{48}\text{Ca}}{^{48}\text{Ca}}\right) = 9.07 \pm 0.18\% \quad (4.40)$$

Exp	Target	$\mathcal{A}_{\text{cor}} \pm d\mathcal{A}_{\text{stat}}$ (ppb)
PREX-II	$^{12}\text{C}$	-5494 330
	$^{48}\text{Ca}$	-5295 290
	$^{208}\text{Pb}$	369 137
CREX	$^{12}\text{C}$	-8167 880
	$^{40}\text{Ca}$	-8405 926
	$^{48}\text{Ca}$	-7873 919
	$^{208}\text{Pb}$	523 2646

Table 4.8: Purity-corrected transverse asymmetry. The statistical uncertainties are calculated following the uncertainty propagation equation.

Using equation 4.38, the asymmetry after the purity correction is shown in Table 4.8

## Detector Non-linearity

For the uncertainty caused by the non-linearity in the detector's response to the incoming electron flux, it is constrained to be  $< 0.5\%$  based on bench tests.

Exp	Target	$\mathcal{A}_{\text{raw}}$ (ppb)	$d\mathcal{A}_{\text{sys}}$ (ppb)	$\frac{d\mathcal{A}_{\text{sys}}}{\mathcal{A}_{\text{raw}}}$
PREX-II	$^{12}\text{C}$	-5268	26	0.50%
	$^{40}\text{Ca}$	-4439	22	0.50%
	$^{208}\text{Pb}$	196.2	1	0.50%
CREX	$^{12}\text{C}$	-7614	38	0.50%
	$^{40}\text{Ca}$	-8363	42	0.50%
	$^{48}\text{Ca}$	-7784	39	0.50%
	$^{208}\text{Pb}$	-2414	12	0.50%

Table 4.9: Systematic uncertainty due to the detector non-linearity.

For uncertainty come from the BCM non-linearity, a conservative estimate of 1% was used, as shown in Table 4.10, the charge asymmetry is the minirun-wise average value.

Exp	Target	$\mathcal{A}_q$ (ppb)	$d\mathcal{A}_q$ (ppb)	$\frac{d\mathcal{A}_q}{\mathcal{A}_q}$
PREX-II	$^{12}\text{C}$	-52.863	0.5	1.00%
	$^{40}\text{Ca}$	-104.763	1.0	1.00%
	$^{208}\text{Pb}$	140.602	1.4	1.00%
CREX	$^{12}\text{C}$	50.09	0.5	1.00%
	$^{40}\text{Ca}$	47.81	0.5	1.00%
	$^{48}\text{Ca}$	27.35	0.3	1.00%
	$^{208}\text{Pb}$	-1.61	0.0	1.00%

Table 4.10: Systematic uncertainty due to the BCM non-linearity

### 4.3.3 Dynamics

#### $\phi$ Angle

It is said above that we aimed to choose the angle  $\phi$  to be exactly  $90^\circ$ . However, it is practically impossible. The actually value typically deviates slightly from the designed value, as determined from the data. By drawing the  $\sin \phi$  distribution from data and calculate the average from the distribution, the measured value of  $\sin \phi$  is determined, which is shown in the following table.

Exp	Target	LHRS $\sin \phi$	RHRS $\sin \phi$	average
PREX-II	$^{12}\text{C}$	0.96660	0.96700	0.9668
	$^{40}\text{Ca}$	0.96430	0.96440	0.9644
	$^{208}\text{Pb}$	0.96625	0.96665	0.9665
CREX	$^{12}\text{C}$	0.96950	0.96790	0.9687
	$^{40}\text{Ca}$	0.97090	0.96920	0.9701
	$^{48}\text{Ca}$	0.97110	0.96880	0.9700
	$^{208}\text{Pb}$	0.96980	0.96830	0.9691

Table 4.11: Average  $\sin \phi$  values for different AT targets.

#### $Q^2$

Similar to the extraction of the  $\phi$  angle, we drew the  $Q^2$  distribution for each target, and then took the mean value. The results are shown in the following table.

Exp	Target	LHRS $Q^2$ (GeV $^2$ )	RHRS $Q^2$ (GeV $^2$ )	Average $Q^2$ (GeV $^2$ )	Average $Q$ (GeV)
PREX-II	$^{12}\text{C}$	$0.0068 \pm 4\text{E-}6$	$0.0066 \pm 5\text{E-}6$	$0.00671 \pm 3.21\text{E-}6$	$0.082 \pm 1.96\text{E-}5$
	$^{40}\text{Ca}$	$0.0068 \pm 5\text{E-}6$	$0.0067 \pm 6\text{E-}6$	$0.00673 \pm 4.17\text{E-}6$	$0.082 \pm 2.54\text{E-}5$
	$^{208}\text{Pb}$ 8	$0.0065 \pm 5\text{E-}6$	$0.0063 \pm 6\text{E-}6$	$0.00640 \pm 4.06\text{E-}6$	$0.080 \pm 2.54\text{E-}5$
	$^{208}\text{Pb}$ 9	$0.0065 \pm 4\text{E-}6$	$0.0063 \pm 5\text{E-}6$	$0.00640 \pm 3.50\text{E-}6$	$0.080 \pm 2.18\text{E-}5$
CREX	$^{12}\text{C}$	$0.0328 \pm 2\text{E-}5$	$0.0334 \pm 2\text{E-}5$	$0.0331 \pm 1.31\text{E-}5$	$0.182 \pm 3.61\text{E-}5$
	$^{40}\text{Ca}$	$0.0306 \pm 2\text{E-}5$	$0.0309 \pm 2\text{E-}5$	$0.0308 \pm 1.22\text{E-}5$	$0.175 \pm 3.48\text{E-}5$
	$^{48}\text{Ca}$	$0.0304 \pm 1\text{E-}5$	$0.0307 \pm 2\text{E-}5$	$0.0306 \pm 1.07\text{E-}5$	$0.175 \pm 3.05\text{E-}5$
	$^{208}\text{Pb}$	$0.0319 \pm 3\text{E-}5$	$0.0322 \pm 3\text{E-}5$	$0.0320 \pm 1.99\text{E-}5$	$0.179 \pm 5.56\text{E-}5$

Table 4.12: Average  $Q^2$  values for different AT targets.

### 4.3.4 Final Result

With Eq. 4.36, the transverse asymmetry is calculated to be:

$$\mathcal{A}_n = \frac{\mathcal{A}_{\text{cor}}}{\mathcal{P}_n \cdot \sin \phi} \quad (4.41)$$

The statistical uncertainty is:

$$d\mathcal{A}_n(\text{stat}) = \frac{d\mathcal{A}_{\text{cor}}(\text{stat})}{\mathcal{P}_n \cdot \sin \phi} \quad (4.42)$$

and the systematic uncertainty is:

$$\left( \frac{d\mathcal{A}_n(\text{sys})}{\mathcal{A}_n} \right)^2 = \left( \frac{d\mathcal{A}_{\text{cor}}(\text{sys})}{d\mathcal{A}_{\text{cor}}} \right)^2 + \left( \frac{d\mathcal{P}_n}{\mathcal{P}_n} \right)^2 \quad (4.43)$$

where

$$d\mathcal{A}_{\text{cor}}^2(\text{sys}) = d\mathcal{A}^2(\text{det nonlin}) + d\mathcal{A}^2(\text{BCM nonlin}) + d\mathcal{A}^2(\text{beam correction}) \quad (4.44)$$

For the  $^{208}\text{Pb}$  and  $^{48}\text{Ca}$  targets, we need to include uncertainties from contaminations. Various systematic uncertainties are summarized in Table 4.13.

Exp Target	PREX-II			CREX			
	$^{12}\text{C}$	$^{40}\text{Ca}$	$^{208}\text{Pb}$	$^{12}\text{C}$	$^{40}\text{Ca}$	$^{48}\text{Ca}$	$^{208}\text{Pb}$
Beam correction	0.03	0.05	0.08	0.04	0.06	0.10	0.03
Polarization	0.06	0.05	< 0.01	0.08	0.08	0.08	< 0.01
Non-linearity	0.03	0.03	< 0.01	0.05	0.05	0.05	0.01
Tgt. impurity	< 0.01	< 0.01	0.04	< 0.01	< 0.01	0.10	0.80
Inelastic	< 0.01	< 0.01	< 0.01	0.08	0.15	0.08	< 0.01
Tot. Syst	0.07	0.08	0.09	0.13	0.18	0.19	0.75
Statistical	0.38	0.34	0.16	1.05	1.10	1.09	3.15
Total	0.39	0.34	0.18	1.05	1.11	1.11	3.23

Table 4.13: AT uncertainty contributions in units of ppm

The final result is shown in Table 4.14:

Exp	Target	$\mathcal{A}_n$ (ppm)	$d\mathcal{A}_{\text{stat}}$ (ppm)	$d\mathcal{A}_{\text{sys}}$ (ppm)	$d\mathcal{A}_{\text{stat+sys}}$ (ppm)
PREX-II	$^{12}\text{C}$	-6.34	0.38	0.07	0.39
	$^{40}\text{Ca}$	-6.12	0.34	0.08	0.34
	$^{208}\text{Pb}$	0.43	0.16	0.09	0.18
CREX	$^{12}\text{C}$	-9.71	1.05	0.10	1.05
	$^{40}\text{Ca}$	-9.98	1.10	0.11	1.11
	$^{48}\text{Ca}$	-9.35	1.09	0.17	1.11
	$^{208}\text{Pb}$	0.62	3.15	0.75	3.23

Table 4.14: Final result of the transverse asymmetry.

Upon comparing the experimental results to theoretical calculations [77], we confirm the anomaly presented in PREX-I AT measurement. Specifically, the transverse asymmetries for  $^{208}\text{Pb}$  are consistently 0 at various  $Q$  values, as shown in Fig. 4.9. On the

other hand, the transverse asymmetries for other light nuclei are relatively close to their corresponding theoretical predictions.

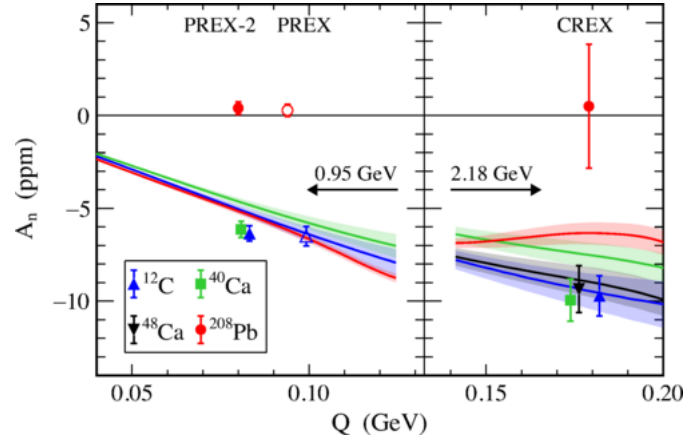


Figure 4.9: Transverse asymmetries measured in PREX-II/CREX [78]. The PREX-I result is also included. Overlapping points are offset slightly in  $Q$  to distinguish them.

# Chapter 5

## Systematic Uncertainties

The control of systematic uncertainty is a highlight of these two high-precision experiments. To minimize systematic uncertainty, a combination of fast and slow helicity reversals was utilized. This approach effectively mitigated many systematic uncertainties introduced by the accelerator affecting the beam. In addition to machine-related uncertainties, the detection process, particularly the acceptance function, constitutes another significant source of systematic uncertainty.

After eliminating the false asymmetry from the beam, the next step involves correcting the background asymmetry, namely, the target contamination and inelastic scattering, as shown in Eq. 5.1.

$$\mathcal{A}_{\text{PV}} = \frac{\mathcal{A}_{\text{cor}}/\mathcal{P} - \sum_i \mathcal{A}_i f_i}{1 - \sum_i f_i} \quad (5.1)$$

Here,  $i$  iterates through the background processes,  $\mathcal{A}_i$  and  $f_i$  refer to the asymmetry and rate fraction, respectively, associated with each specific background process. The rate fraction is defined as:

$$f_i = \frac{R_i}{\sum_i R_i + R_{Pb208}} \quad (5.2)$$

with  $R$  being the scattering rate. In PREX-II, contamination from the diamond foils contributes the largest background correction.

Following the uncertainty propagation formula, the systematic uncertainty of  $\mathcal{A}_{\text{PV}}$  determined to be:

$$(\delta \mathcal{A}_{\text{PV}})^2 = \left( \frac{\partial \mathcal{A}_{\text{PV}}}{\partial \mathcal{A}_{\text{cor}}} \delta \mathcal{A}_{\text{cor}} \right)^2 + \left( \frac{\partial \mathcal{A}_{\text{PV}}}{\partial \mathcal{P}} \delta \mathcal{P} \right)^2 + \sum_i \left[ \left( \frac{\partial \mathcal{A}_{\text{PV}}}{\partial \mathcal{A}_i} \delta \mathcal{A}_i \right)^2 + \left( \frac{\partial \mathcal{A}_{\text{PV}}}{\partial f_i} \delta f_i \right)^2 \right] \quad (5.3)$$

with

$$\frac{\partial \mathcal{A}_{\text{PV}}}{\partial \mathcal{A}_j} = -\frac{f_j}{1 - \sum_i f_i} \quad \frac{\partial \mathcal{A}_{\text{PV}}}{\partial f_j} = \frac{\mathcal{A}_{\text{PV}} - \mathcal{A}_j}{1 - \sum_i f_i} \quad (5.4)$$

## 5.1 $Q^2$ and $\theta$

Physical interpretation of  $\mathcal{A}_{\text{PV}}$  requires accurate knowledge of the scattering angle and the corresponding  $Q^2$ . These quantities are determined using a watercell target. As

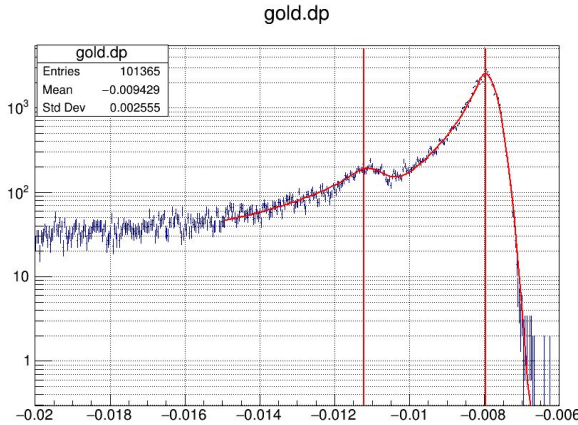


Figure 5.1: Momentum distribution from an optics run with the watercell target. The X-axis is the relative energy difference:  $dp = \frac{p-p_0}{p_0}$ . The two peaks result from  $^1\text{H}$  (left) and  $^{16}\text{O}$  (right), respectively. Plot from Siyu.

shown in Eq. 1.94, the energy difference between the two elastic peaks of  $^1\text{H}$  and  $^{16}\text{O}$  is:

$$\Delta E' = E'_O - E'_H = E \left( \frac{1}{1 + \frac{E(1-\cos\theta)}{M_O}} - \frac{1}{1 + \frac{E(1-\cos\theta)}{M_H}} \right) \quad (5.5)$$

By reconstructing the momentum distribution from the watercell target, as illustrated in Fig. 5.1, the peak energy difference, and therefore, the scattering angle can be extracted. Compared to the production target, the watercell target offers a notable advantage. It mitigates several uncertainties associated with electron detection and trajectory reconstruction by canceling out the energy difference between the two elastic peaks. As a result, the measurements obtained with the watercell target are more precise.

## 5.2 Carbon Contamination in PREX-II

As discussed in Chapter 2, the low thermal conductivity of the  $^{208}\text{Pb}$  foil imposes a limitation on the maximum beam current that can be applied. A pure  $^{208}\text{Pb}$  foil, for example, would melt at  $\sim 10 \mu\text{A}$ . However, by incorporating surrounding diamond foils, the  $^{208}\text{Pb}$  target's capacity can be increased to withstand currents of around  $100 \mu\text{A}$  or higher. Additionally,  $^{12}\text{C}$ , being an isoscalar and spin-0 nucleus, possesses a well-measured PV asymmetry. Therefore, the background associated with  $^{12}\text{C}$  is well understood, providing further advantages in experimental analysis.

In terms of the  $^{48}\text{Ca}$  target in CREX, without the need of auxiliary materials, the main

source of contamination arises from  $^{40}\text{Ca}$ , which is also an isoscalar and spin-0 nucleus, so the background is benign.

## Target Thickness

The  $^{208}\text{Pb}$  foil is  $\sim 0.55$  mm thick, the upstream and downstream diamond foils have thicknesses of half the  $^{208}\text{Pb}$  foil, as shown in Table 5.1. These values were measured in different ways.

The thickness of the diamond foil is measured directly using calipers with an accuracy of 0.0005 in (0.0127 mm), and the average thickness is determined to be 0.255 mm. The variations in thickness from one foil to another are found to be smaller than 5%, with the largest observed variation being 3.6%. Based on these findings, an estimated relative error of 5% is considered reasonable. The measured values are presented in Table 5.1.

As for the  $^{208}\text{Pb}$  foil, its thickness (area density) was inferred from its mass ( $m$ ) and area ( $A$ ):

$$\rho t = \frac{m}{A} \quad (5.6)$$

where  $\rho$  and  $t$  being the density and thickness, respectively. The area is calculated from measurements taken at the four corners, resulting in an average thickness value for the entire foil. However, since the raster area does not cover the entire foil, this introduces some uncertainty in the measurement. Additionally, small irregularities at the edges or corners of the foil contribute to measurement errors.

Considering these factors, along with the variations in thickness observed from foil to foil (with the largest variation being 3.8%), a conservative estimate of 5% is employed as the relative uncertainty for the thickness of the  $^{208}\text{Pb}$  foil.

## Simulation

In the simulation, the  $^{208}\text{Pb}$  foil thickness is set to 0.552 mm (628.176 mg/cm $^2$ ), the upstream diamond foil 0.2554 mm (89.9008 mg/cm $^2$ ) and the downstream diamond foil 0.2556 mm (89.9712 mg/cm $^2$ ). The central point angle being  $4.74^\circ$ , and the raster size is 6 mm  $\times$  4 mm. Only simple cuts are applied to the simulation, as shown in the following code snippet.

```
xcol != -333 && xvdc != -333 // collimator and vdc see the track
&& CollimatorL(xcol, ycol) // Q1 collimator geometry cut
&& (nuclA == 12 || nuclA == 208) // select only C or Pb208
&& Pz_peak- Pz < pcut // radiative tail cut; cut only on lower side
```

where  $\text{Pz}$  is the post target electron momentum and  $\text{Pz\_peak}$  (948.97 MeV) is the momentum peak without the momentum cut; other cuts are explained in the code block.

position	target	Upstream (mg/cm <sup>2</sup> )	Center (mg/cm <sup>2</sup> )	Downstream (mg/cm <sup>2</sup> )	runs
1	C-Pb-C	88	556	88	
2	D#I-Pb-D#J	90	557	90	
3	C-208Pb#1-C	88	620	88	
4	Carbon 1%		445		
5	<b>D#A-208Pb#2-D#B</b>	89.0	632	88.6	3134-3636
6	D#C-208Pb#3-D#D	88.2	626	90.7	
7	D#E-208Pb#4-D#F	89.6	628	91.9	
8	<b>D#G-208Pb#5-D#20</b>	86.8	632	90	4372-4607
9	<b>D#1-208Pb#6-D#2</b>	90	618	90	4865-4980
10	<b>D#3-208Pb#7-D#4</b>	90	639	90	4608-4864
11	<b>D#5-208Pb#8-D#6</b>	90	620	90	4147-4370
12	<b>D#7-208Pb#9-D#8</b>	90	615	90	3822-4146
13	<b>D#9-208Pb#10-D#10</b>	90	623	90	3644-3821
14	C-Hole		N/A		
15	<sup>48</sup> Ca		1016		
16	<sup>40</sup> Ca		1004		

Table 5.1: Mass thickness of each target in the production ladder. Name convention: upstream material#label - central material#label - downstream material#label. Pb208 foils count from 1 to 10, diamond foils count 1-10, A-G, I, J, 20. The first two Pb targets are natural Pb foils, not the pure  $^{208}\text{Pb}$  isotope foil. The third Pb target is sandwiched by graphite, not diamond. Boldface indicates the targets used in PREX-II and CREX. To convert the mass thickness into the real thickness, use the density of  $\rho_D = 3.52 \text{ g/cm}^3$  and  $\rho_{\text{Pb}208} = 11.38 \text{ g/cm}^3$ .

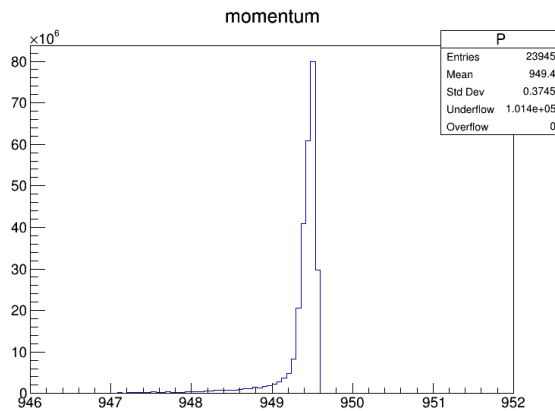


Figure 5.2: Post target electron momentum distribution. The lower end tail comes from multi-scattering and radiation.

With these cuts, we can count the scattering rate from  $^{12}\text{C}$  and  $^{208}\text{Pb}$  directly and

calculate the ratio between them, which is:

$$\frac{R_C}{R_{Pb}} = 6.71\% \quad f_C = \frac{R_C}{R_C + R_{Pb}} = 6.29\% \quad (5.7)$$

To investigate the systematic uncertainty, we varied the thickness of the  $^{208}\text{Pb}$  and diamond foils (both upstream and downstream) by 5% from their nominal values. Additionally, we applied different momentum cuts within the range of 1.8 to 2.6 MeV. The result is presented in Table 5.2 and 5.3.

$^{208}\text{Pb}$ thickness variation	C thickness variation	p cut (MeV)	C rate (MHz)	$^{208}\text{Pb}$ rate (MHz)	$\frac{R_C}{R_{Pb}}\text{ (%)}$	$f_c = \frac{R_C}{R_C + R_{Pb}}\text{ (%)}$
-5%	-5%	2.2	1.26E+2	1.88E+3	6.72	6.30
-5%	0%		1.34E+2	1.90E+3	7.05	6.59
-5%	5%		1.38E+2	1.90E+3	7.23	6.75
0%	-5%		1.22E+2	1.90E+3	6.43	6.04
<b>0%</b>	<b>0%</b>		<b>1.29E+2</b>	<b>1.93E+3</b>	<b>6.71</b>	<b>6.29</b>
0%	5%		1.35E+2	1.89E+3	7.11	6.64
5%	-5%		1.16E+2	1.95E+3	5.94	5.61
5%	0%		1.22E+2	1.94E+3	6.31	5.93
5%	5%		1.28E+2	1.91E+3	6.72	6.30

Table 5.2: Scattering rate from  $^{208}\text{Pb}$  and diamond foils with different foil thicknesses.

$^{208}\text{Pb}$ thickness variation	C thickness variation	p cut (MeV)	C rate (MHz)	$^{208}\text{Pb}$ rate (MHz)	$\frac{R_C}{R_{Pb}}\text{ (%)}$	$f_c\text{ (%)}$
0%	0%	1.80	1.24E+2	1.86E+3	6.68	6.26
		1.90	1.25E+2	1.87E+3	6.69	6.27
		2.00	1.27E+2	1.89E+3	6.70	6.28
		2.05	1.27E+2	1.90E+3	6.70	6.28
		2.10	1.28E+2	1.91E+3	6.71	6.28
		2.15	1.29E+2	1.92E+3	6.71	6.29
		<b>2.20</b>	<b>1.29E+2</b>	<b>1.93E+3</b>	<b>6.71</b>	<b>6.29</b>
		2.25	1.30E+2	1.94E+3	6.72	6.30
		2.30	1.31E+2	1.95E+3	6.73	6.30
		2.35	1.31E+2	1.95E+3	6.73	6.31
		2.40	1.32E+2	1.96E+3	6.74	6.32
		2.60	1.34E+2	1.99E+3	6.74	6.32

Table 5.3: Scattering rate from  $^{208}\text{Pb}$  and diamond foils with different momentum cuts.

The uncertainty for each variation is taken to be the absolute difference from the nominal value, as shown below:

variation	maximum	diff in $f_C$	minimum	diff in $f_C$
Pb	(-5, 0) - (0, 0)	2.98E-3	(+5, 0) - (0, 0)	-3.55E-3
C	(0, +5) - (0, 0)	3.53E-3	(0, -5) - (0, 0)	-2.49E-3
pcut	(2.6) - (2.2)	2.93E-4	(1.8) - (2.2)	-2.88E-4
total		4.63E-3		4.35E-3

Table 5.4: The maximum and minimum difference for each variation. (n1, n2) represents the configuration of the target foils thicknesses. n1 for the Pb foil and n2 for the C foil.

Based on Table 5.4, a conservative error value (the larger one) is used , which gives out the final value of  $f_C$

$$f_C = 0.0629 \pm 0.005 \quad (5.8)$$

The reliability of the simulation can be evaluated by comparing its result with the available optics data.

target thickness	p cut	(MeV)	post target $Q^2$ (GeV $^2$ )				Asym (ppm)	
			Pb	C	C (US)	C (DS)	Pb	C
-5%	-5%	2.2	0.00625	0.00658	0.00658	0.00658	0.55774	0.53861
-5%	0%	2.2	0.00626	0.00656	0.00658	0.00654	0.55809	0.53776
-5%	5%	2.2	0.00627	0.00658	0.00658	0.00657	0.55883	0.53932
0%	-5%	2.2	0.00627	0.00657	0.00657	0.00657	0.55942	0.53917
0%	0%	2.2	0.00626	0.00658	0.00657	0.00660	0.55824	0.53936
0%	5%	2.2	0.00627	0.00658	0.00658	0.00658	0.55847	0.53847
5%	-5%	2.2	0.00625	0.00657	0.00655	0.00658	0.55674	0.53696
5%	0%	2.2	0.00627	0.00658	0.00659	0.00657	0.55782	0.53808
5%	5%	2.2	0.00629	0.00659	0.00659	0.00659	0.55847	0.53962
average			0.00626	0.00658	0.00658	0.00658	0.55820	0.53859

Table 5.5: Average post target  $Q^2$  (left arm) for various thickness configurations. As expected, the  $Q^2$  does not change with varied foil thicknesses. There are some fluctuations in the asymmetry.

Table 5.5 lists the  $Q^2$  and asymmetry obtained from the simulations. These values are then utilized to calculate the combined  $Q^2$ :

$$Q^2 = \frac{R_C Q_C^2 + R_{Pb} Q_{Pb}^2}{R_C + R_{Pb}} = \frac{6.71\% \times 0.00658 + 0.00629}{6.71\% + 1} = 0.00629 \text{ GeV}^2 \quad (5.9)$$

Comparing the simulation  $Q^2$  values with those derived from the optics data in Table 5.6, a notable agreement between the simulation and the data (left arm) is observed. This agreement suggests reliability of the simulation.

arm	$\theta$	$Q^2$ (GeV $^2$ )
Left	$4.748 \pm 0.006$	$0.00627 \pm 0.00002$
Right	$4.813 \pm 0.004$	$0.00642 \pm 0.00001$

Table 5.6: Average  $\theta$  and  $Q^2$  from the optics data.

### Cross Check of the Simulation

Another cross check involves comparing the simulation result with theoretical predictions. Theoretically, the scattering rate is proportional to the cross section and the number of atoms in a unit area.

$$R \propto \sigma \times N = \sigma \times \frac{t}{m} \quad (5.10)$$

Here,  $t$  and  $m$  are, respectively, the area density (mass thickness) and atomic mass. Therefore:

$$\frac{R_C}{R_{Pb}} = \frac{\sigma_C}{\sigma_{Pb}} \times \frac{t_c}{t_{Pb}} \times \frac{m_{Pb}}{m_C} \quad (5.11)$$

Take  $E = 0.95$  GeV and  $\theta = 4.8^\circ$  (based on Table 5.6), the cross section for e- $^{12}$ C and e- $^{208}$ Pb scatterings is numerically solved to be:

$$\sigma_C = 48.001 \text{ mbarn} \quad \sigma_{Pb} = 3386.100 \text{ mbarn} \quad (5.12)$$

The ratio of  $t_C/t_{Pb}$  is calculated as:

target	$t_C$ (US + DS) (mg/cm $^2$ )	$t_{Pb}$ (mg/cm $^2$ )	$t_C/t_{Pb}$	main detector error n	weight $1/\sqrt{n}$	weighted $t_C/t_{Pb}$
Pb208#2	177.6	632	0.281	42.743	0.1530	0.037
Pb208#10	180	623	0.289	33.3465	0.1732	0.043
Pb208#9	180	615	0.293	28.9264	0.1859	0.047
Pb208#8	180	620	0.290	33.5835	0.1726	0.043
Pb208#5	176.8	632	0.280	36.3435	0.1659	0.040
Pb208#7	180	639	0.282	32.7936	0.1746	0.042
Pb208#6	180	618	0.291	47.6238	0.1449	0.036
	179.2	625.6	0.286		1.1700	0.287

Table 5.7: Calculation of the weighted  $t_C/t_{Pb}$ , the main detector error is the uncertainty of the main detector mean value (reg\_asym\_us\_avg); the weighted ratio is calculated as  $\frac{w_j}{\sum_i w_i} \times (t_C/t_{Pb})_j$ .

As shown in Table 5.8, the theoretical value is 4.6% higher than the simulation result.

E (GeV)	$\theta$	Target	$\sigma$ (mbarn)	m	$\frac{R_C}{R_{Pb}}$ (%)	$f_C$ (%)
0.95	4.8°	$^{12}\text{C}$	48.001	12.011	7.04	6.57
		$^{208}\text{Pb}$	3386.100	207.977		

Table 5.8: Theoretical calculation of  $f_C$ .

### Contribution to $\mathcal{A}_{\text{PV}}$

As mentioned before, the asymmetry of the elastic electron-diamond scattering is well understood. The cross section and asymmetry of  $e-^{12}\text{C}$  scattering at various energies and scattering angles are numerically solved from the Dirac equation. These results are compiled and presented in a tabulated form known as “Chuck’s table”. A similar table exists for  $e-^{208}\text{Pb}$  scattering.

According to Chuck’s table, the asymmetry of  $e-^{12}\text{C}$  scattering is taken to be 539.36 ppb, as shown in Table 5.5 with the nominal  $^{208}\text{Pb}$  and nominal diamond thicknesses. The relative uncertainty is taken to be a conservative estimate of 4%.

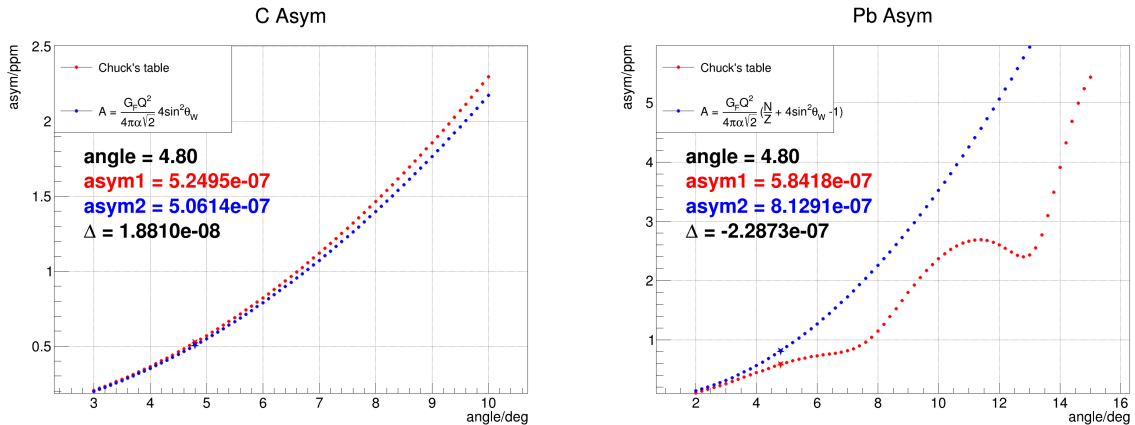


Figure 5.3: Theoretical asymmetries of the  $e-^{12}\text{C}$  and  $e-^{208}\text{Pb}$  scatterings in the experimental dynamics predicted by Chuck’s table. These values include the Coulomb correction. The Chuck’s table is cross checked by the Standard Model Born approximation calculation. The two methods yield similar values for both nuclei.

Using Eq. 5.4, the uncertainty contribution to  $\mathcal{A}_{\text{PV}}$  is calculated and summarized in Table 5.9.

$$\begin{aligned} \frac{\partial \mathcal{A}_{\text{PV}}}{\partial \mathcal{A}_C} \delta \mathcal{A}_C &= -\frac{0.0629}{1 - 0.0629} \times 4\% \times 539.36 = -1.4481 \text{ ppb} \\ \frac{\partial \mathcal{A}_{\text{PV}}}{\partial f_C} \delta f_C &= \frac{550 - 539.46}{1 - 0.0629} \times 0.00463 = 0.0521 \text{ ppb} \end{aligned} \quad (5.13)$$

The uncertainty caused by the error in  $f_C$  is negligible, and the one from  $\mathcal{A}_C$  is also tiny, which in hindsight, justifies our adoption of the sandwich target.

$\mathcal{A}_{cor}/\mathcal{P}$ (ppb)	$\mathcal{A}_C$ (ppb)	$\frac{\delta\mathcal{A}_C}{\mathcal{A}_C}$	$f_C$	$\delta f_C$	rel. error due to $\mathcal{A}_C$	rel. error due to $f_C$
549.34	539.36	4%	6.29%	0.463%	0.26%	0.01%

Table 5.9: Relative uncertainty due to  $\mathcal{A}_C$  and  $f_C$ .

### 5.3 The CREX Acceptance Function

As mentioned earlier, the spectrometer acceptance is primarily defined by the Q1 collimator, although other components can also have some influence on it. The acceptance itself is not tiny (0.00377 sr), points located within the acceptance region may have varying detection efficiencies and different asymmetries. In other words, what we measure is actually the average asymmetry over the acceptance:

$$\mathcal{A}_{mea} = \frac{\int d\theta \sin \theta \mathcal{A}(\theta) \frac{d\sigma}{d\Omega} \epsilon(\theta)}{\int d\theta \sin \theta \frac{d\sigma}{d\Omega} \epsilon(\theta)} \quad (5.14)$$

here  $\epsilon(\theta)$  is the acceptance function, which is defined as the ratio of electrons that reach the main detector over all scattered electrons. This quantity depends on the scattering angle  $\theta$ :

$$\epsilon(\theta) = \frac{N_{det}(\theta)}{N_{sca}} \quad (5.15)$$

From Eq. 5.14, we see the importance of the acceptance function. Firstly, it contributes to the systematic uncertainty of  $\mathcal{A}_{PV}$ ; secondly, only with the acceptance function, can we compare the experimental measurement to theoretical predictions, to interpret our results.

To extract the acceptance function, again, we have to turn to simulations. To ensure the reliability of the simulation result, precise matches of various kinematic variables between the simulation and the optics data are required.

When we take the optics data, we can put in the sieve slit collimators. By reconstructing electron trajectories with the track info from the VDCs and the hole positions in the sieve plane, the scattering angle and beam energy can be inferred.

In terms of the simulation, we tuned some parameters to achieve the best match with the data, which was then used to calculate the acceptance function. The three parameters we explored are listed here:

- Septum current
- Q1 collimator shift
- Pinch point shift

### 5.3.1 Transportation Matrix

The presence of multiple magnetic fields, such as the septum and the HRS, between the target and the detector introduces complexity in determining an analytical expression for the particle transportation between these components. However, it is still possible to approximate and measure this transportation process.

An electron trajectory can be parameterized as:

$$\mathbf{X} = (x, \theta, y, \phi, \delta)^T \quad (5.16)$$

with respect to a reference trajectory (usually the central ray). In the transport coordinate,  $\hat{z}$  is the moving direction of the reference trajectory;  $x$  denotes the displacement in the dispersive plane relative to the reference trajectory, and  $\theta$  represents the ‘velocity’ in the dispersive plane:

$$\theta = \frac{\partial x}{\partial z} \quad (5.17)$$

Similarly,  $y$  and  $\phi$  are displacement and ‘velocity’ in the y-z plane.

$$\phi = \frac{\partial y}{\partial z} \quad (5.18)$$

$\hat{y}$  is oriented such that  $\hat{x}$ ,  $\hat{y}$ ,  $\hat{z}$  are orthogonal to each other and they form a right-handed (RH) coordinate  $\hat{z} = \hat{x} \times \hat{y}$ .

$$\delta = \frac{\Delta p}{p} \quad (5.19)$$

represents the fractional deviation of momentum from that of the reference trajectory.

With these definitions, the electron trajectory can be expressed as a Fourier expansion of the initial state of  $\mathbf{X}_0$ :

$$x_i = \sum_j T_{ij} x_{j,0} + \sum_j \sum_k S_{ijk} x_{j,0} x_{k,0} + \dots \quad (5.20)$$

where  $T_{ij}$  is what we call the transportation matrix, whose elements indicate the reliance of the beam parameters on each other:

$$T_{ij} = \frac{\partial x_i}{\partial x_j} \quad (5.21)$$

Considering the fact that electron trajectories will be very close to the reference trajectory, a first order expansion is good enough to approximate Eq. 5.20. So we write:

$$\begin{pmatrix} x \\ y \\ \theta \\ \phi \\ \delta \end{pmatrix} = T \begin{pmatrix} x_{tg} \\ y_{tg} \\ \theta_{tg} \\ \phi_{tg} \\ \delta_{tg} \end{pmatrix} = \begin{pmatrix} x|x_{tg} & x|y_{tg} & x|\theta_{tg} & x|\phi_{tg} & x|\delta_{tg} \\ y|x_{tg} & y|y_{tg} & y|\theta_{tg} & y|\phi_{tg} & y|\delta_{tg} \\ \theta|x_{tg} & \theta|y_{tg} & \theta|\theta_{tg} & \theta|\phi_{tg} & \theta|\delta_{tg} \\ \phi|x_{tg} & \phi|y_{tg} & \phi|\theta_{tg} & \phi|\phi_{tg} & \phi|\delta_{tg} \\ \delta|x_{tg} & \delta|y_{tg} & \delta|\theta_{tg} & \delta|\phi_{tg} & \delta|\delta_{tg} \end{pmatrix} \begin{pmatrix} x_{tg} \\ y_{tg} \\ \theta_{tg} \\ \phi_{tg} \\ \delta_{tg} \end{pmatrix} \quad (5.22)$$

The ‘tg’ subscript refers to corresponding values on the target plane. With the transportation matrix, it is possible to invert it to propagate backward and calculate the electron state on the target plane based on the information detected by the VDCs. Typically, the calculation starts from the focal plane  $\mathbf{X}_{fp}$ , and then the electron state on the target plane can be determined:

$$\mathbf{X}_{tg} = T^{-1} \mathbf{X}_{fp} \quad (5.23)$$

The reason that we do not use BPMs to ‘measure’ the electron position/angle at the target is that multi-scattering/radiation inside the target foil will distort the electron trajectory.

The typical HRS transportation plots are shown in Fig. 5.4:

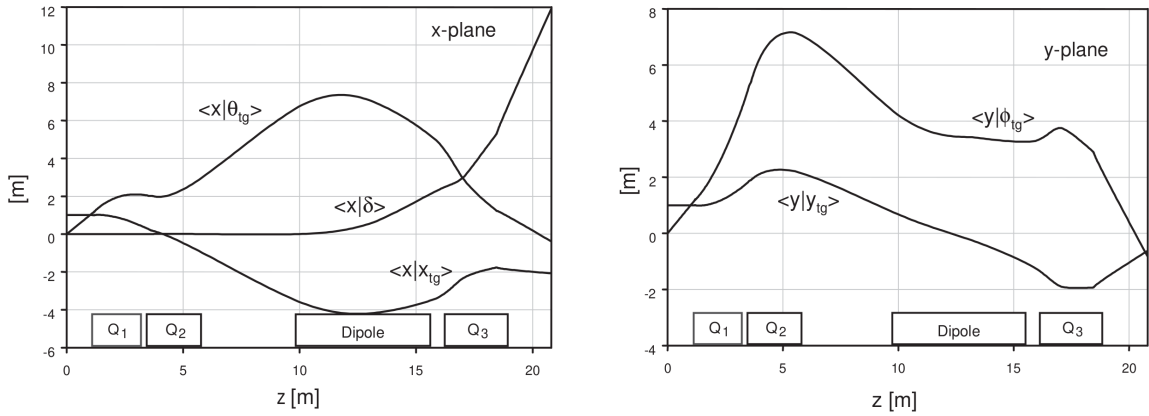


Figure 5.4: HRS transportation plots.

Actually, not every element of  $T$  needs to be measured, some elements are obviously 0. E.g.  $\delta$  should be not be affected by any magnetic field, so

$$T_{5i, i \neq 5} = 0 \quad (5.24)$$

The design of the HRS tells us that the dispersion depends only on  $\delta$ , but not on  $\theta$  or  $\phi$ , therefore

$$x|\theta = 0 \quad (5.25)$$

And different planes should not interfere with each other, which means

$$x|y = x|\phi = \theta|y = \theta|\phi = y|x = y|\theta = \phi|x = \phi|\theta = 0 \quad (5.26)$$

That is to say  $T$  is a sparse matrix.

The transportation matrix is measured with the sieve data. When the sieve slit collimator is inserted, the electron trajectories originating different holes are naturally separated on the focal plane. This separation allows for matching each trajectory to its corresponding sieve hole. With a reasonable initial value of the matrix (from previous experiments), we can reconstruct the electron state on the sieve plane using Eq. 5.23.

By tuning the matrix elements, the one that minimizes the distance between the reconstructed electron trajectory on the sieve plane and the closest hole center is identified as the transportation matrix. The selection of the septum and HRS current is based on the sieve pattern derived from the transportation matrix.

### 5.3.2 Scattering Angle $\theta_{\text{lab}}$

The parameter that directly reflects the quality of our simulations is the scattering angle. For convenience, we used the target coordinate system (TCS) in our simulations, rather than the hall coordinate system (HCS). However, when comparing our results to the data, we utilized values in the lab frame (HCS). The two coordinate systems and the transportation between them are defined below.

- Hall coordinate system: originated at the center of the hall and cross the beam line.  $\hat{Z}$  is along the beam line in the downstream direction;  $\hat{Y}$  points upward and  $\hat{X}$  points to the left to form a RH coordinate system.
- Target coordinate system: which is the transport coordinate system at the target.  $\hat{Z}$  is along the beam trajectory, pointing away from the target,  $\hat{X}$  is on the dispersive plane and points down,  $\hat{Y}$  is perpendicular to the dispersive plane and points away (toward) the beamline for LHRS (RHRS).

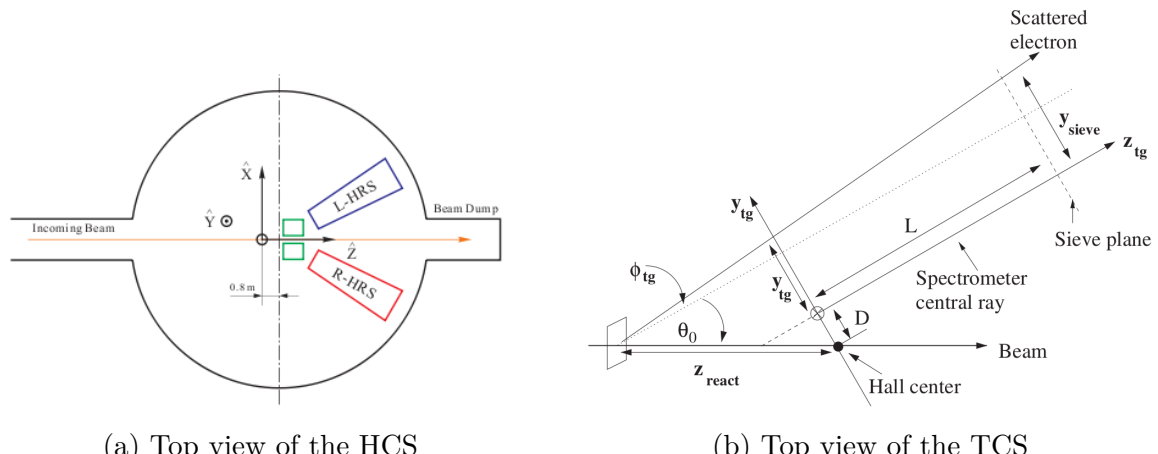


Figure 5.5: Schematic plot of the HCS and TCS. The hall center is the origin of the HCS, but the target does not necessarily lie in the hall center. The distance between the hall center and the sieve plane ( $L$ ) is a constant, which is used to identify the origin of the TCS. In the ideal case, the origins of both coordinate systems will overlap.

The relationship between the HCS and TCS is:

$$\begin{pmatrix} x_{tg} \\ y_{tg} \\ z_{tg} \end{pmatrix} = \begin{pmatrix} \cos(90^\circ) & -\sin(90^\circ) & 0 \\ \sin(90^\circ) & \cos(90^\circ) & 0 \\ 0 & 0 & 1 \end{pmatrix} \begin{pmatrix} \cos(-\theta_0) & 0 & -\sin(-\theta_0) \\ 0 & 1 & 0 \\ \sin(-\theta_0) & 0 & \cos(-\theta_0) \end{pmatrix} \begin{pmatrix} x \\ y \\ z \end{pmatrix} \quad (5.27)$$

which leads to:

$$\left. \begin{array}{l} x_{tg} = -y \\ y_{tg} = x \cos \theta_0 + z \sin \theta_0 \\ z_{tg} = -x \sin \theta_0 + z \cos \theta_0 \end{array} \right\} \iff \left. \begin{array}{l} x = y_{tg} \cos \theta_0 + z_{tg} \sin \theta_0 \\ y = -x_{tg} \\ z = -y_{tg} \sin \theta_0 + z_{tg} \cos \theta_0 \end{array} \right\} \quad (5.28)$$

where  $\theta_0$  is the scattering angle of the central ray in the lab frame.

The distance of an electron from the origin in both coordinate systems is:

$$R = (x^2 + y^2 + z^2)^{1/2} = z_{tg} (\phi_{tg}^2 + \theta_{tg}^2 + 1)^{1/2} \quad (5.29)$$

So the scattering angle in the lab frame will be:

$$\cos \theta = \frac{z}{R} = \frac{-\phi_{tg} \sin \theta_0 + \cos \theta_0}{(\phi_{tg}^2 + \theta_{tg}^2 + 1)^{1/2}} \quad (5.30)$$

For the data,  $\theta_0$  is identified to be  $4.789^\circ$  ( $4.771^\circ$ ) for the LHR (RHR). In the simulation, both arms use  $4.74^\circ$ . Note that  $\theta_{\text{lab}}$  is a post-target quantity, or an apparent quantity as we call it, which includes effects from the post-vertex radiations and multi-scatterings. It is not the ‘real’ scattering angle (vertex quantity) at the vertex where the interesting PV elastic scattering occurs. The correction from the apparent distribution to the vertex distribution is about 1.5%.

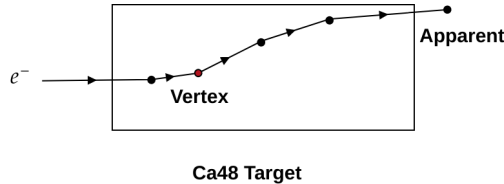


Figure 5.6: Schematic plot of the vertex and apparent quantities.

### 5.3.3 Data

Exp	Arm	Dipole p0 (GeV)	Septum (A)	Q1 (A)	A2 (A)	Q3 (A)
PREX-II	Left	0.95285	333	118.50	407.70	450.76
	Right	0.95284	333	118.55	404.07	446.90
CREX	Left	2.183522	801	225.387	934.273	981.301
	Right	2.183499	801	230.916	925.955	981.301

Table 5.10: PREX-II and CREX tunes of the septum and HRS.

To determine the new tune of the septum and HRS for CREX, we started with the PREX-II tune and scaled it to the CREX momentum. To find the appropriate septum current that would align the central ray with the HRS axis, we conducted a two-step tuning process involving the septum and Q1 current adjustments: coarse and fine tunes.

During the coarse tune, we made a significant step change of 10% in the septum or Q1 current (referred to as the central ray search) to identify the approximate position. Following this, in the fine tune stage, we performed smaller step adjustments of 2.5% to further refine the settings and determine the largest acceptance (known as the inner edge search).

During the central ray search, if the septum current is inappropriate, it will lead to a shift in the central hole observed in the reconstructed sieve pattern plot when we adjust the Q1 current, as shown in Fig. 5.7.

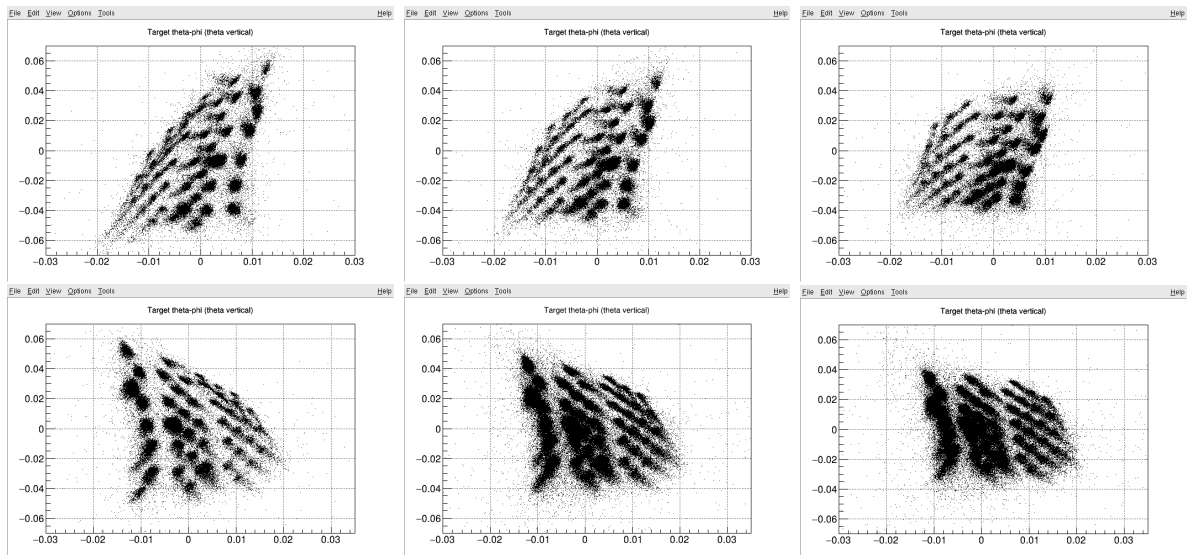


Figure 5.7: Sieve pattern plots for the -10% septum current and varied Q1 currents, from left to right: -10%, nominal and +10% Q1 current. The top (bottom) row shows the right (left) arm plot. With different Q1 currents, the sieve pattern twists, and the central hole shifts in  $\theta$  (vertical axis), so the septum current is not a good value.

Fig. 5.8 indicates that the nominal septum current and the nominal HRS setting is not a bad choice. Then we proceeded to the inner edge search to see more inner holes – holes with the largest (smallest)  $\phi$  in the left (right) arm. It turned out a 5% increment from the nominal value resulted in the largest acceptance. This increment corresponds to a septum current of:  $1.05 \times (333 * 2.183522 / 0.95285) = 801.25$  A.

Once the septum current was selected, we proceeded to minimize the beam spot size on the detector plane, which was achieved with the Q1 current being -17% (-15%) from the nominal value for the left (right) arm, and the Q3 current being -5% from the nominal value for both arms. The current values of the CREX tune are presented in Table 5.10.

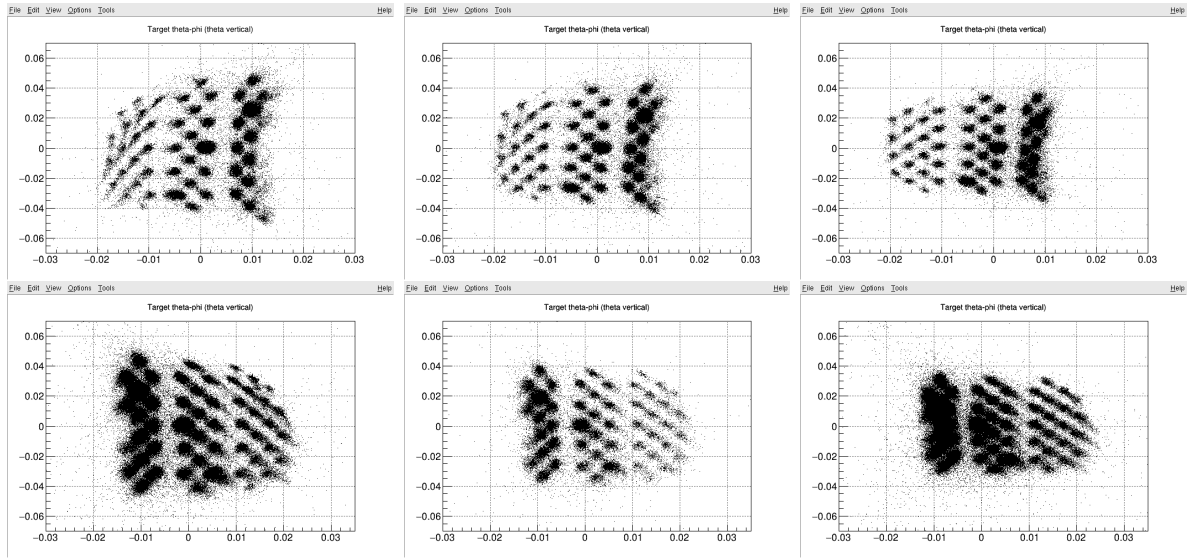


Figure 5.8: Sieve pattern plots for the nominal (scaled from PREX-II) septum current and varied Q1 currents, from left to right: -10%, nominal and +10% Q1 current. The top (bottom) row shows the right (left) arm plot. With different Q1 currents, the sieve pattern twists, but the central hole keeps at the same position, which means the central ray goes through the axis of the HRS.

### 5.3.4 Simulation

The simulation is not an exact reproduction of reality. We used GEANT4 to simulate the geometry of each component based on the design values. The septum magnetic field was scaled from a field map file sampled from the septum with a current density of  $j_0 = -1320 \text{ A/cm}^2$ :

$$B'_{x,y,z} = \frac{j}{j_0} \times \frac{P}{P_0} \times B_{x,y,z} \quad (5.31)$$

where  $j$  is the current density and  $P$  being the electron momentum.

The same operation for the HRS field:

$$B'_{i=Q1,Q2,D,Q3} = \frac{P}{P_0} \times B_i \quad (5.32)$$

With Eq. 5.31, we could vary the septum current to find a value that yields good agreement between the simulated and experimental sieve pattern plots. To further refine the simulation, we scanned through the collimator shift and the pinch point shift. By systematically varying these parameters, we aimed to find the combination that provides the closest agreement between the simulated and measured results across various kinematic variables.

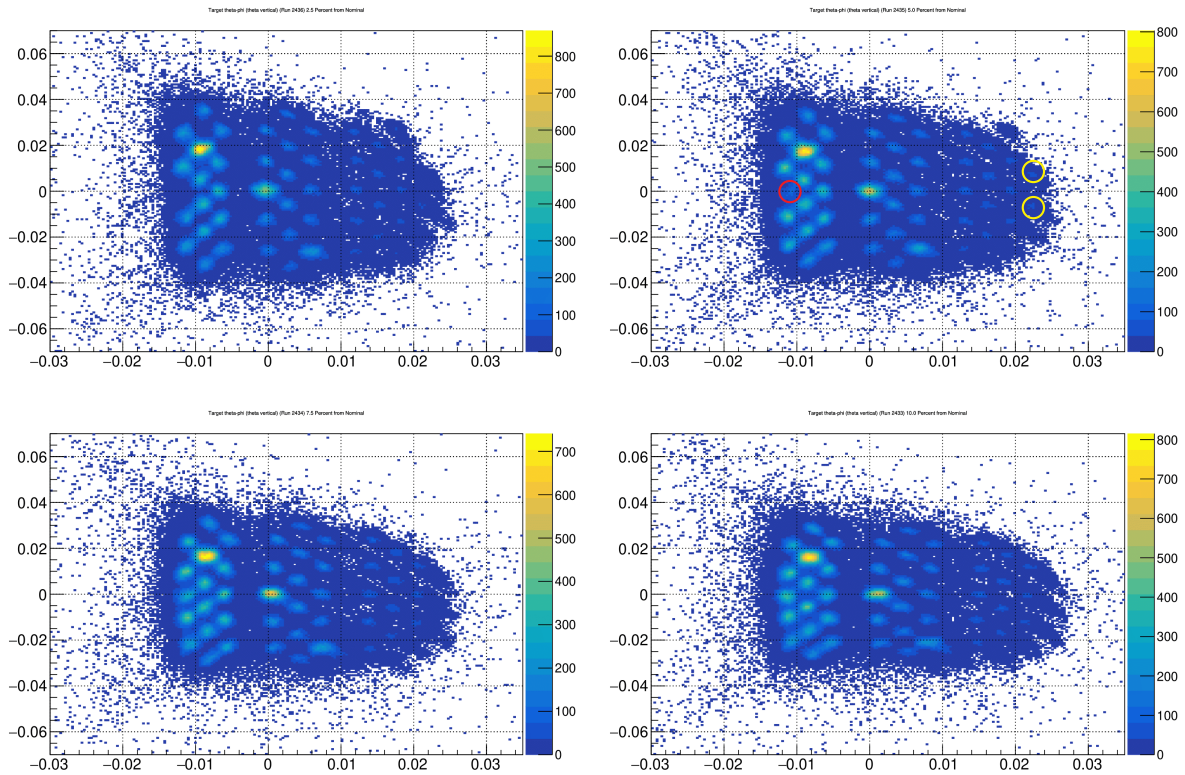


Figure 5.9: Inner edge search in the left arm. Septum currents from top left to bottom right are: +2.5%, +5%, +7.5%, +10% with respect to the nominal value. The inner middle hole begin to appear when the septum current is increased by +5%, and outer holes starts to disappear when the septum current reaches +7.5%. So the best septum current was chosen to be +5%

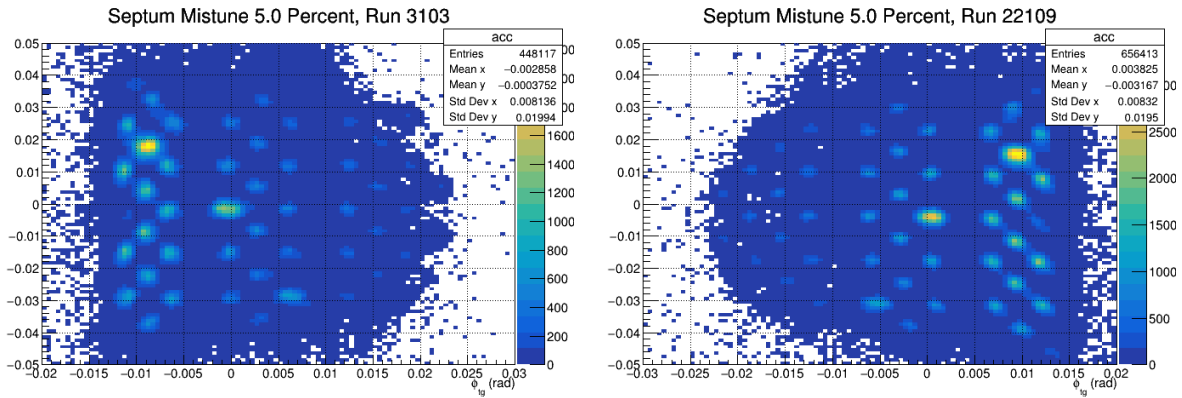


Figure 5.10: Sieve plot of the CREX tune. Centered at  $(-0.3, -1.5)$ , the new beam position for the new target.

Somewhat expected, a coarse scan through the septum current showed that the optimal range for achieving the best match with the data was about 0-5% above the nominal

Q1(%)	Q3 (%)	Left			Right		
		run	$\sigma_y$ (cm)	$\sigma_x$ (cm)	run	$\sigma_y$ (cm)	$\sigma_x$ (cm)
0	0	2524	0.9604	1.634	21604	0.009564	0.01503
-5	0	2525	0.955	1.188		Left arm only	
-10	0	2526	1.005	0.9063		Left arm only	
-15	0	2527	0.1078	0.7314		Left arm only	
-20	0	2528	1.182	0.6801		Left arm only	
-11	0	2529	1.012	0.8767	21609	0.009315	0.007337
-12	0	2530	1.012	0.8349	21610	0.009429	0.006957
-13	0	2531	1.033	0.7835	21611	0.009526	0.006682
-14	0	2532	1.057	0.7515	21612	0.009623	0.06367
-13	+10	2533	1.754	1.929	21613	0.0162	0.0215
-13	+5	2534	1.374	0.7282	21614	0.01276	0.01174
-13	-5	2535	0.8357	0.9751	21615	0.008422	0.008514
-13	-10	2536	0.8855	1.482	21616	0.008891	0.01387
-13	-2	2538	0.9415	0.8761	21618	0.9117	0.7078
-13	-4	2539	0.8602	0.9181	21619	0.8493	0.7912
-13	-7	2540	0.8182	1.154	21620	0.8304	1.027
-13	-9	2541	0.8445	1.389	21621	0.8545	1.268
-15	-5	2542	0.8354	0.8869	21622	0.827	0.7563
-15 (R);-17 (L)	-5	2543	0.8409	0.8315	21623	0.8382	0.7615

Table 5.11: Beam spot sizes with different HRS settings. The septum current being the nominal value.

value, as demonstrated in Fig. 5.11.

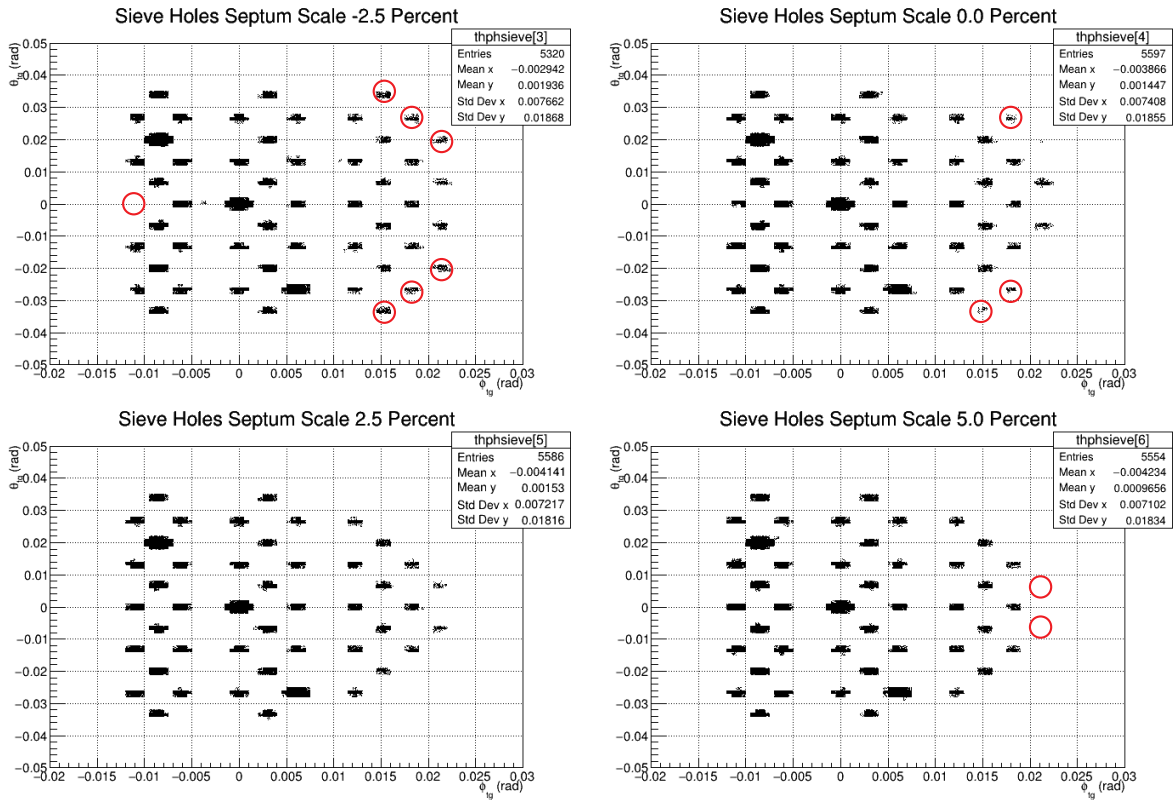


Figure 5.11: Sieve pattern plots from simulations with different septum currents. The red circles label extra or missing holes.

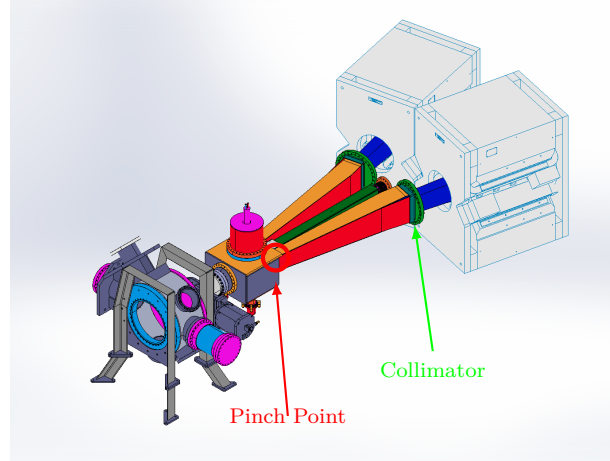


Figure 5.12: Position of the pinch point and the Q1 collimator.

To further refine the simulation, we conducted a scan through the pinch point and collimator shift within the narrowed range of the septum current (from -1% to +5%). The pinch point is the connection point between the septum beampipe and the upstream collimator box, whose misalignment will affect the acceptance; the other parameter we

adjusted was the collimator y position (in the transport coordinate system), which has a significant influence on the acceptance. For each simulation, we compared the average values of the scattering angle  $\theta_{\text{lab}}$ ,  $Q^2$  and asymmetry to the corresponding values obtained from optics runs.

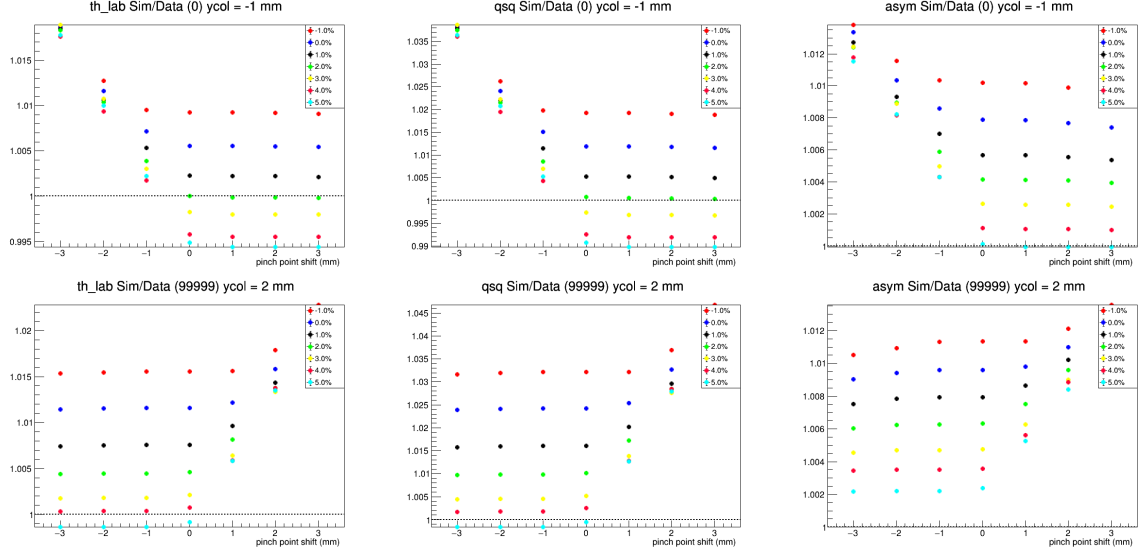


Figure 5.13: Ratio of the average simulation values to the corresponding data values for  $\theta_{\text{lab}}$ ,  $Q^2$  and  $\mathcal{A}$ . Top (bottom) row corresponds to the left (right) arm. Data points whose y values are close 1 are considered as good models.

As illustrated in Fig. 5.13, the acceptance increases as we shift the pinch point towards the beam pipe. For the left arm, this shift is from negative values to positive values, while for the right arm, it is the opposite. Once the nominal value is reached, the acceptance saturates. A similar trend is observed when making shifts in the Q1 collimator.

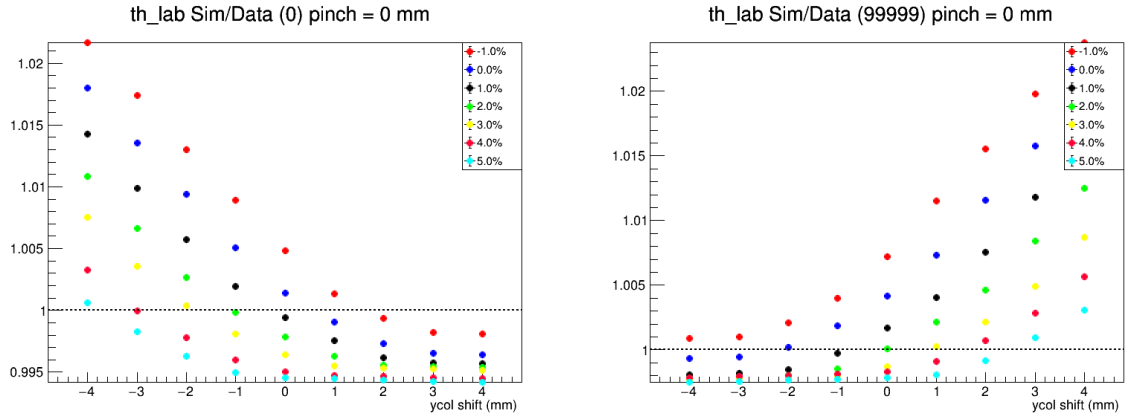


Figure 5.14: The  $\theta_{\text{lab}}$  ratio plot for different models with pinch point shift = 0 mm. The left (right) arm plot is shown in the left (right). The best models are selected from these two plots.

Several corrections are applied to the simulation values, including the position difference between the production target and the calibration target, which is 20 mm; and the correction caused by the transportation matrix, whose optimization depends on the beam position.

$$\phi_a = \phi_r + 0.5 \text{ mrad/mm} \times (x - x_0) + 0.5 \text{ mrad/mm} \times (y - y_0) \quad (5.33)$$

where  $(x, y)$  is the actual beam position and  $(x_0, y_0)$  being the beam position with which the transportation matrix is optimized.  $\phi_a$  and  $\phi_r$  refer to the actual and reconstructed  $\phi_{tg}$ , respectively. An extra acceptance is added to the right arm to get a better match.

From Fig. 5.14, we selected the best model based on had the smallest difference between the simulation and data in  $\theta_{\text{lab}}$  and  $Q^2$ :

	septum	col shift (mm)	pinch point shift (mm)
LHRS	+2%	-1	0
RHRS	+5%	2	0

Table 5.12: The best models we selected for LHRS and RHRS.

Check the best models against optics runs it terms of the distributions of  $\theta_{\text{lab}}$  and  $Q^2$ , as shown in Fig. 5.15. Quite good agreements are achieved for both arms.

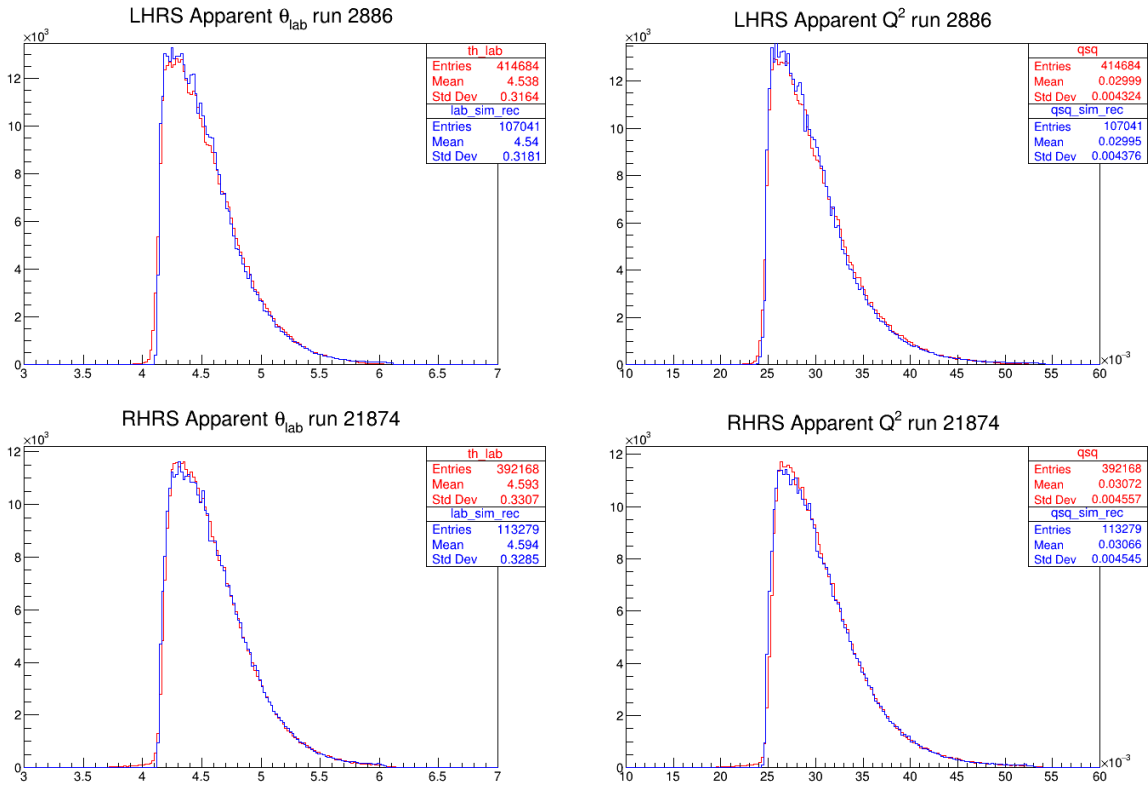


Figure 5.15:  $\theta_{lab}$  and  $Q^2$  comparison between the best models and data (apparent values). The red line is the simulation result while the blue line comes from data.

Using the selected best models, the acceptance function is calculated with Eq. 5.15 and drew in Fig. 5.16.

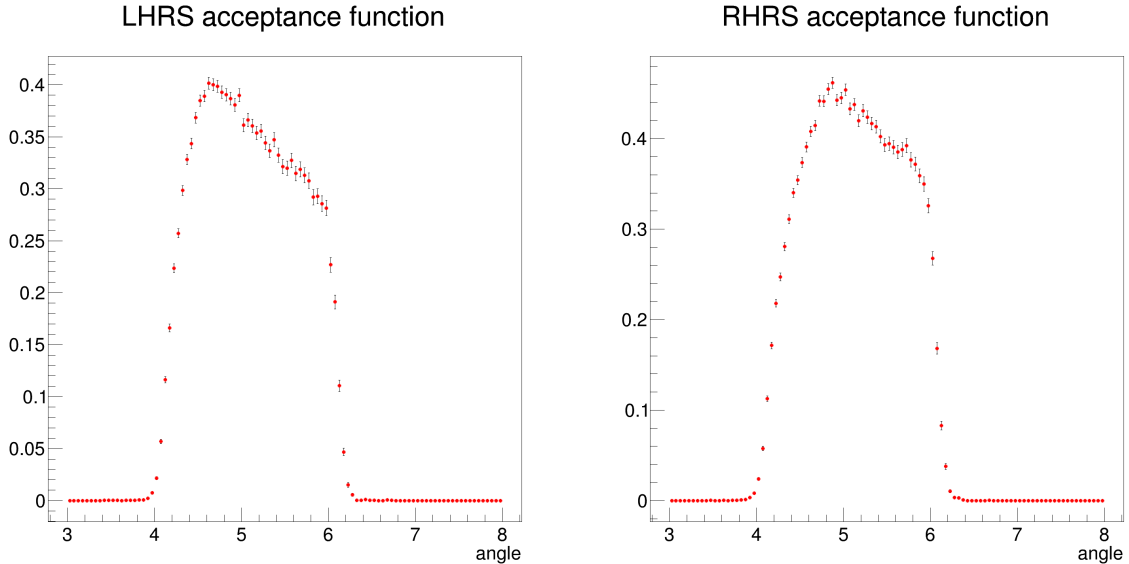


Figure 5.16: Acceptance function extracted with the best models.

## 5.4 Other Systematic Uncertainties

Other systematic uncertainties that are not discussed here can be found in other PREX-II and CREX theses. The detector non-linearity is analyzed by Devi [69], and Ryan has a detailed discussion about the horizontal transverse asymmetry [79].

# Chapter 6

## Results and Discussion

### 6.1 Final Numbers

The overall beam polarization is determined by calculating the inverse-variance weighted average of the Compton and Moller measurements.

	PREX-II	CREX
Compton	$(89.68 \pm 0.15)\%$	$(87.115 \pm 0.453)\%$
Moller	$(89.67 \pm 0.80)\%$	$(87.06 \pm 0.74)\%$
Average	$(89.7 \pm 0.8)\%$	$(87.10 \pm 0.39)\%$

Table 6.1: Beam polarization measured by the Compton and Moller polarimeters.

After applying the beam false asymmetry correction described in chapter 3 and identifying various background asymmetries in chapter 5, the blinded PV asymmetry will be extracted using Eq. 5.1, which we restate here:

$$\mathcal{A}_{\text{PV}} = \frac{\mathcal{A}_{\text{cor}}/\mathcal{P} - \sum_i \mathcal{A}_i f_i}{1 - \sum_i f_i}$$

The list of various corrections to the final result are shown in Table 6.2 and 6.3.

The last step is unblinding, in which we subtract  $\mathcal{A}_{\text{blind}}$  from the blinded  $\mathcal{A}_{\text{PV}}$ . The blinding factor is a secret value that is randomly generated from a  $\pm 900$  ppb box, this secret value is added to each helicity quadruplet (octuplet) asymmetry by the JAPAN analyzer. Surprisingly, the value of  $\mathcal{A}_{\text{blind}}$  for PREX-II is very close to 0, resulting in the unblinded  $\mathcal{A}_{\text{PV}}$  being almost the same as the blinded value. The final asymmetry values are presented in Table 6.4.

#### 6.1.1 Neutron Skin Thickness

With the physical PV asymmetry, the weak FF is calculated using Eq. 1.85.

$$F_W(^{208}\text{Pb}) = 0.368 \pm 0.013 \text{ (exp)} \pm 0.001 \text{ (theo)} \quad (6.1)$$

Correction	Absolute (ppb)	Relative (%)
Beam trajectory and energy	$-60.4 \pm 3.0$	$11.0 \pm 0.5$
Charge correction	$20.7 \pm 0.2$	$3.8 \pm 0.0$
Beam polarization	$56.8 \pm 5.2$	$10.3 \pm 1.0$
Target diamond foils	$0.7 \pm 1.4$	$0.1 \pm 0.3$
Spectrometer rescattering	$0.0 \pm 0.1$	$0.0 \pm 0.0$
Inelastic contributions	$0.0 \pm 0.1$	$0.0 \pm 0.0$
Transverse asymmetry	$0.0 \pm 0.3$	$0.0 \pm 0.1$
Detector nonlinearity	$0.0 \pm 2.7$	$0.0 \pm 0.5$
Angle determination	$0.0 \pm 3.5$	$0.0 \pm 0.6$
Acceptance function	$0.0 \pm 2.9$	$0.0 \pm 0.5$
Total correction	$17.7 \pm 8.2$	$3.2 \pm 1.5$
Statistical uncertainty	16	2.9

Table 6.2: Corrections and corresponding systematic uncertainties to  $\mathcal{A}_{\text{PV}}$  in PREX-II.

Correction	Absolute (ppb)	Relative (%)
Beam trajectory and energy	$68 \pm 7$	$2.5 \pm 0.3$
Beam charge asymmetry	$112 \pm 1$	$4.2 \pm 0.0$
Beam polarization	$382 \pm 13$	$14.3 \pm 0.5$
Isotopic purity	$19 \pm 3$	$0.7 \pm 0.1$
3.831 MeV ( $2^+$ ) inelastic	$-35 \pm 19$	$-1.3 \pm 0.7$
4.507 MeV ( $3^-$ ) inelastic	$0 \pm 10$	$0 \pm 0.4$
5.370 MeV ( $3^-$ ) inelastic	$-2 \pm 4$	$-0.1 \pm 0.1$
Transverse asymmetry	$0 \pm 13$	$0 \pm 0.5$
Detector nonlinearity	$0 \pm 7$	$0 \pm 0.3$
Acceptance	$0 \pm 24$	$0 \pm 0.9$
Radiative corrections	$0 \pm 10$	$0 \pm 0.4$
Total systematic uncertainty	40	1.5
Statistical uncertainty	106	4.0

Table 6.3: Corrections and corresponding systematic uncertainties to  $\mathcal{A}_{\text{PV}}$  in CREX.

Asymmetry	PREX-II	CREX
$\mathcal{A}_{\text{raw}}$	$431.64 \pm 44.01$	$2106 \pm 178.9$
$\mathcal{A}_{\text{cor}}$	$492.02 \pm 13.52$	$2080.3 \pm 83.8$
Blinded $\mathcal{A}_{\text{PV}}$	$549.4 \pm 16.1 \pm 8.1$	$2412.3 \pm 106.1 \pm 38.7$
$\mathcal{A}_{\text{blind}}$	-0.5	-255.7
Unblinded $\mathcal{A}_{\text{PV}}$	$550 \pm 16 \pm 8$	$2668 \pm 106 \pm 40$

Table 6.4: The path to a physical PV asymmetry. All values are in units of ppb.

Here the experimental uncertainty incorporates both statistical and systematic contributions.

The experimental value of the weak radius is determined from the correlation between the weak radius and PV asymmetry. In the correlation plot, the weak radius corresponding to the measured PV asymmetry is obtained as the experimental value. Similarly, the neutron skin thickness is derived using the same approach.

The correlation plot is generated by fitting the weak charge densities, which are predicted by a wide range of DFT models, to a two-parameter Fermi function. By knowing the weak charge density function, the corresponding PV asymmetry and weak radius can be identified for each model, as shown in Fig. 6.1. The two-parameter Fermi function has been discussed in Sec. 1.1.1.

$$\rho_W(r) = \rho_W^0 \frac{\sinh(c/a)}{\cosh(r/a) + \cosh(c/a)}$$

here  $c$  denotes the nuclear size and  $a$  describes the surface thickness.

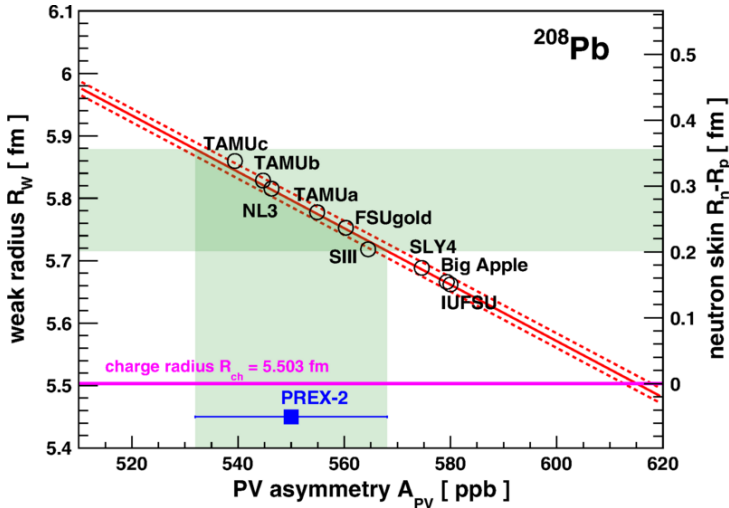


Figure 6.1: Correlation between the weak radius (left vertical axis) or neutron skin thickness (right vertical axis) and  $A_{PV}$  for  $^{208}\text{Pb}$ , as predicted by a series of DFT models [80]. The red solid line describes the fitted correlation based on the predictions of the DFT models, the red dashed line and the green band indicate the  $1-\sigma$  uncertainty for the correlation and measured values, respectively.

The weak charge radius of  $^{208}\text{Pb}$  is extracted to be:

$$R_W(^{208}\text{Pb}) = 5.795 \pm 0.082 \text{ (exp)} \pm 0.013 \text{ (theo)} \text{ fm} \quad (6.2)$$

and the neutron skin thickness of  $^{208}\text{Pb}$ :

$$R_{\text{skin}}(^{208}\text{Pb}) = R_n - R_p = 0.278 \pm 0.078 \text{ (exp)} \pm 0.012 \text{ (theo)} \text{ fm} \quad (6.3)$$

Similarly, the weak radius and neutron skin thickness of  $^{48}\text{Ca}$  can be extracted, as summarized in Table 6.5.

Exp	PREX-II	CREX
Target	$^{208}\text{Pb}$	$^{48}\text{Ca}$
$\langle Q^2 \rangle$ (GeV $^2$ )	$0.00616 \pm 0.00005$	$0.0297 \pm 0.0002$
$\langle \mathcal{A}_{\text{PV}} \rangle$ (ppb)	$550 \pm 16$ (stat) $\pm 8$ (syst)	$2668 \pm 106$ (stat) $\pm 40$ (syst)
$F_W$	$0.368 \pm 0.013$ (exp) $\pm 0.001$ (theo)	$0.1304 \pm 0.0052$ (stat) $\pm 0.0020$ (syst)
$F_{ch} - F_W$	$0.041 \pm 0.013$ (exp) $\pm 0.001$ (theo)	$0.0277 \pm 0.0052$ (stat) $\pm 0.0020$ (syst)
$R_W$ (fm)	$5.795 \pm 0.082$ (exp) $\pm 0.013$ (theo)	$3.640 \pm 0.026$ (exp) $\pm 0.023$ (theo)
$R_n - R_p$ (fm)	$0.278 \pm 0.078$ (exp) $\pm 0.012$ (theo)	$0.121 \pm 0.026$ (exp) $\pm 0.024$ (theo)

Table 6.5: Physical results extracted from PREX-II and CREX.

Combining PREX-I and PREX-II results, the weak radius and the neutron skin are determined to be:

$$\begin{aligned} R_W(^{208}\text{Pb}) &= 5.800 \pm 0.075 \text{ fm} \\ R_{\text{skin}}(^{208}\text{Pb}) &= 0.283 \pm 0.71 \text{ fm} \end{aligned} \quad (6.4)$$

### 6.1.2 Density Dependence of the Symmetry Energy

In nuclear density functional theory, the neutron skin thickness of  $^{208}\text{Pb}$  is correlated with the density dependence of the symmetry energy  $L$ . By plotting the predictions from DFT calculations using a set of energy density functionals, a linear correlation between  $L$  and  $R_{\text{skin}}$  can be established, as demonstrated in Fig. 6.2. Using this correlation, we can determine the symmetry energy slope  $L$  that corresponds to our measured  $R_{\text{skin}}$  in  $^{208}\text{Pb}$ . The values of  $L$  at the nuclear saturation density  $\rho_0 \sim 0.15 \text{ fm}^{-3}$  and the nuclear density  $\rho_1 \sim 0.15 \text{ fm}^{-3}$  are determined to be:

$$L(\rho_0) = 106 \pm 37 \text{ MeV} \quad L(\rho_1) = 71.5 \pm 22.6 \text{ MeV} \quad (6.5)$$

### 6.1.3 Difference Between the Charge and Weak Form Factors

As discussed in subsection 6.1.1, the weak form factor and weak radius are extracted through their correlations with the PV asymmetry, while the correlation depends on the weak charge distribution function  $\rho_W(r)$ . The model dependence of  $F_W$  and  $R_W$  arises from the choice of  $\rho_W(r)$  to match the measured  $\mathcal{A}_{\text{PV}}$ .

Unexpectedly, for  $^{48}\text{Ca}$ , the determination of  $F_W$  at the reference momentum transfer of  $q = 0.8733 \text{ fm}^{-1}$  is insensitive to the shape of  $\rho_W$  [82]. This indicates that the calculated value of  $F_W$  and  $F_{ch} - F_W$  have minimal model dependence. Consequently, in Table 6.5, the entries for  $F_W$  and  $F_{ch} - F_W$  for  $^{48}\text{Ca}$  have only experimental uncertainties, without any theoretical uncertainties.

On the other hand, the large theoretical uncertainty in  $R_W$  for  $^{48}\text{Ca}$  stems from the fact that the correlation equation between  $F_W$  and  $R_W - F_{ch}(q) - F_W(q) \approx q^2(R_W^2 - R_{ch}^2)/6$

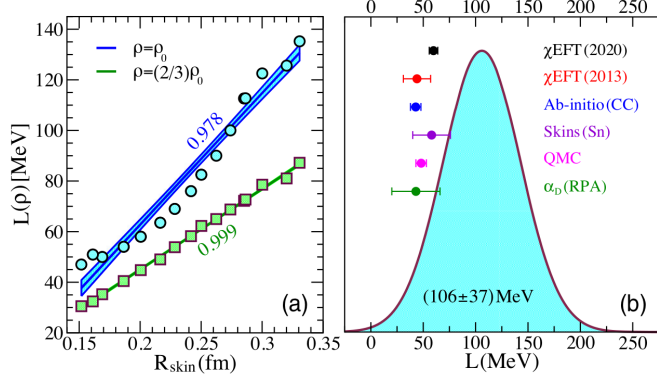


Figure 6.2: Left: correlation between the symmetry energy slope and the neutron skin thickness of  $^{208}\text{Pb}$ . The blue line represents the correlation at the nuclear saturation density, while the green line represents the correlation at the nuclear density. The correlation coefficients are indicated by the numbers along the lines. Right: A Gaussian probability distribution for  $L(\rho_0)$  inferred from the correlation plot on the left. The six data points are theoretical predictions of  $L(\rho_0)$  from different approaches [81].

– is only valid in the limit of  $q \rightarrow 0$ , which is not applicable due to the large value of  $q$  in CREX.

Therefore, for  $^{48}\text{Ca}$ ,  $F_W$  and  $F_{ch} - F_W$  are more reliable than  $R_W$  and  $R_W - R_{ch}$ . A comparison of  $F_{ch} - F_W$  for  $^{48}\text{Ca}$  between experimental result and theoretical predictions, as shown in Fig. 6.3, reveals that various models overestimate the difference between the charge and weak form factors for  $^{48}\text{Ca}$ .

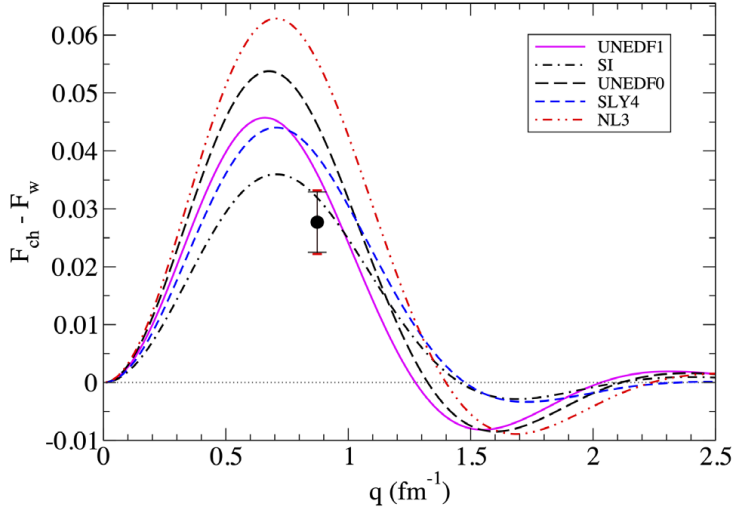


Figure 6.3: The difference between the charge and weak form factor for  $^{48}\text{Ca}$ . The black point indicates the CREX measurement. The curves represent theoretical predictions of  $F_{ch} - F_W$  as a function of  $q$  from a series of EDF models, as listed in the legend.

## 6.2 Physical Implication

### 6.2.1 Nuclear Structure

When comparing the experimental results with theoretical predictions of the neutron skin thicknesses of  $^{208}\text{Pb}$  and  $^{48}\text{Ca}$ , as shown in Fig. 6.4, a slight deviation between the experimental and theoretical values becomes apparent. Among the various models considered, only a few are successful in simultaneously predicting the neutron skin thicknesses (weak FFs) of both  $^{208}\text{Pb}$  and  $^{48}\text{Ca}$ . To a certain extent, our measurements provide guidance for the development of DFT and ab-initio calculations. However, further work is required from both experimental and theoretical perspectives to address and reconcile the difference between them.

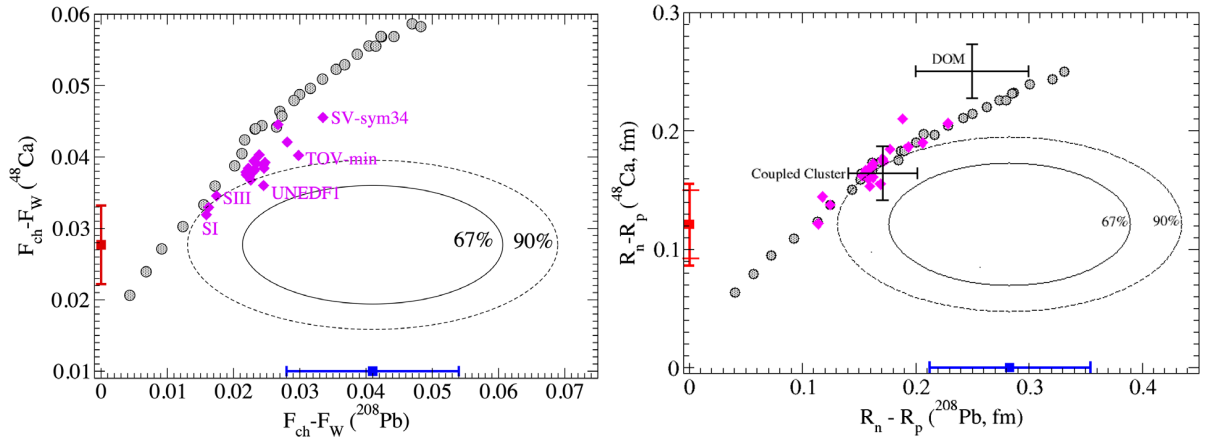


Figure 6.4: Experimental values and theoretical calculations of the FF difference (left) and the neutron skin thickness (right) of  $^{208}\text{Pb}$  and  $^{48}\text{Ca}$ . The two ellipses indicate the 67% and 90% probability intervals. The gray circles and magenta diamonds correspond to the DFT calculations using a range of relativistic and nonrelativistic density functionals, respectively. For clarity, only some of the functionals are labeled. Additionally, Two ab-initio results: coupled cluster and dispersive optical model (DOM) are depicted in the neutron skin thickness plot [82].

### Limit of the Nuclear Landscape

One straightforward application of nuclear DFT is to identify the limits of the nuclear landscape. Every year, a varying number of new nuclides, ranging from just a few to dozens, are discovered [83]. A clear theoretical guidance about the potential existence of neutron-rich nuclei will guide experimental efforts in the search for new rare isotopes, especially considering the challenges posed by the low production rates of such neutron-rich nuclei.

The nuclear chart is defined by the boundaries known as the “drip line”, which determines the maximum number of protons or neutrons for a given number of neutrons

or protons. Specifically, across the drip line, the separation energy of one proton ( $S_{1p}$ ) or neutron ( $S_{1n}$ ) or two protons ( $S_{2p}$ ) or neutrons ( $S_{2n}$ ) changes sign from positive to negative. It is noteworthy that the neutron drip line is currently known only up to neon ( $Z = 10$ ), with the maximum number of neutrons being  $N = 24$  [84].

The neutron separation energy is defined as:

$$\begin{aligned} S_{1n}(Z, N) &= E(Z, N - 1) - E(Z, N) \\ S_{2n}(Z, N) &= E(Z, N - 2) - E(Z, N) \end{aligned} \quad (6.6)$$

where  $E$  is the binding energy. The same definition applies to protons. A positive separation energy indicates that the nucleus is in a bound state, implying stability, while a negative value signifies an unstable state. We are interested in both  $S_{1n}$  and  $S_{2n}$ , rather than solely  $S_{1n}$ , because nuclei with an even number of nucleons tend to be more stable compared to their neighboring nuclei with an odd number of nucleons, due to the nucleonic superfluidity. At present, the estimate of the neutron drip line depends on the choice of theoretical models and associated parameterizations, as shown in Fig. 6.5. By incorporating the PREX-II and CREX results, we can constrain and refine DFT models, consequently, enhancing the robustness of theoretical predictions regarding the location of the neutron drip line.

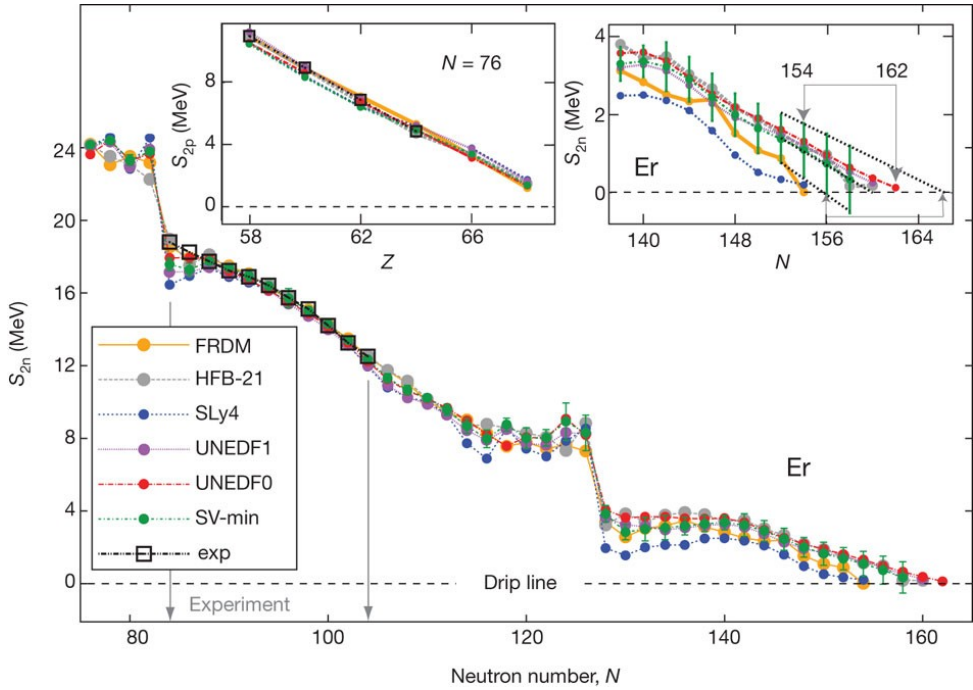


Figure 6.5: Theoretical and experimental two-nucleon separation energies of even-even erbium isotopes [85]. Dots represent DFT calculations and black squares correspond to experimental measurements.

## Nuclear Saturation Density

The invariance of the binding energy per nucleon ( $E_b/A$ ) with respect to  $A$  implies that the interaction between nucleons is proportional to  $A$ , rather than  $A(A-1)$ . This behavior indicates that nucleons saturate in space, leading to a nearly constant interior baryon density. A stricter definition of the saturation density is the nucleon density at which the binding energy per nucleon is minimized.

While the concept of nuclear saturation is well-established, it is never directly observed.  $^{40}\text{Ca}$  is the largest stable symmetric nucleus, its size is still too small to exhibit a nearly constant interior baryon density. For heavy nuclei, their charge densities have been precisely measured, but no direct observation of any interior neutron density. PREX-II is the first experiment to provide a value of the average interior baryon density of a heavy nucleus with minimal reliance on theoretical models.

With the two-parameter Fermi function, the interior weak density is extracted from PREX-II result and determined to be:

$$\rho_W^0(^{208}\text{Pb}) = \frac{3Q_W}{4\pi c(c^2 + \pi^2 a^2)} - 0.0798 \pm 0.0038 \text{ (exp)} \pm 0.0013 \text{ (theo)} \text{ fm}^{-3} \quad (6.7)$$

where  $Q_W$  is the total weak charge of  $^{208}\text{Pb}$  nucleus.

$$Q_W = -117.9 \pm 0.3 \quad (6.8)$$

Combining PREX-I and PREX-II results,  $\rho_W^0$  is modified to be:

$$\rho_W^0(^{208}\text{Pb}) = -0.0796 \pm 0.0038 \text{ fm}^{-3} \quad (6.9)$$

The uncertainty includes contributions from both experiment and theory.

With the well-measured interior charge density, the interior baryon density in  $^{208}\text{Pb}$  is measured to be:

$$\rho_b^0(^{208}\text{Pb}) = 0.1482 \pm 0.0040 \text{ fm}^{-3} \quad (6.10)$$

The extracted density plot is shown in Fig. 6.6.

With the scale factor between the nuclear saturation density ( $\rho_0$ ) and the interior baryon density in  $^{208}\text{Pb}$  ( $\rho_b^0$ ) [86]:

$$f = \frac{\rho_0}{\rho_b^0} \approx 1.02 \pm 0.03 \quad (6.11)$$

The nuclear saturation density becomes:

$$\rho_0 = f \times \rho_b^0 = 0.1510 \pm 0.0059 \text{ fm}^{-3} \quad (6.12)$$

This value is fully consistent with  $\rho_0 = 0.151 \pm 0.001 \text{ fm}^{-3}$  predicted by a relativistic EDF calibrated using exclusively physical observables [87], and lower than the phenomenological estimate of  $\rho_0 = 0.164 \pm 0.007 \text{ fm}^{-3}$  [88] based on some selected density functionals.

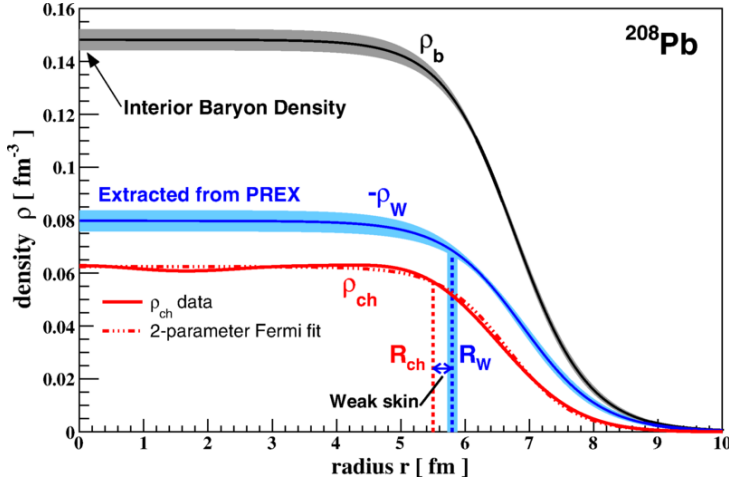


Figure 6.6: Density distributions for the EM charge (red), weak charge (blue) and baryon (black) in the  $^{208}\text{Pb}$  nucleus [80].

### 6.2.2 Neutron Stars

As discussed in the introduction section, the measurement of the neutron skin thickness of  $^{208}\text{Pb}$  and  $^{48}\text{Ca}$  allows us to determine the density dependence of the symmetry energy, which can then be used to constraint the size of a neutron star.

#### Multi-Messenger Measurements of the Neutron Star Radius

NICER (Neutron star Interior Composition ExploreR) [89] is a X-ray telescope that can measure lightcurves of neutron stars (pulsars). Pulsars possess a hot-spot, which is the magnetic pole of the neutron star. The observed light flux fluctuates based on the orientation of this hot-spot. When it faces the Earth, we observe the maximum flux, while minimum flux is observed when it points away from us. These variations occur due to the curvature of space caused by the neutron star. By analyzing the depth of the modulation in the light flux, one can infer the curvature of space near the neutron star, which depends on the radius of the neutron star. This is how NICER measures the radius of a neutron star.

One can measure the size of a neutron star through the gravitational waves as well. The famous LIGO-Virgo event, GW170817 [90], observed the gravitational wave emission from a binary neutron star merger. In such a binary system, the neutron star experiences deformation due to the tidal force exerted by the other body, this property is described by the tidal deformability (quadrupole polarizability):

$$\Lambda = \sum_f \frac{|\langle f | r^2 Y_{20} | i \rangle|^2}{E_f - E_i} \propto R^5 \quad (6.13)$$

Tidal deformability can be probed by detection of the gravitational waves produced by the binary system. LIGO observation of GW170817 sets an upper limit on  $\Lambda$  of a typical

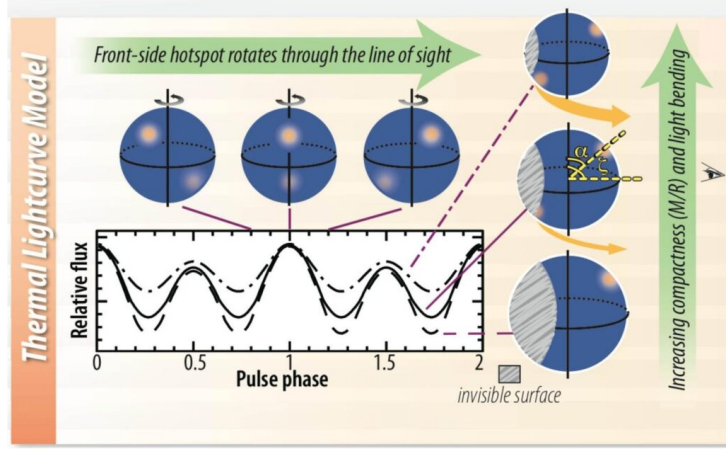


Figure 6.7: Modeling of the light flux from a neutron star. The three curves in the flux panel corresponding to the three neutron stars to the right with different compactness (mass/radius).

$1.4 M_{\odot}$  neutron star[91].

$$\Lambda_{1.4} = 190^{+390}_{-120} \quad (6.14)$$

It favors a smaller deformability ( $< 580$ ) and consequently a smaller neutron star radius ( $< 13$  km)

Observables of a  $1.4 M_{\odot}$  neutron star extracted from various experiments are shown in Fig. 6.8. We see that the combined PREX measurement is consistent with the NICER result, while in mild tension with the LIGO observation.

## Direct Urca Process

The direct Urca processes are neutrino emission processes:



which may explain the rapid cooling of some neutron stars [92].

The rate of the direct Urca process depends on the proton fraction present in the core of a stellar object. This proton fraction, in turn, is controlled by the density dependence of the symmetry energy [93]. Therefore, we can gather insights into the threshold density for the direct Urca process from the measurement of  $R_{\text{skin}}(^{208}\text{Pb})$ , as shown in Fig. 6.9. In particular, a higher neutron skin thickness observed in  $^{208}\text{Pb}$  corresponds to a lower threshold mass (density) required for the occurrence of the direct Urca process. Our measurement of  $R_{\text{skin}}(^{208}\text{Pb}) = 0.283$  fm suggests a threshold mass of  $M_{\star} \approx 0.85 M_{\odot}$  and a corresponding threshold density of  $\rho_{\star} \approx 0.24 \text{ fm}^{-3}$ .

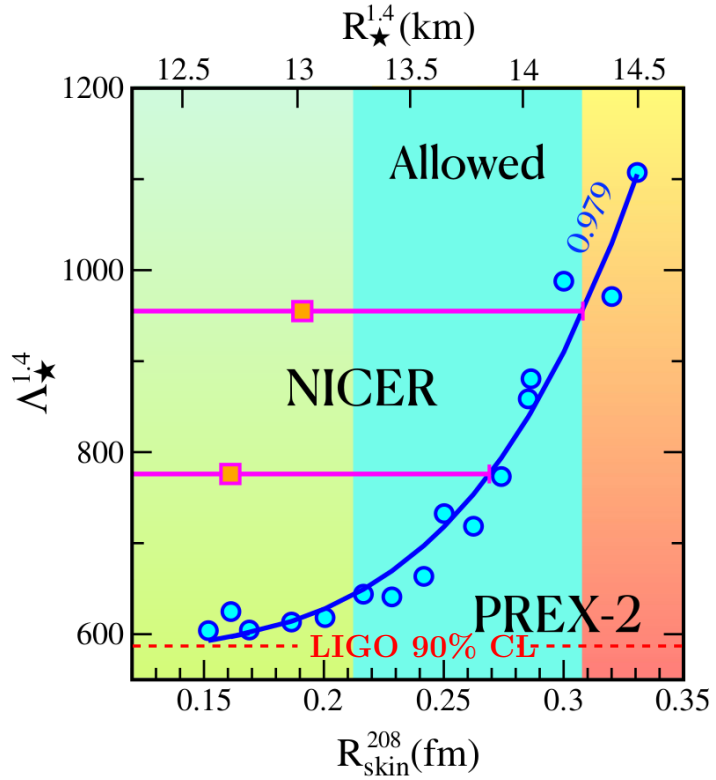


Figure 6.8: Tidal deformability of a  $1.4 M_\odot$  neutron star versus its radius (upper X-axis) and the neutron skin thickness of  $^{208}\text{Pb}$  (lower X-axis). Blue dots represent theoretical predictions from a set of EDFs, while the blue line is a fit to these dots. PREX-2 in the plot refers to the combined result of PREX-I and II. The light blue region corresponds to the radius range allowed by both NICER and PREX-2 [81]

### 6.3 Future Outlook

Parity-violating electron scattering experiments continue to advance and thrive in their development. Several PVES experiments have been proposed to investigate different aspects of EW interactions, including MOLLER [94] and SoLID [52] at JLab, as well as P2 and MREX at Mainz [95].

#### Measurement Of a Lepton Lepton Electroweak Reaction (MOLLER)

As a test of the SM, the weak mixing angle ( $\sin^2 \theta_W$ ) is of great importance and have been measured by different experiments, as shown in Fig. 6.10.

The proposed MOLLER experiment at JLab, as a successor to the SLAC E158 experiment [49], aims to significantly improve the E158 result by a factor of five, which will be a 2.4% relative uncertainty in  $Q_W^e$ , corresponding to a 2.1% relative uncertainty in the measurement of  $\mathcal{A}_{\text{PV}}$  ( $33 \pm 0.7$  ppb). This low energy precision frontier experiment will

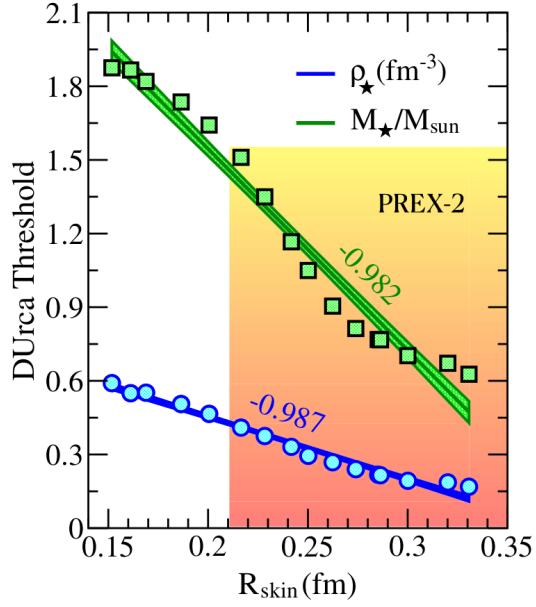


Figure 6.9: The direct Urca threshold densities (blue dots) and corresponding stellar mass (green dots) versus the neutron skin thickness of  $^{208}\text{Pb}$ . PREX-2 in the plot refers to the combined result of PREX-I and II. The shaded area represents the combined PREX  $1-\sigma$  confidence region [81].

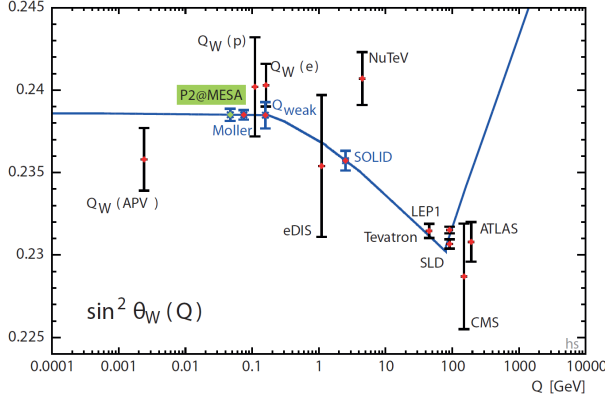


Figure 6.10: Various (proposed) measurements of the running weak mixing angle along the energy scale.

produce the most precise measurement of  $\sin^2 \theta_W$  over the next decade. The high precision of the measurement enables sensitivity to the interference between the known EM amplitude and any possible new neutral currents. This sensitivity allows for probing new particles beyond the Higgs mass, reaching up to a scale of  $\sim 27$  TeV.

## Solenoidal Large Intensity Device (SoLID)

SoLID, another proposal at JLab, focus on probing the parity-violating effect in deep inelastic scattering (PVDIS). SoLID refers to a new spectrometer of large angular and momentum acceptance, meanwhile, it can handle high luminosity. This new apparatus will measure  $\mathcal{A}_{PV}$  to a very high precision of about 0.5% over a wide range of Bjorken  $x$  and  $Q^2$ . The SoLID PVDIS project will employ several different targets. Deuterium will provide a new measurement of the weak mixing angle in the medium energy region, as shown in Fig. 6.10; with a hydrogen target, the proton  $d/u$  ratio can be measured and a heavy nucleus like  $^{208}\text{Pb}$  allows the study of the flavor dependence of the EMC effect [96].

## P2 and MREX

While the MOLLER experiment aims to provide the most precise measurement of the weak mixing angle, the most precise measurement of the weak charge will be carried out by the P2 experiment at Mainz. P2 will measure the weak charge of the proton, a quantity that was previously measured by the Qweak experiment at JLab [50]. Compared to Qweak, P2 plans to improve the measurement precision by a factor of three, aiming for a 0.15% precision in the determination of the weak mixing angle. Similar to MOLLER, the high precision achieved by P2 enables an indirect search for new physics beyond the SM, up to a mass scale of 50 TeV.

Finally, the Mainz radius experiment (MREX) will measure the neutron skin thickness of  $^{208}\text{Pb}$  again, at a lower  $q$  value and will improve the PREX result to a higher precision of 1.4% [95].

Indeed, the advancements in experimental techniques within the field are highly encouraging. The pursuit of higher precision in measuring the parity-violating asymmetry by next-generation PVES experiments positions them as promising candidates for exploring new physics beyond the Standard Model.

These experiments not only have the potential to discover new phenomena and particles but also significantly contribute to our understanding of nuclear physics. By achieving higher precision in PVES measurements, researchers can gain improved insights into nuclear structure, potentially uncovering new aspects that were previously unknown. This continuous drive for precision and the search for new physics create an exciting frontier for scientific exploration in both particle physics and nuclear physics. It is an area where new discoveries and breakthroughs are eagerly anticipated, enriching our understanding of the fundamental nature of matter and the universe.

# Bibliography

- [1] G. Royer. On the coefficients of the liquid drop model mass formulae and nuclear radii. *Nuclear Physics A*, 807(3):105–118, 2008. ISSN 0375-9474. doi: <https://doi.org/10.1016/j.nuclphysa.2008.04.002>. URL <https://www.sciencedirect.com/science/article/pii/S0375947408004739>.
- [2] H. De Vries, C.W. De Jager, and C. De Vries. Nuclear charge-density-distribution parameters from elastic electron scattering. *Atomic Data and Nuclear Data Tables*, 36(3):495–536, 1987. ISSN 0092-640X. doi: [https://doi.org/10.1016/0092-640X\(87\)90013-1](https://doi.org/10.1016/0092-640X(87)90013-1). URL <https://www.sciencedirect.com/science/article/pii/0092640X87900131>.
- [3] I. Angeli and K.P. Marinova. Table of experimental nuclear ground state charge radii: An update. *Atomic Data and Nuclear Data Tables*, 99(1):69–95, 2013. ISSN 0092-640X. doi: <https://doi.org/10.1016/j.adt.2011.12.006>. URL <https://www.sciencedirect.com/science/article/pii/S0092640X12000265>.
- [4] Coupling constants for the fundamental forces. URL <http://hyperphysics.phy-astr.gsu.edu/hbase/Forces/couple.html>.
- [5] B.W. Allardyce, C.J. Batty, D.J. Baugh, E. Friedman, G. Heymann, M.E. Cage, G.J. Pyle, G.T.A. Squier, A.S. Clough, D.F. Jackson, S. Murugesu, and V. Rajaratnam. Pion reaction cross sections and nuclear sizes. *Nuclear Physics A*, 209(1):1–51, 1973. ISSN 0375-9474. doi: [https://doi.org/10.1016/0375-9474\(73\)90049-3](https://doi.org/10.1016/0375-9474(73)90049-3). URL <https://www.sciencedirect.com/science/article/pii/0375947473900493>.
- [6] J.C. Lombardi, R.N. Boyd, R. Arking, and A.B. Robbins. Nuclear sizes in 40, 44, 48ca. *Nuclear Physics A*, 188(1):103–114, 1972. ISSN 0375-9474. doi: [https://doi.org/10.1016/0375-9474\(72\)90186-8](https://doi.org/10.1016/0375-9474(72)90186-8). URL <https://www.sciencedirect.com/science/article/pii/0375947472901868>.
- [7] J. Zenihiro, H. Sakaguchi, T. Murakami, M. Yosoi, Y. Yasuda, S. Terashima, Y. Iwao, H. Takeda, M. Itoh, H. P. Yoshida, and M. Uchida. Neutron density distributions of  $^{204,206,208}\text{Pb}$  deduced via proton elastic scattering at  $E_p = 295$  mev. *Phys. Rev. C*, 82:044611, Oct 2010. doi: 10.1103/PhysRevC.82.044611. URL <https://link.aps.org/doi/10.1103/PhysRevC.82.044611>.

- [8] B. Kłos, A. Trzcińska, J. Jastrzebski, T. Czosnyka, M. Kisielński, P. Lubiński, P. Napiorkowski, L. Pieńkowski, F. J. Hartmann, B. Ketzer, P. Ring, R. Schmidt, T. von Egidy, R. Smolańczuk, S. Wycech, K. Gulda, W. Kurcewicz, E. Widmann, and B. A. Brown. Neutron density distributions from antiprotonic  $^{208}\text{Pb}$  and  $^{209}\text{Bi}$  atoms. *Phys. Rev. C*, 76:014311, Jul 2007. doi: 10.1103/PhysRevC.76.014311. URL <https://link.aps.org/doi/10.1103/PhysRevC.76.014311>.
- [9] A. Krasznahorkay, H. Akimune, A.M. van den Berg, N. Blasi, S. Brandenburg, M. Csatlós, M. Fujiwara, J. Gulyás, M.N. Harakeh, M. Hunyadi, M. de Huu, Z. Matte, D. Sohler, S.Y. van der Werf, H.J. Wołrtche, and L. Zolnai. Neutron-skin thickness in neutron-rich isotopes. *Nuclear Physics A*, 731:224–234, 2004. ISSN 0375-9474. doi: <https://doi.org/10.1016/j.nuclphysa.2003.11.034>. URL <https://www.sciencedirect.com/science/article/pii/S0375947403018712>.
- [10] X. Roca-Maza, B. K. Agrawal, G. Colò, W. Nazarewicz, N. Paar, J. Piekarewicz, P.-G. Reinhard, and D. Vretenar. Sensitivity of the electric dipole polarizability to the neutron skin thickness in  $^{208}\text{pb}$ . In *AIP Conference Proceedings*. AIP, 2012. doi: 10.1063/1.4764239. URL <https://doi.org/10.1063/2F1.4764239>.
- [11] V. Baran, M. Colonna, M. Di Toro, A. Croitoru, and D. Dumitru. Connecting the pygmy dipole resonance to the neutron skin. *Phys. Rev. C*, 88:044610, Oct 2013. doi: 10.1103/PhysRevC.88.044610. URL <https://link.aps.org/doi/10.1103/PhysRevC.88.044610>.
- [12] M. H. Johnson and E. Teller. Proton distribution in heavy nuclei. *Phys. Rev.*, 93: 357–358, Jan 1954. doi: 10.1103/PhysRev.93.357. URL <https://link.aps.org/doi/10.1103/PhysRev.93.357>.
- [13] E.H.S. Burhop, D.H. Davis, J. Sacton, and G. Schorochoff.  $k^-$  meson capture by nuclei and the existence of a neutron halo in heavy nuclei. *Nuclear Physics A*, 132(3):625–628, 1969. ISSN 0375-9474. doi: [https://doi.org/10.1016/0375-9474\(69\)90723-4](https://doi.org/10.1016/0375-9474(69)90723-4). URL <https://www.sciencedirect.com/science/article/pii/0375947469907234>.
- [14] Francesca Sammarruca and Randy Millerson. Nuclear forces in the medium: Insight from the equation of state. *Frontiers in Physics*, 7, 2019. ISSN 2296-424X. doi: 10.3389/fphy.2019.00213. URL <https://www.frontiersin.org/articles/10.3389/fphy.2019.00213>.
- [15] V. Punjabi, C. F. Perdrisat, M. K. Jones, E. J. Brash, and C. E. Carlson. The structure of the nucleon: Elastic electromagnetic form factors, 2015.
- [16] J. B. Bellicard, P. Bounin, R. F. Frosch, R. Hofstadter, J. S. McCarthy, F. J. Uhrhane, M. R. Yearian, B. C. Clark, R. Herman, and D. G. Ravenhall. Scattering of 750-mev electrons by calcium isotopes. *Phys. Rev. Lett.*, 19:527–529, Aug 1967. doi: 10.1103/PhysRevLett.19.527. URL <https://link.aps.org/doi/10.1103/PhysRevLett.19.527>.

- [17] B. Frois, J. B. Bellicard, J. M. Cavedon, M. Huet, P. Leconte, P. Ludeau, A. Nakada, Phan Zuan Hô, and I. Sick. High-momentum-transfer electron scattering from  $^{208}\text{Pb}$ . *Phys. Rev. Lett.*, 38:152–155, Jan 1977. doi: 10.1103/PhysRevLett.38.152. URL <https://link.aps.org/doi/10.1103/PhysRevLett.38.152>.
- [18] L. C. Maximon and R. A. Schrack. The form factor of the Fermi model spatial distribution. *J. Res. Natl. Bur. Stand. B*, 70(1), 1966. doi: 10.6028/jres.070b.007.
- [19] B. G. Todd-Rutel and J. Piekarewicz. Neutron-rich nuclei and neutron stars: A new accurately calibrated interaction for the study of neutron-rich matter. *Phys. Rev. Lett.*, 95:122501, Sep 2005. doi: 10.1103/PhysRevLett.95.122501. URL <https://link.aps.org/doi/10.1103/PhysRevLett.95.122501>.
- [20] C. J. Horowitz. Parity violating elastic electron scattering and coulomb distortions. *Phys. Rev. C*, 57:3430–3436, Jun 1998. doi: 10.1103/PhysRevC.57.3430. URL <https://link.aps.org/doi/10.1103/PhysRevC.57.3430>.
- [21] X. Roca-Maza, M. Centelles, X. Viñas, and M. Warda. Neutron skin of  $^{208}\text{Pb}$ , nuclear symmetry energy, and the parity radius experiment. *Phys. Rev. Lett.*, 106:252501, Jun 2011. doi: 10.1103/PhysRevLett.106.252501. URL <https://link.aps.org/doi/10.1103/PhysRevLett.106.252501>.
- [22] J. Schechter and H. Weigel. The skyrme model for baryons, 1999. URL <https://arxiv.org/abs/hep-ph/9907554>.
- [23] B. Alex Brown. New skyrme interaction for normal and exotic nuclei. *Phys. Rev. C*, 58:220–231, Jul 1998. doi: 10.1103/PhysRevC.58.220. URL <https://link.aps.org/doi/10.1103/PhysRevC.58.220>.
- [24] B. Alex Brown. Neutron radii in nuclei and the neutron equation of state. *Phys. Rev. Lett.*, 85(0):5296–5299, Dec 2000. doi: 10.1103/PhysRevLett.85.5296. URL <https://link.aps.org/doi/10.1103/PhysRevLett.85.5296>.
- [25] Hideki Yukawa. On the Interaction of Elementary Particles. I. *Progress of Theoretical Physics Supplement*, 1:1–10, 01 1955. ISSN 0375-9687. doi: 10.1143/PTPS.1.1. URL <https://doi.org/10.1143/PTPS.1.1>.
- [26] Steven Weinberg. Phenomenological lagrangians. *Physica A: Statistical Mechanics and its Applications*, 96(1):327–340, 1979. ISSN 0378-4371. doi: [https://doi.org/10.1016/0378-4371\(79\)90223-1](https://doi.org/10.1016/0378-4371(79)90223-1). URL <https://www.sciencedirect.com/science/article/pii/0378437179902231>.
- [27] G. Hagen, A. Ekström, C. Forssén, G. R. Jansen, W. Nazarewicz, T. Papenbrock, K. A. Wendt, S. Bacca, N. Barnea, B. Carlsson, C. Drischler, K. Hebeler, M. Hjorth-Jensen, M. Miorelli, G. Orlandini, A. Schwenk, and J. Simonis. Neutron and weak-charge distributions of the  $^{48}\text{Ca}$ nucleus. *Nature Physics*, 12(2):186–190, Feb 2016. ISSN 1745-2481. doi: 10.1038/nphys3529. URL <https://doi.org/10.1038/nphys3529>.

- [28] J. M. Lattimer and M. Prakash. Neutron star structure and the equation of state. *The Astrophysical Journal*, 550(1):426–442, mar 2001. doi: 10.1086/319702. URL <https://doi.org/10.1086/319702>.
- [29] Thomas Mannel. Theory and phenomenology of cp violation. *Nuclear Physics B - Proceedings Supplements*, 167:170–174, 2007. ISSN 0920-5632. doi: <https://doi.org/10.1016/j.nuclphysbps.2006.12.083>. URL <https://www.sciencedirect.com/science/article/pii/S0920563206010711>. Proceedings of the 7th International Conference on Hyperons, Charm and Beauty Hadrons.
- [30] Enrico Fermi. Tentativo di una teoria dei raggi  $\beta$ . *Il Nuovo Cimento (1924-1942)*, 11(1):1–19, Jan 1934. ISSN 1827-6121. doi: 10.1007/BF02959820. URL <https://doi.org/10.1007/BF02959820>.
- [31] T. D. Lee and C. N. Yang. Parity nonconservation and a two-component theory of the neutrino. *Phys. Rev.*, 105:1671–1675, Mar 1957. doi: 10.1103/PhysRev.105.1671. URL <https://link.aps.org/doi/10.1103/PhysRev.105.1671>.
- [32] C. S. Wu, E. Ambler, R. W. Hayward, D. D. Hoppes, and R. P. Hudson. Experimental test of parity conservation in beta decay. *Phys. Rev.*, 105:1413–1415, Feb 1957. doi: 10.1103/PhysRev.105.1413. URL <https://link.aps.org/doi/10.1103/PhysRev.105.1413>.
- [33] M. Goldhaber, L. Grodzins, and A. W. Sunyar. Helicity of neutrinos. *Phys. Rev.*, 109:1015–1017, Feb 1958. doi: 10.1103/PhysRev.109.1015. URL <https://link.aps.org/doi/10.1103/PhysRev.109.1015>.
- [34] E. C. G. Sudarshan and R. E. Marshak. Chirality invariance and the universal fermi interaction. *Phys. Rev.*, 109:1860–1862, Mar 1958. doi: 10.1103/PhysRev.109.1860.2. URL <https://link.aps.org/doi/10.1103/PhysRev.109.1860.2>.
- [35] R. P. Feynman and M. Gell-Mann. Theory of the fermi interaction. *Phys. Rev.*, 109:193–198, Jan 1958. doi: 10.1103/PhysRev.109.193. URL <https://link.aps.org/doi/10.1103/PhysRev.109.193>.
- [36] Sheldon L. Glashow. Partial-symmetries of weak interactions. *Nuclear Physics*, 22(4):579–588, 1961. ISSN 0029-5582. doi: [https://doi.org/10.1016/0029-5582\(61\)90469-2](https://doi.org/10.1016/0029-5582(61)90469-2). URL <https://www.sciencedirect.com/science/article/pii/0029558261904692>.
- [37] Steven Weinberg. A model of leptons. *Phys. Rev. Lett.*, 19:1264–1266, Nov 1967. doi: 10.1103/PhysRevLett.19.1264. URL <https://link.aps.org/doi/10.1103/PhysRevLett.19.1264>.
- [38] Abdus Salam. Weak and Electromagnetic Interactions. *Conf. Proc. C*, 680519:367–377, 1968. doi: 10.1142/9789812795915\_0034.

- [39] F.J. Hasert, S. Kabe, W. Krenz, J. Von Krogh, D. Lanske, J. Morfin, K. Schultze, H. Weerts, G. Bertrand-Coremans, J. Sacton, W. Van Doninck, P. Vilain, R. Baldi, U. Camerini, D.C. Cundy, I. Danilchenko, W.F. Fry, D. Haidt, S. Natali, P. Musset, B. Osculati, R. Palmer, J.B.M. Pattison, D.H. Perkins, A. Pullia, A. Rousset, W. Venus, H. Wachsmuth, V. Brisson, B. Degrange, M. Haguenuer, L. Kluberg, U. Nguyen-Khac, P. Petiau, E. Bellotti, S. Bonetti, D. Cavalli, C. Conta, E. Fiorini, M. Rollier, B. Aubert, D. Blum, L.M. Chouinet, P. Heusse, A. Lagarrigue, A.M. Lutz, A. Orkin-Lecourtois, J.P. Vialle, F.W. Bullock, M.J. Esten, T.W. Jones, J. McKenzie, A.G. Michette, G. Myatt, and W.G. Scott. Observation of neutrino-like interactions without muon or electron in the gargamelle neutrino experiment. *Nuclear Physics B*, 73(1):1–22, 1974. ISSN 0550-3213. doi: [https://doi.org/10.1016/0550-3213\(74\)90038-8](https://doi.org/10.1016/0550-3213(74)90038-8). URL <https://www.sciencedirect.com/science/article/pii/0550321374900388>.
- [40] None None. The frontiers of nuclear science: A long-range plan. 12 2007. doi: 10.2172/1375323. URL <https://www.osti.gov/biblio/1375323>.
- [41] Ya. B. Zel'dovich. Parity nonconservation in the first order in the weak-interaction constant in electron scattering and other effects. *Journal of Experimental and Theoretical Physics*, 9(3):682, 1959. URL [http://www.jetp.ras.ru/cgi-bin/dn/e\\_009\\_03\\_0682.pdf](http://www.jetp.ras.ru/cgi-bin/dn/e_009_03_0682.pdf).
- [42] C.Y. Prescott, W.B. Atwood, R.L.A. Cottrell, H. DeStaebler, Edward L. Garwin, A. Gonidec, R.H. Miller, L.S. Rochester, T. Sato, D.J. Sherden, C.K. Sinclair, S. Stein, R.E. Taylor, J.E. Clendenin, V.W. Hughes, N. Sasao, K.P. Schüler, M.G. Borghini, K. Lübelsmeyer, and W. Jentschke. Parity non-conservation in inelastic electron scattering. *Physics Letters B*, 77(3):347–352, 1978. ISSN 0370-2693. doi: [https://doi.org/10.1016/0370-2693\(78\)90722-0](https://doi.org/10.1016/0370-2693(78)90722-0). URL <https://www.sciencedirect.com/science/article/pii/0370269378907220>.
- [43] P. A. Souder, R. Holmes, D.-H. Kim, K. S. Kumar, M. E. Schulze, K. Isakovich, G. W. Dodson, K. W. Dow, M. Farkhondeh, S. Kowalski, M. S. Lubell, J. Belanca, M. Goodman, S. Patch, Richard Wilson, G. D. Cates, S. Dhawan, T. J. Gay, V. W. Hughes, A. Magnon, R. Michaels, and H. R. Schaefer. Measurement of parity violation in the elastic scattering of polarized electrons from  $^{12}\text{C}$ . *Phys. Rev. Lett.*, 65:694–697, Aug 1990. doi: 10.1103/PhysRevLett.65.694. URL <https://link.aps.org/doi/10.1103/PhysRevLett.65.694>.
- [44] W. Heil, J. Ahrens, H.G. Andresen, A. Bornheimer, D. Conrath, K.-J. Dietz, W. Gasteyer, H.-J. Gessinger, W. Hartmann, J. Jethwa, H.-J. Kluge, H. Kessler, T. Kettner, L. Koch, F. Neugebauer, R. Neuhausen, E.W. Otten, E. Reichert, F.P. Schäfer, and B. Wagner. Improved limits on the weak, neutral, hadronic axial vector coupling constants from quasielastic scattering of polarized electrons. *Nuclear Physics B*, 327(1):1–31, 1989. ISSN 0550-3213. doi: [https://doi.org/10.1016/0550-3213\(89\)90284-8](https://doi.org/10.1016/0550-3213(89)90284-8). URL <https://www.sciencedirect.com/science/article/pii/0550321389902848>.

- [45] Sample at mit-bates. URL <https://bateslab.mit.edu/projects/sample>.
- [46] The g0 experiment. URL <http://research.npl.illinois.edu/exp/G0/publicWeb/>.
- [47] Happex collaboration. URL <https://hallaweb.jlab.org/experiment/HAPPEX/>.
- [48] A4 collaboration at mami. URL <https://www.blogs.uni-mainz.de/fb08-ag-maas/a4-collaboration-at-mami/>.
- [49] P. L. et al. Anthony. Precision measurement of the weak mixing angle in möller scattering. *Phys. Rev. Lett.*, 95:081601, Aug 2005. doi: 10.1103/PhysRevLett.95.081601. URL <https://link.aps.org/doi/10.1103/PhysRevLett.95.081601>.
- [50] D. et al. Androic. First determination of the weak charge of the proton. *Phys. Rev. Lett.*, 111:141803, Oct 2013. doi: 10.1103/PhysRevLett.111.141803. URL <https://link.aps.org/doi/10.1103/PhysRevLett.111.141803>.
- [51] D. et al. Wang. Measurements of parity-violating asymmetries in electron-deuteron scattering in the nucleon resonance region. *Phys. Rev. Lett.*, 111:082501, Aug 2013. doi: 10.1103/PhysRevLett.111.082501. URL <https://link.aps.org/doi/10.1103/PhysRevLett.111.082501>.
- [52] SoLID Collaboration. Precision measurement of parity-violation in deep inelastic scattering over a broad kinematic range. 2008. URL <https://hallaweb.jlab.org/collab/PAC/PAC34/PR-09-012-pvdis.pdf>.
- [53] Moller. URL [https://moller.jlab.org/moller\\_root/](https://moller.jlab.org/moller_root/).
- [54] Mesa-p2. URL <https://www.blogs.uni-mainz.de/fb08p2/>.
- [55] J. Alcorn et al. Basic instrumentation for hall a at jefferson lab. *Nuclear Instruments and Methods in Physics Research Section A: Accelerators, Spectrometers, Detectors and Associated Equipment*, 522(3):294–346, 2004. ISSN 0168-9002. doi: <https://doi.org/10.1016/j.nima.2003.11.415>. URL <https://www.sciencedirect.com/science/article/pii/S0168900203033977>.
- [56] S. et al. Abrahamyan. Measurement of the neutron radius of  $^{208}\text{Pb}$  through parity violation in electron scattering. *Phys. Rev. Lett.*, 108:112502, Mar 2012. doi: 10.1103/PhysRevLett.108.112502. URL <https://link.aps.org/doi/10.1103/PhysRevLett.108.112502>.
- [57] Juliette Mammei et al. Proposal to jefferson lab pac 40 crex: Parity-violating measurement of the weak charge distribution of 48 ca to 0.02 fm accuracy. 2013. URL [https://hallaweb.jlab.org/parity/prex/c-rex2013\\_v7.pdf](https://hallaweb.jlab.org/parity/prex/c-rex2013_v7.pdf).
- [58] Kent D. Paschke et al. Proposal to jefferson lab pac 38 prex-ii: Precision parity-violating measurement of the neutron skin of lead. 2011. URL <https://hallaweb.jlab.org/parity/prex/prexII.pdf>.

- [59] The Hall A Collaboration. Jefferson lab hall a standard equipment manual. Jun 2019. URL <https://hallaweb.jlab.org/github/halla-osp/version/Standard-Equipment-Manual.pdf>.
- [60] E. L. Garwin D. T. Pierce and H. C. Siegmann. *Helv. Phys. Acta*, 47:393, 1974.
- [61] G. Lampel and C. Weisbuch. Proposal for an efficient source of polarized photo-electrons from semiconductors. *Solid State Communications*, 16(7):877–880, 1975. ISSN 0038-1098. doi: [https://doi.org/10.1016/0038-1098\(75\)90884-4](https://doi.org/10.1016/0038-1098(75)90884-4). URL <https://www.sciencedirect.com/science/article/pii/0038109875908844>.
- [62] L.S. Cardman. Polarized electron sources for the 1990’s. *Nuclear Physics A*, 546(1):317–336, 1992. ISSN 0375-9474. doi: [https://doi.org/10.1016/0375-9474\(92\)90518-O](https://doi.org/10.1016/0375-9474(92)90518-O). URL <https://www.sciencedirect.com/science/article/pii/0375947492905180>.
- [63] Caryn A. Palatchi. *Thesis: Laser and Electron Beam Technology for Parity Violating Electron Scattering Measurements*. PhD thesis, 2019. URL [https://misportal.jlab.org/ul/publications/search/advanced\\_search.cfm](https://misportal.jlab.org/ul/publications/search/advanced_search.cfm).
- [64] Philip A. Adderley, Steven Covert, Joseph Grames, John Hansknecht, Kenneth Surles-Law, Danny Machie, Bernard Poelker, Marcy L. Stutzman, Riad Suleiman, and James Clark. Photoinjector improvements at cebaf in support of parity violation experiments. *Nuovo Cimento C*, 35(4), 7 2012. ISSN 1826-9885. doi: 10.1393/ncc/i2012-11288-3. URL <https://www.osti.gov/biblio/1059486>.
- [65] J. M. Grames, C. K. Sinclair, M. Poelker, X. Roca-Maza, M. L. Stutzman, R. Suleiman, Md. A. Mamun, M. McHugh, D. Moser, J. Hansknecht, B. Moffit, and T. J. Gay. High precision 5 mev mott polarimeter. *Phys. Rev. C*, 102:015501, Jul 2020. doi: 10.1103/PhysRevC.102.015501. URL <https://link.aps.org/doi/10.1103/PhysRevC.102.015501>.
- [66] Noah Sherman. Coulomb scattering of relativistic electrons by point nuclei. *Phys. Rev.*, 103:1601–1607, Sep 1956. doi: 10.1103/PhysRev.103.1601. URL <https://link.aps.org/doi/10.1103/PhysRev.103.1601>.
- [67] J. M. Grames, C. K. Sinclair, J. Mitchell, E. Chudakov, H. Fenker, A. Freyberger, D. W. Higinbotham, M. Poelker, M. Steigerwald, M. Tiefenback, C. Cavata, S. Escoffier, F. Marie, T. Pussieux, P. Vernin, S. Danagoulian, V. Dharmawardane, R. Fatemi, K. Joo, M. Zeier, V. Gorbenko, R. Nasseripour, B. Raue, R. Suleiman, and B. Zihlmann. Unique electron polarimeter analyzing power comparison and precision spin-based energy measurement. *Phys. Rev. ST Accel. Beams*, 7:042802, Apr 2004. doi: 10.1103/PhysRevSTAB.7.042802. URL <https://link.aps.org/doi/10.1103/PhysRevSTAB.7.042802>.

- [68] J.-C. Denard, A. Saha, and G. Laveissiere. High accuracy beam current monitor system for cebaf's experimental hall a. In *PACS2001. Proceedings of the 2001 Particle Accelerator Conference (Cat. No.01CH37268)*, volume 3, pages 2326–2328 vol.3, 2001. doi: 10.1109/PAC.2001.987367.
- [69] Devi Lal Adhikari. *Thesis: Neutron Skin Measurement of  $^{208}\text{Pb}$  Using Parity-Violating Electron Scattering*. PhD thesis, 2021. URL [https://misportal.jlab.org/ul/publications/search/advanced\\_search.cfm](https://misportal.jlab.org/ul/publications/search/advanced_search.cfm).
- [70] Hall a images. URL <https://www.jlab.org/help/Ghelp/halla3d.html>.
- [71] K.G Fissum, W Bertozzi, J.P Chen, D Dale, H.C Fenker, J Gao, A Gavalya, S Gilad, C.R Leathers, N Liyanage, R.O Michaels, E.A.J.M Offermann, J Segal, J.A Templon, R Wechsler, B Wojtsekowski, and J Zhao. Vertical drift chambers for the hall a high-resolution spectrometers at jefferson lab. *Nuclear Instruments and Methods in Physics Research Section A: Accelerators, Spectrometers, Detectors and Associated Equipment*, 474(2):108–131, 2001. ISSN 0168-9002. doi: [https://doi.org/10.1016/S0168-9002\(01\)00875-0](https://doi.org/10.1016/S0168-9002(01)00875-0). URL <https://www.sciencedirect.com/science/article/pii/S0168900201008750>.
- [72] Coda. URL <https://coda.jlab.org/drupal/>.
- [73] Roger Flood, Scott Higgins, , and Riad Suleiman. Helicity control board user's guide (draft 2). 2010.
- [74] Epics. URL <https://epics.anl.gov/>.
- [75] Cameron Clarke. *Thesis: Measurement of Parity Violating Asymmetry in Elastic Electron Scattering off  $^{48}\text{Ca}$* . PhD thesis, 2021. URL [https://misportal.jlab.org/ul/publications/search/advanced\\_search.cfm](https://misportal.jlab.org/ul/publications/search/advanced_search.cfm).
- [76] S. et al. Abrahamyan. New measurements of the transverse beam asymmetry for elastic electron scattering from selected nuclei. *Phys. Rev. Lett.*, 109:192501, Nov 2012. doi: 10.1103/PhysRevLett.109.192501. URL <https://link.aps.org/doi/10.1103/PhysRevLett.109.192501>.
- [77] Oleksandr Koshchii, Mikhail Gorchtein, Xavier Roca-Maza, and Hubert Spiesberger. Beam-normal single-spin asymmetry in elastic scattering of electrons from a spin-0 nucleus. *Phys. Rev. C*, 103:064316, Jun 2021. doi: 10.1103/PhysRevC.103.064316. URL <https://link.aps.org/doi/10.1103/PhysRevC.103.064316>.
- [78] D. et al. Adhikari. New measurements of the beam-normal single spin asymmetry in elastic electron scattering over a range of spin-0 nuclei. *Phys. Rev. Lett.*, 128:142501, Apr 2022. doi: 10.1103/PhysRevLett.128.142501. URL <https://link.aps.org/doi/10.1103/PhysRevLett.128.142501>.

- [79] Ryan Richards. *Measurements of the Beam Normal Asymmetry using Polarized Elastic Electron Scattering off Various Spin-0 Nuclei at 1 GeV*. PhD thesis, 2021. URL [https://misportal.jlab.org/ul/publications/search/advanced\\_search.cfm](https://misportal.jlab.org/ul/publications/search/advanced_search.cfm).
- [80] D. et al. Adhikari. Accurate determination of the neutron skin thickness of  $^{208}\text{Pb}$  through parity-violation in electron scattering. *Phys. Rev. Lett.*, 126:172502, Apr 2021. doi: 10.1103/PhysRevLett.126.172502. URL <https://link.aps.org/doi/10.1103/PhysRevLett.126.172502>.
- [81] Brendan T. Reed, F. J. Fattoyev, C. J. Horowitz, and J. Piekarewicz. Implications of prex-2 on the equation of state of neutron-rich matter. *Phys. Rev. Lett.*, 126:172503, Apr 2021. doi: 10.1103/PhysRevLett.126.172503. URL <https://link.aps.org/doi/10.1103/PhysRevLett.126.172503>.
- [82] D. et al. Adhikari. Precision determination of the neutral weak form factor of  $^{48}\text{Ca}$ . *Phys. Rev. Lett.*, 129:042501, Jul 2022. doi: 10.1103/PhysRevLett.129.042501. URL <https://link.aps.org/doi/10.1103/PhysRevLett.129.042501>.
- [83] Discovery of nuclides project. URL <https://people.nscl.msu.edu/~thoennes/isotopes/>.
- [84] D. S. Ahn, N. Fukuda, H. Geissel, N. Inabe, N. Iwasa, T. Kubo, K. Kusaka, D. J. Morrissey, D. Murai, T. Nakamura, M. Ohtake, H. Otsu, H. Sato, B. M. Sherrill, Y. Shimizu, H. Suzuki, H. Takeda, O. B. Tarasov, H. Ueno, Y. Yanagisawa, and K. Yoshida. Location of the neutron dripline at fluorine and neon. *Phys. Rev. Lett.*, 123:212501, Nov 2019. doi: 10.1103/PhysRevLett.123.212501. URL <https://link.aps.org/doi/10.1103/PhysRevLett.123.212501>.
- [85] Erler, Jochen, Birge, Noah, Kortelainen, Markus, Nazarewicz, Witold, Olsen, Erik, Perhac, Alexander M., Stoitsov, and Mario. The limits of the nuclear landscape. *Nature*, 486(7404):509–512, Jun 2012. ISSN 1476-4687. doi: 10.1038/nature11188. URL <https://doi.org/10.1038/nature11188>.
- [86] C. J. Horowitz, J. Piekarewicz, and Brendan Reed. Insights into nuclear saturation density from parity-violating electron scattering. *Phys. Rev. C*, 102:044321, Oct 2020. doi: 10.1103/PhysRevC.102.044321. URL <https://link.aps.org/doi/10.1103/PhysRevC.102.044321>.
- [87] Wei-Chia Chen and J. Piekarewicz. Building relativistic mean field models for finite nuclei and neutron stars. *Phys. Rev. C*, 90:044305, Oct 2014. doi: 10.1103/PhysRevC.90.044305. URL <https://link.aps.org/doi/10.1103/PhysRevC.90.044305>.
- [88] C. Drischler, K. Hebeler, and A. Schwenk. Chiral interactions up to next-to-next-to-next-to-leading order and nuclear saturation. *Phys. Rev. Lett.*, 122:042501, Jan 2019. doi: 10.1103/PhysRevLett.122.042501. URL <https://link.aps.org/doi/10.1103/PhysRevLett.122.042501>.

- [89] The neutron star interior composition explorer mission. URL <https://heasarc.gsfc.nasa.gov/docs/nicer/>.
- [90] B. P. et al. Abbott. Gw170817: Observation of gravitational waves from a binary neutron star inspiral. *Phys. Rev. Lett.*, 119:161101, Oct 2017. doi: 10.1103/PhysRevLett.119.161101. URL <https://link.aps.org/doi/10.1103/PhysRevLett.119.161101>.
- [91] B. P. et al. Abbott. Gw170817: Measurements of neutron star radii and equation of state. *Phys. Rev. Lett.*, 121:161101, Oct 2018. doi: 10.1103/PhysRevLett.121.161101. URL <https://link.aps.org/doi/10.1103/PhysRevLett.121.161101>.
- [92] Paweł Haensel. Urca processes in dense matter and neutron star cooling. *Space Science Reviews*, 74(3):427–436, Nov 1995. ISSN 1572-9672. doi: 10.1007/BF00751429. URL <https://doi.org/10.1007/BF00751429>.
- [93] Edward F. Brown, Andrew Cumming, Farrukh J. Fattoyev, C. J. Horowitz, Dany Page, and Sanjay Reddy. Rapid neutrino cooling in the neutron star mxb 1659-29. *Phys. Rev. Lett.*, 120:182701, Apr 2018. doi: 10.1103/PhysRevLett.120.182701. URL <https://link.aps.org/doi/10.1103/PhysRevLett.120.182701>.
- [94] MOLLER Collaboration. The moller experiment: An ultra-precise measurement of the weak mixing angle using møller scattering. 2014. doi: 10.48550/ARXIV.1411.4088. URL <https://arxiv.org/abs/1411.4088>.
- [95] Dominik et al. Becker. The p2 experiment. *The European Physical Journal A*, 54(11):208, Nov 2018. ISSN 1434-601X. doi: 10.1140/epja/i2018-12611-6. URL <https://doi.org/10.1140/epja/i2018-12611-6>.
- [96] Jean-Jacques et al. Aubert. The ratio of the nucleon structure functions  $F_2^N$  for iron and deuterium. *Phys. Lett. B*, 123:275–278, 1983. doi: 10.1016/0370-2693(83)90437-9. URL <https://cds.cern.ch/record/142300>.

# Appendix A

## Symmetry Energy

$$E_k = C(N^{5/3} + Z^{5/3})$$

Let:  $A = N + Z$  and  $B = N - Z$ , then we have  $N + \frac{A+B}{2}$ ,  $Z = \frac{A-B}{2}$  and  $B \ll A$ :

$$\begin{aligned} E_k &= C \left( \left( \frac{A+B}{2} \right)^{5/3} + \left( \frac{A-B}{2} \right)^{5/3} \right) \\ &= C \left( \frac{A}{2} \right)^{5/3} \left( \left( 1 + \frac{B}{A} \right)^{5/3} + \left( 1 - \frac{B}{A} \right)^{5/3} \right) \\ &= C \left( \frac{A}{2} \right)^{5/3} \left( \left( 1 + \frac{5B}{3A} + \frac{1}{2!} \frac{5}{3} \frac{2}{3} \left( \frac{B}{A} \right)^2 + \dots \right) + \left( 1 + \frac{5}{3} \left( -\frac{B}{A} \right) + \frac{1}{2!} \frac{5}{3} \frac{2}{3} \left( -\frac{B}{A} \right)^2 + \dots \right) \right) \\ &= 2^{-2/3} C \left( A^{5/3} + \frac{5}{9} \frac{B^2}{A^{1/3}} \right) + O\left(\frac{B^4}{A^{7/3}}\right) \\ &= 2^{-2/3} C \left( A^{5/3} + \frac{5}{9} \frac{(N-Z)^2}{A^{1/3}} \right) + O((N-Z)^4) \end{aligned}$$

### A.1 $^{208}\text{Pb}$ Foils Measurement

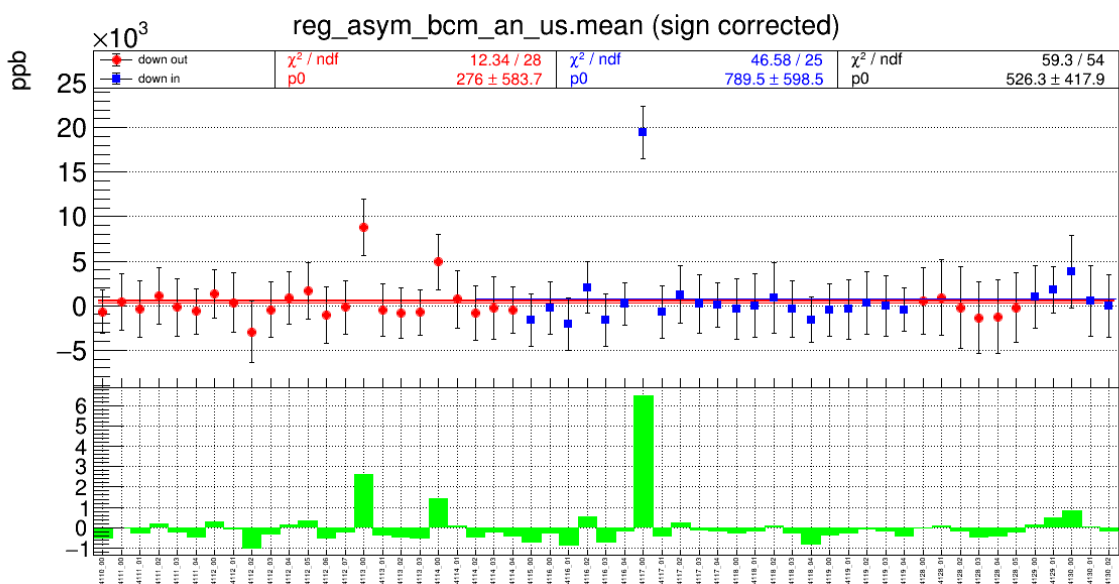


Figure A.1: charge asymmetry outlier in run 4117, minirun 0

Pb #	mass (g)	top left (mm)				top right (mm)				bottom right (mm)				bottom left (mm)				area (mm <sup>2</sup> )	t ( $\mu$ m)	area density (mg/cm <sup>2</sup> )
		x1	y1	x2	y2	x3	y3	x4	y4	x4	y4	x3	y3	x2	y2	x1	y1			
1	3.6526	0.005	-0.015	24.221	0.532	24.956	-23.743	0.655	-24.249	588.3778	545.51	620.792								
2	3.6973	-0.005	-0.012	24.079	-0.2	23.897	-24.338	-0.327	-24.294	584.7683	555.60	632.267								
3	3.6325	-0.009	0.01	24.156	-0.039	24.08	-24.06	-0.194	-23.904	580.4809	549.89	625.774								
4	3.6722	-0.013	-0.003	24.1	-0.302	24.048	-24.386	-0.133	-24.363	584.8886	551.71	627.846								
5	3.6989	-0.002	-0.001	24.199	0.003	24.261	-24.136	0.083	-24.249	585.2287	555.40	632.044								
6	3.6162	-0.005	-0.001	24.328	-0.223	24.012	-24.386	0.026	-24.276	585.1189	543.08	618.028								
7	3.6966	0.001	0.003	24.208	0.007	24.155	-23.991	0.022	-23.869	578.5090	561.50	638.988								
8	3.6315	0.008	0.002	24.115	0.016	23.969	-24.312	-0.158	-24.204	585.2472	545.26	620.507								
9	3.6307	0.005	0.003	24.216	-0.268	23.992	-24.704	-0.149	-24.421	590.6197	540.18	614.727								
10	3.6283	-0.052	-0.029	23.973	-0.225	24.032	-24.234	-0.297	-24.213	582.5811	547.27	622.797								

Table A.1: area was calculated as  $A = \frac{(x_2-x_1)+(x_3-x_4)}{2} \times \frac{(y_1-y_3)+(y_2-y_4)}{2}$ .  $^{208}\text{Pb}$  density is  $11.38 \text{ g/cm}^2$ .

run	#entry	$\theta$			$Q^2$		
		mean	RMS	mean error	mean	RMS	mean error
1853	248697	4.741	0.447	8.96E-4	0.006239	0.001204	2.41E-6
1983	746777	4.747	0.4536	5.25E-4	0.006264	0.001223	1.42E-6
1996	513128	4.740	0.4461	6.23E-4	0.006244	0.001203	1.68E-6
2052	573912	4.741	0.444	5.86E-4	0.006246	0.001198	1.58E-6
2199	387046	4.751	0.466	7.49E-4	0.006286	0.001259	2.02E-6
2291	250751	4.753	0.4633	9.25E-4	0.006282	0.001248	2.49E-6
2292	188412	4.753	0.4622	1.06E-3	0.006281	0.001244	2.87E-6
2293	248789	4.754	0.4637	9.30E-4	0.006284	0.001249	2.50E-6
2294	190029	4.752	0.462	1.06E-3	0.00628	0.001244	2.85E-6
2316	21379	4.752	0.464	3.17E-3	0.00628	0.001252	8.56E-6
2317	105672	4.746	0.4634	1.43E-3	0.006266	0.001251	3.85E-6
2319	15100	4.746	0.4621	3.76E-3	0.006266	0.001247	1.01E-5
2320	100386	4.742	0.4607	1.45E-3	0.006254	0.001243	3.92E-6
20981	245995	4.808	0.4409	8.89E-4	0.006401	0.001202	2.42E-6
21415	156514	4.814	0.4576	1.16E-3	0.006427	0.001245	3.15E-6
21435	19780	4.816	0.4597	3.27E-3	0.006434	0.001256	8.93E-6
21436	367261	4.812	0.4585	7.57E-4	0.006424	0.001252	2.07E-6
21438	59044	4.814	0.461	1.90E-3	0.006428	0.001259	5.18E-6

Table A.2: Optics data. The database used here was different from the final version. That's why the scattering angles were different from that in the published paper.